SIMPLER

FASTER

TOWARDS BROAD APPLICATION OF LASER SPECKLE IMAGING IN ART CONSERVATION AND SOFT MATTER

SOFTER

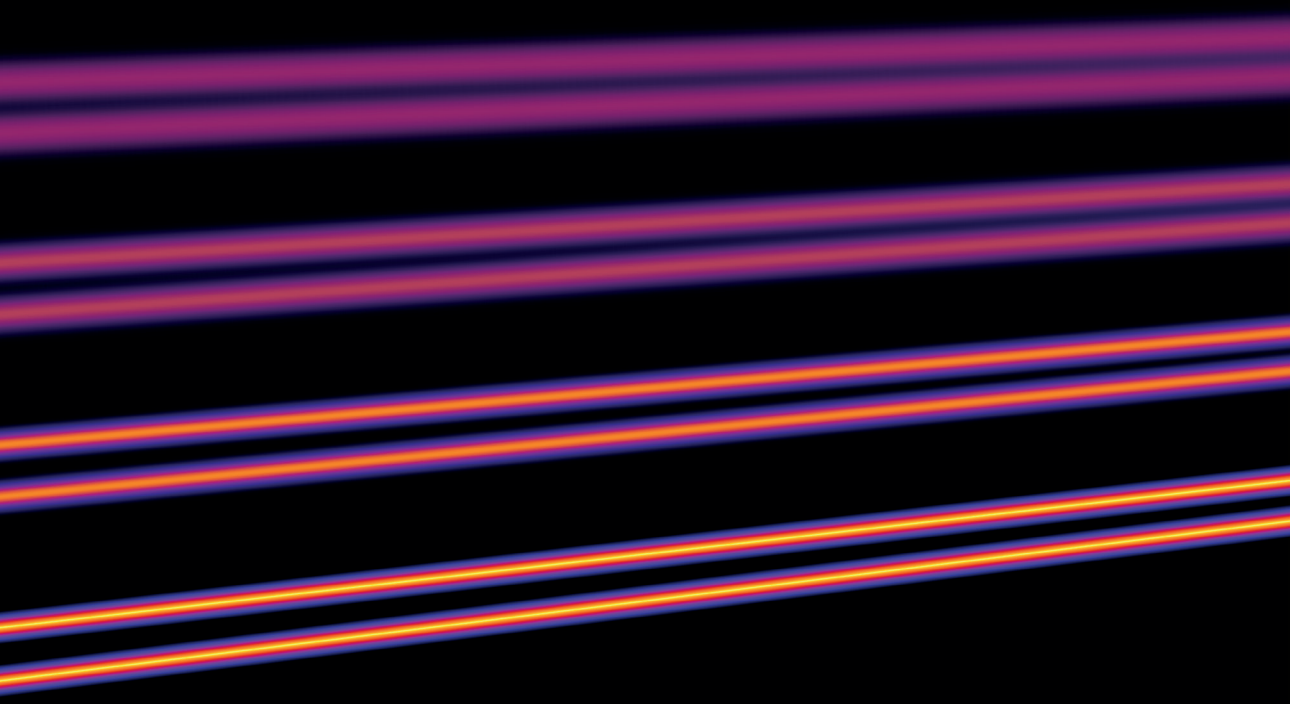

JESSE BUIJS

Propositions

1. Broad application of laser speckle imaging only requires a robust set-up and a successful marketing strategy. (This thesis)

2. Imaging tasks become easier as the laser grows bigger. (This thesis)

3. A granted proposal requires a larger writing effort than a published paper.

4. A multidisciplinary approach shortens the time from fundamental to applied science.

5. Since there is no necessary causality between the number of citations and truthfulness, academia is vulnerable for "fake science".

6. All Star Trek technologies except light-speed travel and teleportation will be feasible before the end of this century.

7. Guinea pigs are perfectly fit for bio-industry without animal-cruelty.

Propositions belonging to the thesis, entitled

Simpler, Faster, and Softer
Towards broad application of Laser Speckle Imaging in art conservation and soft matter

J. Jesse Buijs

Wageningen, 26 April 2022

Simpler, Faster, and Softer

Towards broad application of Laser Speckle Imaging in art conservation and soft matter

J. Jesse Buijs

Thesis committee

Promotors

Prof. Dr J. van der Gucht
Professor of Physical Chemistry and Soft Matter
Wageningen University & Research

Prof. Dr J. Sprakel
Personal chair, Physical Chemistry and Soft Matter
Wageningen University & Research

Other members

Prof. Dr E. van der Linden, Wageningen University & Research
Dr R. van Langh, Rijksmuseum Amsterdam
Dr J. Janssen, Unilever R&D, Wageningen
Prof. Dr J. Crassous, Université de Rennes 1, Rennes, France

This research was conducted under the auspices of Graduate School VLAG
(Advanced studies in Food Technology, Agrobiotechnology, Nutrition and Health Sciences).

Simpler, Faster, and Softer

Towards broad application of Laser Speckle Imaging in art conservation and soft matter

J. Jesse Buijs

Thesis
submitted in fulfilment of the requirements for the degree of doctor
at Wageningen University
by the authority of the Rector Magnificus,
Prof. Dr A.P. J. Mol,
in the presence of the
Thesis Committee appointed by the Academic Board,
to be defended in public
on Tuesday 26 April 2022
at 4 p.m. in the Aula.

J. Jesse Buijs
Simpler, Faster, and Softer — Towards broad application of Laser Speckle Imaging in art conservation and soft matter
191 pages

PhD thesis, Wageningen University, Wageningen, The Netherlands (2022)
With references, with summary in English

ISBN: 978-94-6447-086-4
DOI: https://doi.org/10.18174/562080

Contents

Chapter 1

Introduction

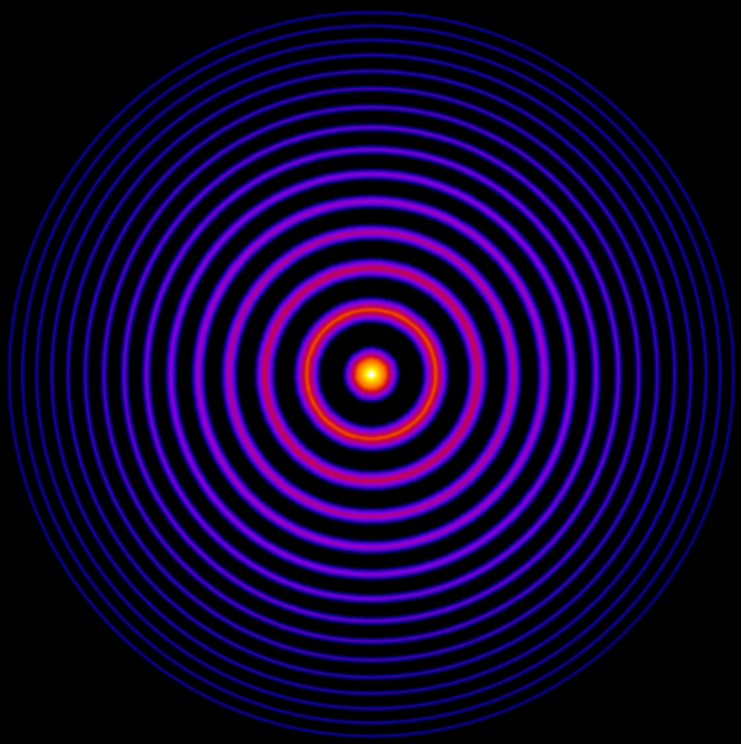

"America produced not only scientists and engineers capable of shaping the destiny of our age, but also artists worthy to keep them company."

The development of spaceflight was undoubtedly a technical and scientific breakthrough in its own right. However, NASA understood very well that much was to gain from inspiring the general public. Therefore they invited artists to their facilities to paint 'whatever interested them'. This resulted in an extraordinary collection and the aforementioned quote. The title of this thesis is loosely inspired by the name of one of the paintings from this collection: '*Higher, faster, and farther*' painted by Dong Kingman which is shown in figure 1.1. The painting shows the Saturn I rocket on the launch-pad. This rocket could fly *higher and faster*, and it took the space program one step *farther* away from Earth.[1] The goal of the space program was to explore the biggest object that we know: space. Contrary, our research is aimed at exploring the small scale: visualizing nano-metric motions inside materials. We explore and improve on a medical imaging technique, Laser Speckle Imaging (LSI),[2] which in essence is a very sensitive motion detector. We make the machine *simpler*, the data analysis *faster*, and show how to detect motion in *softer* materials. This all in an effort to make the technique *broadly applicable*. We will explore application in two fields: *art conservation* and *soft matter* as examples of what LSI could achieve in other fields.

1.1 Ultra-sensitive motion detection

LSI is an extremely sensitive motion detection technique because it uses the principle of interference of light. This principle was already used in 1887, in what has grown to be the most famous negative result experiment: the Michelson-Morley aether experiment. Scientists at that time believed that light-waves had to move through a medium, the so called aether. To prove the existence of the aether, Michelson and Morley built an interferometer (fig. 1.2a), which could measure changes in the speed of light as a result of 'aether wind'. A beam of light was split in two, sent in two perpendicular directions, reflected and recombined. Combining two light beams from the same source gives rise to an interference pattern. If the two paths are equally long, the light-waves will arrive in phase and have constructive interference (fig. 1.2b). If not, there will be destructive interference, dissipating a part or all of the original light intensity (fig. 1.2c). This shift in phase only needs to be a fraction of the wavelength to observe partly destructive interference. Since the wavelength of visible light is in the range of 380 to 750 nanometers, an interferometer can easily be used to detect nanometer shifts. In the case of the aether experiment the whole setup was rotated with the idea that a

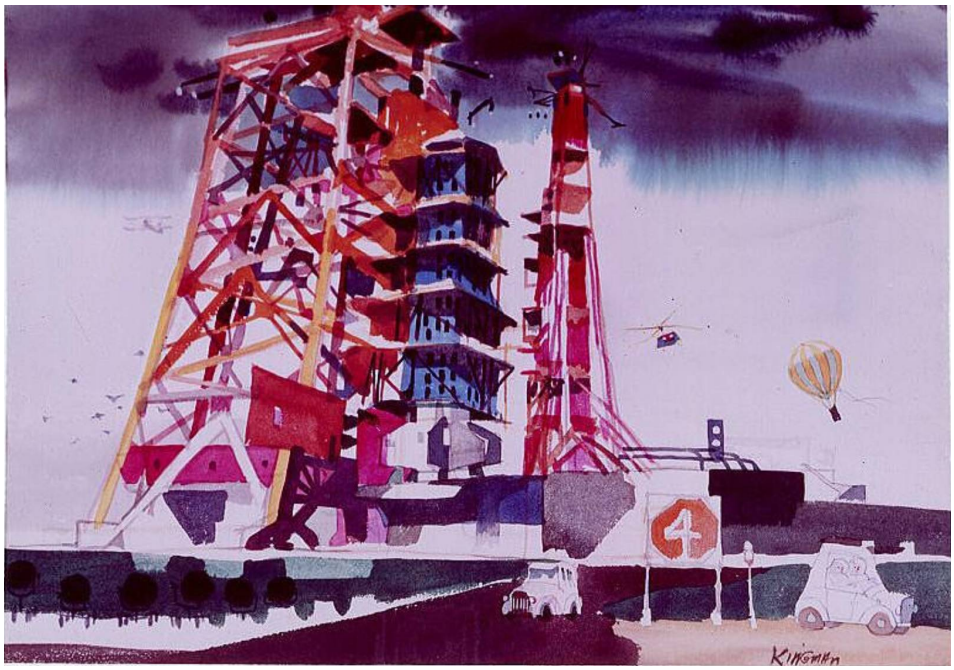

Figure 1.1. The watercolor painting 'Higher, faster, and farther', by Dong Kingman. Description by the National Air and Space Museum: 'Higher, Faster, and Farther. A bright and very colorful scene pays homage to the history of flight. The Saturn 1 complex on Pad 34 provides the setting and suggests the presence of the newest means of flight, the rocket. In the lower left is a flock of flying birds. Above that is a faintly colored bi-plane. On the right are a helicopter and a balloon. On the ground are two cars driving away'[1]

change in the aether wind direction would alter the arrival times of each of the two light beams and change the interference pattern. However, no significant change was observed, leading to the conclusion that if the aether existed, the speed at least was insignificant compared to the speed of light.[3,4] With the emergence of the relativity theory it was also proven that no stationary aether exists. Still, Albert Michelson was awarded the Nobel prize for Physics in 1907 *"for his optical precision instruments and the spectroscopic and metrological investigations carried out with their aid"*.[5]

Almost 130 years later, in 2015, interferometry was again used to perform the most precise experiment in the history of mankind: the measurement of gravitational waves in the *Laser Interferometer Gravitational-Wave Observatory* (LIGO). The basic design of LIGO is the same as the Michelson-Morley interferometer, but each of the parts upgraded with 130 years of technological progress (fig. 1.2d).

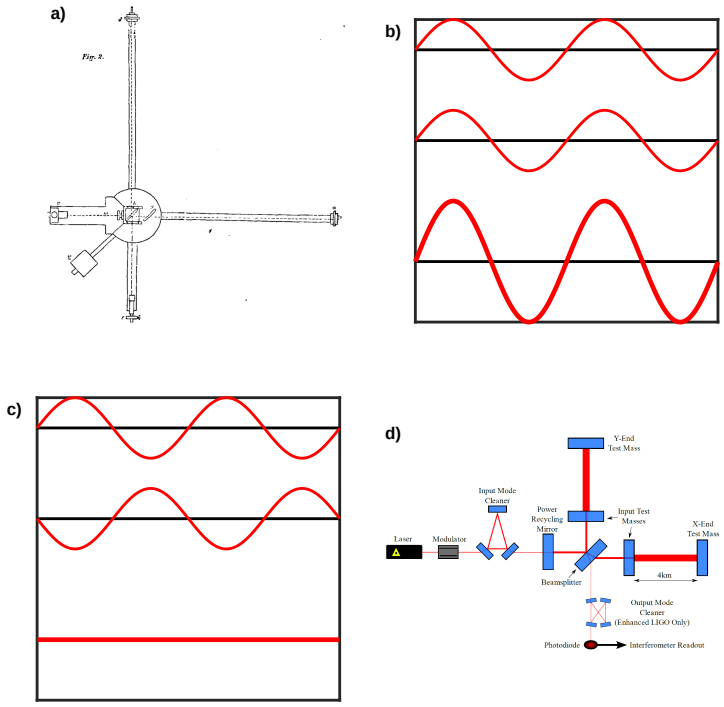

Figure 1.2. a) The original Michelson-Morley interferometry experimental design.[3] A coherent beam of light is split in two by a semi-mirror and sent in two directions. Both beams are reflected back at this semi-mirror, where they now are combined to result in an interference pattern. If the aether wind would change the speed of one of the two beams, the interference pattern would change. **b)** Constructive interference: the top two waves are in phase. If they are combined into the bottom wave their amplitudes add up which results in no loss of intensity. **c)** Destructive interference: the top two waves are out of phase. If they are combined into the bottom wave their amplitudes completely cancel out which results in a total loss of intensity. **d)** A schematic of the LIGO optical design. The global layout of the Michelson-Morley interferometer is still clearly visible in the fact that the beam is split up in two and recombined by the central beamsplitter.[6]

The light source is a state of the art laser, which produces a coherent beam of monochromatic light. This ensures that even after traveling a very long distance the two beams are identical and perfectly in phase. Compared to Michelsons 1.3 meter light-arms, LIGO's arms are 4 kilometers long, which will greatly increase its sensitivity. As if this was not enough, the light travels 280 times up and down each arm so that it has traveled 1120 kilometers before the two paths are recombined.

The light travels trough vacuum to prevent influence from air molecules. If two black holes far away from earth collide, gravitational waves form, which will deform the space around us unnoticeable as they travel past Earth. However, if one of LIGO's 1120 kilometers arms shortens or lengthens by only a few nanometers, the gravitational waves can be detected. This extreme sensitivity also makes LIGO sensitive for vibrations from sources on Earth. Much effort has been put into isolating the setup from its surroundings. To make sure that a measured gravitation wave is not noise from a source on Earth, two identical observatories are in use which are separated 3000 kilometers and extensive data analysis is performed. By timing the measurement of gravitational waves in the two facilities, it is even possible to get an idea from which direction they come. With more than two observatories the exact origin can be determined.[7–10]

1.2 Speckles

Lasers are inherently reliable and pure light sources produce monochromatic and coherent light. This makes them not only very energy-efficient light sources, but also desired for many applications where light quality is important.[11] However, in the early years of laser development it was found that when the laser light hits a rough surface or an opaque (non-transparent) material, the beam quality would immediately degrade.(Fig. 1.3a) A dotted pattern of light and dark spots would appear, which were called speckles. For many, the speckle patterns were regarded only as an annoying problem that should be solved. However, a few scientists started to use the properties of the speckles to create a new group of measurement devices that could measure motion inside materials. It was understood that the speckles originated from the fact that photons travel through an opaque material by scattering many times, so that their path inside the material becomes a walk with steps in random directions. Eventually the photons will exit the material which we can observe. Since the path, and thus the distance each photon has traveled is random, they will interfere randomly.[12,13] Sometimes they will interfere constructively, creating a bright speckle, other times they will interfere destructively, creating a dark speckle. However, the resulting pattern is random, so no information can be obtained about the structure of the material. But if the light-scattering particles inside the material move around, the random-walks of the photons change, and therefore the speckle pattern also changes. Thus, by looking at how fast the speckle pattern changes, information about the motion inside a material can be obtained.

1.2.1 Imaging

The first to visualize flow speeds in a channel by comparing two photographs of a speckle pattern were Grousson and Mallick in 1977.[14] After this, it did not take long before it was used for imaging of more complex materials, such as blood flow in a retina.[2] The method was very well suited for visualizing blood vessels since the red blood cells move faster than the surrounding tissue and was named Laser Speckle Contrast Imaging (LSCI). The potential for using maps of dynamic activity in medical imaging was acknowledged and the technique was further developed for that purpose and applied to many clinical and research areas such as retinal imaging,[2,15–17] perfusion imaging,[18–21] burn wound assessment,[22–24] dermatology,[25,26] rheumatology[27–30] and neurology,[31–34] including monitoring during human brain surgery.[35,36]

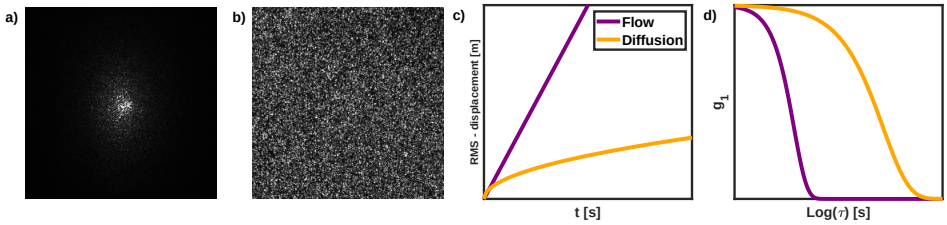

Figure 1.3. a) When a coherent laser beam hits an opaque material or rough reflective surface, speckles will appear. Through multiple scattering of photons, path length differences develop which give rise to this interference pattern and degrade the beam shape. **b)** When an expanded laser field hits an opaque material or rough reflective surface, a speckle field will appear. The speckle field is desired for imaging since the intensity fluctuations can be quantified over the whole imaging field. **c)** The displacement distance of a particle in a constant flow will increase linearly with time. The displacement of a freely diffusing particle will follow a square root increase with time since the random motion will often partially counteract earlier displacements. **d)** Example g_1 correlation functions for a fast flow and a slow diffusion. The fast flow decorrelates steeply at low τ, while the slow diffusion decorrelates with a more gentle slope at higher τ. The decorrelation τ is determined by the speed of the motion and the slope is determined by the type of motion. By measuring the g_1 and fitting it with an exponential decay with a stretching exponent, both the speed and type of motion can be obtained.

Much effort was put in making LSCI quantitative to allow measurement of exact flow speeds and Brownian motion, apparent random motion of small particles as a result of thermal motion of surrounding solvent molecules. Theory was developed to describe how the speckle pattern changes statistically as a result of specific dynamical processes.[37] This theory could also be used to obtain the specifics of the dynamical process from a large set of speckle photographs. However at the time it

was not technically possible to obtain a sufficiently large set of speckle images and available computing power was also insufficient to calculate the results from such a dataset. Instead a methodology with single point detection was developed which could measure the intensity fluctuations of a single speckle fast and long enough to calculate the specifics of the dynamics. The technique was called Diffusing Wave Spectroscopy (DWS)[38,39] and was used to quantify dynamical processes in spatially homogeneous materials such as emulsion stability,[40–42] aggregation in suspensions[43–45] or stability in foams.[46–48]

1.2.2 Quantitative dynamics

In DWS the sample, often a cuvette filled with the material to study, is illuminated by a laser beam. The scattered light is detected by a photon multiplier tube (PMT) which is essentially a one-pixel camera with a megaHertz sampling frequency. The PMT could be placed behind the sample, in the transmission geometry, so that only the light that has traveled completely through the sample is detected. The alternative is to place the PMT next to the laser and aim it at the illumination spot, which is called the back-scatter geometry.[38,49] The transmission geometry is sensitive for smaller motions since in general the photons that arrive at the PMT have scattered more often, so they have probed more displacement events. The back-scatter geometry is more versatile to apply. It can be easily applied to non-cuvette samples and just be aimed at any surface. Thick or light absorbing samples will not transmit light, so they are only measurable in the back-scatter geometry. The measured light intensities are read out from the PMT in real-time by an autocorrelator, a dedicated piece of hardware that performs the intensity fluctuation quantification in real-time. This quantification is performed by calculating the autocorrelation-function of the intensity fluctuations, the correlation is calculated for a range of correlation times(τ). For a τ of one second this means correlating the signal with a one second delayed version of itself. If the correlation is high, the intensity does not change much in that period and thus the particles don't move much and vice versa. The correlation value can be directly related to the root mean squared (rms) displacement of the light-scattering particles in the sample, for that specific τ. To fully determine the behavior of the particles this has to be repeated for many τ. Since the relation between τ and the rms displacement is known for flow (linear) and free diffusion (square root), the correlation function can be fitted directly without calculating the displacement values.(Fig. 1.3c,d)

LSCI and DWS existed and developed pretty much independently from each other, LSCI as an imaging method which was used for qualitative biomedical blood flow imaging and DWS as a fast and quantitative spectroscopic method in

soft matter science. In the meantime digital cameras appeared, and computational power increased exponentially until finally quantitative motion imaging was performed. Modern LSI was born!

Nowadays it is possible to collect speckle images at high framerates and analyze the intensity fluctuations of each pixel in the image thoroughly to obtain quantitative information. This allows an unparalleled insight in the internal motions of complex materials and has helped to solve many questions on topics such as deformation fields,[50–53] granular materials,[54–56] foam stability,[57] drying paint,[58,59] self-healing materials,[60] crack formation,[61,62] liquid crystals,[63,64] food safety[65,66] and agricultural crops.[67–69]

1.3 Challenges and applications

The information obtained from LSI is unique since most optical techniques visualize structure in transparent materials, while LSI visualizes motion in opaque materials. The hardware required to build an LSI is simple and low-cost,[70,71] but the sensitivity is unparalleled since it exploits interference. In the back-scatter geometry, the laser and camera can just be aimed at any light-scattering surface to obtain a result without the need to fine-tune the sample of interest. This accessibility and technical simplicity, combined with the broad range of materials it can be applied to and the uniqueness of the information it yields, makes that LSI has the potential to become a mainstream imaging technique.

Currently, LSI is only used by specialists, which in my view is caused by two main reasons. First, the data analysis is labor-intensive and slow. It is easy to collect a large set of speckle images, but obtaining quantitative motion maps requires self-written software and takes a lot of computational power which results in long waiting times before you can see the result. Second, the technique and what it can measure is not well known and many applications are waiting to be explored. There is also no commercially available setup, so if you want to use LSI you have to build the setup yourself. However, I don't think this is as much of an issue compared to the data analysis complexity as the setup is in essence just a camera and laser with a beam expander.

To move from a specialist to a mainstream technique, it will help if those issues are resolved. The data analysis has to become simpler and faster, and a bigger knowledge base of standardized experiments on a broad range of materials has to be published. Using LSI in multiple fields will have a two-fold advantage: it will build-up on the knowledge-base of standardized experiments and in the same time it will contribute to the acquaintance of LSI with the broader public. With this approach, LSI will move step-by-step towards broad application.

1.3.1 Methodological challenges

It is possible to perform quantitative LSI on digital movies of evolving speckle patterns, but despite recent technological advances the data processing still takes a significant amount of time. After collection and saving of images, it takes a multitude of that time before the quantitative data is available. The main bottleneck is that for every correlation time a separate operation has to be performed to calculate the corresponding correlation value. To obtain a reliable flow value or mean squared displacement (msd), this has to be done for at least ten correlation times. Since one calculation takes roughly as long as the data collection, this means that for a one hour measurement the total time before you know the result is at least ten hours. I believe this is one of the main reasons why LSI is not a widespread technique at the moment. To tackle this issue we explore another way to quantify the data: using the fast Fourier transform (fft) algorithm. This super-efficient algorithm transforms the speckle intensity fluctuations from the time domain to the frequency domain and obtains the amplitude of all available frequencies in one mathematical operation. Because the algorithm needs only one mathematical operation, it can be performed in parallel to the data collection without the need to save the images first and allows real-time data analysis.[72,73] According to the Wiener-Kinchin theorem, the autocorrelation function and the Fourier transform of a signal contain the same information, and thus the fft is a full replacement of the autocorrelation function.[74] To obtain quantitative msd and flow values from the frequency spectrum we need to adjust the existing theory which we attempt in *Chapter 2*. We will test the new algorithm with a simple and portable design of an LSI setup to test the performance while maximizing the accessibility level.

1.3.2 Art conservation

Art conservation science is a field that heavily utilizes medical imaging techniques because both fields have the same requirement: it is of uttermost importance that diagnostic techniques are non-invasive to not damage the patient, whether it is a living human or a centuries old artifact. Conservators have access to a plethora of medical imaging tools such as optical coherence tomography (OCT),[75,76] TeraHertz (THz) imaging,[77–79] 3D-scanning,[80,81] x-ray fluorecence/diffraction (XRF/XRD) imaging,[82–85] neutron imaging,[86,87] Raman scattering microscopy[88,89] and infrared (IR) microscopy,[90–92]. These tools can asses the current state of artifacts and make sure that they stay in the best conditions so that we can view art as the artist originally intended. However, those diagnostic methods assess the chemical or physical structure of the object, so to confirm stability, multiple measurements have to be compared. LSI monitors motion, which can directly answer the question

whether an object is stable or not. Furthermore, LSI can be used to monitor cleaning procedures and give insight in what happens during such a process. This is a leap forward, since current techniques can only compare the state of the object before and after the cleaning procedure. Therefore we think LSI is a promising tool for the conservation study and we start exploring possible applications.

Oil paintings are complex and multi-layered objects. On top of the canvas there is at least one ground layer and a few paint layers and a varnish layer. The transparent varnish layer has a protective as well as an aesthetic purpose as it enhances the colors of the paint. However, the varnish degrades slowly over time and gets a brownish color after a few decades.[93] To keep the paintings original appearance, the varnish has to be removed and reapplied. This removal is done with solvents that dissolve the varnish but not the paint.[94,95] To keep the paint in optimal condition it is still important that as little as possible solvent penetrates into the paint layer. Excess solvent will swell the paint like a sponge, which is a mechanical motion and results in the risk of structural degradation phenomena like cracking. Also when flowing through the paint matrix, it will transport reactive compounds that were already present in the layer, accelerating chemical degradation processes. Conservators are very careful during varnish removal and insight in the solvent behavior will help making decisions and prevent accelerated aging. The knowledge of when the solvent starts penetrating the paint layer and how long it will stay there cannot be obtained with current methods, which is why we will explore if LSI can give this information. The improved LSI setup from *Chapter 2* is portable so that the fragile artifacts don't have to be transported to the lab. LSI is a non-invasive technique because the laser is of sufficiently low power that the valuable object doesn't get damaged. Finally, because the data analysis happens in real-time, it can potentially tell the conservator when to stop adding solvent during the cleaning process.

Pigment particles in the paint will have negligible motion until they are surrounded by solvent. Pigment motion as a result of the solvent interaction can be measured with LSI and followed over time. We will use this approach in *Chapter 3* to quantitatively compare different cleaning methods and give insight in how invasive several different approaches are. We explore several often used cleaning solvents such as water, acetone, ethanol, isopropanol and n-hexane as well as a few potential green alternatives. Those solvents can be delivered to the varnish layer with several methods: traditional cotton swab, microfiber tissue or gel based delivery systems. While the swabbing is performed actively by hand, the latter two are applied and passive solvent and varnish exchange takes place between the painting and solvent delivery method. We not only asses how long the excess solvent stays in the paint layer but we also perform quantitative imaging

to determine how homogeneous the solvent application of each method is. Based on those results we continue with the most reliable cleaning method, and we work towards a workflow that conservators can use in *Chapter 4*. By comparing the invasiveness measured with LSI, with how good the cleaning result is, we aim to support conservators in making well-informed decisions in how to approach the cleaning of oil paintings.

1.3.3 Soft materials

Soft materials are materials that deform easily at room temperature such as liquids, emulsions or gels. Many of those materials contain micro-structures that give them the desired properties to perform the function they are chosen for. Since those micro-structures scatter light, they are excellent materials to study with LSI. And since they are soft, there are many dynamic internal processes that can be studied to gain more insight in the material properties and behavior.

Yoghurt and mayonnaise are food products that fall in this soft matter category. Yoghurt can be classified as a gel, as it is mostly water with a network of collapsed protein particles. Mayonnaise is an emulsion, where closely packed small oil droplets are surrounded by a thin layer of water. Both are a mixture of mainly liquids but behave more like a solid until you start to actively deform them. You can keep an opened bottle of mayonnaise upside-down without spilling until you start shaking. (Try this at home!) This shear-thinning behavior makes that it is easy to stick the mayonnaise to food but still has a saucy mouthfeel. However these food products show also unwanted behavior that has to do with their composition, the expulsion of water, which is called syneresis. Different from phase-separation, syneresis is attributed to rearrangements in the soft material structure such as shrinking of the gel network.[96,97] The resulting water loss alters the properties of the material and the water on top of the food can also falsely be interpreted as a sign of expiration of the product. So if syneresis can be prevented, shelf life will increase and food waste can reduce.

Before syneresis can be prevented, we need to understand the process. To gain more insight in the process we will use LSI to study two syneresis model systems consisting of synthetic microparticles that are connected by thermoresponsive polymers to form a network. When the temperature is increased, the thermoresponsive polymers collapse and the particle network shrinks: controlled syneresis occurs. We will study this behavior in *Chapter 5* and give insight in the spatial variation of local particle motion. We will compare networks of rigid (hard) and deformable (soft) particles and show how those particle properties influence the speed and spatial variation in the controlled syneresis.

1.3.4 Rheology

Soft material behavior is often characterized by a machine called a rheometer. This machine can very precisely deform a material and measure the force that is required to do the deformation. Or the other way around, apply a controlled force and measure how much the material deforms. Shear-thinning of mayonnaise can be proven in a rheometer because increasing the deformation will require cumulatively less extra force. The opposite is true for the shear-thickening of high volume fraction corn starch in water: if you apply more and more force, the measured deformation will increase less and less. The friction between the corn starch particles is high and at a faster deformation rate there is not enough time to relax stuck particles before their neighbors also get stuck.

The rheological information that is obtained is an average of the whole measured sample. If the material is homogeneous, such global information is sufficient. For the case of shear-thickening of corn starch, where the process could be dominated by localized jamming events, this is an oversimplification and insight in the local phenomena can explain much more. Current methods to study the local flow properties are based on magnetic resonance imaging (MRI), particle tracking, particle image velocimetry (piv) analysis algorithms.[98,99] The main drawback of those methods is that to obtain sufficient displacement resolution of the tracking particles, a high magnification has to be used which results in a very limited field of view. Since LSI's displacement sensitivity is not limited by the pixel size, it can quantify small displacements with a large field of view, and thus is a promising method to give more insight into local flow properties of complex fluids. We will test this hypothesis in *Chapter 6* and try to gain new insights in the rheology of high volume fraction corn-starch suspensions.

1.4 Thesis outline

The chapters in this thesis are written as stand-alone scientific articles, but are strongly connected through LSI. The combination of all chapters gives a broader view on the possibilities and versatility of LSI. In the first part of this thesis the focus is on developments that make the technique more accessible and then the focus shifts to the applications that this opens up. In *Chapter 2* we develop a fast algorithm to perform real-time quantitative LSI and incorporate this into a portable set-up. With this set-up we explore application of LSI to the cleaning of oil paintings in *Chapter 3* and in *Chapter 4* we do a more in depth study of one of the more promising cleaning techniques. After two art conservation chapters, we shift the focus to soft matter applications. In *Chapter 5* we employ LSI to study a model

system to better understand the spatial variation during syneresis. In *Chapter 6* we combine LSI with rheology to measure local fluctuations in the flow properties of complex fluids in high resolution. In the final chapter, the *General Discussion*, will reflect upon chapters and identify strengths and weaknesses. From there we will identify existing knowledge gaps and avenues that are open and promising to explore.

References

[1] D. Kingman, Higher, faster, and farther. https://airandspace.si.edu/collection-objects/higher-faster-and-farther/nasm_A19750936000.

[2] A. Fercher, J. D. Briers. *Optics communications* **37**, 326–330 (1981).

[3] A. A. Michelson. *American Journal of Science (1880-1910)* **22**, 120 (1881).

[4] A. A. Michelson, E. W. Morley. *Sidereal Messenger, vol. 6, pp. 306-310* **6**, 306–310 (1887).

[5] A. A. Michelson. *Nobel Lecture* **12**, 1–13 (1907).

[6] J. R. Smith, Enhanced ligo schematics (2021). https://commons.wikimedia.org/wiki/File:Initial_and_Enhanced_LIGO_schematics.png.

[7] B. P. Abbott, R. Abbott, T. Abbott, M. Abernathy, F. Acernese, K. Ackley, C. Adams, T. Adams, P. Addesso, R. Adhikari, *et al.*. *Physical review letters* **116**, 061102 (2016).

[8] R. Weiss. *Reviews of Modern Physics* **90**, 040501 (2018).

[9] B. C. Barish. *Reviews of Modern Physics* **90**, 040502 (2018).

[10] K. S. Thorne. *Reviews of Modern Physics* **90**, 040503 (2018).

[11] A. L. Schawlow. *Scientific American* **219**, 120–139 (1968).

[12] J. W. Goodman, *Laser speckle and related phenomena* (Springer, 1975), pp. 9–75.

[13] J. W. Goodman. *JOSA* **66**, 1145–1150 (1976).

[14] R. Grousson, S. Mallick. *Applied Optics* **16**, 2334–2336 (1977).

[15] T. Sugiyama, Y. Mashima, Y. Yoshioka, H. Oku, T. Ikeda. *Archives of Ophthalmology* **127**, 454–459 (2009).

[16] M. Nagahara, Y. Tamaki, M. Araie, H. Fujii. *Japanese journal of ophthalmology* **43**, 186–195 (1999).

[17] H. Isono, S. Kishi, Y. Kimura, N. Hagiwara, N. Konishi, H. Fujii. *Archives of Ophthalmology* **121**, 225–231 (2003).

[18] J. D. Briers, S. Webster. *Journal of biomedical optics* **1**, 174–179 (1996).

[19] C. Stewart, C. Gallant-Behm, K. Forrester, J. Tulip, D. Hart, R. Bray. *Skin Research and Technology* **12**, 247–253 (2006).

[20] B. Ruth. *Medical engineering & physics* **16**, 105–111 (1994).

[21] H. Cheng, Q. Luo, Q. Liu, Q. Lu, H. Gong, S. Zeng. *Physics in Medicine & Biology* **49**, 1347 (2004).

[22] C. Stewart, R. Frank, K. Forrester, J. Tulip, R. Lindsay, R. Bray. *Burns* **31**, 744–752 (2005).

[23] C. Crouzet, J. Q. Nguyen, A. Ponticorvo, N. P. Bernal, A. J. Durkin, B. Choi. *Burns* **41**, 1058–1063 (2015).

[24] R. Mirdell, F. Iredahl, F. Sjöberg, S. Farnebo, E. Tesselaar. *Burns* **42**, 648–654 (2016).

[25] Y.-C. Huang, T. L. Ringold, J. S. Nelson, B. Choi. *Lasers in Surgery and Medicine: The Official Journal of the American Society for Laser Medicine and Surgery* **40**, 167–173 (2008).

[26] Y.-C. Huang, N. Tran, P. R. Shumaker, K. Kelly, E. V. Ross, J. S. Nelson, B. Choi. *Lasers in Surgery and Medicine: The Official Journal of the American Society for Laser Medicine and Surgery* **41**, 563–571 (2009).

[27] A. Della Rossa, M. Cazzato, A. d'Ascanio, A. Tavoni, W. Bencivelli, P. Pepe, M. Mosca, C. Baldini, M. Rossi, S. Bombardieri. *Clin Exp Rheumatol* **31**, 109–114 (2013).

[28] B. Ruaro, A. Sulli, E. Alessandri, C. Pizzorni, G. Ferrari, M. Cutolo. *Annals of the rheumatic diseases* **73**, 1181–1185 (2014).

[29] T. Son, H.-J. Yoon, S. Lee, W. S. Jang, B. Jung, W.-U. Kim. *Journal of biomedical optics* **19**, 106010 (2014).

[30] J. Dunn, K. Forrester, L. Martin, J. Tulip, R. Bray. *Lasers in surgery and medicine* **43**, 21–28 (2011).

[31] A. K. Dunn, H. Bolay, M. A. Moskowitz, D. A. Boas. *Journal of Cerebral Blood Flow & Metabolism* **21**, 195–201 (2001).

[32] C. Ayata, A. K. Dunn, Y. Gursoy-Özdemir, Z. Huang, D. A. Boas, M. A. Moskowitz. *Journal of Cerebral Blood Flow & Metabolism* **24**, 744–755 (2004).

[33] A. J. Strong, E. L. Bezzina, P. J. Anderson, M. G. Boutelle, S. E. Hopwood, A. K. Dunn. *Journal of Cerebral Blood Flow & Metabolism* **26**, 645–653 (2006).

[34] J. S. Paul, A. R. Luft, E. Yew, F.-S. Sheu. *Neuroimage* **29**, 38–45 (2006).

[35] A. B. Parthasarathy, E. L. Weber, L. M. Richards, D. J. Fox, A. K. Dunn. *Journal of biomedical optics* **15**, 066030 (2010).

[36] S. Nomura, T. Inoue, H. Ishihara, H. Koizumi, E. Suehiro, F. Oka, M. Suzuki. *World neurosurgery* **82**, e753–e757 (2014).

[37] J. Goodman, *Statistical Optics* (Wiley, New York, 1985).

[38] D. J. Pine, D. A. Weitz, P. M. Chaikin, E. Herbolzheimer. *Physical review letters* **60**, 1134 (1988).

[39] D. J. Pine, D. A. Weitz, J. Zhu, E. Herbolzheimer. *Journal de Physique* **51**, 2101–2127 (1990).

[40] E. ten Grotenhuis, M. Paques, G. A. van Aken. *Journal of colloid and interface science* **227**, 495–504 (2000).

[41] Y. Hemar, D. S. Horne. *Colloids and Surfaces B: biointerfaces* **12**, 239–246 (1999).

[42] H. G. Ruis, K. van Gruijthuijsen, P. Venema, E. van der Linden. *Langmuir* **23**, 1007–1013 (2007).

[43] M. Alexander, D. G. Dalgleish. *Colloids and Surfaces B: Biointerfaces* **38**, 83–90 (2004).

[44] E. M. Furst, A. P. Gast. *Physical Review E* **58**, 3372 (1998).

[45] H. M. Wyss, S. Romer, F. Scheffold, P. Schurtenberger, L. J. Gauckler. *Journal of colloid and interface science* **241**, 89–97 (2001).

[46] D. Weitz, J. Zhu, D. Durian, H. Gang, D. Pine. *Physica Scripta* **1993**, 610 (1993).

[47] A. Gopal, D. Durian. *Journal of Colloid and Interface Science* **213**, 169–178 (1999).

[48] S. Cohen-Addad, R. Höhler. *Physical Review Letters* **86**, 4700 (2001).

[49] P. Kaplan, M. H. Kao, A. Yodh, D. J. Pine. *Applied Optics* **32**, 3828–3836 (1993).

[50] J. S. Steckenrider, J. Wagner. *Experimental mechanics* **31**, 8–13 (1991).

[51] B. F. Pouet, S. Krishnaswamy. *Optical Engineering* **32**, 1360–1369 (1993).

[52] D. Coburn, J. Slevin. *Applied optics* **34**, 5977-5986 (1995).

[53] M. Erpelding, A. Amon, J. Crassous. *Physical review E* **78**, 046104 (2008).

[54] J. Crassous, J.-F. Metayer, P. Richard, C. Laroche. *Journal of Statistical Mechanics: Theory and Experiment* **2008**, P03009 (2008).

[55] A. Amon, R. Bertoni, J. Crassous. *Physical Review E* **87**, 012204 (2013).

[56] A. Amon, A. Mikhailovskaya, J. Crassous. *Review of Scientific Instruments* **88**, 051804 (2017).

[57] D. A. Sessoms, H. Bissig, A. Duri, L. Cipelletti, V. Trappe. *Soft Matter* **6**, 3030–3037 (2010).

[58] P. Zakharov, F. Scheffold. *Soft Materials* **8**, 102–113 (2010).

[59] H. M. Van Der Kooij, R. Fokkink, J. Van Der Gucht, J. Sprakel. *Scientific reports* **6**, 1–10 (2016).

[60] H. M. van der Kooij, A. Susa, S. J. García, S. van der Zwaag, J. Sprakel. *Advanced materials* **29**, 1701017 (2017).

[61] T. Verho, P. Karppinen, A. H. Gröschel, O. Ikkala. *Advanced Science* **5**, 1700635 (2018).

[62] H. M. van der Kooij, S. Dussi, G. T. van de Kerkhof, R. A. Frijns, J. van der Gucht, J. Sprakel. *Science advances* **4**, eaar1926 (2018).

[63] H. M. van der Kooij, S. A. Semerdzhiev, J. Buijs, D. J. Broer, D. Liu, J. Sprakel. *Nature communications* **10**, 1–9 (2019).

[64] H. M. van Der Kooij, D. J. Broer, D. Liu, J. Sprakel. *ACS applied materials & interfaces* **12**, 19927–19937 (2020).

[65] J. Yoon, K. Lee, Y. Park. *arXiv preprint arXiv:1603.07343* (2016).

[66] K. Zhou, C. Zhou, A. Sapre, J. H. Pavlock, A. Weaver, R. Muralidharan, J. Noble, T. Chung, J. Kovac, Z. Liu, *et al.*. *ACS sensors* **5**, 3140–3149 (2020).

[67] R. A. Braga, I. M. Dal Fabbro, F. M. Borem, G. Rabelo, R. Arizaga, H. J. Rabal, M. Trivi. *Biosystems engineering* **86**, 287–294 (2003).

[68] A. Zdunek, A. Adamiak, P. M. Pieczywek, A. Kurenda. *Optics and Lasers in Engineering* **52**, 276–285 (2014).

[69] M. Z. Ansari, A. K. Nirala. *The European Physical Journal Applied Physics* **70**, 21201 (2015).

[70] O. Yang, B. Choi. *Optics letters* **37**, 3957–3959 (2012).

[71] L. M. Richards, S. S. Kazmi, J. L. Davis, K. E. Olin, A. K. Dunn. *Biomedical optics express* **4**, 2269–2283 (2013).

[72] G. D. Bergland. *IEEE spectrum* **6**, 41–52 (1969).

[73] E. A. Robinson. *Proceedings of the IEEE* **70**, 885–907 (1982).

[74] N. Wiener. *Acta mathematica* **55**, 117–258 (1930).

[75] B. J. Rouba, P. Karaszkiewicz, L. Tymioska-Widmer, M. Iwanicka, M. Góra, E. Kwiatkowska, P. Targowski. *J Nondestructive Testing* **13** (2008).

[76] H. Liang, B. Peric, M. Hughes, A. Podoleanu, M. Spring, D. Saunders, *O3A: Optics for Arts, Architecture, and Archaeology* (International Society for Optics and Photonics, 2007), vol. 6618, p. 661805.

[77] K. Fukunaga, Y. Ogawa, S. Hayashi, I. Hosako. *IEICE Electronics Express* **4**, 258–263 (2007).

[78] E. Abraham, A. Younus, J.-C. Delagnes, P. Mounaix. *Applied Physics A* **100**, 585–590 (2010).

[79] K. Fukunaga, N. Sekine, I. Hosako, N. Oda, H. Yoneyama, T. Sudou. *Journal of the European Optical Society-Rapid publications* **3** (2008).

[80] E. Bunsch, R. Sitnik, J. Michonski, *Computer Vision and Image Analysis of Art II* (International Society for Optics and Photonics, 2011), vol. 7869, p. 78690D.

[81] I. Trinks, M. Díaz-Andreu, R. Hobbs, K. Sharpe. *Advancing large-scale high-resolution near-surface geophysical prospection* p. 207 (2005).

[82] J. K. Delaney, P. Ricciardi, L. D. Glinsman, M. Facini, M. Thoury, M. Palmer, E. R. d. l. Rie. *Studies in Conservation* **59**, 91–101 (2014).

[83] G. Van der Snickt, K. Janssens, J. Dik, W. De Nolf, F. Vanmeert, J. Jaroszewicz, M. Cotte, G. Falkenberg, L. Van der Loeff. *Analytical chemistry* **84**, 10221–10228 (2012).

[84] S. Legrand, F. Vanmeert, G. Van der Snickt, M. Alfeld, W. De Nolf, J. Dik, K. Janssens. *Heritage Science* **2**, 1–11 (2014).

[85] S. Pagès-Camagna, E. Laval, D. Vigears, A. Duran. *Applied Physics A* **100**, 671–681 (2010).

[86] R. Van Langh, E. Lehmann, S. Hartmann, A. Kaestner, F. Scholten. *Analytical and bioanalytical chemistry* **395**, 1949–1959 (2009).

[87] F. Hameed, B. Schillinger, A. Rohatsch, M. Zawisky, H. Rauch. *Nuclear Instruments and Methods in Physics Research Section A: Accelerators, Spectrometers, Detectors and Associated Equipment* **605**, 150–153 (2009).

[88] G. D. Smith, R. J. Clark. *Studies in Conservation* **46**, 92–106 (2001).

[89] G. D. Smith, R. J. Clark. *Journal of archaeological science* **31**, 1137–1160 (2004).

[90] S. Prati, E. Joseph, G. Sciutto, R. Mazzeo. *Accounts of chemical research* **43**, 792–801 (2010).

[91] F. Casadio, L. Toniolo. *Journal of Cultural Heritage* **2**, 71–78 (2001).

[92] G. Capobianco, M. P. Bracciale, D. Sali, F. Sbardella, P. Belloni, G. Bonifazi, S. Serranti, M. L. Santarelli, M. C. Guidi. *Microchemical Journal* **132**, 69–76 (2017).

[93] R. M. Kabbani. *The Chemical Educator* **2**, 1–18 (1997).

[94] C. Stavroudis, S. Blank (1989).

[95] S. Škorja. *Consequences of the Rome Guidelines on Varnishing–Conservation Realities Eighty-Four Years Later* .

[96] H. Modler, M. Kalab. *Journal of Dairy Science* **66**, 430–437 (1983).

[97] T. Amatayakul, F. Sherkat, N. P. Shah. *International Journal of Dairy Technology* **59**, 216–221 (2006).

[98] V. Rathee, D. L. Blair, J. S. Urbach. *Proceedings of the National Academy of Sciences* **114**, 8740–8745 (2017).

[99] L. Bécu, S. Manneville, A. Colin. *Physical review letters* **96**, 138302 (2006).

Chapter 2

$$F(\omega) = \int_{-\infty}^{\infty} I(t) e^{-2\pi i \omega t} dt$$

FOURIER TRANSFORMS FOR FAST AND QUANTITATIVE LASER SPECKLE IMAGING

Laser speckle imaging is a powerful imaging technique that visualizes microscopic motion within turbid materials. At current two methods are widely used to analyze speckle data: one is fast but qualitative, the other quantitative but computationally expensive. We have developed a new processing algorithm based on the fast Fourier transform, which converts raw speckle patterns into maps of microscopic motion and is both fast and quantitative, providing a dynamic spectrum of the material over a frequency range spanning several decades. In this chapter we show how to apply this algorithm and how to measure a diffusion coefficient with it. We show that this method is quantitative and several orders of magnitude faster than the existing quantitative method. Finally we harness the potential of this new approach by constructing a portable laser speckle imaging setup that performs quantitative data processing in real-time on a tablet.

This chapter was published as: Buijs, J., Gucht, J. van der & Sprakel, J., 'Fourier transforms for fast and quantitative Laser Speckle Imaging', *Scientific Reports* **2019**, 1-9

2.1 Introduction

Laser Speckle Imaging (LSI) is a versatile method to quantify and visualize the internal dynamics in complex and opaque materials. Initially devised as a medical imaging technique to map blood flow patterns beneath the skin,[1–3] LSI has emerged in recent years as a quantitative tool in material science.[4–6] Recent applications of the method include the quantification of flow patterns, the study of spatially-inhomogeneous Brownian motion and a non-invasive and complete micromechanical analysis in single micrometric pixels.[7–11] LSI operates on the basis of multiple light scattering, which occurs in highly opaque materials, and does not require labeling of the material of interest. Its suitability to probe processes in opaque materials offers substantial benefits over single-scattering or fluorescence based methods, which rely on optical transparency and therefore preclude the study of a wide range of practical materials. This makes LSI suitable for the study of dynamical processes in a wide variety of scenarios, ranging from solid-liquid transitions and crack patterns in drying films and droplets,[10] quantitative analysis of the mechanisms of fracture and self-repair,[11,12] to structural rearrangements in granular materials.[13]

LSI derives the internal dynamics in an opaque material by quantifying the intensity fluctuations of multiply scattered light. When a turbid material is illuminated by a coherent light source, the photons injected into the material undergo a large number of scattering events before exiting and traveling to the detector. Due to the numerous scattering events, the photon paths and polarization are completely randomized and can be described by diffusive statistics. Path length differences between photons that have traveled through the material lead to a characteristic interference, or speckle pattern. Motion of the scattering elements within the material changes the interference conditions, and thus leads to intensity variations that are analyzed to ascertain the rate and type of motion that has occurred. In Diffusing Wave Spectroscopy (DWS), a single speckle is detected to probe the average dynamics within the material,[14] while the entire speckle pattern is collected in LSI to gain spatially-resolved information.

To go from the raw data to a measure for the dynamics, various approaches are available. In medical imaging, a measure for the spatial or temporal variance of a set of speckles is most commonly used to calculate the speckle contrast; this method is often denoted as Laser Speckle Contrast Analysis (LASCA).[15–17] While this approach can not easily be applied to quantify different dynamical processes at different frequencies, it is used because the computational efficiency is high. This has enabled real-time data treatment, which is crucial in a clinical setting.[18,19] Efforts to obtain quantitative data from LASCA have been successful but at the

cost of slowing the method down to the point where real-time data analysis is not feasible.[20] Quantitative LASCA requires sets of speckle images with a range of exposure times, thereby increasing data acquisition time by at least a factor of ten, and introduces an additional curve-fitting step.

Quantitative LSI, such as often used in material science scenarios,[7–11] requires the measurement of dynamics over a wide frequency range, so that different dynamical processes (such as Brownian motion, flow, and deformation) can be distinguished and quantified. This is usually performed by calculating the autocorrelation function of the temporal intensity trace.[21] This approach is identical to data treatment in DWS, thus benefiting from established DWS theory to obtain quantitative data, such as the mean-squared displacement of scattering particles, from which diffusion coefficients and flow rates can be extracted,[22–26] or to obtain a spatially-resolved invariant of the strain tensor to enable strain field visualisation.[12,27,28] While quantitative, this approach is computationally intensive and not suited for real-time LSI. The current trade-off between computational efficiency and the level of detail in the information gained for an LSI experiment is harsh. This poses the need for a universal analysis method that is both quantitative over a wide frequency range and fast.

In this chapter we propose a new method for LSI analysis that uses Fourier transformations (FT) to acquire the power spectral density to quantify speckle fluctuations in the frequency domain.[29] According to the Wiener-Kinchin theorem the power spectral density and autocorrelation function contain the same quantitative information.[30,31] However, the power spectrum can be calculated in a fraction of the time, owing to the very efficient Fast Fourier Transform (FFT) algorithm.[32] Therefore the same quantitative information can be obtained much faster. Once the power spectrum has been calculated, the autocorrelation function can be readily obtained as its Fourier transform. The power spectral density of speckle intensity fluctuations has been calculated before, however not with the aim to spatially visualize dynamics.[33,34] For DWS the FFT has been used to calculate the correlation function efficiently, but no information was extracted from the power spectrum directly.[35,36] Therefore a framework to extract quantitative results from the power spectral density does not exist.

In the following, we will present a framework for the extraction of quantitative data from Fourier transform LSI (FT-LSI) experiments. We benchmark the performance of this approach to both LASCA and conventional LSI, and confirm its validity by measuring the diffusion coefficients of Brownian particles. We find that for big data sets FT-LSI, is several orders of magnitude faster than LSI. The result of the FT-LSI is a full power spectrum for every pixel which holds significantly more information than the single speckle contrast value obtained

with LASCA. The combination of computational efficiency and access to the entire the power spectrum, enables result display in the form of a spectrogram, which gives a full overview of the power spectral density as function of both time and frequency. We calculate a spectrogram for the scenario of a short flow pulse through a micro-channel and show how it enables direct observation of both flow start-up and cessation within a microchannel. Finally, we show that the strongest advantage of this method is its ability to perform real-time quantitative analysis. To demonstrate this, we build a portable LSI set-up which is controlled by a tablet and develop software that performs the FT-LSI in real-time. We use this set-up to study the heat welding of plastic layers during 3D printing.

2.2 Results

2.2.1 Theory

Traditionally, quantitative LSI starts from the intensity autocorrelation function g_2, as a function of the lag time τ. Speckle images, separated in time by τ, are correlated to obtain a map of local dynamics. The g_2 autocorrelation function is computed as

$$g_2(t,x,y,\tau) = \frac{\langle I(t,x,y)\cdot I(t+\tau,x,y)\rangle}{\langle I(t,x,y)\rangle\langle I(t+\tau,x,y)\rangle} \tag{2.1}$$

To increase statistics, averaging can be performed in time and/or space, but at the cost of spatial and/or temporal resolution. Using the Siegert relation the g_2 can be converted to field autocorrelation function g_1

$$g_1(\tau) = \frac{1}{\sqrt{\beta}}\cdot\sqrt{g_2(\tau)-1} \tag{2.2}$$

where β is an instrumental constant, which is determined in experiments from the extrapolated intercept of g_2 to $\tau = 0$. A common route to obtain quantitative information from these correlation functions, is to extract the strain and the mean squared displacement of the scatterers:[12,13,37]

$$g_1(\tau) = \exp\left[-2\gamma k_0 l^*\sqrt{3f(U)+\langle\Delta r^2(\tau)\rangle/l^{*2}}\right] \tag{2.3}$$

where γ is a numerical constant, $k_0 = 2\pi n/\lambda$ is the wavevector, with refractive index n and wavelength λ, l^* is the photon transport mean free path, $f(U)$ an invariant of the strain tensor and $\langle\Delta r^2(\tau)\rangle$ the mean squared displacement. For the simple case of scatterers that perform purely diffusive motion in a material

free of mechanical deformations, the diffusion coefficient D can be obtained from $\langle \Delta r^2(\tau) \rangle = 6D\tau$, and the equation above simplifies to:

$$g_1(\tau) = \exp -\sqrt{\kappa|\tau|} \tag{2.4}$$

where $\kappa = \gamma^2 k_0^2 6D$. This equation can be generalized to non-diffusive dynamics, such as directional flow or sub-diffusive motion in densely packed materials. In conventional LSI, this can be done by introducing a stretching parameter α in the exponent

$$g_1(\tau) = \exp\left[-|\kappa \cdot \tau|^{\alpha} \right] \tag{2.5}$$

Where α describes the nature of the motion: α is $\frac{1}{2}$ for diffusive motion, 1 for ballistic motion and $< \frac{1}{2}$ for sub-diffusive processes. Note that Eq. 2.4 is equal to Eq. 2.5 with $\alpha = \frac{1}{2}$.

The Wiener-Kinchin theorem[30,31] states that the same information is accessible in the frequency domain. Such an approach benefits from very efficient fast Fourier transform (FFT) algorithms. With slight modifications to the theory, the same quantitative data can be extracted. We start with the analytical Fourier Transform of Eq. 2.5 which according to the Wiener-Kinchin theorem is equal to the power spectrum. For low frequencies this gives:

$$\lim_{\omega \to 0} P(\omega) = \frac{2}{\kappa} \cdot \Gamma\left(1 + \frac{1}{\alpha}\right) \tag{2.6}$$

and for high frequencies:

$$\lim_{\omega \to \infty} P(\omega) \approx \frac{2\kappa^{\alpha}}{|\omega|^{1+\alpha}} \cdot \Gamma(1+\alpha) \cdot sin\left(\frac{\alpha\pi}{2}\right) \tag{2.7}$$

These two limits are separated by a critical corner frequency ω^*, that is found at:

$$\omega^* = \left[\frac{\Gamma(1+\frac{1}{\alpha})}{\Gamma(1+\alpha) sin(\frac{\alpha\pi}{2})} \right]^{-\frac{1}{1+\alpha}} \cdot \kappa \tag{2.8}$$

For the simplest case of purely diffusive motion of the scatterers $\alpha = \frac{1}{2}$, the analytical form of the power spectrum reads:

$$P(\omega) = \sqrt{\frac{\pi\kappa}{2}} \cdot \frac{1}{|\omega|^{\frac{3}{2}}} \left\{ cos\left(\frac{\kappa}{4|\omega|}\right) \left[1 - 2C\left(\sqrt{\frac{\kappa}{2\pi|\omega|}}\right) \right] + sin\left(\frac{\kappa}{4|\omega|}\right) \left[1 - 2S\left(\sqrt{\frac{\kappa}{2\pi|\omega|}}\right) \right] \right\} \tag{2.9}$$

which uses two Fresnel integrals

$$C(x) = \int_0^x cos(t^2)dt \qquad \text{and} \qquad S(x) = \int_0^x sin(t^2)dt \tag{2.10}$$

At low frequencies the power spectrum converges to a horizontal asymptote described by

$$\lim_{\omega \to 0} P(\omega) = \frac{4}{\kappa} \tag{2.11}$$

while at high frequencies the power spectrum converges to

$$\lim_{\omega \to \infty} P(\omega) \approx \sqrt{\frac{\pi\kappa}{2}} \cdot \frac{1}{|\omega|^{\frac{3}{2}}} \tag{2.12}$$

These two limits are separated by a critical corner frequency ω^*

$$\omega^* = \frac{1}{2} \cdot \left(\frac{\pi}{4}\right)^{\frac{1}{3}} \cdot \kappa \tag{2.13}$$

On a log-log scale, both the high and low frequency domains approach a straight line, as is shown in Fig. 2.1a. Equations 2.11-2.13 can be used to determine the diffusion coefficient from an experimental power spectrum. From the slope of the high frequency domain we can determine α, which gives insight into the nature of the scatterer motion. Since the slope is equal to $-(1+\alpha)$, we have a slope of $-\frac{3}{2}$ for diffusive motion and a slope of -2 for ballistic motion, in agreement with previous results.[38,39] For diffusive motion, the diffusion coefficient can be extracted both from the frequency-independent plateau at low frequencies (2.11 and 2.6) and from the corner frequency (2.13 or 2.8).

It should be noted that this analysis is valid only for ergodic samples. As shown previously,[40] the presence of a non-fluctuating component in the scattered light modifies the correlation function g_2 and complicates the analysis. Since the power spectrum is directly related to g_2, it is equally affected by non-fluctuating scatterers. An approach to correct for non-ergodicity was presented by by Zakharov *et al.*,[41] who directly measured the fraction of non-mobile scatterers in the sample. A similar work-around can be applied for FT-LSI. However, in this chapter we will only consider ergodic samples, for which such corrections are not needed.

2.2.2 Validation

To verify the predictions made above, we study a sample of diffusing colloidal particles in a simple viscous solvent. We take 1 μm polystyrene spheres suspended in a $50/50 wt\%$ mixture of glycerol and water. The cuvette is placed in a backscatter

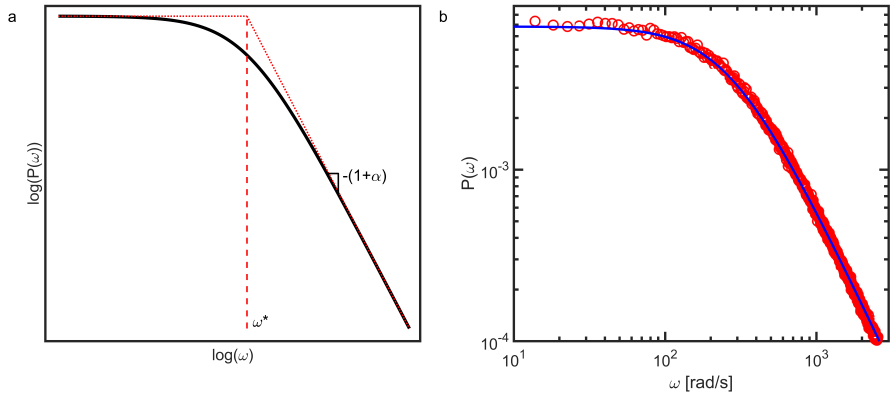

Figure 2.1. a) Theoretical power spectrum of speckle intensity fluctuations, described by Eq.2.6-2.8. The critical frequency ω^* is obtained from the intercept between the fit of two straight lines through the low and high frequency domains. The type of dynamics, described by α, can be obtained from the slope of the high frequency domain. **b)** Experimental power spectrum (○) of the diffusion of 1μm polystyrene spheres in a 50/50 mixture of water and glycerol. The power spectrum is also computed by taking the Fourier transform of the autocorrelation function of the same raw speckle data (—).

LSI instrument, which is described in section 2.4, and $N = 10^5$ images are collected at a rate of 10^4 images per second.

The power spectrum of the speckle intensity fluctuations is calculated using two approaches. First, the FFT algorithm is used to transform the intensity fluctuations per speckle to the frequency domain. The resulting amplitudes are squared to obtain the power spectrum and averaged over all speckles in the field of view. Further details regarding the procedure and normalization are provided in section 2.4. Secondly, the g_1 autocorrelation function is calculated in real space, according to Eq. 2.1 and 2.2, interpolated with an exponential decay which is then Fourier transformed to the frequency domain.

The power spectra obtained in these two approaches are identical within experimental noise, as shown in Figure 2.1b. This confirms the validity of the Wiener-Kinchin theorem for this method. Moreover, the experimental power spectra (Fig. 2.1b) have the same shape as that predicted by our theoretical analysis (Fig.2.1a). This is the first confirmation that Fourier analysis can be applied to obtain quantitative data from LSI experiments.

As further validation, we perform a set of experiments on colloids diffusing in solvents of varying viscosity. We prepare suspensions of $1\mu m$ polystyrene spheres

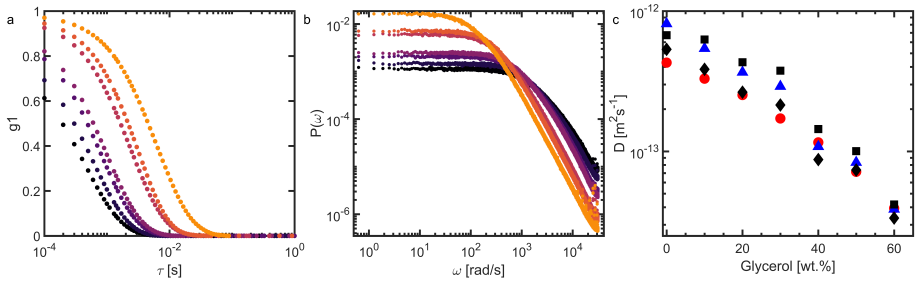

Figure 2.2. a) Correlation functions calculated for the diffusion of $1\mu m$ polystyrene particles in a water-glycerol mixture. The dark color corresponds to 0% glycerol, which increases with steps of 10% to a maximum of 60% for the lightest series. **b)** Power spectral densities calculated for the diffusion of $1\mu m$ polystyrene particles in a water-glycerol mixture. The dark color corresponds to 0% glycerol, which increases with steps of 10% to a maximum of 60% for the lightest series. **c)** Diffusion coefficients calculated with Stokes-Einstein (●), LSI (▲) and FT-LSI using the critical frequency (■) and the height of the plateau (♦).

in glycerol:water mixtures containing between 0 to 60 wt% glycerol. The diffusion coefficient can be computed using the Stokes-Einstein relation:

$$D = \frac{k_B T}{6\pi\eta r} \tag{2.14}$$

with $k_B T$ the thermal energy, η the fluid viscosity and r the particle radius.

Also here, we collect $N = 10^5$ speckle images at a rate of 10^4 images per second for every sample. The corresponding g_1 curves are shown in Fig. 2.2a and power spectra obtained by direct FFT in Fig. 2.2b. We note that all power spectra exhibit the predicted $\omega^{-3/2}$ slope in the high frequency limit. Both the correlation functions and power spectra exhibit the expected trends. The decorrelation is shifted to larger correlation times as the glycerol concentration increases (Fig. 2.2a) and the power spectra show an increase in the low-frequency plateau value and a decrease in the corner frequency ω^*, as predicted above.

Diffusion coefficients are obtained from the real-space correlation curves using Eq. 2.3. For the FT-LSI data, we determine the corner frequency ω^* as the intersection between two fits through the low frequency plateau and high-frequency power law regimes. In this FT-LSI approach, we determine diffusion coefficients both from the height of the plateau, using Eq. 2.6, as well as from ω^* on the basis of Eq.2.8. We find a good agreement between the calculated diffusion coefficients and those obtained in the conventional approach and the two methods

emerging from the FT-LSI analysis. This lends further confirmation that FT-LSI can yield accurate and quantitative measurements.

2.2.3 Computational efficiency

The main advantage of the FT-LSI approach is its computational efficiency. To benchmark this, we compare the time it takes to compute a spatially-resolved LSI map using three different methods: i) LASCA, which is fast but not quantitative, ii) LSI, which is quantitative but slow and iii) FT-LSI which we will show is as fast as LASCA, and as shown above is as quantitative as conventional LSI.

LASCA estimates a measure for the rate of scatterer motion from the blurring of speckles by computing their intensity variance. It uses the contrast function K, defined as:

$$K = \frac{\sigma}{\langle I \rangle} \tag{2.15}$$

where σ is the standard deviation of the intensity of a speckle over time and $\langle I \rangle$ is its temporal average.

In quantitative LSI, the raw data is converted into an intensity-intensity autocorrelation function (Eq. 2.1) as a function of lag time τ, which is limited at the low end by the acquisition rate and at the high end by the length of the time series. To increase the statistical reliability of the data, averaging in space and/or time is often performed, at the cost of spatial and/or temporal resolution.

FT-LSI uses a direct conversion of the raw speckle data into the frequency domain using fast Fourier transform routines (as described in detail section 2.4). The result is squared and normalized to obtain the power spectrum.

We compare the computational efficiency of these three approaches (Fig. 2.3). We see how the conventional approaches differ widely in their efficiency; LASCA, performed on a single correlation time equal to the inverse of the frame rate, is substantially faster than the computation of the full autocorrelation function, but contains only qualitative data. By contrast, our FT-LSI approach results in data with the same information density as LSI, but operates as fast as LASCA. The calculation time t of FT-LSI and LASCA scales as $t \propto N \log N$, with the number of images N, compared to $t \propto N^2$ for LSI. It should be noted that multi-tau correlation schemes have been developed for DWS, which speed up calculation of the correlation function significantly. In such schemes, the correlation function is calculated not for all correlation times, but for a sequence of logarithmically spaced correlation times, with reduced time averaging to obtain correlation curves with negligible loss of accuracy.[42] Such correlation schemes have not yet been applied to LSI, but would obviously speed up correlation LSI. A lower limit for the calculation time for correlation LSI is the time needed to compute the correlation for a single

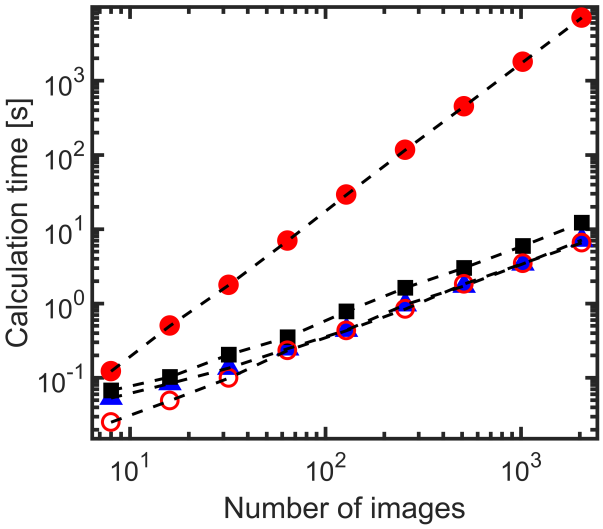

Figure 2.3. Calculation time as a function of data-set size with the amount of images containing 640x480 pixels each. Each calculation was repeated ten times and averaged, however variations were minimal. The three methods we compare are LSI (full correlation ●, single τ correlation ○), LASCA (▲) and FT-LSI (full spectrum ■).

τ. This is slightly faster than FT-LSI and comparable to LASCA (Fig. 2.3), but only yields information for a single correlation time for each pixel. Obviously, the computation time of multi-tau schemes will increase as a wider frequency range must be probed, and for these cases FT-LSI is a very attractive alternative. The computational efficiency of FT-LSI thus brings real-time quantitative imaging within reach, even for very large data sets.

2.2.4 Flow imaging

We have shown above how FT-LSI can be used to quantify simple Brownian motion. To explore the range of scenarios in which FT-LSI can be applied, we now consider the case of directional flow in a Brownian suspension. Traditional LSI and LASCA have been used extensively to study blood flow patterns in a medical context.[1,2,17,43–49] But the use of LSI to image flow fields could also be of interest in other scenarios, such as the real-time monitoring of industrial production processes that involve flow of complex fluids.

Convective processes in fluids that contain Brownian particles contain a mixture of different types of motion, which is often spatially and temporally inhomogeneous.

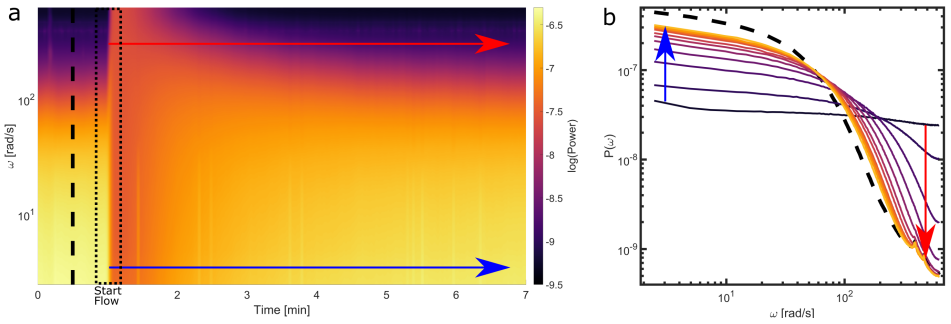

Figure 2.4. a) A spectrogram of flow in a channel to explore the time-frequency domain of the measurement. There is no flow in the first minute and the system is in equilibrium. At t=1 min we apply a 6 second flow burst after which the channel slowly goes back to equilibrium. **b)** Evolution of the power spectrum as the flow channel goes back to equilibrium. The dotted line is the power spectrum at t=30 seconds (equilibrium). After the start of the pressure pulse, power spectra are shown for 30 second intervals. In both figures the blue arrow shows the power evolution of the low frequencies and the red arrow the power evolution of the high frequencies.

To reduce this complexity, a spatially-averaged spectrogram, generated by FT-LSI is a convenient starting point as it gives a complete overview of the temporal evolution of the entire frequency-dependent response of the fluid of interest, for example to identify transitions between motion dominated by convective and diffusive motion.

To explore this, we create a simple microchannel that is created from a sacrificial template in PDMS (details described in the section 2.4) and loaded with a dispersion of titanium dioxide particles in a $90/10wt\%$ glycerol-water mixture. The suspension is left to equilibrate in the channel in the absence of flow, and we begin our FT-LSI recording. One minute after the imaging starts, we apply a pressure pulse, corresponding to an imposed flux of 100 μL/min that lasts for 6 seconds. After this, the pressure is switched off and we continue recording how the convective motion relaxes back to a quiescent state in which Brownian motion dominates. We compute the full spectrogram for this experiment, which is shown in Fig. 2.4a, and extract representative power spectra at 30 second intervals, as shown Fig. 2.4b.

The spectrogram shows a sharp transition at the time of the pressure pulse, where the motion of the scatterers transitions from diffusive motion to directional flow. In agreement with the theoretical predictions above, this change in motion causes the power of low frequencies to decrease and that of high frequencies to increase. When the pressure is removed, the relaxation of the convective flow to the quiescent state is much more gradual, and takes several minutes to complete.

Extracting power spectra at selected time points enables a more detailed view on the process (Fig.2.4b). We observe that the transition from convective to Brownian motion in the relaxation regime of the experiment follows the trends predicted by the theoretical framework, with a plateau that shifts upwards as convective motion ceases, while the slope of the high-frequency limit goes from ≈ -2 to $-3/2$. Within this approach, quantitative visualization of even complex flow scenarios can be performed with relative ease.

2.2.5 Portable real-time FT-LSI

The FT-LSI method paves the way to quantitative real-time imaging as the procedure can resolve spectrally-decomposed maps of scatterer dynamics at high rates. This could be particularly advantageous in clinical settings, where a fast diagnosis is beneficial. Such real-time LSI also benefits time-sensitive experiments as it allows rapid adjustments to the measurements in-situ. Furthermore it results in substantial data-reduction, as it does not require storage of all raw speckle images. Several real-time approaches based on the qualitative LASCA routine have been proposed,[18,19,33] however real-time quantitative LSI was not possible to date.

To resolve this, we have developed software that performs quantitative FT-LSI in real-time with minimal computational requirements, such that it can be performed on a simple tablet computer, which is connected to a portable LSI set-up. This is inspired by recent advances in portable LSI setups,[43,50] that enable measurements outside the laboratory.

A photograph of the portable and cordless LSI setup is shown in Fig. 2.5a and a schematic drawing in Fig. 2.5b. The sample is illuminated with a 50mW laser diode (λ =685nm, CNI lasers) which is powered from a power bank. The beam is expanded by a single lens in front of the laser. Speckle patterns are collected with a simple CMOS camera (Thorlabs), equipped with an objective with variable zoom and iris (Navitar). The ambient light is removed with a notch filter, whose transmission band is centered at the laser wavelength, placed between the camera and the objective. The setup is mounted on a compact platform with active vibration reduction (Accurion). The tablet controls the camera via USB and collects and processes the speckle images in a home-built application, coded in the python language. The software collects 50 speckle images per second with a resolution of 640x512 pixels. The power spectrum is continuously calculated for each pixel and visualized for one single frequency as a spatially-resolved power map. For data sets of 32 speckle images per power spectrum, we can calculate 4 FT-LSI images per second, which makes the experiment responsive to real-time adjustments.

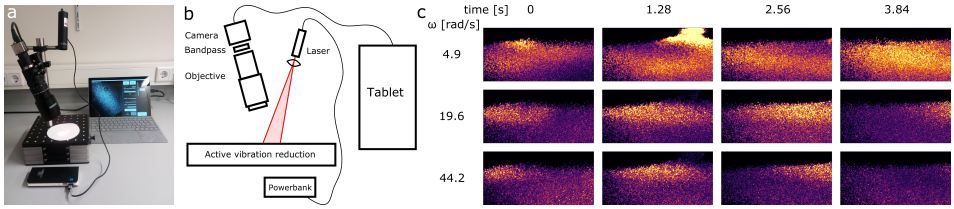

Figure 2.5. a) Photograph of the portable LSI setup. **b)** Schematic drawing of the portable LSI setup. **c)** FT-LSI images collected with the portable LSI setup of molten ABS plastic extruded from a 3D printer. The extruder moves from left to right and deposits a very thin layer on the already printed material. Light colors correspond to high power, dark colors to low power.

As a demonstration, we use the portable FT-LSI setup to study the layer bonding process during 3D-printing. Molten ABS plastic is extruded from a heated nozzle and a thin layer is deposited on previously printed layers. To weld newly printed layers onto previously deposited material, which has cooled down on contact with the printing plate, heat transfer from the new layer into the existing structure is paramount. Entanglement of the polymers during this layer bonding process is critical for printing strong objects. We use FT-LSI to follow the 3D-printing process in real time and present the results in Fig. 2.5c. In these images, the nozzle moves from left to right and deposits a 200μm thick layer on a 3 mm high existing object. There is a clear increase in dynamics around the deposition area, which reflects an increase in the polymer fluidity as a result of the heat transport from the new layer into the existing structure. This effect is visible several seconds after the nozzle has passed and spreads to a depth of at least 3 mm, which is equal to 15 layers in this case. With FT-LSI the layer bonding process can be studied and followed in real time.

This example shows the ability of the FT-LSI set-up to perform in versatile situations. No modifications to the 3D-printer were needed and the portability of the FT-LSI set-up enabled it to be placed inside the printer without issue.

2.3 Discussion

In this chapter we have presented a new FT-LSI analysis, which uses fast fourier transforms to obtain quantitative data with very high computational efficiency, offering orders-of-magnitude acceleration of quantitative data analysis. This advancement could be very benificial in the medical field, where current real-time approaches only give access to qualitative data. There also are a plethora of non-medical applications where this approach could become useful. For example,

in understanding layer bonding in 3D printing, as exemplified above, in the monitoring of complex fluid flow patterns or in the micromechanical imaging of extreme mechanics.[10–12] LSI has become more versatile by combining the real-time analysis with a portable setup. Setup portability allows measurements of complex systems in-situ as well as monitoring adjustments directly. The miniaturization of imaging technologies like LSI is an ongoing process and there are many more challenges left to tackle. Tablets and phones already come with built in cameras; if these cameras can be used directly, with small built in LED-lasers, this could enable direct blood flow imaging at the consumer level.

2.4 Methods

2.4.1 Backscatter LSI

Laser Speckle Imaging measurements in the backscatter detection geometry are performed on a set-up that has been described in detail elsewhere.[10,11] For illumination a 532nm laser (Cobolt Samba, 1W) is used. Two cameras were used on this set-up. To obtain 10^4 images per second a high speed camera (Fastec, HiSpec 1) was used with a small field of view ($128 * 8$). For the flow channel experiment a camera with live-streaming capabilities (Stemmer, Dalsa Genie) was used to stream images at 200 fps, with a resolution of 640*480 pixels for a longer period. This instrument is used for all experiments, except when specified otherwise.

2.4.2 FT-LSI routine

The FT analysis of LSI data starts by computing the power spectral density. We perform the FFT on a time sequence of N speckle patterns, where N is a power of 2 for computational efficiency. Each (xyt)-voxel is treated as an intensity time series of length N; all voxels are transformed simultaneously as a three dimensional matrix. First, we subtract the mean intensity for each voxel, to represent the time trace as intensity fluctuations around a mean of zero. This matrix is transformed to the frequency domain with the standard fft routine. Amplitudes corresponding to negative frequencies are discarded to obtain the single-sided amplitude spectrum, which is squared to obtain the power. The power is normalized by dividing by the frame rate and the trace lenght N, as well as dividing by $\langle I^2 \rangle - \langle I \rangle^2$. The result is a three dimensional matrix $P(x, y, \omega)$ containing power spectral densities for each xy pixel. The frequencies ω are equally spaced between 0 and ($\pi *$ frame rate), with $N/2 + 1$ unique frequencies. This matrix is either averaged spatially, or the result of a single frequency is mapped to a surface to obtain a power image for a particular frequency.

2.4.3 Channel fabrication

The flow channel is created using the ESCARGOT method.[51] First the channel is 3d-printed (Ultimaker) with ABS plastic and the object is embedded in a silicone elastomer (Sylgard 184, Dow Corning), which is cured at 60°C. Subsequently, the entire device is submerged in acetone to dissolve the ABS and leave a hollow channel in the silicone device. The channel has a rectangular cross-section with a width of 2.0 mm and a height of 600 μm. For the flow experiment, we introduce a suspension of of 2wt% titania nanoparticles, in a 10/90wt% water/glycerol mixture, using a syringe.

2.4.4 Real-time FT-LSI

To enable real-time FT-LSI imaging, we have developed a software application in the Python 2.7 programming language. The program runs over three separate threads to allow parallel real-time data collection and processing.

The first (main) thread contains a graphical user interface (GUI) to control the acquisition and analysis settings. This GUI continuously displays the most recent FT-LSI image at a selected frequency, using the pygame module. The second thread continuously collects the most recent speckle image from the camera and places it in a circular buffer in the main thread. Optionally the raw speckle images are saved to disk for later analysis. The third thread continuously performs the FT-LSI algorithm. The analysis starts with the n most recent speckle images from the main thread and performs the FT-LSI routine described above. The power image, at a single frequency, is rescaled and displayed in a color heat map. Optionally, also analyzed images are also saved to disk, as well as the quantitative $P(x, y, \omega)$ data for later analysis.

References

[1] A. Fercher, J. D. Briers. *Optics communications* **37**, 326–330 (1981).

[2] J. D. Briers. *Optica Applicata* **37** (2007).

[3] J. D. Briers, G. J. Richards, X.-W. He. *Journal of biomedical optics* **4**, 164–176 (1999).

[4] F. Wintzenrieth, S. Cohen-Addad, M. Le Merrer, R. Höhler. *Physical Review E* **89**, 012308 (2014).

[5] C. A. Nader, F. Pellen, P. Roquefort, T. Aubry, B. Le Jeune, G. Le Brun, M. Abboud. *Optics letters* **41**, 2521–2524 (2016).

[6] Z. Hajjarian, H. T. Nia, S. Ahn, A. J. Grodzinsky, R. K. Jain, S. K. Nadkarni. *Scientific reports* **6**, 37949 (2016).

[7] P. Zakharov, F. Scheffold. *Soft Materials* **8**, 102–113 (2010).

[8] A. Amon, A. Bruand, J. Crassous, E. Clément, *et al.*. *Physical review letters* **108**, 135502 (2012).

[9] M. Z. Ansari, A. K. Nirala. *Journal of Optics* **45**, 357–363 (2016).

[10] H. M. Van Der Kooij, R. Fokkink, J. Van Der Gucht, J. Sprakel. *Scientific reports* **6**, 34383 (2016).

[11] H. M. van der Kooij, A. Susa, S. J. García, S. van der Zwaag, J. Sprakel. *Advanced Materials* **29**, 1701017 (2017).

[12] H. M. van der Kooij, S. Dussi, G. T. van de Kerkhof, R. A. Frijns, J. van der Gucht, J. Sprakel. *Science advances* **4**, eaar1926 (2018).

[13] A. Amon, A. Mikhailovskaya, J. Crassous. *Review of Scientific Instruments* **88**, 051804 (2017).

[14] D. Pine, D. Weitz, J. Zhu, E. Herbolzheimer. *Journal de Physique* **51**, 2101–2127 (1990).

[15] H. Cheng, Q. Luo, S. Zeng, S. Chen, J. Cen, H. Gong. *Journal of biomedical optics* **8**, 559–564 (2003).

[16] J. D. Briers, S. Webster. *Journal of biomedical optics* **1**, 174–180 (1996).

[17] M. Draijer, E. Hondebrink, T. van Leeuwen, W. Steenbergen. *Lasers in medical science* **24**, 639 (2009).

[18] O. Yang, D. J. Cuccia, B. Choi. *Journal of biomedical optics* **16**, 016009 (2011).

[19] Y.-C. Huang, T. L. Ringold, J. S. Nelson, B. Choi. *Lasers in Surgery and Medicine: The Official Journal of the American Society for Laser Medicine and Surgery* **40**, 167–173 (2008).

[20] A. Nadort, K. Kalkman, T. G. Van Leeuwen, D. J. Faber. *Scientific reports* **6**, 25258 (2016).

[21] K. Schätzel. *Applied Physics B* **42**, 193–213 (1987).

[22] T. Gisler, D. A. Weitz. *Physical review letters* **82**, 1606 (1999).

[23] T. Mason, K. Ganesan, J. Van Zanten, D. Wirtz, S. C. Kuo. *Physical review letters* **79**, 3282 (1997).

[24] E. Sarmiento-Gomez, I. Santamaría-Holek, R. Castillo. *The Journal of Physical Chemistry B* **118**, 1146–1158 (2014).

[25] Y. Hemar, D. Pinder. *Biomacromolecules* **7**, 674–676 (2006).

[26] A. Ochab-Marcinek, R. Hołyst. *Soft Matter* **7**, 7366–7374 (2011).

[27] M. Erpelding, B. Dollet, A. Faisant, J. Crassous, A. Amon. *Strain* **49**, 167–174 (2013).

[28] M.-Y. Nagazi, G. Brambilla, G. Meunier, P. Marguerès, J.-N. Périé, L. Cipelletti. *Optics and Lasers in Engineering* **88**, 5–12 (2017).

[29] E. A. Robinson. *Proceedings of the IEEE* **70**, 885–907 (1982).

[30] N. Wiener, *et al.*. *Acta mathematica* **55**, 117–258 (1930).

[31] W. Lu, N. Vaswani. *arXiv preprint arXiv:0904.0602* (2009).

[32] G. Bergland. *IEEE spectrum* **6**, 41–52 (1969).

[33] P. M. Pieczywek, J. Cybulska, A. Zdunek, A. Kurenda. *Computers and Electronics in Agriculture* **142**, 70–78 (2017).

[34] D. Wang, J. Ranger, A. Moyer. *Advances in Optics* **2014** (2014).

[35] P. Zakharov, F. Cardinaux, F. Scheffold, *Saratov Fall Meeting 2005: Coherent Optics of Ordered and Random Media VI* (International Society for Optics and Photonics, 2006), vol. 6164, p. 61640K.

[36] P. Zakharov, F. Scheffold, *Light Scattering Reviews 4* (Springer, 2009), pp. 433–467.

[37] L. Djaoui, J. Crassous. *Granular Matter* **7**, 185–190 (2005).

[38] S. Takesue, T. Mitsudo, H. Hayakawa. *Physical Review E* **68**, 015103 (2003).

[39] J. Mo, A. Simha, S. Kheifets, M. G. Raizen. *Optics express* **23**, 1888–1893 (2015).

[40] P. Zakharov, A. Völker, A. Buck, B. Weber, F. Scheffold. *Optics letters* **31**, 3465–3467 (2006).

[41] P. Zakharov, A. Völker, M. Wyss, F. Haiss, N. Calcinaghi, C. Zunzunegui, A. Buck, F. Scheffold, B. Weber. *Optics express* **17**, 13904–13917 (2009).

[42] D. Magatti, F. Ferri. *Applied optics* **40**, 4011–4021 (2001).

[43] R. Farraro, O. Fathi, B. Choi. *Journal of biomedical optics* **21**, 094001 (2016).

[44] C. Stewart, C. Gallant-Behm, K. Forrester, J. Tulip, D. Hart, R. Bray. *Skin Research and Technology* **12**, 247–253 (2006).

[45] B. Ruaro, A. Sulli, E. Alessandri, C. Pizzorni, G. Ferrari, M. Cutolo. *Annals of the rheumatic diseases* **73**, 1181–1185 (2014).

[46] A. J. Strong, E. L. Bezzina, P. J. Anderson, M. G. Boutelle, S. E. Hopwood, A. K. Dunn. *Journal of Cerebral Blood Flow & Metabolism* **26**, 645–653 (2006).

[47] C. Stewart, R. Frank, K. Forrester, J. Tulip, R. Lindsay, R. Bray. *Burns* **31**, 744–752 (2005).

[48] K. R. Forrester, J. Tulip, C. Leonard, C. Stewart, R. C. Bray. *IEEE transactions on biomedical engineering* **51**, 2074–2084 (2004).

[49] A. K. Dunn, H. Bolay, M. A. Moskowitz, D. A. Boas. *Journal of Cerebral Blood Flow & Metabolism* **21**, 195–201 (2001).

[50] B. Lertsakdadet, B. Y. Yang, C. E. Dunn, A. Ponticorvo, C. Crouzet, N. Bernal, A. J. Durkin, B. Choi. *Journal of biomedical optics* **23**, 036006 (2018).

[51] V. Saggiomo, A. H. Velders. *Advanced Science* **2**, 1500125 (2015).

Chapter 3

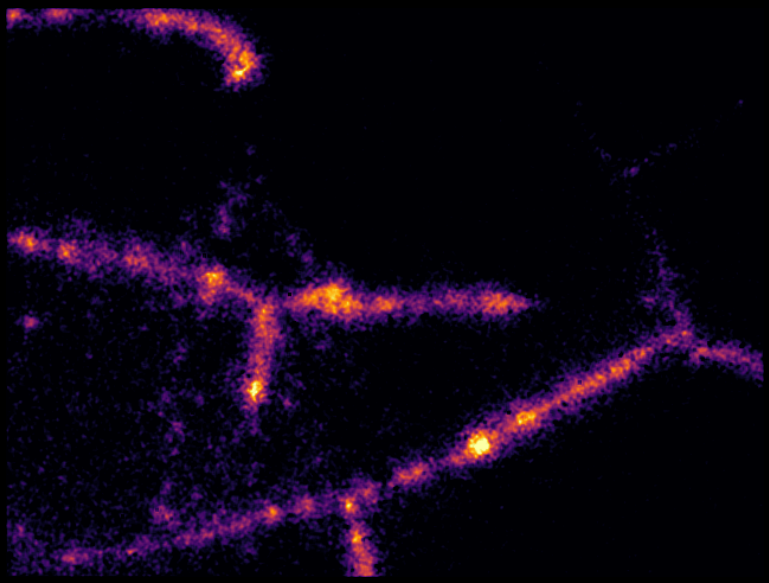

QUANTIFYING SOLVENT ACTION IN OIL PAINT USING PORTABLE LASER SPECKLE IMAGING

The exposure of oil paintings to organic solvents for varnish removal or to water for the removal of surface dirt can affect the chemical and physical properties of oil paint in an undesired way. Solvents can temporarily plasticise and swell the polymerised oil paint binding medium, enhancing both the thermal mobility and mechanical displacement of pigments embedded in this film. The enhancement of these microscopic motions can affect both the chemical and physical stability of the object as a whole. In order to minimise solvent exposure during cleaning, an analytical method that can quantitatively measure the microscopic motions induced by solvent uptake, is required first.

In this chapter, we use Fourier Transform Laser Speckle Imaging (FT-LSI) and a newly developed portable FT-LSI setup as highly resolved motion detection instruments. We employ FT-LSI to probe pigment motion, with high spatiotemporal resolution, as a proxy for the destabilising effects of cleaning solvents. In this way, we can study solvent diffusion and evaporation rates and the total solvent retention time. In addition, qualitative spatial information on the spreading and homogeneity of the applied solvent is obtained. We study mobility in paint films caused by air humidity, spreading of solvents as a result of several cleaning methods and the protective capabilities of varnish. Our results show that FT-LSI is a powerful technique for the study of solvent penetration during oil paint cleaning and has a high potential for future use in the conservation studio.

This chapter was published as: Baij, L., Buijs, J., Hermans, J. J., Raven, L., Iedema, P. D., Keune, K., & Sprakel, J., 'Quantifying solvent action in oil paint using portable laser speckle imaging', *Scientific reports* **2020**, 10(1), 1-12.

3.1 Introduction

Cleaning is considered to be an important step in the conservation of oil paintings.[1,2] However, it is known that the exposure of oil paints to organic solvents for varnish removal, or to water for the removal of surface dirt, can affect the physicochemical properties of the paint in an undesired way.[3–5] For example, exposure to organic solvents can lead to embrittlement of paint[6,7] and to the extraction[8–14] and redistribution[15] of soluble paint components. An increased rate of formation of degradation products, such as crystalline metal soaps (complexes of metal ions and long-chain saturated fatty acids), has also been reported.[15,16] Although a considerable amount of progress has been made,[3,4,17–19] the knowledge of the influence of solvent-based cleaning on fundamental chemical processes in oil paint does not currently allow for a reliable assessment of the risks involved in cleaning. Besides effects induced by solvent exposure, it is known that factors such as relative humidity (RH),[20,21] fluctuations in temperature[22] and exposure to light[23] can enhance the alteration and degradation of oil paints. However, it remains difficult to assess the importance of factors such as RH in terms of their influence on paint chemistry.

What exactly defines the impact of solvent action on paint is a complex interplay between many different chemical and physical phenomena. After the application of solvent, solvent swelling[24–26], –diffusion[27], –evaporation[28,29], –leaching (extraction)[9–14] and chemical reactions[15,16] occur simultaneously. It is not possible to quantitatively measure the total physicochemical influence of these combined processes during cleaning practice, and conservators often assume that minimal exposure to water or solvents limits the risks associated with cleaning. However, minimising solvent exposure starts with identifying which processes, methods and solvents are least invasive and measuring these processes under realistic treatment conditions. This crucial question has remained largely unanswered because of the lack of analytical techniques that enable quantitative comparison of parameters that define the impact of solvent exposure on paint. Effectively, the task of minimising solvent exposure during solvent-based cleaning requires a method that can quantitatively monitor the retention time and concentration of solvents reside inside oil paint. Ideally, such a technique should enable a quantitative comparison of cleaning methods or solvents on real paintings, should be portable and able to deal with heterogeneous paint surfaces. In addition, the instrumentation should feature an intuitive interface and should be easy to operate. Lastly but very importantly, data processing and interpretation should be fast (preferably on-the-fly) and should be easy to use for conservators. With such an analytical technique in hand, a conservator could then monitor how

long a paint layer is exposed to a certain concentration of solvent and combine this with information on when the varnish removal is complete, thereby limiting the risks associated with solvent exposure to the paint layers

In an attempt to classify solvents according to their diffusion coefficients, the authors have previously studied the diffusion of a range of solvents and water in linseed oil based ionomers and pigmented ZnO based paints using time-dependent attenuated total reflection Fourier transform infrared (ATR-FTIR) spectroscopy.[27] Important findings were that strongly swelling solvents generally diffuse faster than weakly swelling solvents and that all studied model systems showed similar diffusion behaviour, regardless of the presence of pigments.[27] While being good models for intact oil paint, these systems contain relatively pristine binding medium without (micro) cracks. Moreover, time-dependent ATR-FTIR spectroscopy does not allow the measurement of porous or brittle paints because it relies on constant and reproducible contact between the sample and the ATR crystal throughout the measurement. Another quantitative technique used to study solvent presence in paint is the NMR MOUSE (Mobile Universal Surface Explorer).[30] Fife *et al.* compared the stiffness of two paintings from the same artist and time, one of which was never cleaned and one that had been repeatedly exposed to organic solvents.[7] It was shown that the painting that had undergone numerous solvent-based varnish removals was significantly stiffer throughout the depth of the painting. Angelova *et al.* employed the NMR MOUSE to study water ingress in acrylic emulsion paints.[31] However, due to the limited time-resolution of the NMR MOUSE, the uptake of rapidly diffusing solvents can not be monitored.[29] Moreover, the NMR-MOUSE does not provide spatially-resolved information which can assess the homogeneity of the result after the cleaning treatment.

In this chapter, we aim to develop a real-time, quantitative and non-invasive tool to probe the destabilising effects of solvents on paint surfaces. To do so, we use Fourier transform laser speckle imaging (FT-LSI) to probe the motion of pigment particles in the paint film. Enhanced motion of these pigments, due to plasticisation or swelling of their matrix, is a proxy for the presence, and effects, of solvents. This enables us to obtain spatially-resolved information on solvent penetration in oil paint. LSI is a light-scattering technique that was developed in the 1980s as a medical imaging tool to visualise subcutaneous blood flow.[32] A great advantage of LSI is that it does not require specific sample preparation and can be used non-invasively on any opaque surface. LSI has recently been applied to study the evolution of dynamics in drying paint[33,34] and to capture the slow dynamics of drying artist oil paints and varnishes.[35] In the study by Pérez,[35] slow drying processes were monitored using discontinuous data collection at 10 fps every minute and data processing was performed after the raw speckle image

collection. In this chapter, we use recently developed quantitative methods for on-the-fly data processing on a portable and low-cost (≈ 5k euro) LSI setup.[36] With this setup we can collect up to 60 fps of raw speckle images continuously, allowing for the measurement of fast dynamics of solvent penetration during cleaning at a high frame-rate. Because organic solvents are transparent and do not scatter light, the measured LSI dynamics in oil paint observed after solvent exposure are the result of nanoscale motions of scattering pigment particles induced by solvent transport inside the paint. In our measurements, the nanoscale motions of scattering pigments are composed of two components: (1) thermal motion that probe the local mechanical (microrheological) properties of the paint and (2) convective motion induced by solvent molecules due to swelling or de-swelling of the paint matrix during solvent sorption or desorption. We investigate how transport phenomena, such as solvent diffusion and flow, are related to the measured LSI signal and to what extent either of these transport phenomena occur in our paint samples.

ZnO and linseed oil (ZnO-LO) based model systems are used to investigate solvent transport in oil paint models and to study how the rate of the investigated transport processes depends on paint degradation or environmental conditions. ZnO is widely used in oil paintings[37] and associated to many types of degradation phenomena, most importantly the breakdown of ZnO itself[38] and the formation of crystalline zinc soaps.[16,39] Linseed oil (LO) is widely used in oil paintings because it possesses excellent drying properties and consists of a mixture of triacylglycerides (TAGs) that mostly contain linolenic acid (C18:3), linoleic acid (C18:2), and oleic acid (C18:1) side chains. Upon drying and ageing, LO forms a tightly crosslinked polymer network. The network structure of the polymeric binding medium determines the rate and type of solvent transport in the paint. In this chapter, we perform experiments on lab-made model paint samples because this allows for full control over the sample composition, type of support, sample geometry and history of the samples.

To investigate the detection limit of the LSI setup for solvents inside paint, we set out to study complete swelling and de-swelling with ethanol, a solvent commonly used to dissolve aged natural varnishes on oil paintings. Subsequently, the effects of different relative humidity (RH) conditions in ZnO-LO films are measured and compared within a range of relative humidities recommended for museums.[40] Next, the relation between the rate and type of solvent transport and the paint degradation on a molecular level are investigated using both LSI and ATR-FTIR. Finally, different solvent application times and methods of solvent application are compared. The effects of varnishes are systematically studied using artificially aged dammar varnish with different thicknesses. A range of solvents

that is typically used for varnish or surface dirt removal, as well as a selection of green solvents that have been suggested as new alternatives for some of these solvents, is compared.

Our preliminary experiments on aged model paint samples are expected to aid conservators in making informed decisions when choosing solvents or application methods. Ultimately, a portable FT-LSI setup with on-the-fly data processing could become a valuable analytical tool in the conservation studio by providing measurable criteria for the selection of solvents and cleaning methods during the initial phase of cleaning and solubility tests on real paintings.

3.2 Results and Discussion

3.2.1 De-swelling of a saturated paint film

The most extreme case of solvent transport in paint is complete swelling and de-swelling. The degree of equilibrium (maximum) swelling serves as an important parameter that determines the effects of solvents on oil paint and swelling has been extensively studied in the literature.[24–27,41]

To determine the detection limit of the FT-LSI setup for solvent in oil paint, a ZnO-LO model system on glass support was saturated in ethanol for 2 hours to achieve complete swelling,[27] after which the de-swelling process was monitored using LSI. After removal from the ethanol bath, the paint was left to dry to the air in the FT-LSI set-up (Figure 3.1a), which is described in the methods section. The speckle patterns were analysed in real-time using a recently established Fourier-transform algorithm. Fourier inversion of the temporal intensity fluctuations for each speckle, give access to a function, the power-spectral density, or power spectrum in short, that contains all relevant information about the type and rate of the dynamic processes that occur inside the paint film. The power spectrum for a specific dynamical process will show a low frequency plateau and a decay at frequencies higher than a characteristic decay frequency, where the slope (on a log-log representation) is indicative of the nature of the scatterer motion; with a slope = -1.5 for diffusive motion and -2 for convective motion. The characteristic decay frequency is a measure for the rate of the dynamics; slow diffusion leads to decay at high frequencies, while fast diffusion leads to decay at much lower frequencies. For a complete overview of the method we refer to Buijs *et al.*[36]

During the de-swelling process, raw speckle images were collected over the course of 20 hours and analysed to obtain the power spectra that are shown in Figure 3.1b. Ethanol is transparent to green light and therefore cannot be measured with FT-LSI. However, the presence of ethanol or other solvents will temporarily

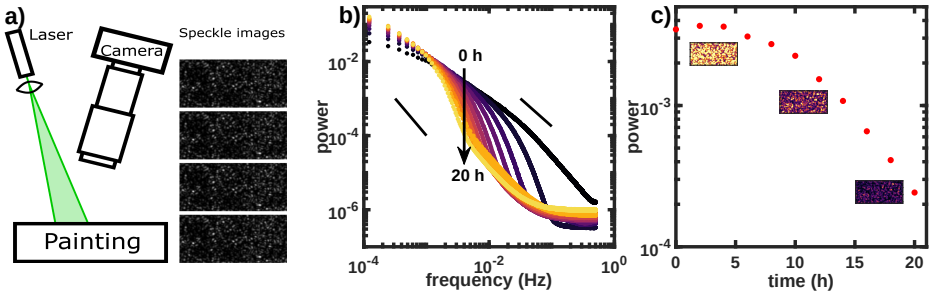

Figure 3.1. a) Schematic representation of a typical FT-LSI experiment where the laser illuminates a painting, resulting in interfering back-scattered light. These characteristic speckle patterns are captured with a camera. Microscopic motion of light scattering pigments in the paint results in a change in the speckle pattern over time. The change in the speckle pattern over time is quantified using the Fourier transform, which provides a power spectrum for every pixel and results in a 4-dimensional dataset (x, y, time, frequency). **b)** Power spectra of the de-swelling of a ZnO model system, showing the power of motion as a function of the measured frequency range from 0 hours (black) to 20 hours (light yellow) after the start of the de-swelling. Indicative slopes of -2 (left black line) for convective behaviour and -1.5 (right black line) for diffusive behaviour are indicated. **c)** In depth analysis of the 0.0033 Hz frequency (arrow in b). We map the power of this frequency for every pixel to obtain a false-colour movie. The three snap-shots of the movie are presented and show a spatially homogeneous decrease of dynamics. By averaging every frame spatially we obtain the time-trace which gives a good overview of the whole experiment.

plasticise the chemically-crosslinked oil paint network, increasing the mobility of scatterers embedded therein, creating an acceleration of the temporal fluctuations in the scattered intensity that is detected with FT-LSI. Investigating Figure 3.1b over the whole frequency range, it becomes clear that from t=20 h to t=0 h (increasing ethanol concentration), the power spectra and the inflection point shift to lower frequencies, which indicate that the effective diffusion coefficient increases with increasing ethanol concentration. The shape of the power spectra deviates from characteristic shape described in the previous paragraph and reference [36] because we measure a mixture of processes with different nature and characteristic timescales such as thermal motion, de-swelling and flow through micro-channels.

The value of the power spectral density at a given frequency, or power, can be used as a scalar proxy for the amplitude of dynamic processes, *e.g.* the relatively plasticity of the paint film. By following the power at a given frequency in time, temporal changes in the plasticity can be directly monitored. Figure 3.1c shows the power of the 0.0033 Hz frequency over the course of 20 hours. From this time-trace it is clear that, although the power has decreased by one order of magnitude, there still is a measurable change of dynamics going on after 20 hours. Using the

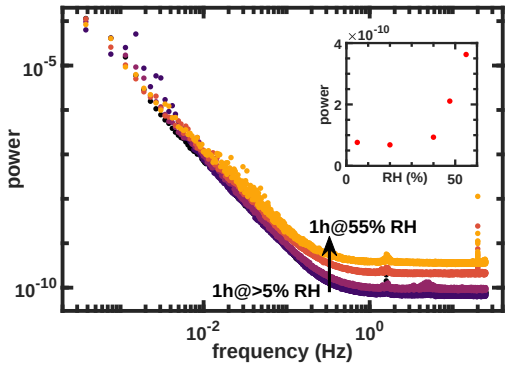

Figure 3.2. Power spectra of ZnO model painting with increasing humidity (dark to light yellow). Inset: mean power at high (>1 Hz) frequency. The dynamics increase significantly above 40% RH.

theoretical description of (de)swelling of our paint models,[27] the swelling at t=20 h is predicted to be <0.5% of the equilibrium swelling (at t=0 h). It is thus clear that FT-LSI is able to measure motion that is induced by the presence of very small amounts of solvents inside the paint (Figure 3.1c).

3.2.2 Air humidity

Having established that FT-LSI is sensitive to low concentrations of solvents in paint, we investigated if subtle differences in environmental RH on the paint plasticity can be measured with LSI. The effects of environmental RH on oil paint are an important aspect in determining climate conditions in museums, which are often advised around 50% with limited fluctuations.[40] For oil paintings, it is known that high RH conditions can result in an increased rate of ester hydrolysis of TAGs in the oil binder and influence certain autoxidation pathways.[38,42] Ester hydrolysis can lead to the release of highly concentrated saturated fatty acids (SFAs) in an oil paint, thereby increasing the risks of (crystalline) metal soap formation when metal ions (for example derived from lead white ($2\,PbCO_3Pb(OH)_2$) or zinc white (ZnO)) are present.[16,43] Even when the paint is already cured, high RH can also stimulate the formation of carboxylic acid groups.[38] The increased formation of carboxylic acid groups can indirectly lead to the formation of crystalline zinc soaps, because carboxylic acid groups stimulate the formation of amorphous zinc carboxylates,[38] which are intermediates in the formation of crystalline zinc soaps.[16]

With the molecular mechanisms of paint degradation described above in mind, a ZnO model system was measured with LSI at different RH levels inside a climate

box. For each humidity, the sample was left to equilibrate for 1 hour and then measured for 1 hour at room temperature (RT) after which the RH was increased for the next measurement cycle. The obtained power spectra are shown in Figure 3.2 and the inset shows the average measured power at high frequencies (>1 Hz). A strong increase in dynamics at humidities above 40% was observed, which is the result of increased molecular motion in the paint. The fact that relatively small differences in RH conditions (40–50–55% RH, inset of Figure 3.2) induce large changes in the dynamics inside oil paint, underlines the great potential of FT-LSI for monitoring the effects of solvents and water inside oil paint. Two explanations may contribute to the measured sudden increase in molecular motion around 40% RH: (1) moisture plasticises and swells the paint and (2) chemical paint alteration mechanisms, such as ester hydrolysis, could speed up significantly at this RH. It should be noted that it is currently unclear to what extent either of these two factors contribute to the measured power spectrum. Most likely, both these processes will go hand-in-hand. As such, our results may lead to re-evaluation of safe storage conditions for oil paintings. In the future, it could be worthwhile to investigate the relation between bulk viscoelasticity and RH with dynamic mechanical analysis (DMA). Since the glass transition temperature (T_g) of ZnO-LO is close to RT,[27] it may be that subtle differences in RH induce a transition to the rubbery regime, providing further explanation for the strong increase in molecular motions.

3.2.3 Effects of ester hydrolysis on solvent transport

Due to the wide variety in the composition of paint materials and the conditions during the drying and storage of paintings, a wide variety of different porosities and network structures is found in paintings. Differences in porosity are expected to have a strong effect on the rate of solvent transport in paint and the retention of solvents inside paints. To describe solvent transport, a distinction is often made between convective solvent transport in micro-channels and solvent diffusion in the inherent free volume of the polymer network.[44] Convective transport in paint is generally several orders of magnitude faster that diffusion.[45] In our experiments, a range of processes consisting of solvents sorption, desorption and evaporation contribute to the total FT-LSI signal intensity and decay rate that is measured. The rate of FT-LSI signal decay thus gives information on sorption, desorption and evaporation combined. Although the extent to which sorption, desorption and evaporation contribute to the measured signal is currently unknown, these processes combined define the *retention time*: the time solvents are retained in the paint layer. Knowing the solvent retention time and the rate of signal decay can help to decrease the risks associated with solvent-based cleaning because these

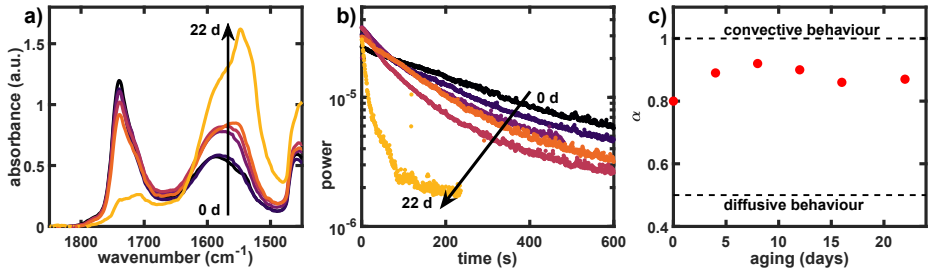

Figure 3.3. a) ATR-FTIR spectra normalised on the CH_2 stretching vibration (2929 cm^{-1}) and **b)** FT-LSI signal decay (1.6 Hz) for series ZnO-LO-0d–22d series where the series are coloured increasingly dark from 0d to 22d following the trend of the arrow. **c)** Stretching exponent α where α = 0.5 corresponds to purely diffusive motion and α = 1 corresponds to purely convective behaviour. ROI for FT-LSI-signal integration were chosen as described in Figure 3.A.3. The fitting procedure to obtain α is shown in Figure 3.A.5.

important parameters determine how long the paint is plasticised by solvents. To investigate if LSI can monitor such differences, we studied solvent transport in oil paints that were subjected to prolonged exposure to very high RH conditions.

A series of ZnO-LO paints that were subjected to accelerated ageing at 97% RH at 60 °C for 4 to 22 days (designated ZnO-LO-0d to ZnO-LO-22d) were used for these experiments. Because ZnO-based model paints easily hydrolyse in high RH conditions, the effects of ester hydrolysis on solvent retention and transport can be studied. Upon ageing, an increasingly matte appearance and extensive yellowing was observed. At the same time, hydrolysis of the esters in linseed oil, the liberation of free fatty acids (FAs) and, eventually, the formation of zinc soaps took place. Figure 3.3a shows a collection of ATR-FTIR spectra, clearly showing the increasing concentration of amorphous zinc carboxylates[38,46,47] (COOZn, broad band at 1585 cm^{-1} in Figure 3.3a) and ultimately, the formation of crystalline zinc soaps after 22 days of ageing (sharp peak at 1540 cm^{-1} in Figure 3.3a).

Solvent retention was measured by placing a 3 μL droplet of ethanol on top of the sample, waiting for the appearance of a dry surface (t_0, as seen in the images by the droplet shrinking) and subsequent integration of the total intensity of the FT-LSI signal in a Region of interest (ROI) in the centre of the droplet. Movie ZnOLO-22d (section 3.A.7) shows the raw speckle images obtained during the ZnO-LO-22d measurement side-by-side with the analysed FT-LSI movie. The FT-LSI signal decay for the ZnO-LO-0d–22d series is displayed in Figure 3.3b, showing a significant increase in signal decay rate with increased ageing. In this series, the 1.6 Hz frequency was chosen in order to detect the fast changes in dynamics encountered during solvent exposure. Besides the significant increase in

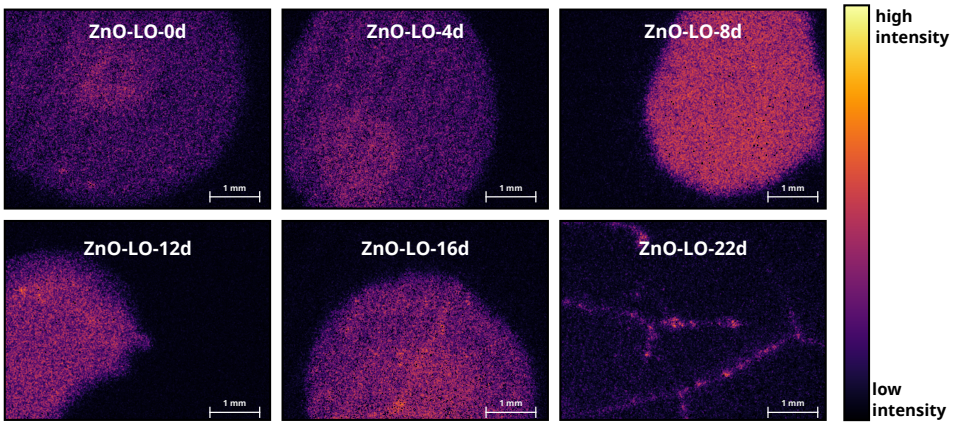

Figure 3.4. FT-LSI images (1.6 Hz) for ZnO-LO-0d–22d one minute after ethanol application (3 μL droplet). Increasing solvent spreading and micro-crack formation upon ageing at 97% RH and 60 °C for 4 to 22 days. Solvent spreading and penetration rate correlates with increasing COOZn concentration upon ageing (ZnO-LO-0d–16d) and finally significant ester hydrolysis and zinc soap formation in ZnO-LO-22d.

signal decay rate upon ageing, major qualitative differences in the FT-LSI images were observed in the strongly aged sample (see 22 days aged sample in Figure 3.4). Especially ZnO-LO-22d clearly shows the appearance of micro-channels after solvent application.

The increased amount of crack formation in aged samples may explain the increased transport in lateral direction (Figure 3.4, ZnO-LO-22d), and therefore the increased rate of solvent uptake. It has been shown in the literature that the rate of solvent sorption (k_S) in oil paint is faster than desorption (k_D) and the two rates are related by $k_D/k_S \approx 0.65$ in most cases.[24] If there is no significant interaction between solvent and paint that depends on the ageing, solvent desorption will also be faster in films that have been more severely aged. The combined faster spreading of the solvent due to transport in lateral direction and the faster desorption due to faster evaporation may explain the increased decay rate for samples with increased ageing, finally resulting in lower solvent retention in aged samples.

To investigate the type of solvent transport in more detail, the stretching exponent α was calculated (Figure 3.3c). The value of α gives information about the nature of the measured motion: if $\alpha = 0.5$, the motion is purely diffusive and if $\alpha = 1$, the motion is purely convective.[34] The α factor was computed by fitting the slope of the power spectrum with a straight line where the slope is equal to $-(1 + \alpha)$ on a log-log axis.[36] The motion of pigment particles probed by LSI are the result of both the microrheological properties of the paint and the

convective motion of the swelling. Figure 3.3c indicates that the pigment motion is partly diffusive and partly convective over the whole ageing series and does not show a significant change in α upon ageing. The solvent itself will have flow-like behaviour through micro-channels and cracks, but does not translate this motion directly to the pigment particles and therefore this is not noticeable in the computed α-values. In Supplementary Movie ZnOLO-22d (section 3.A.7) it is visible that the solvent spreads out over a large area through cracks in the ZnO-LO-22d while Supplementary Movie ZnOLO-0d shows that the solvent remains localised in the area of the droplet in the ZnO-LO-0d sample. However, the mechanisms behind the plasticisation and swelling do not change. Consequently, a larger area is affected by the solvent in the aged films for a shorter period of time.

We conclude that there is a correlation between solvent retention (Figure 3.3b and Figure 3.4) and the degree of ageing measured by increased ester hydrolysis (Figure 3.3a): increasingly aged samples show faster FT-LSI signal decay and more solvent spreading. Because the solvent is transferred out of the ROI that was used for integration of the LSI signal, it remains difficult to say to what extent this faster signal decay originates from either evaporation or convective transfer. In any case, our measurements confirm that an increase in crack formation results in an increase in both the rate of evaporation and the rate of solvent transport. As a result, the area of the paint that is exposed to solvents is significantly increased in aged samples, even when solvents are applied locally.

3.2.4 Effects of solvent exposure time and varnishes

The effects of solvent exposure time and the presence of varnish on the solvent delivery inside the paint layer were investigated using Evolon® CR tissue with a 51% loading of ethanol (Evolon-51%, see section comparing application methods).[48] This cleaning method is known for it's effectiveness in varnish removal and features an excellent reproducibility (see Figure 3.A.1). The FT-LSI signal decay was measured for a series of 15–300 seconds exposure of Evolon-51% ethanol on an unvarnished ZnO-LO model system. The results are displayed in Figure 3.5a, showing that the rate of FT-LSI signal decay strongly decreases with increasing exposure time. As expected, longer application times result in increased solvent delivery in the paint, as shown in Figure 3.5a.

In a control experiment testing solvent-swollen varnish on glass, we investigated if varnish leftovers (without scattering pigments) can significantly contribute to the measured LSI signal. It was found that solvent-swollen varnish is an important contribution on short timescales (see Figure 3.A.2) due to the rapidly changing refractive index of the varnish when swollen with solvent. As a result, interpreting

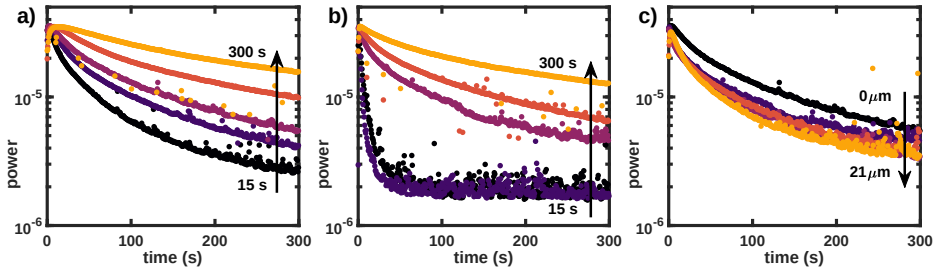

Figure 3.5. FT-LSI signal decay (1.6 Hz) time-series: 15–300 seconds Evolon-51% ethanol exposure, **a)** unvarnished, **b)** varnished (<7 μm) and **c)** varnish layers with increasing thickness ranging from <7–21 μm and constant exposure time of 60 s. ROI for FT-LSI-signal integration were chosen as described in Figure 3.A.3.

the relative contribution of scattering inside the paint and scattering inside the varnish in measurements where varnish is left on the paint surface after solvent exposure, is difficult. To test if varnish removal was complete, a portable UV lamp was used to judge if varnish fluorescence was absent after all measurements. This method is also routinely used by conservators to determine if varnish removal is complete.

Figure 3.5b shows the effect of a thin (9 μm) varnish layer. Judging by the similar signal decay rates obtained for 15 and 30 s exposure time, the solvent does not reach the paint layer in the first $\approx$ 30 s and the FT-LSI signal is dominated by the quickly decaying signal of swollen varnish. The incomplete removal of varnish after 15 and 30 s was confirmed by the presence of UV fluorescence, indicating that the relatively intense dynamics in the first seconds after solvent application may be partly explained by the signal of swollen varnish in the measurements using 15 and 30 s exposure time. Exposure times of 60 s or more yield similar results to the unvarnished samples, indicating that the varnish layer was indeed removed and unhindered solvent transport into the paint layer was possible after $\approx$ 60 s.

To explore the effects of the varnish thickness on the relative amount of solvent delivered to the paint in more detail, a series of varnished model systems with and increasing thickness of < 7–21$\pm$2 μm was prepared (thickness determined by optical coherence tomography,[49] OCT, see Figure 3.A.4). In this series, the solvent exposure time was kept constant at 60 s. The results are displayed in Figure 3.5c, clearly confirming that the presence of thicker varnishes results in smaller amounts of solvent penetrating into the paint layer. However, this effect is subtle compared to the exposure time series because doubling the varnish thickness did not double the protective duration.

3.2.5 Comparison of solvents

Conservators use a wide range of different (mixtures of) organic solvents to dissolve and remove discoloured natural resin varnishes. The composition of these varnishes determines the choice of solvents for their effective removal, keeping the minimal influence to the underlying paint layers in mind. Like polymerised drying oils, varnishes generally increase in polarity upon ageing by the increasing formation of oxidised products. The increased polarity of the varnish can change its solubility in organic solvents significantly and require increasingly polar solvents to dissolve aged varnishes.

To investigate if FT-LSI can discriminate between the activity of different solvents, a series of solvents used for the cleaning of paintings was tested on an unvarnished paint surface. It is known that solvents can have vastly different diffusion rates, with water being among the slowest diffusing solvents and acetone one of the quickest.[24,27,41,50] During conservation cleaning practice, solvent diffusion- and evaporation rate are important because these combined factors determine how long solvents are present in a paint and how far they diffuse inwards. We used FT-LSI to measure this combined effect of diffusion and evaporation of acetone, ethanol, isopropanol, dimethyl carbonate (DMC), ethyl lactate (EL), γ–valerolactone (γ–VL) and *n*-hexane. Acetone, ethanol, isopropanol and hexanes are widely used in conservation studios, whereas DMC, EL and γ–VL have recently been suggested as green alternatives for varnish removal.[29,51]

FT-LSI probes changes in the dynamics of scattering pigments inside the paint film and therefore the power of the FT-LSI signal is not easily converted into a solvent concentration. The pigment motion is governed by the local visco-elasticity of the paint film, which is influenced by the presence of varying amounts of solvent in a complex way that is currently unknown. In principle, a thorough calibration of the solvent content on the scatterer motion would enable such a conversion but would need to be performed for each different type of matrix and solvent as it is sensitive to chemical details. However, for initial monitoring of solvent presence during artwork cleaning, such a conversion is not required.

The FT-LSI signal decay of the 1.6 Hz frequency is displayed for a series of solvents in Figure 3.6. The solvents were applied as a 20 μL droplet, left on the surface for 60 s and carefully dried with filter paper. Although the translation of the FT-LSI signal into diffusion rates is not straightforward, it is interesting to observe that the trends in FT-LSI signal decay displayed in Figure 3.6 are in agreement with known trends in diffusion rates: acetone > ethanol > isopropanol > water ≈ hexane.[27] The signal decay rates of EL and DMC are comparable and close to acetone, both are much faster than γ–VL. This effect can be partly explained by

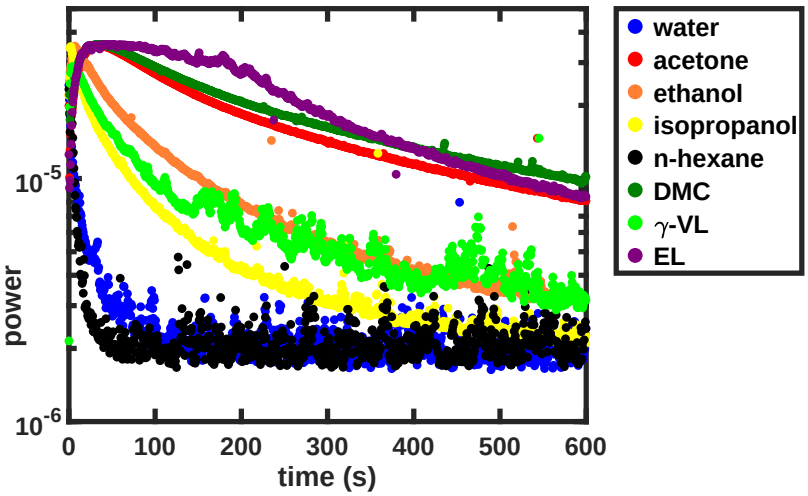

Figure 3.6. FT-LSI signal decay (1.6 Hz) for a series of solvents applied as a 20 μL drop, left on the surface for 60 s and dried with filter paper. ROI for FT-LSI-signal integration were chosen as described in Figure 3.A.3.

the fact that ethanol or acetone are much faster diffusing solvents than hexane and water,[27] resulting in further solvent penetration and longer plasticisation.

It should be noted that the FT-LSI signal does not necessarily correlate with the rate of varnish dissolution or leaching of soluble paint components, since these processes are governed by the solubility of these components in a given solvent. For example, although the FT-LSI signal decay rate for acetone, DMC and EL are highly similar, their rate of varnish dissolution on aged dammar varnish is vastly different, with acetone being faster than DMC and both acetone and DMC much faster than EL. The rate of leaching of soluble paint components is an important factor in cleaning studies but can not be measured by LSI. However, if solvent penetration in the paint is limited, it should be safe to assume that leaching is also minimised.

3.2.6 Comparison of solvent application methods for varnish removal

Besides flexibility in the choice of solvents, a conservator can utilise a variety of methods to apply the solvents. Most of these methods have been developed to minimise the amount of solvent exposure and mechanical action on the surface and to increase the reproducibility of the cleaning action, resulting in a more homogeneously cleaned surface. We have used the portable FT-LSI setup[36] to

compare four methods of solvent application for varnish removal from ZnO-LO model paints, using ethanol as a solvent in all cases:

- The cotton swab, traditionally widely used for varnish removal
- Evolon® CR tissue, an alternative used for varnish removal and composed of a Nylon/polyethylene terephthalate (PET) fabric.[48] The Evolon® tissue can be loaded with different amount of solvent by equilibrating known amounts of tissue and solvent in a sealed container overnight. In our tests, the Evolon tissue was always covered with a thin sheet of Mylar® (biaxially-oriented PET) during application.
- Nanorestore® Max Dry (MD) gel, can be used for varnish or surface dirt removal and consists of semi-interpenetrating polyhydroxyethylmethacrylate (pHEMA) and polyvinylpyrrolidone (PVP) networks.[52]
- the 'SRAL method', employing the spreadable hydroxypropylcellulose (HPC, marketed as Klucel G) gel loaded with cleaning solvent on an impregnation tissue, removing the gel with an absorbing tissue and subsequent rinsing with a lower polarity solvent and a cotton swab.[53] Isopropanol was chosen for rinsing.

The resulting comparison of different methods of solvent application measured on the portable LSI setup is displayed in Figure 3.7. Although the signal decay rates shown in Figure 3.7 are not pure diffusion coefficients, the relative signal decay rates can be used as a measure of the amount of ethanol delivered into the paint. In this set of measurements, the absolute signal intensity is much higher compared to the lab-based LSI. These differences are not relevant for the comparison of different methods of solvent application within this data set. Figure 3.7 shows that the swab and Evolon feature a similar and relatively fast decay rate. Keeping in mind that the swab method was used until a satisfying varnish removal was obtained (< 10 s), the dynamics are initially quite intense. The fast decay to a low intensity indicates that the amount of solvent delivered deeper into the paint by the swab and Evolon is small. This result is not in contradiction with our earlier result showing that the swab extracts more free FAs from deeper paint layers compared to Evolon or MD gel, because in that study all methods were compared at the same exposure time.[15] It should be noted that the time required to completely remove the varnish with Evolon was < 60 s, implying that even shorter contact times could be used with this method. The initial signal intensity for the SRAL method (excluding clearance) and for the MD gel are much higher than the other methods, probably because a significant amount of varnish remained on the surface (see also Figure 3.8) after the

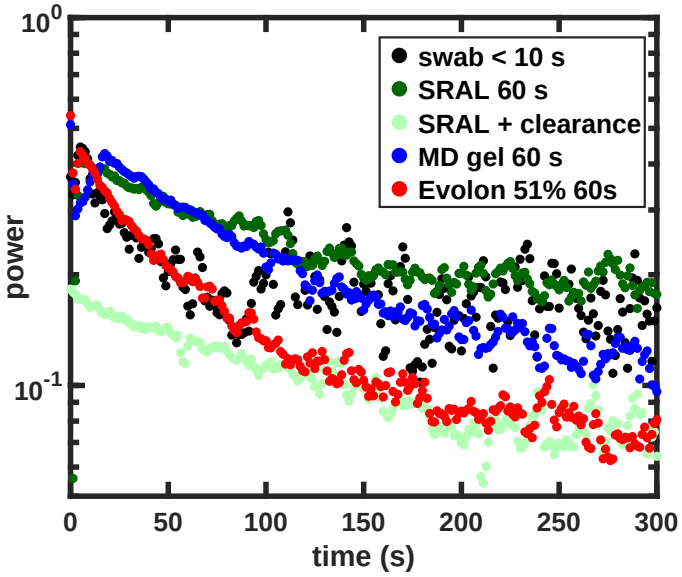

Figure 3.7. FT-LSI signal decay (1.6 Hz) for ethanol applied using the cotton swab, Evolon tissue, MD gel and SRAL method measured using the portable LSI setup. Except for the swab, the surface was always exposed to ethanol for 60 s, the swab was used until a satisfying result was obtained (< 10 s). The dotted line in the Evolon image marks the edge of the evolon tissue. For comparison, the SRAL method was measured with and without isopropanol rinsing. The initial varnish thickness was 9 μm. ROI for signal integration as described in Figure 3.A.3.

treatment. If varnish is left on the surface, the evaporation of solvent is hindered, explaining the relatively slow decay rate and high signal intensity even after 300 s. If the SRAL method is directly cleared with a swab afterwards, the signal intensity is very low due to the use of isopropanol, a slowly diffusing solvent (see Figure 3.6).

A valuable addition to the quantitative information obtained from the portable FT-LSI signal integration is obtained from the LSI images displayed in Figure 3.8 where the homogeneity of the solvent application can be compared qualitatively. Figure 3.8 shows that the Evolon tissue results in the most homogeneous application of the solvent. Diffusion of ethanol vapour outside the regions of the Evolon tissue (marked with a dotted line) is also observed, likely because the Evolon tissue is covered with a sheet of Mylar during application. Ethanol diffusion outside the regions of application may explain the formation of tidelines (unwanted regions were varnish is deposited outside the area of solvent application) which is frequently noted by conservators. It is often claimed that rigid gels such as the MD gel allow a more precise application of the solvent. Interestingly, this is not

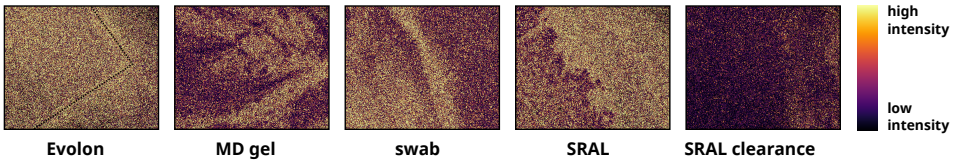

Figure 3.8. Scaled FT-LSI images obtained using the portable LSI setup. The images were taken directly after the simulated treatment with ethanol applied using the cotton swab, Evolon tissue, MD gel and SRAL method. Except for the swab, the surface was always exposed to ethanol for 60 s, the swab was used until a satisfying result was obtained (< 10 s). The images from the SRAL method are shown with and without isopropanol rinsing. The initial varnish thickness was 9 μm. The total area that was exposed to Evolon tissue was 1×1 cm, the dashed lines approximately indicate the boundaries where Evolon tissue was applied.

actually the case judging from the portable FT-LSI image for the MD gel. The relative heterogeneity visible in the image of the MD gel can be explained by the fact that the MD gel did not completely remove the varnish within 60 s, but rather redistributed part of the varnish over the area of application. For a fair comparison, the swab method was not used for 60 s but until a satisfying result was obtained (< 10 s, as judged by the conservator using a portable UV lamp). Although the initial FT-LSI signal intensity is similar to the other methods, the varnish removal is very quick. A downside of the swab methods is also evident, showing that swabbing results in certain areas receiving more pressure and thus more solvent than others, judging from the heterogeneity that is visible in Figure 3.8. The portable FT-LSI images show a heterogeneous solvent application by the SRAL method, but after clearance with isopropanol, the activity is homogeneous as well as of lower intensity than other methods.

Despite the higher noise levels compared to the lab-based setup, the data from the portable FT-LSI setup (Figure 3.7 and 3.8) clearly shows quantitatively different results for different solvent application methods. Most importantly, the FT-LSI images (Figure 3.8) are computed and displayed real-time during the measurement, immediately showing the qualitative differences and making the portable FT-LSI a valuable tool for conservators.

3.3 Conclusions

LSI is a powerful and sensitive technique to study the motion of scattering pigments inside oil paint, showing the presence of solvent during solvent cleaning real-time. LSI detects the presence of ethanol in oil paint for more than 20 hours after saturation with solvent. In a set of measurements with increasing relative

humidity, a strong increase in dynamics at humidities above 40% was observed, underlining the great sensitivity of LSI for detection low concentrations of solvents inside oil paints.

Increasingly aged paints showed solvent spreading over a larger area but a shorter overall solvent retention. A correlation between increased ester hydrolysis of the binding medium and rapid solvent flow in micro-cracks could be made. The effects of increasing solvent exposure time using Evolon tissue on varnished and unvarnished paints were studied. Increasing exposure times were shown to result in slower signal decay, indicating that more solvent is delivered inside the paint. Thin varnish layers protected the paint temporarily from solvent sorption, showing how long solvent exposure can be with minimal solvent penetration into the paint. LSI provides quantitative and qualitative spatial information on cleaning methods, which are required for a reliable risk assessment of application times or -methods. Important quantitative differences in the LSI signal decay rate and intensity could be identified for different solvents and solvent application methods. Moreover, we obtained qualitative spatial information regarding the heterogeneity of solvent application for different cleaning methods. Because LSI is an affordable, portable and non-invasive technique that provides real-time results, it can be a powerful asset in the conservation studio during initial cleaning and solubility tests.

Future work could be directed at comparing different solvent (mixtures) at different application times to find an optimum between varnish solubility and the amount of solvent delivered to the paint. An important future challenge in the development of LSI for cleaning tests on large paintings is the reduction of background vibrations of the canvas or panel during the testing procedure. Ideally, LSI could then be used to develop a standardised cleaning test procedure to tailor cleaning strategies to the unique properties of a given painting.

3.4 Methods and Materials

Lab-scale FT-LSI LSI measurements were performed on a home-built set-up that was described previously.[34] Surfaces were illuminated by a 532 nm laser (Cobolt Samba, 1 W) which was expanded with a Galilean beam expander. The backscattered light was captured by a zoom lens (Qioptiq) and the speckle patterns are captured with a camera (Stemmer, Dalsa Genie). The speckle images were saved at high frame-rates (up to 200 fps) and analysed later with Fourier analysis. The maximum laser power used in experiments on the portable FT-LSI was 10 mW. Since the beam was expanded to an area with a diameter of >1 cm, the light intensity at the sample was about 0.13 mW/mm^2. This instrument was used for all LSI experiments, except when specified otherwise.

Portable FT-LSI The other LSI experiments were performed on a portable FT-LSI set-up that was described in[36] and can be used in the conservation studio. Surfaces were illuminated by a 532 nm laser (Cobolt Samba, 20 mW) which was expanded by a single bi-concave lens. The backscattered light was captured by a variable zoom objective (Navitar) and the speckle patterns were captured with a camera (Thorlabs, DCC3240N). The speckle images were collected at medium frame-rates (50 fps) and Fourier analysis is performed in real time on a tablet. The maximum laser power used in experiments on the portable FT-LSI was 5 mW. Since the beam was expanded to an area with a diameter of >1 cm, the light intensity at the sample was about 0.064 mW/mm^2. The total cost of the hardware needed to construct the portable FT-LSI setup is around 5k euro.

Fourier analysis The FT analysis was performed as we described previously.[36] We start by computing the power spectral density. We perform the FFT on a time sequence of N speckle patterns, where N is a power of 2 for computational efficiency. Each (xyt)-voxel is treated as an intensity (I) time series of length N; all voxels are transformed simultaneously as a three dimensional matrix. First, we subtract the mean intensity for each voxel, to represent the time trace as intensity fluctuations around a mean of zero. This matrix is transformed to the frequency domain with a standard fast Fourier transform (fft) routine. Amplitudes corresponding to negative frequencies are discarded to obtain the single-sided amplitude spectrum, which is squared to obtain the power. The power is normalized by dividing by the frame rate and the trace lenght N, as well as dividing by $< I^2 > - < I >^2$. The result is a three dimensional power matrix P(x;y;w) containing power spectral densities for each xy pixel. The frequencies w are equally spaced between 0 and ($\pi*$ frame rate), with N=2+1 unique frequencies. This matrix is either averaged spatially to obtain an averaged power spectrum, or the result of a single frequency is mapped to a surface to obtain a FT-LSI image for a particular frequency. On the lab scale FT-LSI all speckle images are first saved and FT analysis is performed later. On the portable FT-LSI the FT analysis is performed in real time on a stream of images.

Sample preparation Sample preparation was performed as we described previously.[38] Model paint samples containing ZnO (Sigma Aldrich, ≥99%) were made by grinding the pigments with cold-pressed untreated linseed oil (Kremer pigmente) in a 1:1 (w/w) ratio to a smooth paste with mortar and pestle. The Pigment Volume Concentration (PVC) was 19% in all samples. The mixture was applied to 50×75 mm glass slides and spread with a draw-down bar to achieve a wet thickness of 190 μm. The samples were cured in the dark in air at 60 °C for

0–22 days at 97% RH, resulting in a dry thickness of about 150 μm. Humidity was controlled using a saturated K_2SO_4 solution (for 97% RH) in a closed container and was determined using a Rotronic HL-1D temperature and humidity data logger. For ATR-FTIR analysis, 5×5 mm squares of the films were cut and lifted off the glass. Samples were varnished using a brush with a dammar solution in shellsol A and subsequently aged for 7 day under UV-A and UV-B radiation. The total radiation dosage was 1.4×10^7 J/cm^2 (UV-A) and 5.2×10^7 J/cm^2 (UV-B). Cross-sections of varnished model systems were embedded in Technovit® 2000 LC resin and cured in a Technovit® 2000 LC Technotray POWER - Light Polymerization Unit for for 30 min. The cross-section was sanded down using a MOPAS XS Polisher and wet and dry (Micromesh) polishing techniques.

Simulated cleaning test procedure The simulated cleaning test procedures were performed as we described previously.[15] Nanorestore® Max Dry (MD) was used as received from CSGI (www.csgi.unifi.it). Gels were kept in a sealed container loaded with ethanol for at least 12 hour before use and dried with paper tissue before application. Evolon® CR tissue (www.deffner-johann.de/evolonr-cr.html) was cut into 1×1 cm squares, washed with acetone and ethanol using a Buchner funnel, dried and subsequently loaded with ethanol. The Evolon samples with controlled loading were kept overnight in a sealed container loaded with ethanol. Strips of 2×5 cm were loaded with 51% (92.3 mg Evolon / 149.1 mg ethanol) before use. During solvent application, Evolon and gel samples were covered with a Mylar® (biaxially-oriented polyethylene terephthalate) film to avoid solvent evaporation from the top. Hand-rolled cotton swabs were used and swabbing was carried out by a trained conservator. Swab cleaning was always carried out by Laura Raven, Rijksmuseum.

ATR-FTIR spectroscopy ATR-FTIR spectroscopy was performed as we described previously.[38] ATR-FTIR spectra were measured on a Perkin-Elmer Frontier FT-IR spectrometer fitted with a Pike GladiATR module and a diamond ATR-crystal. Spectra were averaged over 4 scans. To integrate overlapping absorption bands, automated data correction and integration algorithms were written using Wolfram Mathematica software.

OCT OCT measurements of varnish thickness were performed on a Thorlabs Telesto PS OCT with a central wavelength of 1300 nm. This setup features a max depth of 3.75 mm in air, a depth resolution of 5.5 μm in air and 3.7 μm at a refractive index of 1.5. The lateral resolution (beam diameter) was 13 μm, the field of view 10×10 mm and the working distance 2.5 cm.

3.A Appendix

3.A.1 Triplo Evolon loaded with 51% ethanol

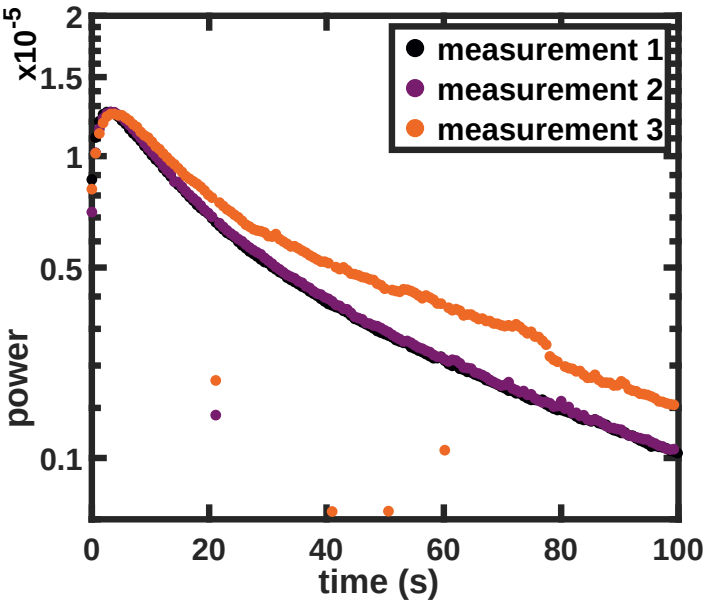

Figure 3.A.1. FT-LSI signal decay for a triplicate measurement using Evolon loaded with 51% ethanol on unvarnished paint. The black and purple series are nearly identical while the orange series measures a slightly higher activity. This deviation is probably caused by inaccurate application of solvent rather than inaccuracy of the measurement. This means that measurements are very sensitive to small deviations in the preparation. However the measured difference is small compared to measured trends in this chapter.

3.A.2 The effect of Varnish on the LSI signal

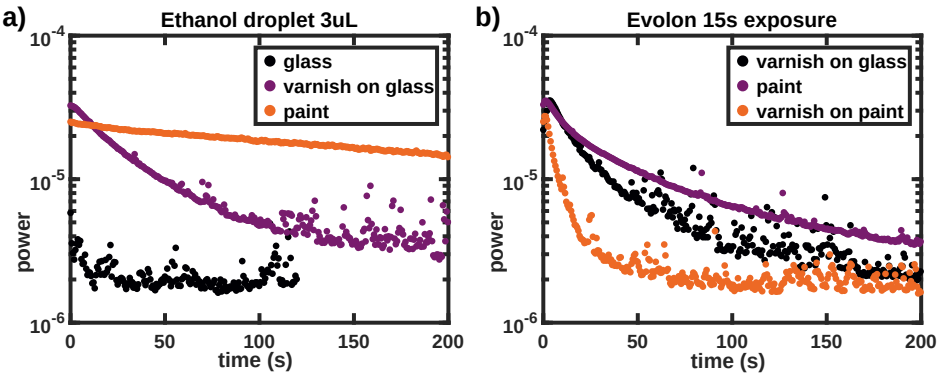

Figure 3.A.2. a) FT-LSI signal decay (1.6 Hz) for a 1 minute exposure of a drop of ethanol on glass, varnish and paint separately. Paint and varnish have the same signal initially, but the signal for varnish decays much faster. The wetted glass gives a baseline signal. **b)** FT-LSI signal decay (1.6 Hz) for a 15s evolon exposure, after which a varnish layer is not completely removed. The varnish signal is not neglegible compared to the paint signal. However, in the measurements discussed in the main text it was judged with a UV lamp that there was no varnish left.

3.A.3 Choice of ROI for integration of FT-LSI signal

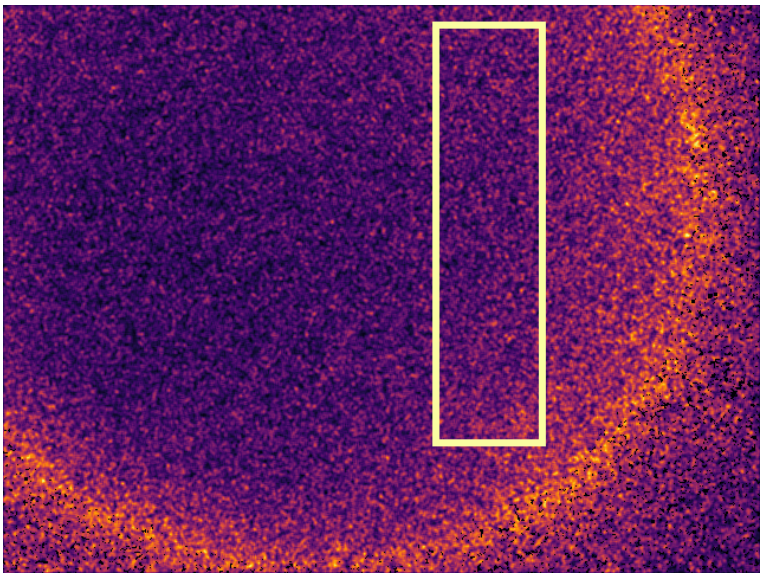

Figure 3.A.3. Example of ROI for integration and computation of FT-LSI signal decay. In all cases, the ROI was chosen in such a way the the region was as large as possible while still spatially homogeneous drying is observed (every pixel in the square dries at approximately the same rate).

3.A.4 OCT analysis of varnished model paints

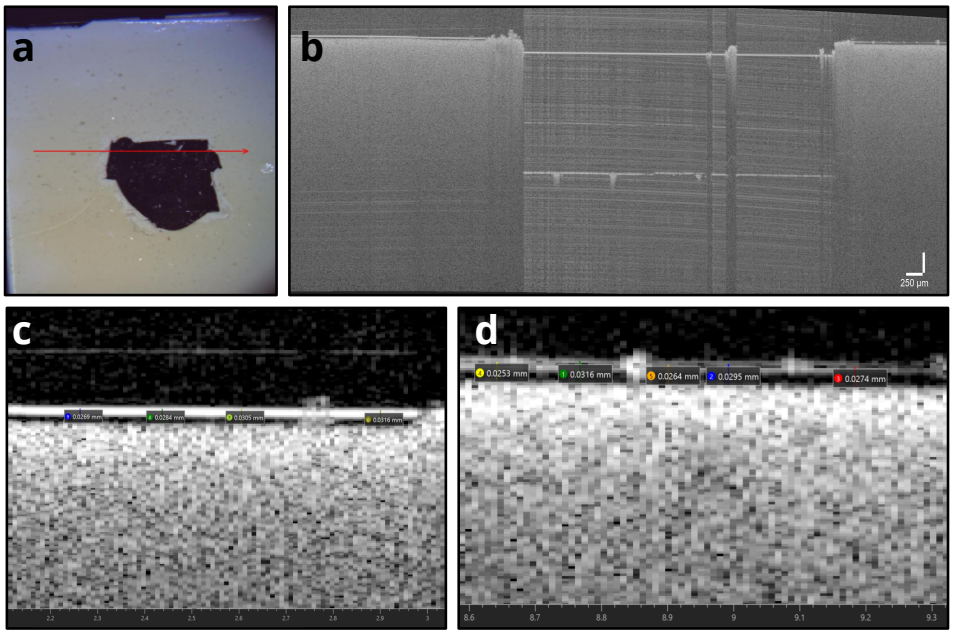

Figure 3.A.4. **a)** Area used for OCT scanning. **b)** overview OCT image, **c)** and **d)** zoomed in examples of thickness determination, average thickness 0.03 mm, standard deviation 0.002 mm.

3.A.5 Varnish thicknesses of LO-ZnO samples

Sample	Thickness (ri=1.0)	Thickness (ri=1.46)
LO-ZnO-1layer	30 μm	21 μm
LO-ZnO-2layer	20 μm	14 μm
LO-ZnO-3layer	13 μm	9 μm
LO-ZnO-4layer	<10 μm	<7 μm

Table 3.1. Varnish thicknesses of LO-ZnO samples with 1–4 varnish layers. A constant (1:1 wt.) pigment to oil ratio was used. Samples were varnished with a dammar solution in shellsol T using a brush and subsequently aged for 7 day under UV-A and UV-B radiation. The total radiation dosage was 1.4×10^7 J/cm^2 (UV-A) and 5.2×10^7 J/cm^2 (UV-B). The average refractive index (ri) of dammar was determined to be 1.425.

3.A.6 Fitting of the power spectra to obtain α

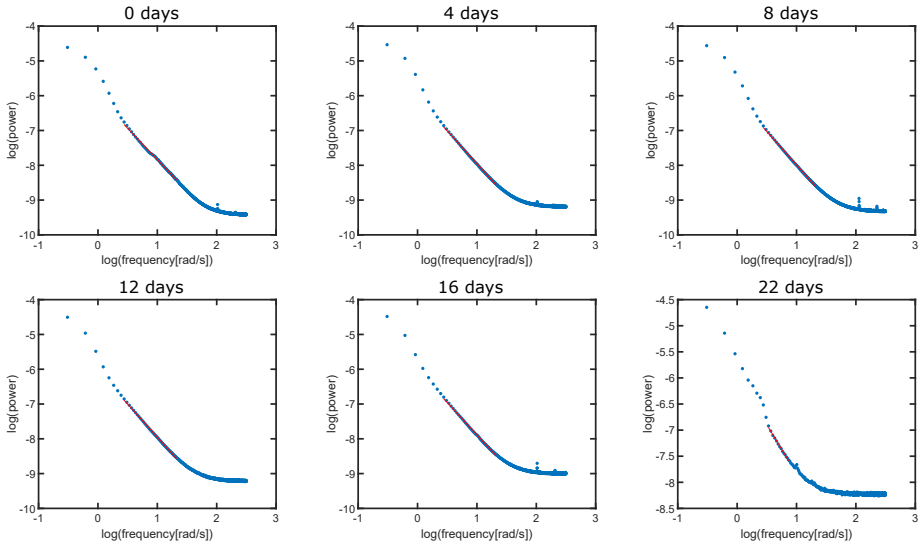

Figure 3.A.5. The power spectra (blue dots) belonging to the experiments shown in Figure 3 (main text) are fitted with a linear function on a log-log scale. The fitting result (red line) for each of the six samples is shown with the accelerated aging time in the title of each sub-figure. From the slope of this fit the parameter α (Figure 3c, main text) is calculated, which gives information over the nature of the measured motion (convective vs diffusive).

3.A.7 Movies

Movie ZnOLO-22d: Spreading of solvent through a cracked paint

Movie ZnOLO-22d shows spatial information obtained from a LSI experiment with a drop of ethanol on the ZnO-LO-22d cracked paint. The left half shows the raw speckle images which are shown exactly how they are obtained from the LSI camera. The right half shows analysed FT-LSI images where the magnitude of the 1.6 Hz frequency is visualised with a colour-map, where lighter colours correspond to higher dynamics. Both movies are played in parallel at 4x speed. Key moments in the movie are: application of the solvent (0 s), start of droplet area shrinking due to evaporation (4 s), disappearance of liquid on top of paint due to swelling and evaporation (10 s), liquid has disappeared everywhere except in the cracks (22 s). The movie has been compressed to facilitate online accessibility (2 times x-compression, 2 times y-compression and 4x frame-rate reduction) and can be viewed from this link or the QR-code in figure 3.A.6.

Figure 3.A.6. QR code to the speckle and LSI movie of the ZnOLO-22d paint model.

Movies ZnOLO-0–16d: Drop of ethanol on a young paint

Movies ZnOLO-0–16d show spatial information obtained from LSI experiments with a drop of ethanol on ZnO-LO-0–16d paint. The movies show analysed FT-LSI images where the magnitude of the 1.6 Hz frequency is visualised with a colour-map, where lighter colours correspond to higher dynamics. The movies are played at 4x speed. The movies have been compressed to facilitate online accessibility (2 times x-compression, 2 times y-compression and 2x frame-rate reduction), and can be viewed from this link or the QR-code in figure 3.A.7.

Figure 3.A.7. QR code to the LSI movies of the ZnOLO-0-16d paint models].

References

[1] H. Ruhemann, J. Plesters, *The cleaning of paintings; problems and potentialities;* (Faber, London, 1968).

[2] J. H. Stoner, R. A. Rushfield, *The conservation of easel paintings* (Routledge London, 2012).

[3] A. Phenix, K. Sutherland. *Studies in Conservation* **46**, 47–60 (2001).

[4] M. F. Mecklenburg, A. E. Charola, R. J. Koestler. *Smithsonian Contributions to Museum Conservation* **3**, 1–243 (2013).

[5] L. Baij, J. J. Hermans, B. A. Ormsby, P. Noble, K. Keune, P. D. Iedema. *in preparation* (2020).

[6] G. Hedley, M. Odlyha, A. Burnstock, J. Tillinghast, C. Husband. *Studies in Conservation* **35**, 98–105 (1990).

[7] G. R. Fife, B. Stabik, A. E. Kelley, J. N. King, B. Blümich, R. Hoppenbrouwers, T. Meldrum. *Magnetic Resonance in Chemistry* **53**, 58–63 (2015).

[8] D. Erhardt, J.-S. Tsang. *Studies in Conservation* **35**, 93–97 (1990).

[9] J. D. van den Berg, K. J. van den Berg, J. J. Boon. *Journal of Chromatography A* **950**, 195–211 (2002).

[10] K. Sutherland. *Studies in conservation* **48**, 111–135 (2003).

[11] A. Spyros, D. Anglos. *Analytical Chemistry* **76**, 4929–4936 (2004).

[12] A. Spyros, D. Anglos. *Applied Physics A: Materials Science and Processing* **83**, 705–708 (2006).

[13] S. Zumbuhl, N. C. Scherrer, N. L. Engel, W. Muller, *ICOM-CC, 17th Triennial Conference*, no. Chipperfield 1999 (2014), pp. 1–11.

[14] A. Casoli, Z. Di Diego, C. Isca. *Environmental Science and Pollution Research* **21**, 13252–13263 (2014).

[15] L. Baij, A. Astefanei, J. Hermans, F. Brinkhuis, H. Groenewegen, L. Chassouant, S. Johansson, G. Corthals, C. Tokarski, P. Iedema, K. Keune. *Heritage Science* **7**, 31 (2019).

[16] L. Baij, J. J. Hermans, K. Keune, P. Iedema. *Angewandte Chemie International Edition* **57**, 7351–7354 (2018).

[17] K. Kahrim, A. Daveri, P. Rocchi, G. De Cesare, L. Cartechini, C. Miliani, B. G. Brunetti, A. Sgamellottia. *Spectrochimica Acta - Part A: Molecular and Biomolecular Spectroscopy* **74**, 1182–1188 (2009).

[18] P. Baglioni, M. Baglioni, N. Bonelli, D. Chelazzi, R. Giorgi, *Nanotechnologies and Nanomaterials for Diagnostic, Conservation and Restoration of Cultural Heritage* (Elsevier, Dordrecht, 2019), pp. 171–204.

[19] L. V. Angelova, B. Ormsby, J. Townsend, R. Wolbers, eds., *Gels in the conservation of art* (Archetype Publications, London, 2018).

[20] G. M. Foster, S. Ritchie, C. Lowe. *Journal of Thermal Analysis and Calorimetry* **73**, 119–126 (2003).

[21] B. Ormsby, G. Foster, T. Learner, S. Ritchie, M. Schilling. *Journal of Thermal Analysis and Calorimetry* **90**, 503–508 (2007).

[22] S. Michalski. *Art in Transit: Studies in the Transport of Paintings* pp. 223–248 (1991).

[23] L. Monico, G. Van der Snickt, K. Janssens, W. De Nolf, C. Miliani, J. Verbeeck, H. Tian, H. Tan, J. Dik, M. Radepont, M. Cotte. *Analytical Chemistry* **83**, 1214–1223 (2011).

[24] N. Stolow. *Journal of the Oil and Colour Chemists' Association* **40**, 377–402 (1957).

[25] A. Phenix. *Journal of the American Institute for Conservation* **41**, 43 (2002).

[26] A. Phenix. *Journal of the American Institute for Conservation* **41**, 61 (2002).

[27] L. Baij, J. J. Hermans, K. Keune, P. D. Iedema. *Macromolecules* **51**, 7134–7144 (2018).

[28] L. Masschelein-Kleiner, *Les solvants*, Cours de conservation (Institut royal du patrimoine artistique, Bruxelles, 1994).

[29] S. Prati, G. Sciutto, F. Volpi, C. Rehorn, R. Vurro, B. Blümich, L. Mazzocchetti, L. Giorgini, C. Samorì, P. Galletti, E. Tagliavini, R. Mazzeo. *New Journal of Chemistry* **43**, 8229–8238 (2019).

[30] B. Blümich, P. Blümler, G. Eidmann, A. Guthausen, R. Haken, U. Schmitz, K. Saito, G. Zimmer. *Magnetic Resonance Imaging* **16**, 479–484 (1998).

[31] L. V. Angelova, B. Ormsby, E. Richardson. *Microchemical Journal* **124**, 311–320 (2016).

[32] A. Fercher, J. Briers. *Optics Communications* **37**, 326–330 (1981).

[33] H. M. van der Kooij, J. Sprakel. *Soft Matter* **11**, 6353–6359 (2015).

[34] H. M. van der Kooij, R. Fokkink, J. van der Gucht, J. Sprakel. *Scientific Reports* **6**, 34383 (2016).

[35] A. Pérez, R. González-Peña, R. Braga Jr., Á. Perles, E. Pérez?Marín, F. García-Diego. *Sensors* **18**, 190 (2018).

[36] J. Buijs, J. van der Gucht, J. Sprakel. *Scientific Reports* **9**, 13279 (2019).

[37] H. Kühn, *Artist's pigments: A handbook of their history and characteristics, vol. 1*, R. Feller, ed. (Cambridge University Press and National Gallery of Art, Cambridge and London, 1986), pp. 169–186.

[38] L. Baij, L. Chassouant, J. J. Hermans, K. Keune, P. D. Iedema. *RSC Advances* **9**, 35559–35564 (2019).

[39] S. Hageraats, K. Keune, M. Refregiers, A. van Loon, B. H. Berrie, M. Thoury. *Analytical Chemistry* p. acs.analchem.9b02443 (2019).

[40] B. Ankersmit, M. H. Stappers, *Managing Indoor Climate Risks in Museums*, Cultural Heritage Science (Springer International Publishing, Cham, 2017).

[41] S. Zumbühl. *Studies in Conservation* **59**, 24–37 (2014).

[42] F. Modugno, F. D. Gianvincenzo, I. Degano, I. Dorothé Van Der Werf, I. Bonaduce, &. Klaas, J. Van Den Berg, F. Di Gianvincenzo, I. Degano, I. D. van der Werf, I. Bonaduce, K. J. van den Berg. *Scientific Reports* **9**, 5533 (2019).

[43] F. Casadio, K. Keune, P. Noble, A. van Loon, E. Hendriks, S. Centeno, G. Osmond, *Metal Soaps in Art: Conservation and Research*, Cultural Heritage Science (Springer International Publishing, Cham, 2019).

[44] G. van der Wel, O. Adan. *Progress in Organic Coatings* **37**, 1–14 (1999).

[45] S. Michalski. *Studies in Conservation* **35**, 85–92 (1990).

[46] J. J. Hermans, K. Keune, A. van Loon, R. W. Corkery, P. D. Iedema. *RSC Advances* **6**, 93363–93369 (2016).

[47] J. J. Hermans, L. Baij, M. Koenis, K. Keune, P. D. Iedema, S. Woutersen. *Science Advances* **5**, eaaw3592 (2019).

[48] M. Vergeer, K. J. van den Berg, S. van Oudheusden, M. Stols-Witlox. *CMOP proceedings* p. Accepted (2019).

[49] T. Arecchi, M. Bellini, C. Corsi, R. Fontana, M. Materazzi, L. Pezzati, A. Tortora. *Optics and Spectroscopy* **101**, 23–26 (2006).

[50] A. Phenix. *Smithsonian Contributions to Museum Conservation* **3**, 69–76 (2013).

[51] S. Prati, F. Volpi, R. Fontana, P. Galletti, L. Giorgini, R. Mazzeo, L. Mazzocchetti, C. Samorì, G. Sciutto, E. Tagliavini. *Pure and Applied Chemistry* **90**, 239–251 (2018).

[52] J. A. L. Domingues, N. Bonelli, R. Giorgi, E. Fratini, F. Gorel, P. Baglioni. *Langmuir* **29**, 2746–2755 (2013).

[53] G. Fife, J. V. Och, B. Stabik, N. Miedema, K. Seymour. *ICOM-CC 16th triennial conference Lisbon 19-23 September 2011: preprints* (2011).

Chapter 4

UNDERSTANDING AND OPTIMIZING EVOLON CR FOR VARNISH REMOVAL FROM OIL PAINTINGS

Evolon® CR is increasingly used in paintings conservation for varnish removal from oil paintings. Its key benefits over traditional cotton swabs are limiting solvent exposure and reducing mechanical action on the paint surface. However, this non-woven microfilament textile was not originally engineered for conservation use and little is known about its chemical stability towards organic solvents. Moreover, the physical processes of solvent loading and release by Evolon® CR, as well as solvent retention inside paint after cleaning, have not been studied. These three topics were investigated using a multi-analytical approach, aiming for an improved understanding and optimized use of Evolon® CR for varnish removal. Our results show that the tissue is generally chemically and physically stable to organic solvents when exposed on timescales that are typical in conservation practice. However, a pre-treatment step of Evolon® CR is necessary to avoid the release of unwanted saturated fatty acids into the paint during varnish removal. We show that the primary mechanism of solvent uptake by the fibers is *ad*sorption rather than *ab*sorption and that the dominant factor dictating the maximum solvent load is the volume of the voids between the fibers. Finally, solvent induced dynamics after application of solvent-loaded Evolon® CR within the paint film was monitored using portable laser speckle imaging on model paints. A method to quantify solvent-retention in real-time was developed and revealed that the presence of varnish on paintings results in lower dynamics of solvents within the paint in comparison to unvarnished paint. Comparing various solvents, it was found that cleaning with acetone resulted in a roughly six-fold increase in dynamics compared to ethanol and isopropanol.

This chapter was published as: Baij, L., Liu, C., Buijs, J., Alvarez-Martin, A., Westert, D., Raven, L., Geels, N., Noble, P., Sprakel, J., & Keune, K., 'Understanding and Optimizing Evolon CR for Varnish Removal from Oil Paintings', *Heritage Science* **2021**, 9, 155.

4.1 Introduction

The growing corpus of scientific literature dealing with the physicochemical aspects of oil paint alterations has led to concerns by conservators about unwanted adverse effects of solvents on paint films.[1] Due to the limited knowledge regarding the short- and long-term chemical and physical stability of oil paintings, exposure of paint films to solvents should be kept to a minimum. To address these concerns, cleaning methods employing gels, gel composites or emulsions (with or without the aid of tissues) have been developed as alternatives to traditional swab cleaning.[2–13] Gel cleaning can reduce the amount of solvent or water released into a paint film.[1] However, the application and clearance of spreadable gels using a brush or swab requires mechanical action and poses the risk of leaving behind gel residues with unknown long-term effects on the stability of the paint.[14] The use of rigid gels with either physical or chemical cross-links can reduce the risks of residues but such gels are not always compatible with organic solvents used for varnish removal on oil paint.

In the last 5 years, a new method of minimising solvent exposure has been developed using Evolon® CR, a speciality-grade, non-woven microfiber cloth. This tissue is loaded/humidified with the conservator's choice of solvent, and subsequently placed in direct contact with the paint surface, upon which the solvent is released and the varnish is solubilised and poulticed into the cloth. This procedure aims to reduce the amount of solvent necessary for varnish removal, and results in significantly reduced mechanical action and solvent exposure.

Evolon® fabrics have been developed for a range of applications, including dust-mite-proof mattress covers, anti-allergen pillows, cosmetic wipes, filtration, technical packaging, kitchen towels, and more.[15] Evolon® CR is a specific type within the Evolon® family that has been designated for use in conservation (C=Conservation, R=Restoration). Manufactured by Freudenberg and marketed by Deffner & Johann, it is a blend of 70% polyester and 30% polyamide fibers spun into segmented filaments, and features a specific density of 77.4 g/m^2.[16,17]

Previous studies

In a 2018 publication describing the application of Evolon® CR in a conservation treatment, Tauber *et al.* presented a procedure called *controlled loading*, where the amount of solvent loaded into the tissue is regulated and kept below its maximum saturation. Controlled loading is achieved by weighing known amounts of Evolon® CR and solvent, and sealing them in a closed container (glass tube) overnight or 12 hours. This procedure aims to achieve a homogeneous distribution of the solvent or solvent vapour throughout the tissue.[17] It is assumed that a

homogeneous distribution of the solvent inside the tissue would directly translate to a homogeneous controlled release of the solvent into the varnish layer, which appears confirmed by the homogeneity of the resulting varnish removal as observed by Tauber *et al.*[17]

The use of Evolon® CR has numerous advantages in addition to reduced solvent exposure of the painting. Firstly, it enables a systematic approach to varnish removal, which is especially beneficial when working on large-scale paintings with different conservators. Secondly, it permits a more reproducible method of applying solvent compared to swab cleaning, potentially permitting a means of standardising varnish removal. Thirdly, the application process of lightly pressing the fabric to increase contact with the painted surface involves little mechanical action. As a fabric, Evolon® CR can be used in sheets of any size, and can be custom cut to match the shape of elements in painting. Additionally, discoloured varnish and retouches poulticed into the fabric can provide invaluable information about the varnish and retouching used in previous restorations. Finally, the used sheets of Evolon® CR can be kept as documentation of the cleaning process and analysed.[17] For example, the elemental composition of overpaint visible on used sheets of Evolon® CR can be analyzed using XRF and the composition of the removed varnish using GC/MS.

Several researchers have already made seminal contributions to the improved understanding of Evolon® CR's use in conservation practice. In 2019, Vergeer *et al.* used ethanol mixed with a fluorescein isothiocyanate protein indicator dye to visualise solvent distribution in a paint film and found considerable variation depending on the method of application.[16]

Baij *et al.* systematically compared the use of Evolon® CR with traditional swab and rigid gel cleaning.[17,18] By monitoring the saturated fatty acid (SFA) extraction from the paint film, it was found that the use of Evolon® CR with controlled loading and rigid Nanorestore® gel cleaning led to significantly reduced SFA extraction compared to the use of free solvents and cotton swabs.[18]

In a continued study, Baij and Buijs *et al.* employed portable Fourier transform laser speckle imaging (FT-LSI) to visualise and monitor solvent retention in model oil paint films. The experiments demonstrated that Evolon® CR with controlled loading resulted in a decreased solvent retention inside the paint compared to both swab and rigid gel cleaning.[19]

Though it has many promising benefits, Evolon® CR remains a new material in conservation practice. Despite the aforementioned research, Evolon® CR's chemical stability and the physical mechanism of solvent uptake and release remain unknown. Moreover, practical and procedural aspects for use by conservators are not yet optimized or fully researched.

This chapter

This work aims to build upon the existing body of research and focuses on exploring three main questions related to Evolon® CR's material stability, physical mechanism of action and practical considerations for conservators.

1. **Is Evolon® CR chemically inert to the organic solvents ethanol and acetone**, which are commonly used for varnish removal? Is pre-treatment necessary? From a material standpoint, Evolon® CR was not specifically engineered for conservation.[20] Considering the common practice of overnight solvent loading, it is important to understand the material tolerance for solvents and whether chemicals or additives used in the manufacturing process are released from the tissue into the painting during its use.

2. **What is the physical process of solvent uptake and release during controlled loading of Evolon® CR?** Understanding the mechanism of solvent uptake in Evolon® CR is important in developing an accurate protocol for controlled loading. Adsorbed vs. absorbed solvent may not equally be available for subsequent release to the varnish layer on the painting. Understanding the physical process of solvent uptake and to what extent these processes are able to release solvent is critical for obtaining an accurate understanding of the true quantity of solvent the painting will be exposed to.

3. **What is happening in the paint film during and after cleaning with Evolon® CR?** Here we focus on the cleaning process from the painting's perspective, and attempt to understand what is occurring chemically and physically in the dammar varnish and in our zinc white-based oil paint models during and after varnish removal using Evolon® CR.

This work evaluates the first two questions focusing on the chemical stability and physical mechanism of action of Evolon® CR using thermally-assisted hydrolysis and methylation pyrolysis gas chromatography mass spectrometry (THM-Py-GC/MS) to study chemical degradation and optimal pre-treatment procedure, scanning electron microscopy (SEM) to assess physical degradation post solvent exposure, HIROX microscopy to investigate *in situ* change upon solvent exposure, gravimetric analysis to determine the maximum solvent loading, and nitrogen adsorption and mercury intrusion experiments to determine absorption vs. adsorption processes in solvent uptake. We aim to improve our understanding of the release of solvents by Evolon® CR into mock up paint films and use attenuated total reflection Fourier transform infrared (ATR-FTIR) spectroscopy to investigate the possibility of triggering a reaction between components released by unwashed

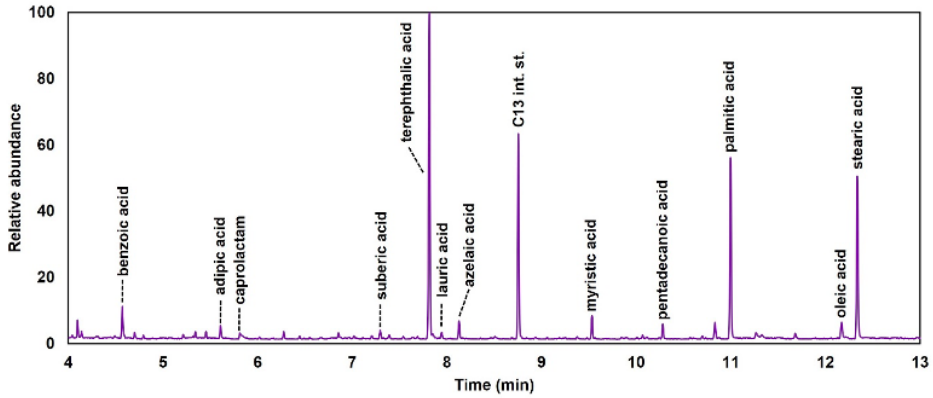

Figure 4.1. THM-py-GC/MS chromatogram showing the extracted components from unwashed Evolon® CR.

Evolon® CR and components present in the paint. Portable FT-LSI is used to study solvent retention in paint films, and UV photography to quantify the effectiveness of varnish removal. Finally, an overview of the most important implications for the conservation field will be presented in the conclusion.

4.2 Results

4.2.1 THM Py-GCMS

Characterisation of Evolon® CR The characterisation of the composition of Evolon® CR revealed two characteristic monomers: caprolactam and terephthalic acid (TPA) (Figure 4.1). Both compounds are commonly used during the production of nylon and polyester fibers.[21] Benzoic acid (BZA), styrene and benzyl derivatives were also detected. Although BZA is used in the manufacture of caprolactam and TPA,[22] these fragments mainly originate from TPA fragmentation during pyrolysis,[23] Surprisingly, SFAs, such as adipic acid (2C6), suberic acid (2C8), lauric acid (C12:0), azelaic acid (2C9), myristic acid (C14:0), pentadecanoic acid (C15:0) palmitic acid (C16:0), oleic acid (C18:1), stearic acid (C18:0), were also detected in the chromatogram (Figure 4.1). This might suggest the addition of SFAs during the polymerisation process, since SFAs and their aluminium salts are commonly added to tailor the physical properties of many polymers.[24]

Influence of washing protocol In order to propose the most optimal pre-treatment prior to the solvent loading step, solvent extracts containing small amounts of

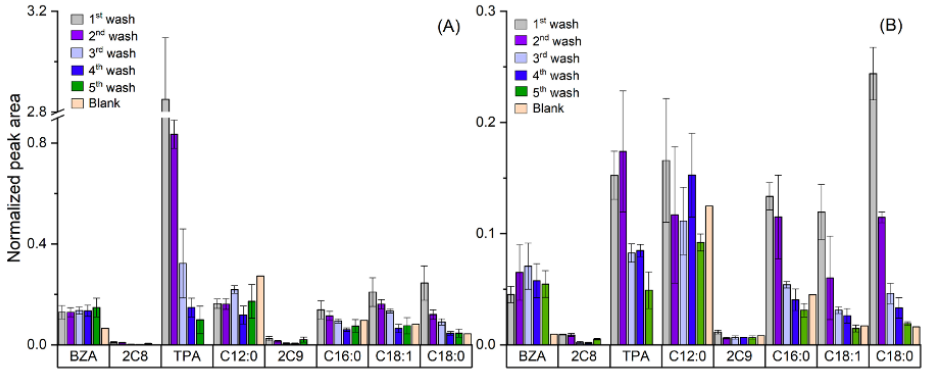

Figure 4.2. Peak area normalised to the internal standard (C13:0) of the main compounds extracted from Evolon® CR after iterative washing with **a)** acetone and **b)** ethanol. Benzoic acid (BZA), suberic acid (2C8), terephthalic acid (TPA), lauric acid (C12:0), azelaic acid (2C9), palmitic acid (C16:0), oleic acid (C18:1), stearic acid (C18:0). Error bars indicate standard deviation (1σ).

monomers extracted from the Evolon® CR tissue were analysed using Py-GC/MS. Measurements were performed on solvent extracts from Evolon® CR after being immersed in acetone or ethanol as part of the washing protocols examined in this chapter: untreated or machine washed Evolon® CR followed by (1) a single wash with a 24 h solvent exposure time, or (2) five iterative washing steps with a 1 min solvent exposure time (see Materials & Methods).

Figures 4.2a and b show the main compounds extracted from the untreated Evolon® CR after the sequential rinsing with acetone or ethanol normalised to a tridecanoic acid (C13:0) internal standard. Although the pure solvents used in this study also contained SFAs and BZA in small quantities, a clear increase of these compounds was observed after the first washing of the Evolon® CR when compared to the blank. After each solvent exposure, a clear decrease in the extracted amount of TPA, 2C8, C12:0, 2C9, C16:0, C18:1 and C18:0 was observed. However, the amount of BZA remained constant after each extraction with no significant variation observed for the remaining SFAs monitored. After the 5th extraction, the extracted amounts of SFAs were within the same range as the signals for pure solvents, indicating that the tissue no longer contains solvent-releasable components. Thus, five washes appear to be optimal. Although the amounts of TPA found in the extracts are greatly reduced after washing with acetone and ethanol, small amounts of TPA are detected even after three or five washing iterations.

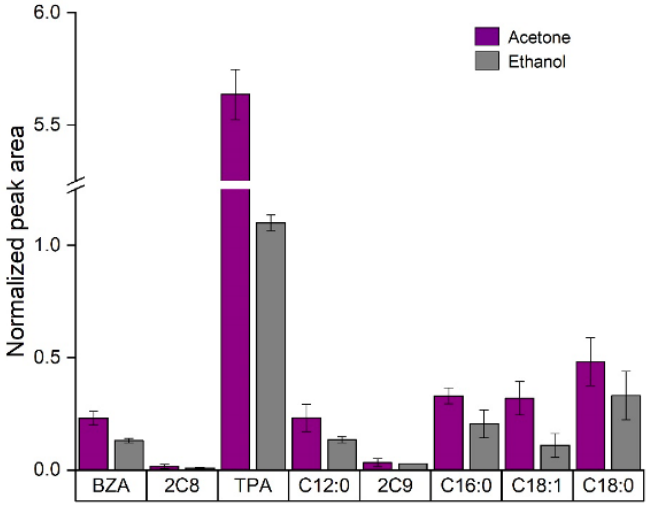

Figure 4.3. Peak area normalised to the internal standard (C13:0) of the main compounds extracted from Evolon® CR after 24h washing with acetone or ethanol. Benzoic acid (BZA), suberic acid (2C8), terephthalic acid (TPA), lauric acid (C12:0), azelaic acid (2C9), palmitic acid (C16:0), oleic acid (C18:1), stearic acid (C18:0). Error bars indicate standard deviation (1s).

The second washing procedure tested was the full immersion of untreated Evolon® CR in the designated solvent (either acetone or ethanol) for 24 h (Figure 4.3). The most significant difference with respect to the iterative washing protocol was the high release of TPA into both acetone and ethanol (Figure 4.A.1 and 4.A.2). It is important to note that after 24 h continuous immersion, the extracted amounts of SFAs are in the same range as those after the 2nd or 3rd iterative wash, indicating that a washing procedure that involves sequential rinsing steps with fresh solvent each time is more effective than one, single long immersion.

By comparing the extraction efficiency of both acetone and ethanol, the data shows that the amount of TPA detected in the solvent extracts was 18 times higher with acetone than with ethanol for 1 min iterative washes, and 5 times higher for the 24 h wash. Moreover, acetone shows a slight increase in SFA extraction efficiency for both washing protocols.

The extraction of SFA followed the same behaviour when Evolon® CR was washed in a washing machine at 60°C (data not shown). The only significant difference was that caprolactam, not detected in any of the solvent extracts of the untreated Evolon® CR, was detected when washed at 60°C in the washing machine. This finding may be explained by the mechanical action of the washing machine

in combination with the elevated temperature of the wash cycle, causing greater extraction of residual monomers from the manufacturing process or hydrolysis of the fibers during washing.

4.2.2 SEM

Scanning electron microscopy (SEM) was used to evaluate potential physical degradation or changes to fiber structure upon solvent exposure to acetone and ethanol. Evolon® CR tissues fully submerged in solvent for 1 min, 24 hrs, and 7 days were studied.

In general, no fiber rearrangement or reorganisation on a global level was observed after solvent exposure of any duration. The main differences observed were changes to the appearance of individual fibers, with greater solvent exposure times resulting in fraying of the fibers. At 2000× total magnification, it is clear that individual Evolon® CR fibers are square shaped. Fraying manifests itself primarily along the longitudinal edges of the square shaped fibers (Figure 4.4B–D).

We observed a distinct difference in fiber-edge fraying in the tissue that had been exposed for 7 consecutive days (Figure 4.4D) compared to the tissues exposed for 24 hrs and 1 min (Figure 4.4B and C), but only a subtle difference between tissues exposed for 24 hrs and 1 min. The tissues exposed for 24 hrs and 1 min appear similar to the non-solvent exposed control, with the exception of having fewer particulate material adhered on individual fibers in the solvent exposed tissues. This observation could be the result of rinsing of the fibers upon solvent exposure.

The same general effect was observed for tissues exposed to ethanol, except fraying occurs with shorter exposure times (1 min exposed tissues already have frayed edges, see figure 4.A.3). The frayed edges of ethanol exposed tissues also generally have a smoother look compared to acetone exposed fibers. Finally, we observed little difference between the non-solvent exposed control and the tissue that had been machined washed at 60°C (fig. 4.A.4).

4.2.3 HIROX microscopy

To compliment the SEM analysis of dried tissues post-solvent exposure, HIROX microscopy was used to visualise any potential *in situ* change upon solvent wetting with water, ethanol, or acetone.

Average fiber widths for dry fibers were 5.60 μm (± 0.69 μm) and solvent-wetted fibers were 6.03 μm (± 0.83 μm) for water, 6.13 μm (± 1.38 μm) for ethanol, and 6.06 μm (± 0.79 μm) for acetone. All solvent-wetted fibers appear to swell to a similar value (ca. 6.06 μm). While this value represents a slight increase over the

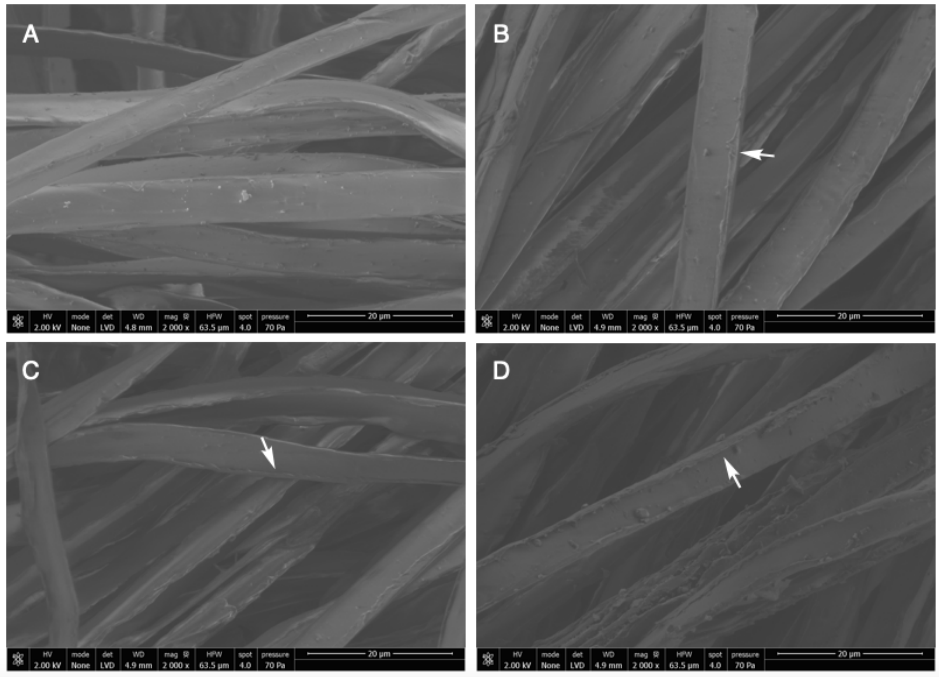

Figure 4.4. SEM images at 2000× magnification of **A)** no solvent exposure, **B)** 1 min exposure, **C)** 24 h exposure, and **D)** 7 day consecutive exposure in acetone. White arrows indicate fraying along squared edges of individual fibers.

dry fiber width, it should be noted that once wetted, fiber edges appear fuzzier. Diameter measurements were taken by measuring the outermost edge to the outermost edge of the fiber, thus this optical effect contributes to an apparent widening of fiber diameters when measured under the microscope. We attribute the measured increase to these optical effects than a true swelling of solvent-wetted fibers. Stereomicrograph images and diameter measurements are shown in figure 4.A.5.

4.2.4 Gravimetric analysis

To empirically determine the maximum solvent load of a fully saturated tissue, Evolon® CR tissue was investigated using gravimetric analysis. For analysis, 5×5 cm squares of Evolon® CR were weighed dry, submerged in solvent and reweighed while fully saturated. The solvents evaluated: –water, ethanol, acetone, and isooctane– were chosen for their chemical- and polarity differences.

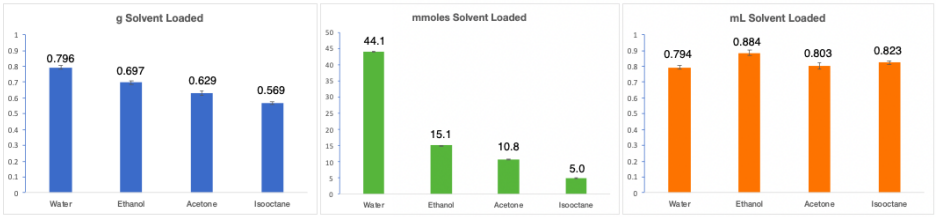

Figure 4.5. Graphical representation of total mass, molarity, and volume of solvent taken up by the tissue for four chemically different solvents, demonstrating that maximum absorption appears to be dictated by filling volumetric space.

Weight gain results were averaged over at least five measurements and converted into molarity and volume. Assessing these three methods of representing solvent load - mass, molarity, and volume (Figure 4.5) - proved useful. We observed moderate variation when represented in weight (range of 0.535 g to 0.716 g) and large variation when represented as mmoles (range of 4.70 mmol to 39.7 mmol). When represented by volume, the maximum solvent loads appears to be in the range of 0.716–0.798 mL. Figure 4.5 clearly shows that the volume gain remains fairly constant while weight and molarity strongly vary. The same trend was reproduced when using a slightly modified method of assessing the weight-gain of a fully saturated tissue (Materials & Methods).

4.2.5 Nitrogen adsorption and mercury intrusion

To determine the porosity of Evolon® CR, nitrogen adsorption experiments (capable of detecting pore sizes in the sub-nanometer to nanometer range) were performed on the tissue. In these experiments, materials are measured to determine the volume of an adsorbent gas that can be retained in its bulk, which is a quantitative measure of that material's porosity. The adsorption isotherm Figure 4.6 obtained for Evolon® CR shows an essentially constant P/P_0 until nitrogen condensation occurs as evidenced by the infinite spike at $P/P_0 = 1$. The very low volume of nitrogen uptake of 0.4 cm^3/g (associated with a surface area of 1.6 m^2/g) and the constant adsorption isotherm suggest that Evolon® CR is effectively non-porous.

To compliment the nitrogen adsorption experiment, mercury (Hg) intrusion was used to analyse pores and voids by filling the sample with Hg at increasing pressure. Full raw data plots (fig. 4.A.7-4.A.11) show that the majority of the Hg intrusion is complete at low pressures which is indicative for a large inter-particulate space, and that the intrusion process occurs in a calculated pore size range of 100–1000 nm. The latter finding corroborates the nitrogen adsorption

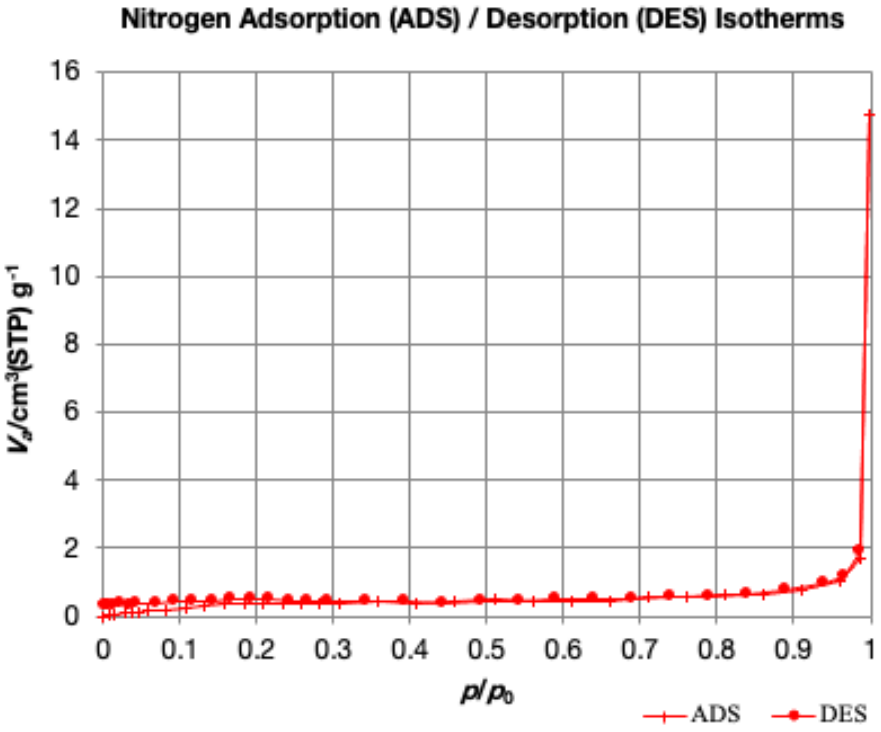

Figure 4.6. Nitrogen adsorption and desorption isotherms showing lack of porosity in tissue fibers.

results that the tissue is in fact non-porous and suggests that the intruded Hg is purely filling interstitial space between fibers.

4.2.6 Time-dependent ATR-FTIR

To probe potential chemical reactions of SFAs and other solvent extractable components if released into a paint film during cleaning, time-dependent ATR-FTIR spectroscopy was used to track the development of new functional groups (indicative of chemical reactivity) in paint films during cleaning. A zinc-containing oil paint binding medium model system was exposed to unwashed, ethanol-saturated Evolon® CR.

From Figure 4.7, it is clear that crystalline zinc soaps are formed in the zinc ionomer model system when exposed to ethanol-saturated unwashed Evolon® CR. The formation of crystalline zinc soaps was not observed when pure ethanol

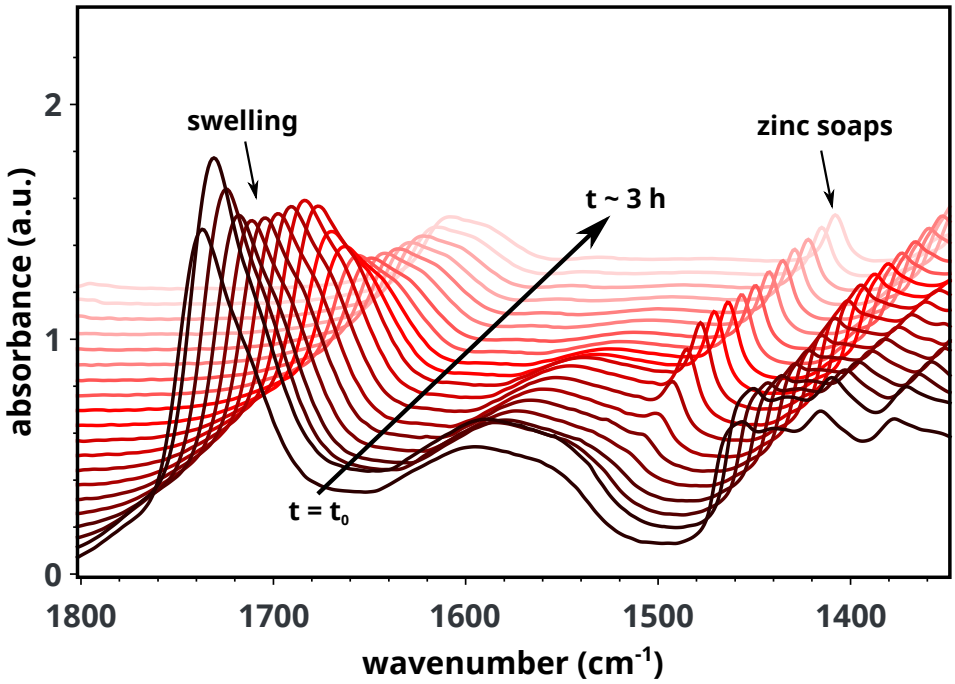

Figure 4.7. A selection of ATR-FTIR spectra recorded on a zinc-containing oil paint binding medium model system exposed to unwashed Evolon® CR loaded with ethanol (no controlled loading) for over 3 h. After about 50 minutes, a small peak assigned to crystalline zinc soaps (1540 cm^{-1}) is visible, which continues to increase before stabilising after about 100 minutes.

was delivered to the ionomer films in absence of Evolon,[25] demonstrating that untreated Evolon® CR releases enough SFAs to promote zinc soap formation after 50 min of solvent exposure (Figure 4.7, sixth spectrum counting from t_0). Attempts to conduct this measurement procedure[25] on Evolon® CR with controlled solvent loading were unsuccessful since the amount of solvent was too small to be detected before evaporation.

Figure 4.7 shows that the swelling of the zinc ionomer model system (as indicated by the decrease of the ester band at 1738 cm^{-1}) is distinctly different from the swelling profiles measured in previous studies on the uptake of solvents released by conservation cleaning gels[26] and pure solvents.[25] Since the unusual swelling-behaviour only becomes apparent at timescales that are longer than typically used in conservation practice (> 30 min), the in-depth investigation of this phenomenon is beyond the scope of this chapter.

4.2.7 Portable FT-LSI & UV photography

We here employ portable laser speckle imaging (LSI) to measure and quantify solvent action after application of Evolon® CR on varnished and unvarnished oil paint model systems. Various solvents are tested for the removal of artificially aged dammar varnish (see Materials & Methods) and the uptake of solvent by the oil paint models.

LSI can be used to track the motion of light-scattering particles in real-time and spatially-resolved. Using this technique, solvent action inside a painting can be observed *in situ*.[19,27] Since translucent solvent molecules do not scatter light, the motion of opaque pigment particles mobilised through the solvation process are measured and used as a proxy for solvent induced dynamics. These dynamics comprise solvent sorption, desorption and evaporation from the paint film, which together define the 'retention time' (the time that solvents are retained inside the paint layer). Knowing the solvent retention time and the rate of signal decay (the rate at which solvents disappear from the paint layer) can help to decrease the risks associated with solvent-based cleaning because these parameters determine how long the paint is plasticised by solvent.

Varnished versus unvarnished paint To investigate the possible 'protective' capacity of varnishes against solvent-uptake by the paint, a series with increasing exposure times of Evolon® CR on varnished and unvarnished paint models was measured and the decay times compared. For these experiments, the Evolon tissue was loaded with ethanol at 51% loading capacity according to the method by Tauber *et al.*[17]

Investigating the rate of LSI signal decay (referred to here as time trace) for Evolon® CR exposure times of 10, 90 and 300 seconds (Figure 4.8a), it is clear that the intensity of the dynamics within the paint increases with increasing exposure time. The resulting decay times (see Materials & Methods) are plotted for different Evolon® CR exposure times in Figure 4.8b. The transformation of the time traces in Figure 4.8a to the decay times in Figure 4.8b is visualised by the red dashed lines in Figure 4.8a. Figure 4.8b shows the decay times for a series of Evolon® CR exposure times on model paints that contain a thin layer of varnish. The measured decay times for varnished paint are consistently lower, indicating that solvent uptake by the paint is slower due to the presence of varnish.

Comparison of solvents An advantage of Evolon® CR is that it can be loaded with different solvents or combinations of solvents to tailor the method to dissolve a specific varnish. We here investigate the intensity and decay of dynamics caused

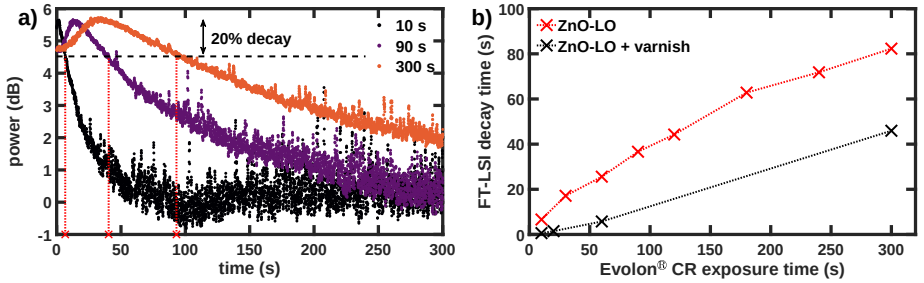

Figure 4.8. a) FT-LSI time traces recorded after 10, 90 and 300 seconds Evolon® CR (51% ethanol) exposure on an unvarnished paint model. With increasing Evolon® CR exposure, the decay becomes slower. We quantify the decay time as following: the time it takes (X) after removing the Evolon® CR, to decay to 80% of the maximum signal intensity (dashed line). **b)** The relationship between the Evolon® CR exposure time and the FT-LSI decay time for varnished and unvarnished paint models. In both cases the decay time increases with increased Evolon® CR exposure time, but for the varnished paint models the measured dynamics are much lower.

by different solvents using real-time analysis of LSI data for ethanol, acetone and isopropanol. Both varnished and unvarnished paint models are studied and the LSI measurements are combined with UV-photography to assess the effectiveness of varnish removal.

Differences are most easily visualised by plotting the decay time versus the exposure time, as done in Figure 4.9a–b. Comparing the decay times obtained for 51%-loaded acetone, ethanol and isopropanol tissues on unvarnished paint (Figure 4.9a), large differences are immediately apparent. For example, the decay time for 10 s acetone exposure is roughly equal to the decay time for 90 s ethanol exposure, and slightly higher than 120 s isopropanol. This agrees with our previous result that the diffusion rate is leading in how long the solvent stays in the paint layer[19], and we now confirm that this is also true for controlled application with Evolon® CR.

Figure 4.9b displays the decay times after application of Evolon® CR loaded with 51% acetone, ethanol and isopropanol on varnished paint models. As expected, the decay time increases with increasing exposure time for all solvents. Comparing the results obtained for model paints without varnish (Figure 4.9a) and with varnish (Figure 4.9b), the protective capacity of the varnish layers can be observed: the decay time of the solvent signal in the paint is roughly two-times smaller in the presence of varnish.

To asses the effectiveness of the varnish removal procedures we also performed UV-fluorescence imaging on each treated area. The mean intensity value of each treatment, a measure for the amount of varnish present, is shown in figure 4.9c

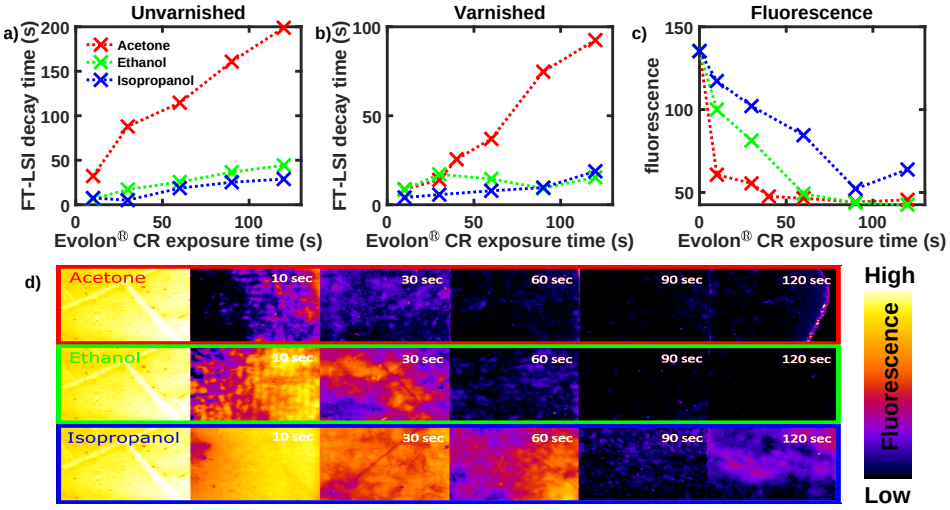

Figure 4.9. For all panels the color coding is as following: red for acetone, green for ethanol and blue for isopropanol. **a)** FT-LSI decay times for unvarnished paint models. **b)** FT-LSI decay times for varnished paint models. **c)** Spatially averaged fluorescence measurements after Evolon® CR exposure. After all varnish has been removed, fluorescence is still present from the ZnO-LO paint model at an intensity level of 44 (arbitrary units). **d)** UV fluorescence photographs after Evolon® CR exposure.

and the collected image in figure 4.9d. In general, longer exposures result in better varnish removal with acetone being the fastest (40 s), isopropanol the slowest (90 s) and ethanol in the middle (60 s). We did not observe significant differences in the spatial homogeneity of varnish removal.

Both FT-LSI and UV-fluorescence data from cleaning tests contain valuable information that can support conservators in making an informed decision on how to proceed with cleaning a painting. Taking as an example the data obtained from the model system in figure 4.9, we envision that this data could be applied to aid conservation decision making through the following logic: 90 s isopropanol is not the cleanest based on UV-fluorescence imaging so it is not further considered; 60 s acetone and 90 s ethanol have comparable UV-fluorescence data and thus good cleaning performance, however acetone has a much higher FT-LSI decay time, thus ethanol is the better choice. Having selected ethanol as the best solvent, routine decisions can be made (i.e. can 60 s instead of 90 s ethanol be used to minimize solvent exposure while maintaining acceptable varnish removal.

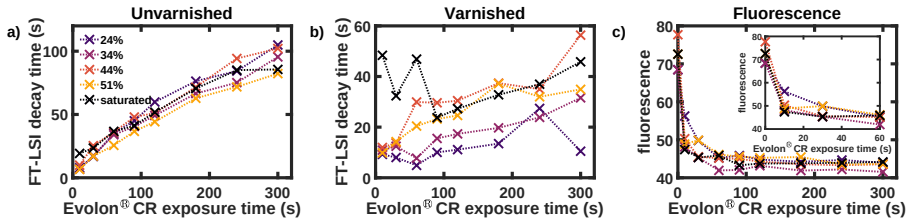

Figure 4.10. FT-LSI decay times obtained after exposure to Evolon® CR with varying ethanol loadings on **a)** paint and **b)** paint + varnish. **c)** UV fluorescence measurements for samples shown in b.

Solvent loading A series of measurements using Evolon® CR with different solvent loading was tested on paint models with and without varnish. The loading percentages and procedures used by conservators were taken from the aforementioned publication by Tauber, *et. al.*[17]. Figure 4.10a shows a collection of decay times for Evolon® CR loaded with 24–51% ethanol and one saturated (gently squeezed) Evolon® CR tissue for different application times (10-300 s).

Surprisingly, our experiments do not show a significant influence of the solvent loading on the decay time for unvarnished model systems (Figure 4.10a). The fact that a higher loading does not result in longer decay times may be explained by either the solvent uptake by the paint being rate-limiting, or by the rate of solvent release from Evolon® CR being independent of the loading. However, the experiments on varnished paint models (Figure 4.10b), clearly show that 24% and 34% loadings result in shorter decay times over the whole range of exposure times, compared to 44%, 51% and saturated loading. The inset in Figure 4.10c shows an expansion of the UV fluorescence intensity for the most relevant exposure times: 10–60 s. In the first 60 s, the different loadings perform similar in terms of residual fluorescence, which is below 50 (arbitrary intensity) units in all cases. However, the higher decay times in Figure 4.10b for 44%, 51% and saturated loading, indicate that more solvent is taken up by the paint. These results lead to the conclusion that for these models 24% and 34% loadings minimize the decay time while retaining optimal varnish removal. We note again that such a procedure is varnish-dependent and will in practice be required to be carried out for every unique varnish layer (assuming different solubilities) and each individual painting.

4.3 Discussion

The analyses detailed above provide an improved understanding of key questions regarding the use of Evolon® CR for varnish removal: its chemical stability, the

mechanics of solvent uptake and release in the tissue, and solvent action on the paint film.

1. Is Evolon® CR chemically inert to solvents used for varnish removal? Is pre-treatment necessary? Py-GC/MS and SEM analysis demonstrated that Evolon® CR is chemically and physically stable on typical time-scales used by conservators for varnish removal (less than 24 h), and that acetone extracts greater amounts of monomers compared to ethanol. The effect of long solvent exposure on the physical degradation of Evolon® CR was also confirmed by SEM analyses after immersing the tissue in solvent for 7 days. These results support that solvent exposure of Evolon® CR should be kept to a minimum, and that Evolon® CR should not be consistently reloaded with solvent due to solvent-induced physical degradation of the tissue. To minimize waste, it is currently common practice to re-use Evolon® CR squares previously loaded with solvent. Our results suggest this practice should be avoided considering the physical degradation to the tissue with prolonged solvent exposure. Combined results from Py-GC/MS and ATR-FTIR analyses show that pre-treatment is required to extract SFAs from the Evolon® CR, limiting the risk of unwanted reactions[18] (e.g. metal soap formation) in the painting. Different washing methods/steps were evaluated by Py-GC/MS, showing that the amount of SFAs released from the Evolon® CR depends on the solvent and immersion time. Untreated Evolon® CR followed by iterative washing (at least 3 times) with short time exposures of solvent showed the best compromise between SFA-extraction efficiency and retained physical properties of the tissue.

2. What is the physical process of solvent intake and release during controlled loading? Results obtained from the nitrogen adsorption and Hg intrusion experiments showed that solvent uptake by Evolon® CR occurs predominantly through adsorption in the interstices between fibers, with negligible amounts of absorption into the fibers themselves. Gravimetric analysis also demonstrated that the total volume of solvent loaded was roughly consistent with widely differing solvents, corroborating that the tissue's maximum loading capacity is dictated by the filling of voids in its interstices. This interpretation is supported by HIROX analysis, which showed subtle to negligible amounts of fiber swelling upon wetting.

Our findings suggest that calculations for controlled loading should be based on available volumetric space in fiber interstices. Table 4.1 highlights the empirically determined maximum solvent load for acetone and ethanol based on volume (taken from the gravimetric analysis experiments) and compares it with those obtained using the currently practised method that a solvent's maximum uptake capacity is 4 times the weight of the utilised Evolon® CR tissue (based on information provided from the manufacturer that Evolon® CR is capable of absorbing up to 4 times its own weight in water). As shown, there is a discrepancy in the calculated

	Maximum Loading by Interstitial Volume		Maximum Loading by Weight of Evolon® CR	
	5 cm x 5 cm tissue	**per cm² of Evolon® CR**	5 cm x 5 cm tissue	**per cm² of Evolon® CR**
Acetone	0.803 mL	**0.032 mL**	1.059 mL	**0.042 mL**
Ethanol	0.884 mL	**0.035 mL**	1.105 mL	**0.044 mL**

Table 4.1. Comparison of two methods of calculating maximum solvent loading in Evolon® CR; all values reported are an average of measurements on 6 independent squares of tissue.

maximum load, explained by the fact that water is more dense than both acetone and ethanol. Thus, using water as the benchmark to calculate maximum loading for organic solvents results in an overestimation of the maximum loading capacity.

3. What happens in the paint film during and after cleaning with Evolon® CR? ATR-FTIR measurements demonstrated that zinc soaps can potentially form in the treated paint film after using Evolon® CR that has *not* been pre-washed. It should be noted that although the ionomer model system used in this ATR-FTIR study readily reacts with SFAs, the peaks associated with crystalline zinc soaps were detected only after approximately 50 minutes of solvent exposure (Figure 4.7, sixth spectrum counting from t_0). The relatively slow rate of crystalline zinc soap formation may be explained by a slow release of SFAs by the untreated (no pre-washing with ethanol) tissue, a slow rate of diffusion of SFAs in the ionomer film or a combination of these factors. Previous experiments indicated that fast-diffusing solvents, such as acetone, can accelerate SFA diffusion and zinc soap formation.[28] Based on this data, we believe SFA diffusion is unlikely to be the rate-determining factor for zinc soap formation.

Finally, we note that although typical contact times between the loaded Evolon® CR tissue and paint surface during a treatment are significantly shorter than 50 minutes (usually on the order of 1 minute), it is still possible that small amounts of SFAs could be released into the paint film potentially inducing metal soap formation over the long-term in the dry state (after the Evolon® CR is removed).[18]

The potential formation of zinc soaps using Evolon® CR with controlled solvent loading was not investigated with ATR-FTIR due to current limitations in experimental set up. Since the extraction of soluble components from the painting is lower for Evolon® CR with controlled solvent loading,[18] and the pre-treatment procedure (washing with ethanol) effectively removes SFAs from Evolon® CR, we

assume that the combination of controlled loading and pre-treating the Evolon® CR will lead to a low risk of solvent-mediated metal soap formation.

Specific studies dealing with the possible harmful effects of TPA on paint layers were not found. However, the breakdown of TPA into aliphatic carboxylic acids under strong UV conditions is known to be accelerated by the presence of photoactive pigments such as ZnO or TiO_2.[29] TPA can also react with zinc ions when heated in dimethylformamide at 100°C for four days.[30] These studies suggest that the possible effects of TPA-deposits on paint surfaces need attention.

The varnished versus unvarnished FT-LSI studies showed consistently lower decay times for varnished model systems, illustrating that the presence of varnish hinders the uptake of solvent in the painting. This important research outcome reflects empirical knowledge of conservators that varnish delays paint swelling and is consistent with previous LSI studies.[19] To give a quantitative representation of this phenomenon, our data shows that the dynamics caused by 120 seconds Evolon® CR on unvarnished paint is equal to the dynamics caused by 300 seconds Evolon® CR on top of a thin varnish layer.

The evaluation of various solvents with FT-LSI shows that the signal decay times vary considerably for different solvents. These results are in good agreement with previous results obtained for pure diffusion coefficients of solvents in oil paint models.[25] However, it remains difficult to relate decay times or time traces measured with LSI to pure diffusion coefficients of solvents because the FT-LSI signal is composed of both the swelling of the paint matrix due to solvent sorption and the variation in thermal motions inside the paint. Both these parameters depend on the rate of evaporation of solvents from the paint surface. Since the time traces are in agreement with the order of diffusion and swelling coefficients for solvents, we hypothesise that evaporation is likely not the rate-determining factor for the retention of solvents in paint. Such a situation is expected when the uptake of solvent is much faster than solvent evaporation. It would be interesting to investigate if the (relative) decay times for solvents changes for increasingly porous paints or models on canvas supports, because that would suggest that evaporation becomes dominant for such systems.

Finally, FT-LSI studies on solvent loading demonstrated that when varnish is not yet fully removed, acetone and ethanol cause comparable dynamics, but when the varnish is removed, acetone causes roughly six times longer-lasting dynamics than ethanol. Isopropanol causes the shortest-lasting dynamics, but is also slowest in the removal of aged dammar varnish. It should be noted that when varnish is still present, the LSI signal is composed of both dynamics inside the varnish and dynamics inside the paint and it has thus far not been possible to separate these contributions. Therefore, the LSI signal that is detected before the varnish is fully

removed cannot be taken as a pure measure of the dynamics inside paint (Figure 4.9d). In contrast, the dynamics measured after the varnish is fully removed are fully representative of solvents that plasticise the paint.

We thus arrive at an ideal solvent choice for the removal of varnish from our model systems: ethanol, which combines the generation of relatively low-intensity dynamics and a short retention of solvent in the paint with effective varnish removal within 60 s. It should be noted that this conclusion is valid specifically for the combination of aged dammar varnish on ZnO-based oil paint that we used for our experiments.

4.4 Conclusions

As the paintings conservation field has rapidly discovered the potential of Evolon® CR for varnish removal from oil paintings, the need to advance our understanding of this material and the steps necessary for safe and optimal usage increases. This analytical study contributes to the growing corpus of scientific cleaning studies by researching Evolon® CR's chemical stability, physical mechanisms of solvent uptake and release, and solvent action on a painted surface. The findings presented here have important practical implications that should be considered when proceeding with an Evolon® CR-mediated varnish removal.

Primarily, we suggest a solvent-based pre-treatment of Evolon® CR (as received from the manufacturer) to remove residual SFAs before proceeding with solvent loading for varnish removal. This washing procedure is expected to significantly reduce the probability of Evolon® CR-induced metal soap formation, and is therefore an important step in safeguarding the chemical and structural integrity of the pictorial layers for the future. Studies dealing with the possible harmful effects of residual TPA on paint layers were not found and this topic may need attention.

The current practice of *controlled loading* is still encouraged with the additional caveat that solvent loading should ideally occur the day before intended use, as this work shows that Evolon® CR is chemically and physically stable on timescales of less than 24 h. For the same reasons, our results suggest that during the testing phase pre-solvent loaded, but unused tissue squares should not be dried and re-subjected to controlled loading in an effort to conserve the Evolon® CR tissue. Finally, it was found that solvent-uptake occurs predominantly through adsorption in the interstitial voids. Therefore, to provide greater consistency in solvent loading irrespective of the choice of solvent, a solvent loading method based on solvent volume is preferred over calculating solvent weight or mmoles.

FT-LSI analyses revealed that a higher solvent loading does not result in significantly longer solvent decay times (i.e. longer solvent retention), but rather increasing solvent exposure times *do*. This is particularly observed with prolonged (over)exposure to Evolon® CR, as the initial hindrance of solvent uptake by the paint due to the presence of varnish is eventually overcome. Since acetone induces roughly six times longer-lasting dynamics (i.e. solvent induced motions) of pigment particles in a paint layer as compared to ethanol or isopropanol when used for varnish removal, conservators should be especially reserved with its use if other effective and less invasive solvents are available.

Finally, with regard to the adoption of FT-LSI analyses in conservation practice, FT-LSI in combination with UV photography is a relatively quick method to assess the effectiveness and the retention of solvent inside the paint when evaluating a particular varnish removal method. Since there are no other methods that can quantitatively and non-invasively assess the retention of solvents with high temporal and spatial resolution, our methodology provides a significant improvement in terms of reducing the risks associated with solvent-based varnish removals. However, a few challenges also remain. On a practical level, minimisation of canvas sway and vibration is critical for success in measuring larger paintings during testing. These movements tend to dominate the exceptionally minute displacements detectable by FT-LSI. We have obtained FT-LSI timetraces with comparable quality to those from paint models on small canvas and panel paintings, but for larger canvasses ($> 0.5 \times 0.5$ m), further research is still needed to find optimal adjustments to the setup (e.g. via use of a larger vibration damping table or conservation methods such as the fitting of padded backing boards to minimize canvas sway). The second challenge is accessibility and adoption. We hope that our development of a self-constructed, portable FT-LSI setup, constructed from a commercially available green laser and camera will facilitate easy accessibility of this technique in the future. However, until these limitations have been resolved and FT-LSI secures a definitive place in the conservator's analytical toolkit, tailoring of solvent testing with Evolon® CR will still need to be done empirically through gradual testing of different solvents, solvent loading, and contact times aided by careful visual observation.

This chapter improved our understanding regarding the use of Evolon® CR for varnish removal and showed that it can be safely employed when adhering to the recommended guidelines. Apart from continuing the development and implementation of FT-LSI for the paintings conservation field, future research avenues could explore less wasteful pre-treatments, and how support (e.g. lined and unlined canvas supports), paint type and structure (e.g. medium rich, porous and wax-resin impregnated paint) influence solvent decay times measured with

FT-LSI when using Evolon® CR for varnish removal. Outstanding questions that concern the more practical aspects of using Evolon® CR for varnish removal, such as line formation, will be addressed in future publications.

4.5 Materials & Methods

4.5.1 THM-Py-GC/MS

Sample preparation First, untreated Evolon® CR tissue was characterised by THM-Py-GC/MS (from now on Py-GC/MS) to identify its monomer composition. 100 μg of untreated Evolon® CR was cut, inserted in an Eco Cup SF (Frontier Laboratories, Japan) and placed with the sampler in the pyrolyzer.

To identify the substances released from the Evolon® CR during the washing process, the solvent extracts were analysed by Py-GC/MS. Solvent extracts were obtained by exposing 1×1 cm of Evolon® CR to 1 mL of the designated solvent for a set period of time. Two washing methods were evaluated: (1) a single 24 h exposure to solvent, and (2) iterative 1 min exposures totalling five iterations per series, wherein the solvent extract is analysed after each iteration. The iterative washing protocol consisted of immersing the Evolon® CR for 1 min in clean, fresh solvent (either acetone or ethanol), letting the tissue dry to completion, and repeating for a total of five washes (see Appendix for detailed procedure). Both methods of washing were set up in triplicate. Solvent extracts were analysed by Py-GC/MS as follows: 100 μL of the solvent extract was taken and evaporated under a stream of nitrogen at room temperature. This dry residue was redissolved in 10 μL of 25 % TMAH in methanol. 3 μL of the final solution were transferred to an Eco Cup SF and placed in the pyrolyzer for analysis.

Another pre-treatment option was explored in parallel; washing the Evolon® CR in a washing machine (at 60°C, without detergent) as a more environmental and cost-friendly alternative to solvent washing. After this pre-treatment, Evolon® CR was subsequently exposed to solvents according to the methods explained above.

Instrument and analysis parameters Untreated Evolon® CR tissue and solvent extracts were analyzed using a multi-shot pyrolyzer PY-3030D (Frontier Laboratories, Japan) coupled with a Thermo Trace 1310 GC system interfaced to a ISQ 7000 single quadrupole mass spectrometer (Thermo Fisher Scientific, USA). The pyrolyzer was used in the programmable temperature mode; after sample introduction the pyrolyzer was heated from 350°C to 660°C at 500°C/min, total time of 1 min. Pyrolyzer interface was set at 290°C. The temperature of the SSL

injector was 200°C and the split ratio was 1:32. The septum purge flow was set at 0.5 ml/min. The GC separation was achieved using a Supelco SLB5 MS (20 m × 0.18 mm × 0.18 m) capillary column. Chromatographic conditions: 35°C (1.5 min), 60°C/min to 100°C, 14°C/min to 250°C, 20°C/min to 300°C (2 min), helium flow rate (range of 0.6–1.3 mL/min). MS parameters: electron impact ionization (EI, 70 eV) in positive mode; ion source temperature was kept at 240°C; transfer line temperature was 270°C; scan range 29–600 amu with a dwell time of 0.2 min. Py-GC/MS data was processed with Xcalibur software (Thermo Fisher Scientific, USA) and the NIST 14 mass spectral library.

4.5.2 SEM

Sample preparation Solvent exposed Evolon® CR tissue samples were obtained by exposing 1×1 cm cut squares of Evolon® CR to 1 mL of solvent for a set period of time, and subsequently analysing the solvent exposed tissue. Set time periods were 7 days continuous exposure, 24 h, and 1 min. Additionally, a non-solvent exposed tissue was analysed as a control and a tissue that had been washed in a commercial washing machine at 60°C (no detergent). All solvent exposure lengths were timed such that all tissues were removed from solvent, prepped for analysis and analysed on the same day. All samples were analysed dry and within 3 hours after having been exposed to solvent.

Upon complete drying of each solvent exposed tissue, the tissues were cut into squares of roughly 5 ×5 mm and mounted onto an aluminium slot head stub by double sided copper tape. These discs were then positioned on the analysis stage and inserted into the SEM chamber for analysis.

Instrument and analysis parameters Analyses were performed on an XL30 SFEG electron microscope (FEI, Eindhoven, The Netherlands) on low vacuum with GAD. Images were captured at 2 kV accelerating voltage, 70 Pa, and spot size of 4. For each sample, at least two locations were documented at 350× and 2000× total magnification. On average, one image was captured at 350× as a general overview image of the chosen location, and 2–3 different areas imaged at 2000× to give representative detail images.

4.5.3 HIROX microscopy

Instrument and analysis parameters Optical imaging was performed on a RH-2000 HIROX digital microscope under bright field illumination, and imaged at 140×, 400×, and 700×. Fiber measurements were carried out using the HIROX RH-2000 software, and measured at 2000× magnification for the dry and water-wetted

tissues, and 1000× magnification for the ethanol- and acetone-wetted tissues. The use of a lower magnification reduced time needed for focusing on individual fibers, which was necessary for the more volatile solvents.

The tissues were laid over a sheet of Mylar (to protect the HIROX analysis stage). The dry tissue was imaged as such and the solvent-wetted tissues were imaged immediately after applying drops of solvent directly onto the tissue. 30 independent measurements were taken and averaged for the dry tissue and water-wetted tissue. 40 independent measurements were taken and averaged for the ethanol- and acetone-wetted tissues. The higher number of measurements was done to compensate for potential inaccuracies in measurement due to fiber movement during the solvent evaporation process. The tissue was regularly re-wetted during the measurement process for both ethanol and acetone.

During experimentation, it was difficult to obtain a good focus at high magnification on individual fibers after wetting, rendering it impossible to track changes to a single fibers as it was being wetted. In the case of acetone, fibers were observed to move subtly after wetting (likely due to acetone's high rate of evaporation). Hence, it was decided to image multiple locations and use average fiber widths.

4.5.4 Gravimetric analysis

Sample preparation Evolon® CR tissue was accurately cut into 5×5 cm squares using a grid and scalpel roller along guide lines. Subsequently, the solvent was poured into a shallow, circular tin plate, with a diameter large enough that the cut squares could float/lie without folding.

Experimental procedure Each cut square was weighed dry on a Sartorius BP211D balance accurate to 0.01 mg, and its weight recorded. The tissue was subsequently laid to float on the surface of the solvent and left to stand until the tissue was fully saturated. With water this process took a few seconds, but with the organic solvents, saturation was immediate. Upon saturation, the tissue was removed by tweezers, and rapidly laid on a clean paper towel to blot dry excess solvent. The blotting process was rapid – solvent soaked Evolon® CR tissue was simply left to make full contact with the paper towel, after which it was immediately lifted off by tweezer and weighed on the balance. No pressure or squeezing was applied to the tissue during the blotting process. To compensate for inherent variation due to rapid evaporation of the organic solvents and the blotting process, the weighing experiment outlined above was done in quintuplicate for each solvent.

To further ensure accuracy in how 'full' saturation was assessed and to ensure our finding were reproducible, a second method was tested in sextuplicate. For

this method, the tissue was shaken until drops of excess solvent ceased to drip. At this point only the very bottom corner of the tissue was briefly allowed to touch a dry paper towel to remove the building droplet and the tissue immediately weighed.

4.5.5 Nitrogen adsorption

Sample preparation Analysed tissues were pre-treated under vacuum at 200°C for 6 h to remove residual moisture from tissue interstices.

Instrument and analysis parameters The pre-treated tissues were analysed using a BELSORP-maxII porosimeter using the standard conditions of nitrogen as the adsorptive gas at 77 K. Results were analysed on a BELSORP version 1.1.1.4 software.

4.5.6 Mercury intrusion

Instrument and analysis parameters Evolon® CR tissues directly cut off the roll were analysed on a PASCAL 400 porosimeter using step-wise increases in pressure. The tissue was subjected to incremental increases in pressure up to a maximum of 200 MPa pressure, and the interparticle space calculated using the SOLID version 1.6.5 software.

4.5.7 Time-dependent ATR-FTIR spectroscopy

Time-Dependent ATR-FTIR Spectroscopy was carried out by placing a piece of untreated Evolon® CR immersed in ethanol on top of the zinc ionomer model paint film. With the piece of Evolon® CR on top, the bottom of the zinc ionomer film was then measured continuously for over 3 hours with ATR-FTIR Spectroscopy. This method and the synthesis of the zinc ionomer binding medium model system (Znpol) is described in more detail in the 'Portable FT-LSI & UV photography section.

ATR-FTIR spectra were measured on a Perkin-Elmer Frontier FT-IR spectrometer fitted with a Pike GladiATR module and a diamond ATR-crystal. Spectra were averaged over 4 scans. For analysis, 5 × 5 mm squares of the films were cut and lifted off the glass. During time-dependent measurements, the ATR module was flushed with nitrogen to ensure a constant background signal. In order to measure spectra of polymer samples while they were exposed to solvents or solutions, a custom built stainless steel cylinder was used as described in[28]. The cell volume was sealed with two solvent resistant O-rings between the top plate

and the pressure clamp of the ATR module. The polymer sample was covered by a $\varnothing$ = 10 mm porous sintered metal disk, and a small but constant pressure was applied to the polymer sample by a spring placed between the pressure clamp of the ATR module and the porous disk. The inlet was kept sealed with parafilm during measurements to avoid solvent evaporation.

4.5.8 Portable FT-LSI & UV photography

Sample preparation Model paint samples containing ZnO (Sigma Aldrich, ≥99%) were made by grinding the pigments with cold-pressed untreated linseed oil (Kremer Pigmente) in a 1:1 (w/w) ratio to a smooth paste with mortar and pestle. The Pigment Volume Concentration (PVC) for wet paint was 14% in all samples. The mixture was applied to 50 × 75 mm glass slides and spread with a draw-down bar to achieve a wet thickness of 190 μm. The samples were cured in the dark in air at 60 °C for 7 days at 97% RH. Humidity was controlled using a saturated K_2SO_4 solution (for 97% RH) in a closed container and was determined using a Rotronic HL-1D temperature and humidity data logger. After drying, the paint reaches a dry thickness of about 150 μm and a dry PVC around 18% for all samples. Samples were varnished using a brush with a dammar solution in 35 wt% Shellsol A and Shellsol T and subsequently aged for 7 days under UV-A and UV-B radiation. The total radiation dosage was 1.4×10^7 J/cm^2 (UV-A) and 5.2×10^7 J/cm^2 (UV-B).

Simulated cleaning test procedure Model oil films were prepared in the same manner as those for ATR-FTIR studies. Evolon® CR tissue was cut into 1 × 1 cm squares, washed with a large excess of acetone and ethanol using a Buchner funnel, dried and subsequently loaded with solvent.[1] For fully saturated tissues (no controlled loading), the Evolon® CR was dipped into the solvent, squeezed using nitrile gloves and directly used for cleaning. For controlled loaded tissues, loadings of 24%, 34%, 44% or 51% loading were assessed, and prepared as described in Tauber *et al.*[17] During solvent application, Evolon was covered with a glass cover slip to avoid solvent evaporation from the top. LSI data acquisition is started immediately upon removal of the Evolon® CR.

FT-LSI instrument and analysis parameters LSI measurements were performed on a custom-built portable FT-LSI set-up as schematically demonstrated in Figure 4.1. Previously published FT-LSI analyses as described in Baij and Buijs *et*

[1] This washing method is not representative of conservation practice, but is expected to yield efficient extraction of SFAs.

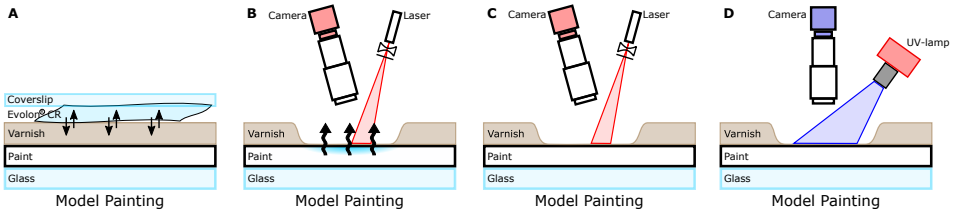

Figure 4.1. Experimental workflow: **A)** Simulated cleaning test procedure. **B)** The FT-LSI measurement starts immediately after the simulated cleaning test procedure. **C)** The FT-LSI measurement stops when the measured dynamics decrease significantly. **D)** UV photography is performed to determine the cleaning result.

al.[19] mostly employed a non-portable, lab-based instrument. We here employ a portable set up which can be easily dismantled and transported for analysis of objects *in situ*. To our knowledge, this is the first report of portable LSI coupled with real-time analysis and UV photography.

In all measurements, paint surfaces were illuminated by a 685 nm CNI laser at 70 mW, amplified using a single bi-concave lens and ground glass diffuser. The effective light intensity at the sample was 45 mW and covered an area with a diameter of 8 cm, resulting in a light intensity of 0.90 mW/cm^2 on the sample. Back-scattered light was captured using a Navitar variable zoom objective camera, and speckle patterns captured with a Thorlabs DCC3240N camera at medium frame-rates (50 fps). The solvent induced dynamics were quantified in real-time by Fourier transform analysis on speckle fluctuations as previously described in Buijs *et al.*.[27] The dynamics of the pigment particles (*i.e.* thermal or solvent induced motions) were measured in terms of power. The measured power was expressed in decibel (dB) using dry paint as the reference such that a power above zero dB corresponds directly to solvent-induced dynamics. Slow dynamics were observed by analysing batches of 128 speckle patterns from a 15 fps stream while faster dynamics employed batches of 32 speckle patterns from a 50 fps stream.

The 'decay time' is defined as the time it takes for the measured signal intensity to decay to 80% of its original intensity. A smoothed version of the time trace was used for decay time determination to reduce the effect of noise. For all other purposes the original time-trace was used.

UV-photography After each FT-LSI measurement, varnish removal was determined with UV-photography using a 365 nm Thorlabs UV LED lamp (1150 mW, M365LP1) and Genie Nano M640 Mono camera (640×480 resolution, 40 ms exposure time). A 400 nm longpass UV filter (Thorlabs, FEL0400) was used to remove UV light from the lamp and ensure measurement of fluorescence exclusively from

the sample. The entire set-up was assembled inside a dark box to avoid interference of other light sources.

List of abbreviations

- ATR-FTIR: attenuated total reflection Fourier transform infrared spectroscopy
- BZA: benzoic acid
- COOR: ester
- COOM: metal carboxylate
- 2C6: adipic acid
- 2C8: suberic acid
- 2C9: azelaic acid
- C12:0: lauric acid
- C13:0: tridecanoic acid
- C14:0: myrisitc acid
- C15:0: pentadecanoic acid
- C16:0: palmitic acid
- C18:0: stearic acid
- C18:1: oleic acid
- FT-LSI: Fourier transform laser speckle imaging
- Hg: mercury
- LO: linseed oil
- LSI: laser speckle imaging
- PVC: pigment volume ratio
- SEM: scanning electron microscopy
- SFA: saturated fatty acid
- THM-Py-GC/MS: thermally-assisted hydrolysis and methylation pyrolysis gas chromatography mass spectrometry

- TMAH: tetramethylammonium hydroxide
- TPA: terephthalic acid
- UV: ultraviolet
- ZnO: zinc oxide

4.A Appendix

4.A.1 THM py-GCMS analysis

Iterative washing sample preparation The first iteration was prepared by placing five 1 cm x 1 cm squares of Evolon® CR into a vial, and immersing with 5 mL of the designated solvent (for a ratio of 1 mL solvent for each 1 cm2 of tissue). All tissues were removed after 1 min of solvent immersion and left to dry to completion. The 5 mL solvent extract was set aside for analysis, and represents the 'first rinse'. Of the five dried tissues, one was set aside for direct Py-GC/MS analysis of the tissue, and represents a 'singly washed' tissue. The remaining four Evolon® CR squares were placed in a fresh vial, and immersed for 1 min in 4 mL of designated solvent (again for a ratio of 1 mL solvent for 1 cm2 of tissue). After 1 min solvent exposure, the tissues were removed, and the 4 mL solvent extract set aside for analysis, representing the 'second rinse'. Of the four dried tissues, each now having been exposed to solvent twice, one was set aside for direct Py-GC/MS analysis, representing a 'doubly washed' tissue, and the remaining three were re-immersed in 3 mL of fresh solvent. This process was continued such that by the end of the series, there were five total solvent extracts representing a first, second, third, fourth, and fifth/final rinse, and five total Evolon® CR tissue samples representing tissues washed 1x, 2x, 3x, 4x, and 5x.

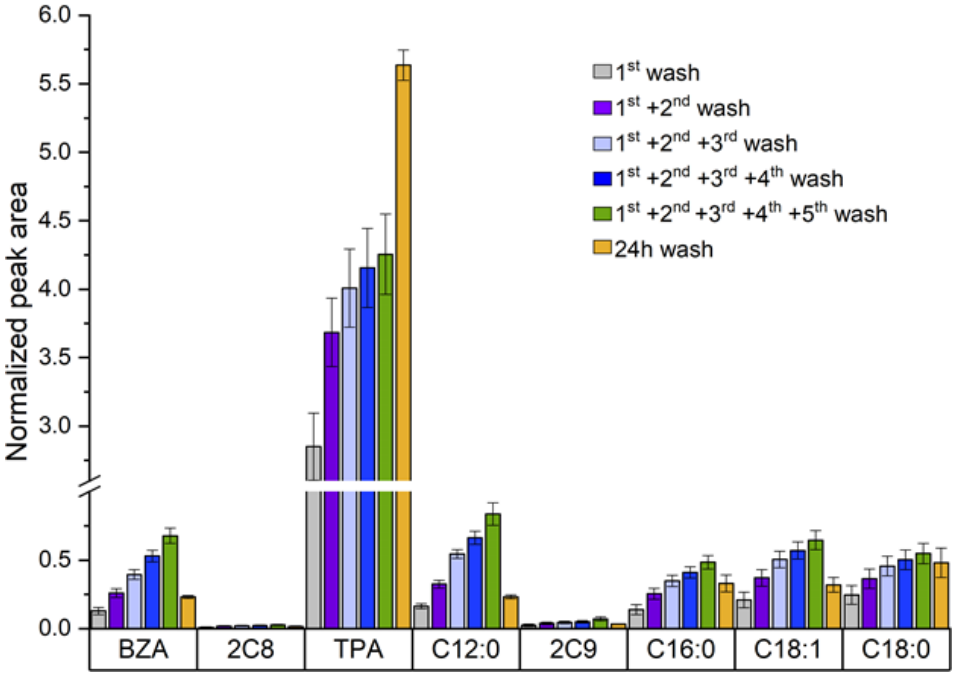

Figure 4.A.1. The sum of peak areas normalized to the internal standard (C13) of the main compounds extracted from Evolon® CR after iterative washing (accumulative) or 24h immersion with acetone. Benzoic acid (BZA), suberic acid (2C8), terephthalic acid (TPA), lauric acid (C12:0), azelaic acid (2C9), palmitic acid (C16:0), oleic acid (C18:1), stearic acid (C18:0). Error bars indicate standard deviation (1s).

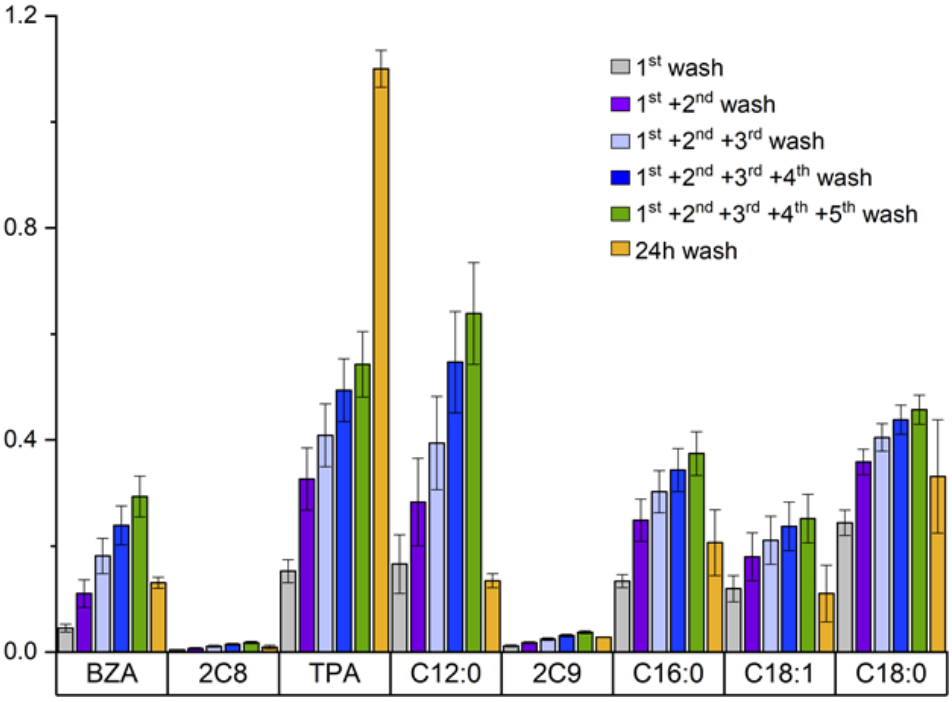

Figure 4.A.2. The sum of peak areas normalized to the internal standard (C13) of the main compounds extracted from Evolon® CR after iterative washing (accumulative) or 24h immersion with ethanol. Benzoic acid (BZA), suberic acid (2C8), terephthalic acid (TPA), lauric acid (C12:0), azelaic acid (2C9), palmitic acid (C16:0), oleic acid (C18:1), stearic acid (C18:0). Error bars indicate standard deviation (1s).

4.A.2 SEM analysis

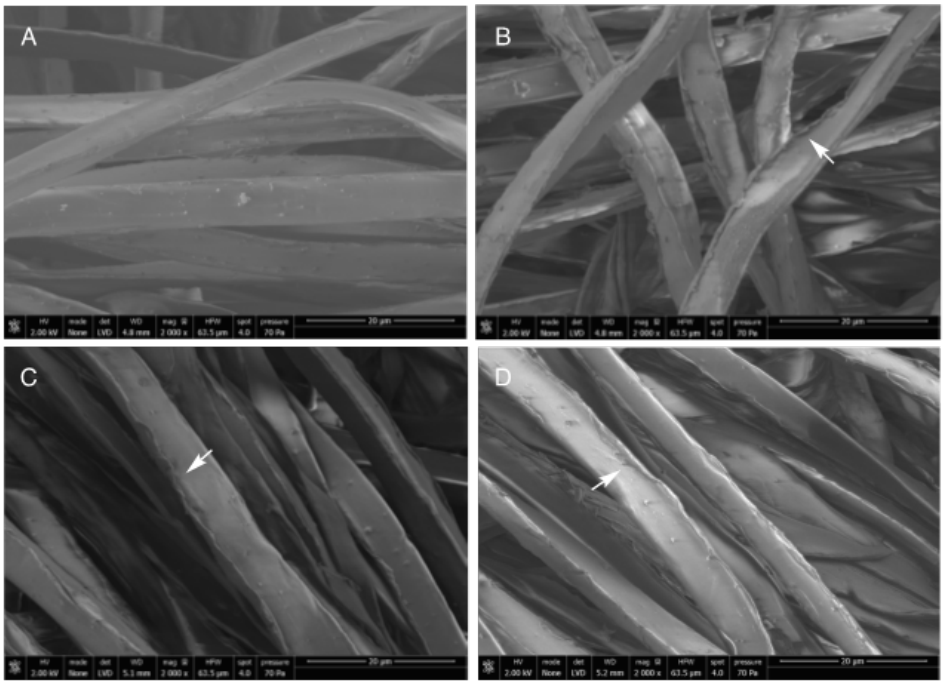

Figure 4.A.3. SEM images at 2000x magnification of **a)** non-solvent exposed tissue, **b)** 1 min exposure, **c)** 24 h exposure, and **d)** 7 day consecutive exposure in ethanol. White arrows indicate fraying along squared edges of individual fibers.

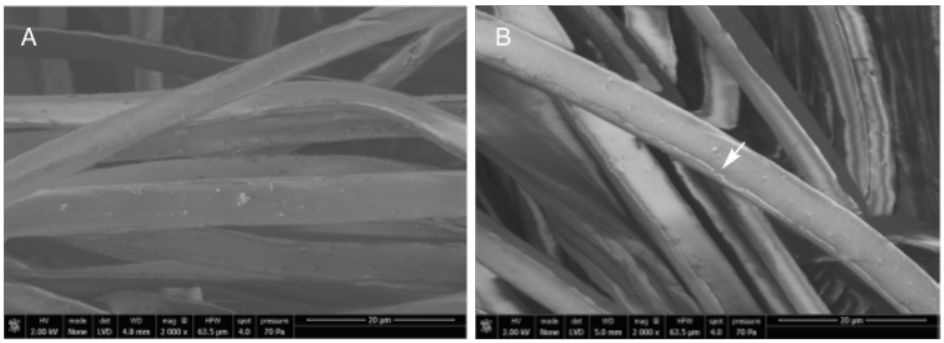

Figure 4.A.4. SEM images at 2000x magnification of **a)** non-solvent exposed tissue, **b)** non-solvent exposed tissue machine washed at 60 ºC without detergent. White arrows indicate fraying along squared edges of individual fibers.

4.A.3 HIROX microscopy

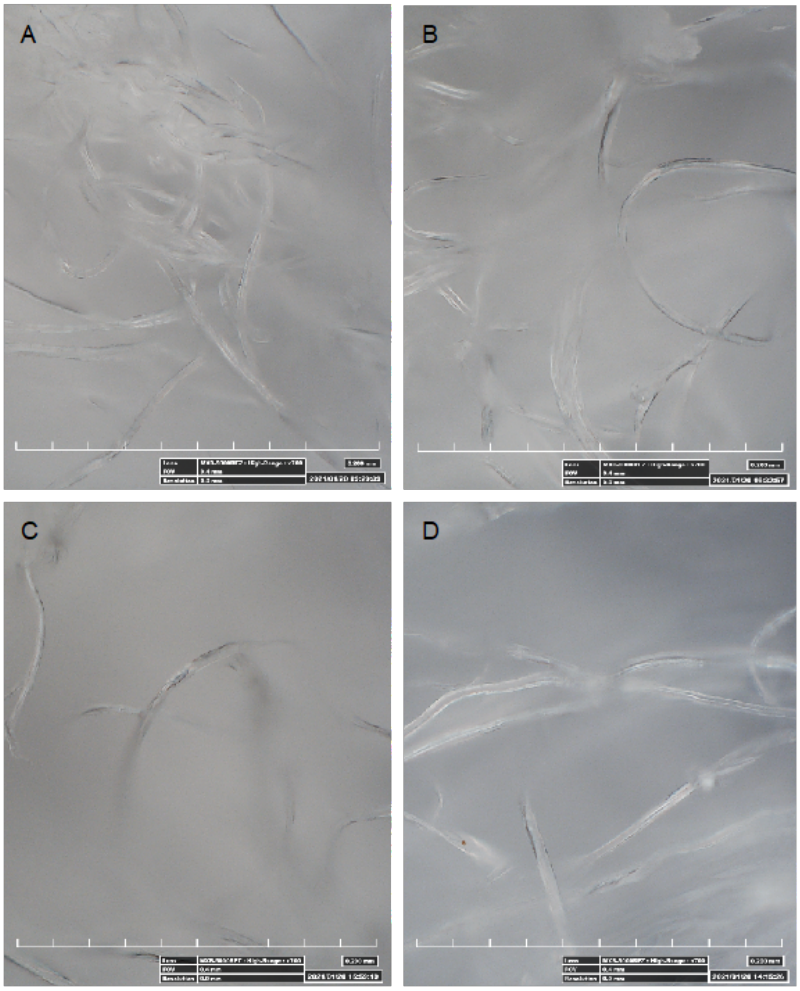

Figure 4.A.5. HIROX microscope images at 7000x magnification of **a)** non-solvent wetted (control), **b)** acetone wetted, **c)** EtOH wetted, and **d)** water wetted tissue.

	Dry Tissue (mm)	Acetone Wetted (mm)	EtOH Wetted (mm)	Water Wetted (mm)
1	0.00515	0.00570	0.00653	0.00620
2	0.00486	0.00593	0.00556	0.00490
3	0.00462	0.00643	0.00575	0.00495
4	0.00472	0.00646	0.00426	0.00584
5	0.00497	0.00603	0.00726	0.00565
6	0.00471	0.00672	0.00440	0.00599
7	0.00443	0.00643	0.00633	0.00701
8	0.00570	0.00415	0.00622	0.00727
9	0.00518	0.00484	0.00572	0.00758
10	0.00496	0.00653	0.00612	0.00783
11	0.00613	0.00625	0.00595	0.00683
12	0.00548	0.00528	0.00645	0.00546
13	0.00571	0.00587	0.00591	0.00584
14	0.00580	0.00720	0.00506	0.00545
15	0.00548	0.00599	0.00674	0.00599
16	0.00682	0.00640	0.00693	0.00566
17	0.00641	0.00587	0.00843	0.00616
18	0.00647	0.00642	0.00787	0.00597
19	0.00583	0.00451	0.00611	0.00519
20	0.00544	0.00634	0.00583	0.00694
21	0.00643	0.00625	0.00620	0.00665
22	0.00689	0.00562	0.00637	0.00716
23	0.00651	0.00625	0.00603	0.00698
24	0.00643	0.00661	0.00689	0.00514
25	0.00634	0.00590	0.00644	0.00485
26	0.00585	0.00635	0.00549	0.00508
27	0.00552	0.00666	0.00612	0.00529
28	0.00519	0.00683	0.01267	0.00606
29	0.00475	0.00475	0.00521	0.00573
30	0.00530	0.00579	0.00477	0.00516
31		0.00653	0.00497	
32		0.00654	0.00452	
33		0.00779	0.00556	
34		0.00780	0.00549	
35		0.00642	0.00551	
36		0.00582	0.00567	
37		0.00620	0.00558	
38		0.00440	0.00465	
39		0.00532	0.00628	
40		0.00540	0.00753	
Min	0.00443	0.00415	0.00426	0.00485
Max	0.00689	0.00780	0.01267	0.00783
Average	**0.00560**	**0.00606**	**0.00613**	**0.00603**
Deviation	0.00069	0.00079	0.00138	0.00083

Table 4.A.1. Tabulated measurements of diameter of individual fibers.

4.A.4 Nitrogen Adsorption

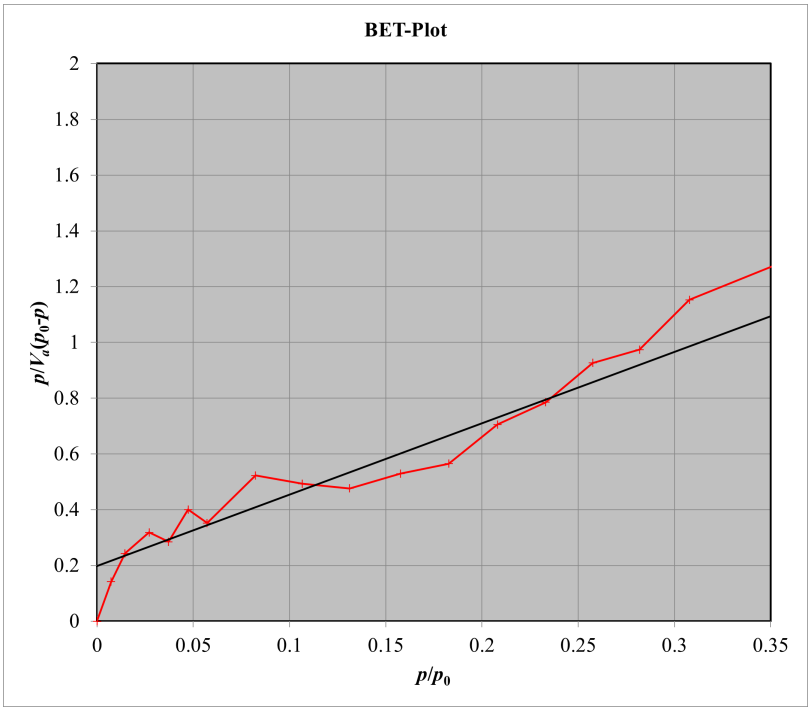

Figure 4.A.6. BET plot; BET method BELMaster ver. 7.2.0.4

Start point	6	
End point	15	
Slope	2.562	
Intercept	0.1977	
Correlation coefficient	0.9452	
Vm	0.3624	[cm3(STP) g-1]
as,BET	1.5773	[m2 g-1]
C	13.958	
Total pore volume (p/p0=0.9900)	0.0086889	[cm3 g-1]
Average pore diameter	22.034	[nm]

Table 4.A.2. BET fitting parameters

Instrument	**BELSORP-maxII**	
Serial No.	129	
Software Version	Ver. 1.1.1.4	
Sample mass	0.1655	[g]
Manifold volume	33.996	[cm3]
Free space	36.584	[cm3]
Adsorptive	N2	
Manifold temperature	49.9	[C]
Adsorption temperature	77.355	[K]
Thermal transpiration correction	Used	
Non-idality correction	YES(virial)	
Free space determination method	AFSM	
Molecular diameter	0.354	[nm]
Saturation vapor pressure	104.7	[kPa]
Saturation vapor pressure measurement	Update continuously	
Molecular cross-sectional area	0.162	[nm2]
Adsorptive molecular weight	28.013	
Smoothing	Not used	
Mask	Not used	
Adsorption data point number	32	
Desorption data point number	32	

Table 4.A.3. BET instrument and measurement parameters

4.A.5 Mercury intrusion

TEST INFORMATION

Test date:	26-03-21	
Sample name:	Evolon CR	
Comment:	Tracy Lin	
Sample mass (g):	0.1684	
Sample skeleton density (g/cm3):	1.13	
Test file name:	C:\Solid\Instr2\Data\2021\210326.P44	
Combined with file (140):		
Mercury surface tension (N/m):	0.48	
Mercury contact angle (°):	140.0	
Test filling volume (mm3):	408.3 at P < 1 Pa	
Starting hydr. press. of test (MPa):	0.0164	
(Dil+Hg+Sample) weight (g):	144.012	
Corrected weight (Dil.+Hg+Sample) (g):	144.054	

ANALYTICAL CONDITIONS

Maximum test pressure (MPa):	200	
Increase speed:	6	
Increase method:	Pascal	Stepwise
Decrease speed:	9	
Decrease method:	Pascal	Stepwise
Temperature of test (°C):	24.9998	
Mercury density @ test (g/cm3):	13.5340	

Figure 4.A.7. Mercury intrusion experimental parameters

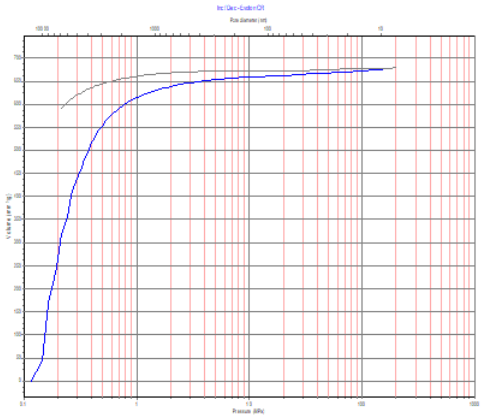

RESULTS WITHOUT COMPRESSIBILITY CORRECTION

Total intruded volume (mm³)	114.47		
Total intruded volume (mm³/g):	679.73	at pressure of MPa:	200.6141
Spec. Vol. by skeleton dens. (mm³/g) Vd:	532.08		
Bulk density (g/cm3):	0.7057		
Envelope density (g/cm3):	0.7057	at pressure of MPa:	0.116 Diam.(nm) 12640.1
Apparent density (g/cm3):	1.3563	at pressure of MPa:	200.6141 Diam.(nm) 7.3
Porosity by skeleton density (%):	37.55	Calculated by skeleton density of 1.13 g/cm³	
Porosity by Hg intrusion (%):	47.97		
Inaccessible porosity (%):	-10.42		

Figure 4.A.8. Mercury intrusion experimental results

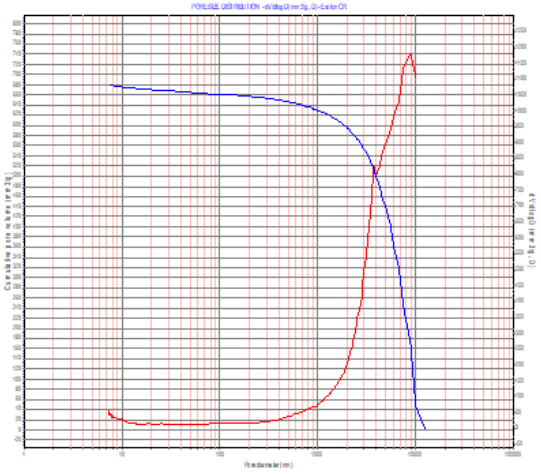

Derivative calculated with			
Moving average points :	21		
Smoothing factor:	0.00		
Calc. press . range (MPa):	0.0 to 200.614		
Total pore volume (mm3/g):	679.73		
Total pore surface area (m2/g):	5.442	with model :	Cylindrical and Plate
Average pore diameter (nm):	499.62	Hydraulic (4V/A)	
Median pore diameter (nm):	6377.62	at (mm3/g) :	339.86
Modal pore diameter (nm):	8869.89	at dV/dlogD (mm3/g, D) :	1181.60
Span:	1.2997	at Min. Vol. (%) 10.0	at Max. Vol. (%) 90.0

Figure 4.A.9. Total pore-size obtained from Mercury intrusion

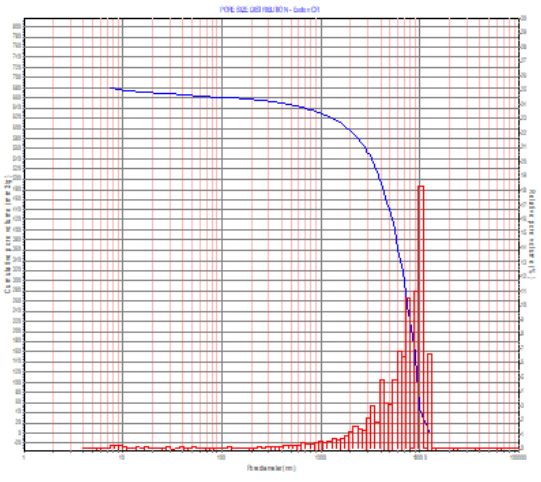

Figure 4.A.10. Total pore-size histogram

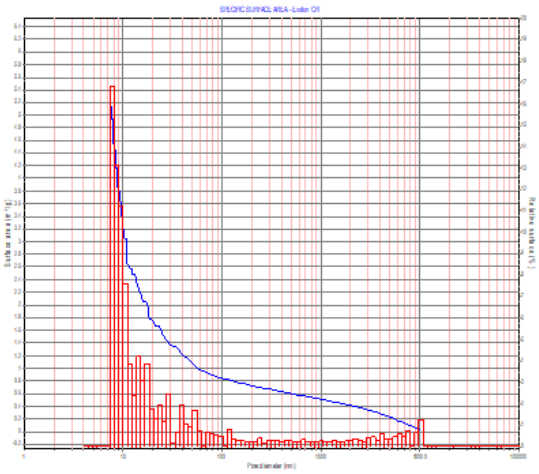

Figure 4.A.11. Total pore-surface histogram

References

[1] L. Baij, J. Hermans, B. Ormsby, P. Noble, P. Iedema, K. Keune. *Heritage Science* **8**, 43 (2020).

[2] N. Khandekar. *Studies in Conservation* **45**, 10–20 (2000).

[3] R. Wolbers, *Cleaning Painted Surfaces: Aqueous Methods* (Archetype Publications, London, 2000).

[4] D. Stulik, D. Miller, H. Khanjian, N. Khandekar, R. Wolbers, J. Carlson, W. C. Peterson, *Solvent Gels for the Cleaning of Works of Art: The Residue Question* (The Getty Conservation Institute, Los Angeles, 2004).

[5] C. Samorì, P. Galletti, L. Giorgini, R. Mazzeo, L. Mazzocchetti, S. Prati, G. Sciutto, F. Volpi, E. Tagliavini. *ChemistrySelect* **1**, 4502–4508 (2016).

[6] L. V. Angelova, B. Ormsby, E. Richardson. *Microchemical Journal* **124**, 311–320 (2016).

[7] F. Volpi, Green Strategies for the Cleaning of Works of Art Setting Up of an Analytical Protocol for the Evaluation of Cleaning, Ph.D. thesis, alma (2017).

[8] L. V. Angelova, B. Ormsby, J. Townsend, R. Wolbers, eds., *Gels in the conservation of art* (Archetype Publications, London, 2018).

[9] G. R. Fife, *Gels in the Conservation of Art*, B. Ormsby, J. H. Townsend, R. Wolbers, eds. (Archetype Publications, London, 2017), pp. 257–261.

[10] A. Bartoletti, R. Barker, D. Chelazzi, N. Bonelli, P. Baglioni, J. Lee, L. V. Angelova, B. Ormsby. *Heritage Science* **8**, 9 (2020).

[11] D. Chelazzi, R. Giorgi, P. Baglioni. *Angewandte Chemie International Edition* **57**, 7296–7303 (2018).

[12] D. Chelazzi, R. Bordes, R. Giorgi, K. Holmberg, P. Baglioni. *Current Opinion in Colloid and Interface Science* **45**, 108–123 (2020).

[13] P. Baglioni, D. Chelazzi. *Chemistry – A European Journal* **27**, 10806 (2021).

[14] J. Chung, B. Ormsby, J. Lee, A. Burnstock, K. van den Berg. *ICOM-CC 18th Triennial Conference Preprints, Copenhagen, 4-8 September 2017* (2017).

[15] G. Robert, B. Jean, R. Georges, Nonwoven lap formed of very fine continuous filaments (1999).

[16] M. Vergeer, K. J. van den Berg, S. van Oudheusden, M. Stols-Witlox, *Evolon® CR microfibre cloth as a tool for varnish removal* (2019).

[17] G. Tauber, S. Smelt, P. Noble, K. Kirsch, A. Siejek, K. Keune, H. van Keulen, S. Smulders-De Jong, R. Erdman. *AIC Paintings Specialty Group Postprints* **31**, 45–50 (2018).

[18] L. Baij, A. Astefanei, J. Hermans, F. Brinkhuis, H. Groenewegen, L. Chassouant, S. Johansson, G. Corthals, C. Tokarski, P. Iedema, K. Keune. *Heritage Science* **7**, 31 (2019).

[19] L. Baij, J. Buijs, J. J. Hermans, L. Raven, P. D. Iedema, K. Keune, J. Sprakel. *Scientific Reports* **10**, 10574 (2020).

[20] Freudenberg, personal communication.

[21] S. Zhang, J. Zhang, L. Tang, J. Huang, Y. Fang, P. Ji, C. Wang, H. Wang. *Polymers* **11** (2019).

[22] E. Arceo, J. A. Ellman, R. G. Bergman. *ChemSusChem* **3**, 811–813 (2010).

[23] A. B. Elmas Kimyonok, M. Ulutürk. *Journal of Energetic Materials* **34**, 113–122 (2016).

[24] E. S. Lower. *Pigment & Resin Technology* **11**, 13–18 (1982).

[25] L. Baij, J. J. Hermans, K. Keune, P. D. Iedema. *Macromolecules* **51**, 7134–7144 (2018).

[26] L. Baij, K. Keune, J. J. Hermans, P. Noble, P. D. Iedema, *Gels in the Conservation of Art*, B. Ormsby, J. H. Townsend, R. Wolbers, eds. (Archetype Publications, London, 2017), pp. 316–321.

[27] J. Buijs, J. van der Gucht, J. Sprakel. *Scientific Reports* **9**, 13279 (2019).

[28] L. Baij, J. J. Hermans, K. Keune, P. Iedema. *Angewandte Chemie International Edition* **57**, 7351–7354 (2018).

[29] A. Shafaei, M. Nikazar, M. Arami. *Desalination* **252**, 8–16 (2010).

[30] H. F. Clausen, R. D. Poulsen, A. D. Bond, M. A. S. Chevallier, B. B. Iversen. *Journal of Solid State Chemistry* **178**, 3342–3351 (2005).

Chapter 5

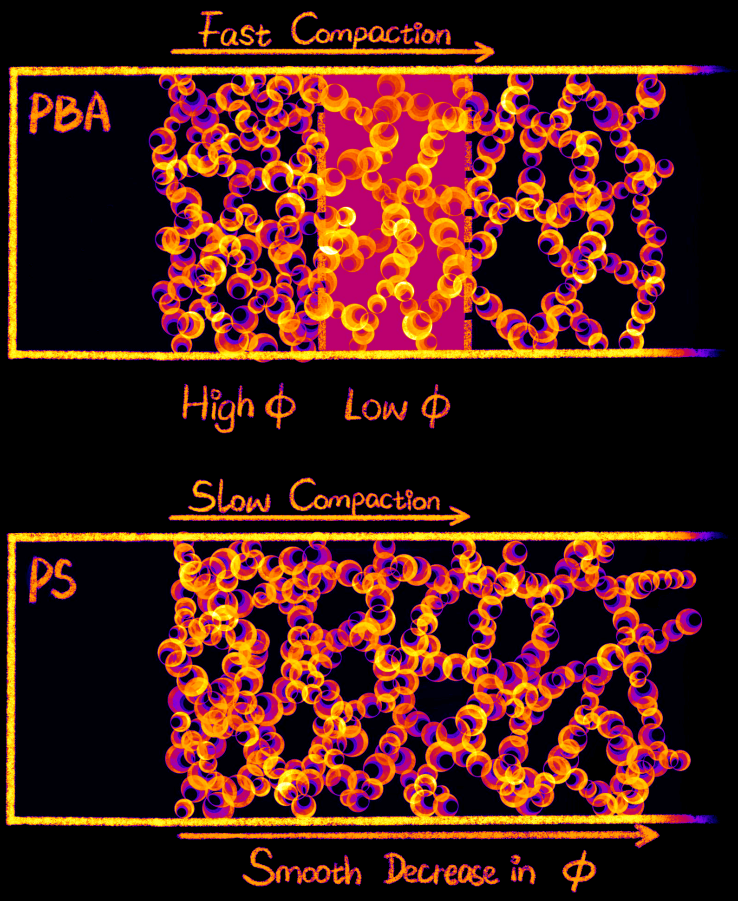
Fast Compaction
PBA
High ϕ
Low ϕ
Slow Compaction
PS
Smooth Decrease in ϕ

SPATIALLY HETEROGENOUS DYNAMICS IN COLLOIDAL GELS DURING SYNERESIS

Syneresis, the compaction of a material accompanied by fluid expulsion, is a typical mechanical instability which exists among colloidal gel based materials and that negatively affects the quality of relevant applications. We shed light onto the internal dynamics of model colloidal gels undergoing syneresis using Laser Speckle Imaging (LSI). The resulting dynamical maps capture the distinct differences in spatial and temporal relaxation patterns between colloidal gels comprising solid and liquid particles. This indicates different mechanisms of syneresis between the two systems and highlights the importance of the constituent particles and their mobile or restrictive interfaces in the mechanical relaxation of the colloidal gels during syneresis.

This chapter is under review as: Wu, Q., Buijs, J., Groot, S. de, Kooij, H. M. van der, Gucht, J. van der & Kodger, T. E., 'Spatially Heterogenous Dynamics in Colloidal Gels during Syneresis'

5.1 Introduction

Colloidal gels are soft solids in which attractions between colloidal particles drive a thermodynamic instability that through aggregation results in a space-spanning network structure of which the unique mechanical and transport properties can be suitably tuned.[1,2] Colloidal gels are widely encountered in applications such as drug delivery systems, food products, coatings, and more.[3,4] While a colloidal gel forms, particles tend to maximize contact with each other to minimize the interfacial energy cost in the network; this leads to local compaction in the structure. The heterogeneity of this compaction leads to randomly distributed regions of inhomogenous deformations, each of which generates a displacement field around it due to the elasticity of the network. These inhomogeneities can be considered as localized internal stress built within the network.[5,6] When this internal stress is of sufficient amplitude or is facilitated by external stress, colloidal gels may suffer from a specific mechanical failure known as syneresis,[7,8] i.e. the contraction of the material accompanied by the expulsion of fluid. Syneresis is a typical mechanical instability encountered in food colloids, which is characterized by the appearance of fluid after a scoop in products like yoghurt and low-fat manufactured food. Unlike yielding of a solid network and fluidization of a gel induced by applied strains, the syneresing material itself does not necessarily undergo a solid to liquid transition, which indicates that the governing mechanisms are different from strain induced yielding.

Syneresis has been studied most intensively with macroscopic samples such as cheese and yoghurt, a colloidal gel formed by casein micelles. To date, the investigations have been centered on bulk syneretic properties, i.e. dimensional changes, rate of fluid expulsion and structural rearrangement obtained indirectly by rheology.[9] Correlations have been found between the expulsion of fluid and parameters like pH and temperature.[7,10,11] Additionally, internal and external stresses applied to the material robustly influence the magnitude of syneresis.[12,13] Rearrangements within the network play a crucial role in determining the ease of fluid expulsion; these structural changes have been probed using rheology, notable by the quantity $\tan \delta$, which represents the ratio of the dissipated energy due to relaxation of interparticle bonds and the energy elastically stored caused by a small distortion of the bonds.[10,14] Such ensemble measurements, however, do not capture the spatial heterogeneity typical of a material undergoing syneresis. More specifically, syneresis is not purely a surface phenomenon, rather, it occurs over an unknown distance into the sample and over an unknown time scale. When syneresis occurs, while the material may retain its initial shape and does not appear to flow on the macroscopic scale, on the microscopic scale the material

must undergo rearrangements leading to progressive fluid expulsion. Arriving at a deeper causation between microscopic dynamics and bulk syneresis in a colloidal gel is a crucial step towards understanding the mechanical response of such colloidal materials.

Revealing how the fluid and particle dynamics at the microscale govern syneresis is challenging as it involves a diverse range of time and length scales, which calls for methods which reveal and quantify the spatiotemporal heterogeneities. Conventional optical microscopy is not suitable for this task as turbidity inherent to particle dispersions such as colloidal gels and related commercial products, causes multiple scattering of light and insufficient light transmission. We therefore apply a light scattering technique, Laser Speckle Imaging (LSI), which utilizes the turbidity to resolve the dynamics within non-transparent materials and is the imaging counterpart of Diffusive Wave Spectroscopy.[15,16] LSI has been widely applied in medical imaging since the 1980s to visualise, for instance, subcutaneous flow of blood,[17–20] but in the last few years it has been also used to understand phenomena such as self-healing of polymers and delayed fracture in soft solids.[21,22] The technique relies on the illumination of a material with an expanded beam of coherent light. The photons of the coherent light are scattered multiple times by the optically turbid material and then the back-scattered light is captured by a camera. As the illuminating light is coherent, interference of these scattered waves creates a pattern known as a speckle image. In an evolving sample, such as a colloidal gel undergoing syneresis, the dynamics of the speckle pattern change which creates contrast for analysis.[23,24] LSI thus uses changes in photon path-length resulting from nanoscale particle movement at millisecond to hour time scale and micron to centimeter spatial resolution. In this chapter, we use LSI to create highly resolved dynamic maps of model colloidal gels during syneresis. These measurements allow for identification and characterization of the microscopic dynamics that govern syneresis.

5.2 Results and discussion

5.2.1 Spatiotemporal analysis of syneresis via d_2

Colloidal dispersions consisting of polystyrene particles (PS) or polybutylacrylate particles (PBA) with an averaged radius, $\langle r \rangle$ = 275 nm, at ϕ=0.01 and 0.02 respectively, in aqueous density matched solution are prepared in non-adhesive capillaries.[25] Both types of particles have 0.1wt% of a thermoresponsive surfactant adsorbed onto their surface. Upon heating to 32 °C, reversible and temperature-triggered adhesive forces are induced between the particles, with an attractive

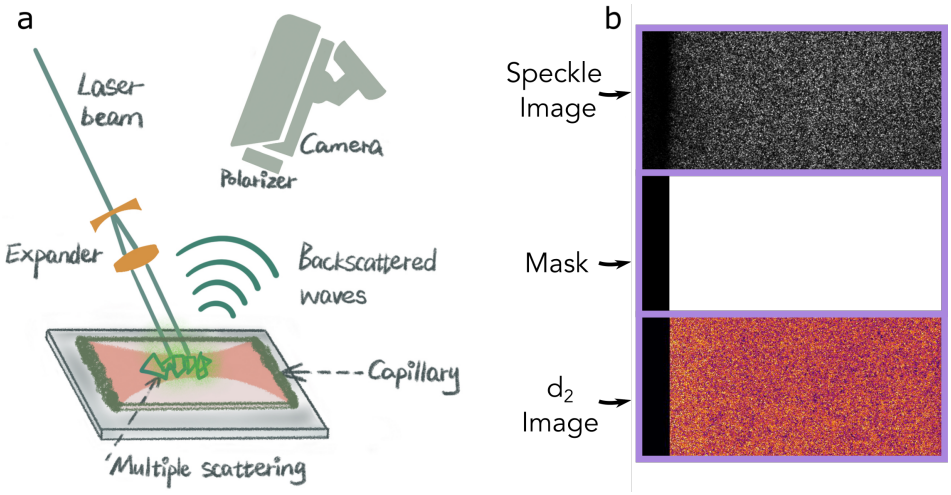

Figure 5.1. a) Schematic illustration of back-scatter LSI set-up. The syneresing sample is illuminated with a coherent plane light wave, which is multiply scattered by the turbid sample, giving rise to a raw speckle image captured by the camera, modified from[21]; **b)** Example images of a raw speckle image, a binary threshold mask and resultant image of multiplying the mask with the d_2 map. Each purple rectangle represents one image.

strength $\gg k_BT$,[26,27] leading to rapid colloidal gelation. Immediately after formation, gels undergo compaction, expelling the continuous fluid as seen in the recorded movies (fig. 5.A.1).

We start an LSI measurement by heating a climate chamber which contains all of the optical elements.[16] After the temperature in the climate chamber reaches 32°C, the sample is inserted and data collection begins. A coherent light illuminates the sample and back scattered light is detected by a camera, illustrated in Fig. 5.1 (a). Photon path length differences within the turbid sample generate a speckle pattern as shown in Fig. 5.1 (b). While the absolute intensities in the snapshots of the speckle pattern are irrelevant, information on the internal dynamics of the colloidal gel during syneresis in time and space is extracted from analyzing the temporal fluctuations of the raw speckle images via the contrast function $d_2\,(t, x, y, \tau)$[16,28,29]

$$d_2(t,x,y,\tau) = \frac{\langle [I(t,x,y) - I(t+\tau,x,y)]^2 \rangle}{\langle I(t,x,y)\rangle \langle I(t+\tau,x,y)\rangle} \tag{5.1}$$

with averaging over time where I is the speckle intensity at position (x, y), t is the age of the sample which provides the temporal dimension and τ sets the time lag between which images are autocorrelated, and hence the relaxation time of the

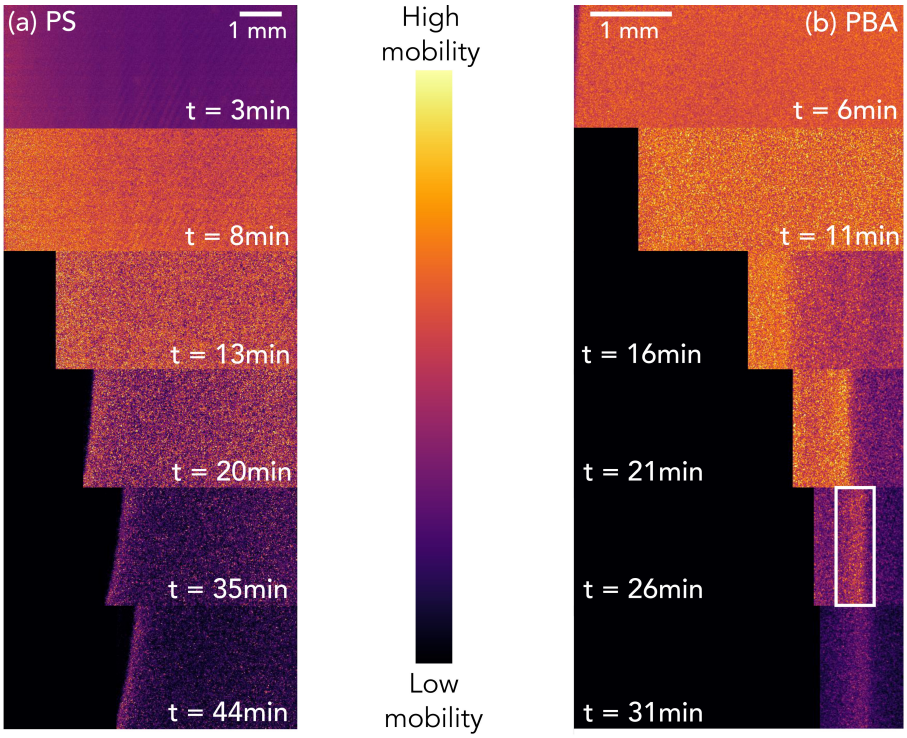

Figure 5.2. Time-lapse d_2 maps of **a)** the PS and **b)** the PBA gel during syneresis, τ=0.125 s. Left end of d_2 maps represents the capillary wall. Note the activity band in the PBA gel indicated with a white rectangle for t = 26 min.

dynamics of focus; small values of τ correspond to fast, high-frequency dynamics, while large values of τ enable the study of low-frequency processes. Based on d_2, spatiotemporal maps of the dynamics can be created.[30,31] High d_2 values indicate decorrelation of the signal and hence signify enhanced local mobilty. Fluctuations occur in the void area in the field of view, thus the d_2 maps are multiplied with a binary threshold mask, shown in Fig. 5.1 (b), to eliminate these fluctuations.

We monitor the syneresis process over time with LSI and compute d_2 values which encode the dynamics of the colloidal gel during syneresis, as shown in Fig. 5.2. These d_2 maps of PS and PBA colloidal gels for τ=0.125 s are shown as an example of the temporal development of dynamics during syneresis, where t = 0 min is defined as the moment when T=32 °C. The edge of the colloidal gel corresponds to the capillary wall at t = 0 min and moves as syneresis occurs. Compared with the PS gel, a more substantial syneresis is observed in the PBA gel, which manifests in higher d_2 values. During the first 8 minutes for the PS gel (Fig.

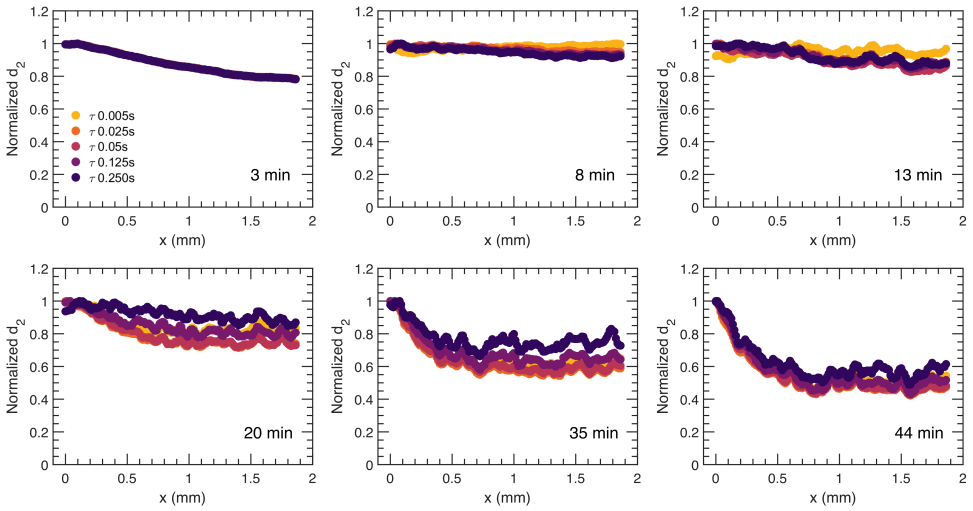

Figure 5.3. Profiles of normalized d_2 for the PS colloidal gel at relaxation times, $\tau = 0.005, 0.025, 0.05, 0.125, 0.250$ s as a function of distance to the moving gel edge for increasing sample age, $t = 3, 8, 13, 20, 35, 44$ minutes. $x(t)$ = 0 mm represents the edge of the sample at the corresponding age. To highlight the spatial dependence, a normalized d_2 value is used as the absolute d_2 changes dramatically as the gel forms, synereses, and subsides.

5.2 (a)), mobility increases within the entire sample while there is no sign yet of macroscopic syneresis as the gel is still forming. When syneresis proceeds, the colloidal gel detaches from the capillary wall and mobility in the bulk decreases, while around the gel edge a relatively high mobility remains. For the PBA gel (Fig. 5.2 (b)), higher mobility emerges after 6 minutes, indicated by the higher d_2 value. The mobility near the moving gel edge remains high while the mobility in the bulk starts to decrease after 16 minutes, which is similar to the PS gel but this higher dynamic activity region extends over a wider range and occurs much earlier. Meanwhile, a zone of increased dynamic activity develops behind the gel edge, which lingers until the end of syneresis (Fig. 5.2 (b), white rectangle). After 26 minutes, the rate of syneresis slows down and d_2 at the gel edge decreases as well. In general, the mobility in the bulk slows down faster than the mobility near the edge, suggesting that there is spatial dependence of the dynamics during relaxation.

5.2.2 Spatial relaxation with different relaxation times

For a more quantitative description of the spatial dependence of the local dynamics in the direction of syneresis as observed in Fig. 5.2, a normalized d_2, with the value

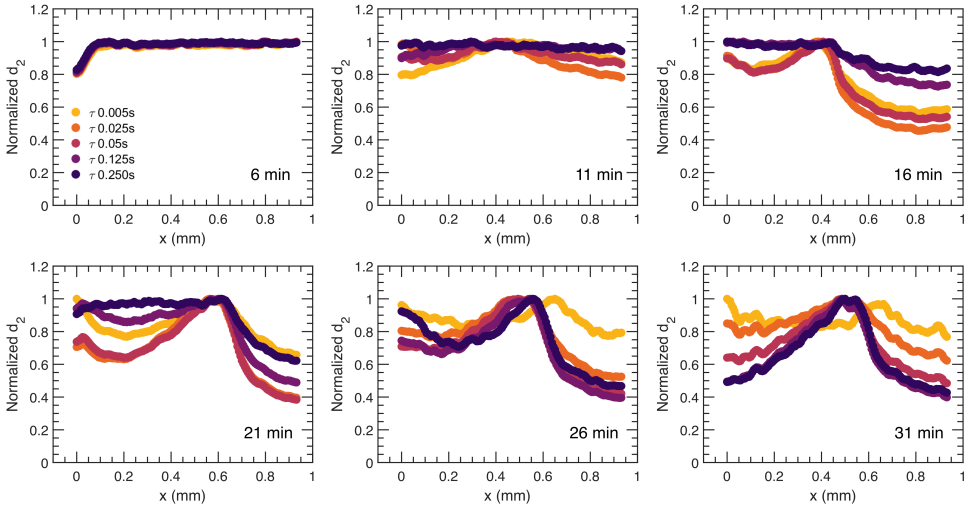

Figure 5.4. Profiles of normalized d_2 for the PBA colloidal gel at relaxation times, $\tau = 0.005, 0.025, 0.05, 0.125, 0.250$ s as a function of distance to the moving gel edge for increasing sample age, $t = 6, 11, 16, 21, 26, 31$ minutes. $x(t) = 0$ mm represents the edge of the sample at the corresponding age.To highlight the spatial dependence, a normalized d_2 value is used as the absolute d_2 changes dramatically as the gel forms, synereses, and subsides.

of d_2 being divided by the relative maximum for that sample, is computed and displayed as a function of distance to the moving gel edge, x, for different times after gelation, t, and for different correlation times, τ, in Fig. 5.3 and 5.4, for PS and PBA gels, respectively. As shown in Fig. 5.3, for the PS gel, the dynamic activity decreases gradually away from the edge in a similar manner for all τ, implying that dynamic processes have similar spatial dependence.

In contrast to the dynamics in the PS gel, the normalized spatial d_2 profile is much more diverse in the PBA gel (Fig. 5.4), showing a band of enhanced dynamic activity a few hundred microns behind the edge of the gel, which we call the activity band (Fig. 5.2 (b), white rectangle). The activity band already rises for small τ at 11 minutes and appears in all τ after 21 minutes. Additionally, the spatial d_2 pattern shows a dependence on τ, which suggests that in several locations different dynamic processes occur such as diffusion and ballistic or advective motion as a result of the compaction. We will investigate those differences through a mean squared displacement analysis in section 2.3.

To investigate the distinct spatial dependence of d_2 between the two types of colloidal gels, we take a closer look at the activity band in the PBA gel. Firstly, the position of the peak of the band and the moving gel edge with respect to the

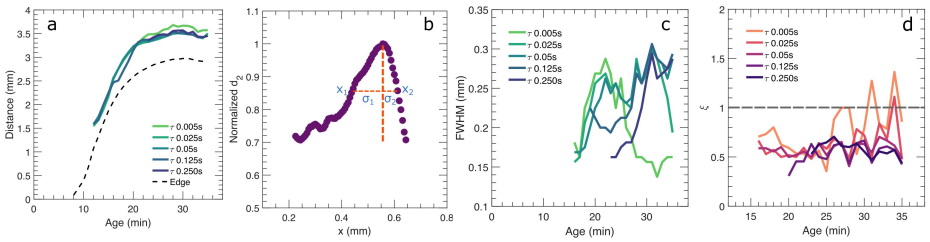

Figure 5.5. a) Distance from the moving gel edge of the PBA gel (dashed line) and peak of the activity band (solid lines) to the glass capillary wall: the shrinkage of the sample over time is displayed together with the location of the peak of the activity band, as a function of age, t. **b)** Example for determination of FWHM and asymmetry ratio. **c)** FWHM of the activity band over different τ as a function of t. **d)** The asymmetry of the activity band distribution, represented by $\xi = \sigma_2/\sigma_1$, at different τ as a function of t.

capillary wall is calculated; the macroscopic motion of the whole gel is substantial, as indicated by the distances from the moving gel edge to the capillary wall as a function of t in Fig. 5.5 (a) (dashed line). For all calculated τ, the activity band grows further away with respect to the moving gel edge in the first 20 minutes and retains the same distance to the gel edge as the macroscopic movement of the gel subsides which is indicated by the plateau for the later ages in Fig. 5.5 (a) (dash line).

The shape of the activity band also changes over time as seen in Fig. 5.4; to study this evolution for different τ, we calculate the full width at half maximum (FWHM) and an asymmetry ratio, ξ, of the activity band distribution as a function of t, depicted in Fig. 5.5 (c,d). An example of determination of the FWHM and ξ is shown in Fig. 5.5 (b) with FWHM $= x_2 - x_1$ and $\xi = \sigma_2/\sigma_1$. A ξ below 1 indicates that the majority of the rise in mobility is on the left side of the band, nearest to the moving gel edge, not the gel side of the sample. We note that the ages before the complete development of the activity band for different τ are neglected, as seen in Fig. 5.4. The activity band develops earlier for the three smaller τ; the width of the band increases with the macroscopic compaction of the gel. For the two larger value of τ, the activity band widens after the macroscopic compaction subsides with increasing t; this indicates a slowing down of the dynamic activity of the centre of the activity band. In terms of ξ, for all τ at all t, the band is asymmetric, $\xi < 1$, indicative of a wider band of relaxation on the side of the gel edge compared to the side towards the bulk. This may indicate that this side is more elastic: When stressed, the stress is distributed over a larger length for a more elastic material.

We note that the noise in data of $\tau = 0.005$ s at later ages can be attributed to the flattening of the band, as shown in Fig. 5.4.

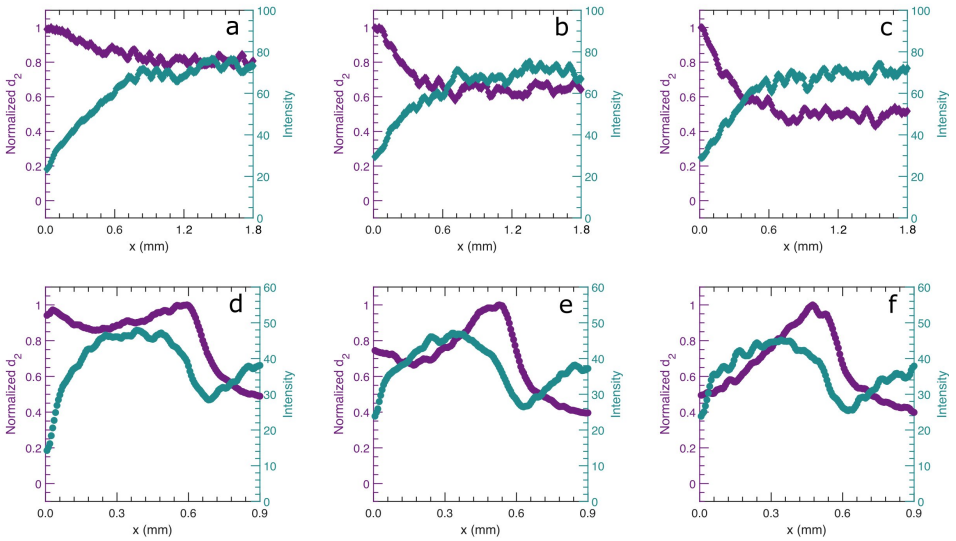

Figure 5.6. Profiles of normalized d_2 and the average back-scattered light intensity as a function of distance from the moving gel edge. $x(t) = 0$ mm represents the moving gel edge of (**a-c**) the PS colloidal gel at t = 20, 35 and 44 min and (**d-f**) the PBA colloidal gel at t = 21, 26 and 31min.

To examine the spatial variation in the density of the gel, we also monitor the average light intensity. We assume that regions of high particle density scatter more strongly so that a higher average back-scattered light intensity correlates with a higher local particle volume fraction. Both the average light intensity and the profile of normalised d_2 ($\tau = 0.125$ s) are shown as a function of distance from the moving gel edge in Fig. 5.6. In all cases, we observe that the intensity decreases towards the edge of the gel. We believe, however, that this is not caused by a decrease in local density, but rather by an asymmetry in the photon paths: while photons can reach the detector from all directions in the bulk of the sample, locations near the moving gel edge only receive photons from the right, leading to a lower photon count when $x \approx l^*$ from the sample edge. Therefore, we disregard the region of lower intensity of approximately 300 μm near the edge, and consider this $x = 0$. With these reservations, there is nevertheless a significant difference between the PS and PBA gels. While in the PS gel the apparent density is more or less homogeneous, for the PBA gel, the density is reduced in the region where the dynamic activity is higher and slightly behind it. Hence, the dynamics appear to be faster in regions of lower density. The expulsion of liquid during syneresis

inevitably increases the overall particle density. This process starts at the edge of the sample, as evidenced from the high dynamic activity during the first 20 minutes of syneresis. This increases the local density there; in the PBA gel this apparently leads to a very dense region at the front where the dynamics are slowed, probably because of the high elasticity.[32] Further compaction must occur in the region behind this dense front, where the density is lower. By contrast in the PS gel, we find a more uniform compaction and the highest/fastest dynamics are always localized at the edge as syneresis proceeds to later age.

5.2.3 Governing dynamics

To elucidate the nature of the observed dynamics, we extract the mean square displacement, $\langle \Delta r^2 \rangle$, of the particles from the LSI measurements based on contrast function, d_2. A detailed explanation is delineated in section 4.2. The multi-speckle averaged $\langle \Delta r^2(\tau) \rangle$ for selected regions at different locations in both PS and PBA gels are shown in Fig. 5.7. For both the PS and PBA gel, we select a rectangular area in the bulk, parallel to, but far from the moving gel edge, denoted as "bulk". For the PBA gel, two more locations denoted as "band" and "valley" are defined, residing at the peak of the activity band and at the spatial average region between the moving gel edge and the peak of the activity band, respectively. The rectangular areas have a dimension of 0.125×1.5 mm for the PS gel and 0.0625×3 mm for the PBA gel.

For the PS gel (Fig. 5.7 (a)), $\langle \Delta r^2(\tau) \rangle$ shows diffusive behaviour during the early ages, as evidenced from the power-law slope close to 1. As the sample ages and experiences syneresis, the slope increases to around 2 for larger τ, indicative of ballistic motion, caused by the directional motion of the compacting gel. A transition from sub-diffusive to ballistic motion is observed in the PBA gels (Fig. 5.7(b)), although the initial diffusive regime is not observed here, probably because the elastic gel forms more rapidly for the PBA gel. Also, the transition to ballistic motion occurs at an earlier age than for the PS gels as syneresis begins early for these samples. From these data, we conclude that syneresis is driven by directional particle movement at the microscopic scale.

Next, we compare $\langle \Delta r^2(\tau) \rangle$ in different locations in the PS and PBA gel in the regime where syneresis occurs and directional motion is observed. For the PS gel, at later ages during syneresis, $\langle \Delta r^2(\tau) \rangle$ decreases gradually with increasing distance to the gel moving gel edge, indicating that the particle velocity is highest near the edge and decreases towards the bulk of the sample (Fig. 5.7(c)). In the PBA gel, $\langle \Delta r^2(\tau) \rangle$ varies non-monotonically with the distance to the moving gel edge with $\langle \Delta r^2(\tau) \rangle$ at t = 21 and 26 minute in the PBA gel as seen in Fig. 5.7 (d) for

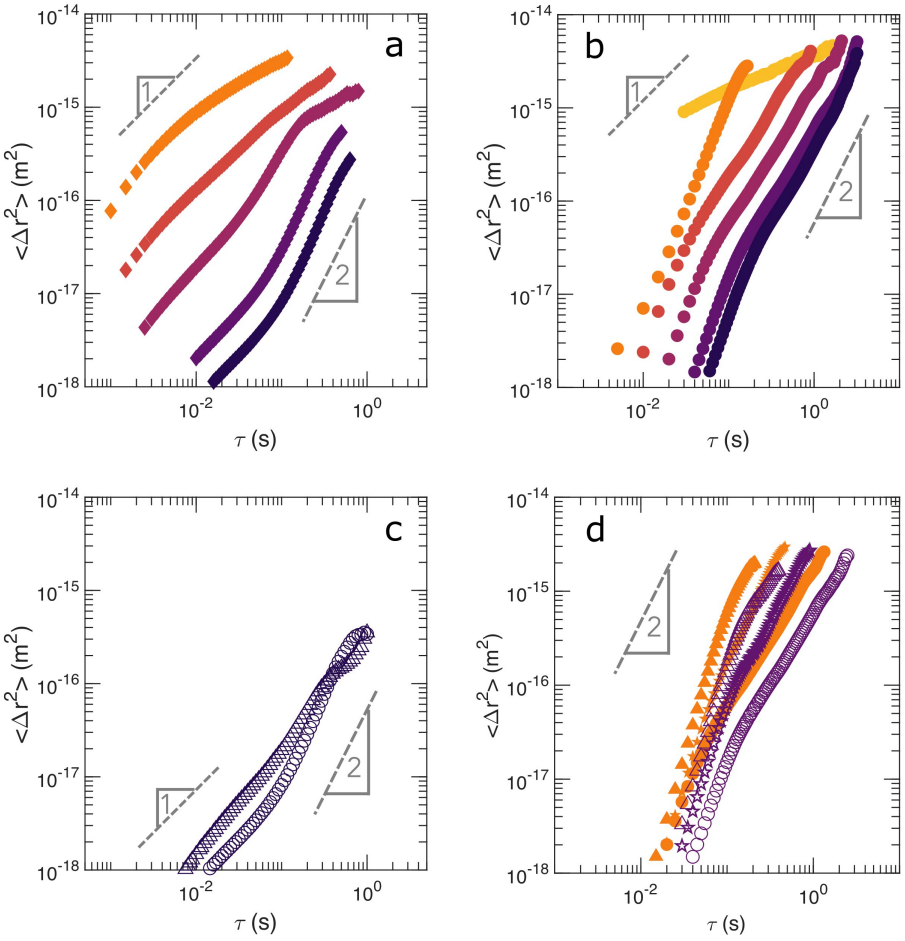

Figure 5.7. Mean square displacement ,$\langle \Delta r^2(\tau) \rangle$, of **a)** the PS gel in the bulk region during syneresis as a function of τ. Darkening symbol shade represents t = 8, 13, 20, 35 and 44 min; **b)** of the PBA gel in the bulk region, darkening symbol shade represents t = 6, 11, 16, 21, 26 and 31 min; **c)** of the PS gel at the edge (triangle) and the bulk (circle) during syneresis at t = 44 min; **d)** of the PBA gel at the activity band (triangle), valley (pentagram) and bulk (circle) during syneresis as a function of τ. Closed and open symbols represent t = 21 and 26 min, respectively.

valley, band and bulk regions. As seen in Fig. 5.5 (a), the velocity of macroscopic edge displacement during syneresis in the PBA gel is approximately 2mm/10min $\approx 3\mu m/s$. Considering purely ballistic motion for simplicity, $\langle \Delta r^2(\tau) \rangle = v^2 \times \tau^2$, for τ =0.1s yields $\langle \Delta r^2(\tau) \rangle = 10^{-13} m^2$ which is close to the same order of magnitude as $\langle \Delta r^2(\tau) \rangle$ in the band, shown in Fig. 5.7 (d). As expected from the higher volume

fraction and lower d_2, the valley region indeed has smaller $\langle \Delta r^2(\tau) \rangle$ than the band region. The smallest $\langle \Delta r^2(\tau) \rangle$ is found in the bulk region, furthest from the moving gel edge in the field of view. Lastly, we note that the slope of the $\langle \Delta r^2(\tau) \rangle$ appears to decrease for $\tau > 1$s for the PS gel and for the PBA gel within the activity band and bulk. This may relate to a non-uniformity in the directional motion during the macroscopic compaction of the gel, as we have observed using PIV measurements on exceedingly thin samples also undergoing syneresis.[25] This results in a more diffusive motion away from the edge, the band, the valley and then to bulk with the difference in $\langle \Delta r^2(\tau) \rangle$ between different regions growing larger as τ increases. This difference is a direct result of the more diffusive motion of the syneresing gel from the edge approaching the bulk; as the gel compacts towards the center of the capillary, distant regions from the moving gel edge experience less directional motion during syneresis. This is possible to elucidate only with LSI due to sample turbidity.

5.3 Conclusion

We have looked at the dynamics during syneresis in colloidal gels using a non-invasive technique, LSI. The spatially resolved d_2 maps allow distinguishing relative differences in the dynamics between different locations in the sample. In the PS gel, all dynamic processes have a similar spatial dependence and slow down gradually as a function of distance to the gel edge, while in the PBA gel, a pronounced activity band emerges a few hundred microns behind the gel edge. Moreover, the PBA gel exhibits spatial heterogeneity in volume fraction during syneresis; a dense region between the gel edge and the activity band is followed by a lower density zone around the activity band location. The PS gel, by contrast, shows a more uniform density. This difference between the two types of gels may be attributed to the different particle nature, i.e. solid or liquid.

Colloidal gels comprising of liquid particles consist of strands that can bend easily and bear stress mostly by stretching particle bonds. By contrast, solid particle gels exhibit surface asperities and a lack of surface mobility, resulting in stress being born by bending of gel strands.[25] We propose that this difference manifests in the spatial dependence of the dynamics during syneresis, as schematically illustrated in Fig. 5.8. Because the elastic resistance to compaction is lower for liquid particle (PBA) gels, these gels experience fast compaction locally near the gel edge, resulting in a dense region. After a while, compaction in this region slows down as a consequence of the elastic stresses, and further syneresis proceeds in the region behind the dense zone, visible as an activity band of enhanced dynamics. By contrast, solid (PS) gels resist stress to a higher extent, arriving at a compaction

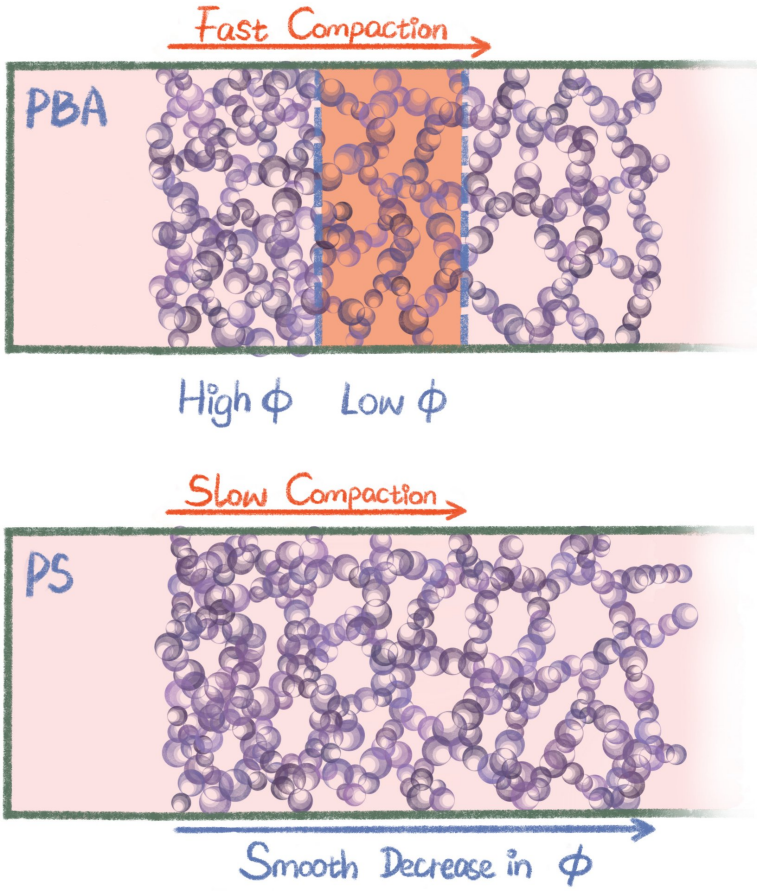

Figure 5.8. Schematic illustration of a proposed scenario for the PBA and the PS gel during syneresis.

that happens more slowly. Possibly this allows for rearrangement of the material over longer length scales, so that the compaction occurs gradually throughout the sample. These differences may explain why syneresis is most readily observed in colloidal gels composed of liquid droplets, like yoghurt and cheese, and less for solid particles like paints and coatings. However, even in solid particle based colloidal gels, syneresis may still be appreciable as shown in these PS gels.

5.4 Materials & Methods

5.4.1 Sample preparation

Poly(N-isopropylacrylamide)(pNIPAM) surfactant is synthesized according to a published method.[27] Polystyrene (PS) particles of 275 nm radius are synthesized using dispersion polymerisation of styrene (Sigma) at 80°C for 2 hours using AIBN (Sigma) as a radical initiator.[33] The dispersion is filtered and washed by centrifugation (3x) into 0.1 wt% pNIPAM surfactant and 100 mM NaCl solution to a final ϕ=0.2. The recipe for the synthesis of polybutylacrylate (PBA) droplets by UV initiated emulsion polymerization is as follows: a disperse phase, comprising of butyl acrylate with 0.3wt% 2,2-Dimethoxy-2-phenylacetophenone as initiator, and the continuous phase, comprising of 3 mM NaCl and 1 wt% pNIPAM, are mixed with a ratio 1/4 (v/v%). The mixture is vortexed and then bath-sonicated at 10 °C for 25 min. After bubbling with N_2 for 10 min in a sealed vial, the mixture is exposed to UV light for 10 min while gently mixing at 10 °C. The mixture is left overnight for complete polymerization at room temperature. PBA has a low glass transition temperature (T_g) and thus exists as liquid at room temperature. The particles have an average radius, $\langle r \rangle$=275 nm, as determined by dynamic light scattering. PBA droplets are filtrated and dialyzed against 0.1 wt% pNIPAM surfactant and 100 mM NaCl solution to a final ϕ=0.2 approximately.

PEM coating is prepared according to the following procedure according to[34]: solutions of 1 wt% cationic polymer, polydiallyldimethylammonium chloride (M_w = 4×10^5 - 5×10^5 g/mol, Sigma), in 1M NaCl and 1wt% anionic polymer, sodium polystyrene sulfonate ($M_w \sim 2 \times 10^5$ g/mol, Sigma) in 1M NaCl are prepared. The solutions are filtered with 0.45 μm hydrophilic filter. To begin the process, the glass container is cleaned using a plasma cleaner. This makes the glass anionic, negatively charged. Cationic polymer solution is first added to the container and then rinsed away with sufficient amount of deionized water by filling the container completely many times and then leaving it empty after 5 minutes. Cationic and anionic layers are added alternatively for 3 layers each with thorough rinsing in between. This PEM coating prevents adhesion of the colloidal gel to the wall.

Dispersions of PS particles, ϕ = 0.01, and PBA droplets, ϕ = 0.02, are injected into PEM coated rectangular cross-section capillarys (Rectangle Boro Tubing, 0.9 × 9.0 mm). At both ends of the capillary a hydrophobic paste (Krytox GPL205) is applied to prevent adhesion to the epoxy gel (Devcon) for capillary closure. During the LSI measurement, samples are situated in a thermostatic chamber at 32°C.

5.4.2 Laser speckle imaging and analysis

The set-up of LSI is illustrated schematically in Fig. 5.1 with further technical details of the set-up are discussed elsewhere.[16] Briefly, coherent light (λ= 532 nm, Cobolt Samba, 1W) is expanded to a diameter of 1cm by a Galilean beam expander and illuminates the sample being directed downward onto the sample via two mirrors, at a small angle with respect to the detection path to avoid intensity enhancement by coherent backscattering. The backscattered light is reflected by a mirror onto a linear polariser perpendicular to the polarisation of the incident laser beam and collected by a Qioptiq zoom lens, 1.8× and the depth-of-focus is 0.1mm, and focused through an iris diaphragm with the speckle size tuned by the diaphragm to be slightly larger than the pixel size, typically 2–3 pixels. The back-scattered light is then captured by one of two cameras discussed below. The samples are situated on a platform which is connected to a computer-controlled balance (Sartorius, model WZA224-NC), logging the sample mass with 0.1 mg resolution and 1 Hz frequency to confirm that sample evaporation does not occur. A climate chamber is applied to the set-up, which controls the ambient temperature of the sample, as well as minimizes air convection and stray light.

The laser power, exposure time and frame rate are important for capturing the right information. To prevent blurring of the speckles and to capture fast changing speckles, the exposure time is set as short as possible where it could still cover the full dynamic range of the camera. This minimizes over- and under-exposure hence data loss. Two different cameras are used: (i) Dalsa Genie camera (Stemmer Imaging) for the PBA colloidal gel and yoghurt at 200 fps and 100 fps, respectively. (ii) HiSpec 1 camera (Fastec Imaging) for the PS colloidal gel at 2000 fps. The field of view is 640×480 pixels (4×3 mm) with Dalsa Genie camera and 640×240 (8×1.5 mm).

The contrast function, d_2 (Eq.5.2) is calculated to resolve dynamics during syneresis, which vary significantly in both time and space. Symmetric normalization, i.e. the denominator with the product of mean intensities at times t and $t + \tau$ is used instead of the square of the mean intensity, which diminishes intensity drift-induced artefacts.[16]

$$d_2(t, x, y, \tau) = \frac{\langle [I(t, x, y) - I(t + \tau, x, y)]^2 \rangle}{\langle I(t, x, y) \rangle \langle I(t + \tau, x, y) \rangle} \tag{5.2}$$

Note that fast macroscopic movement of the syneresing colloidal gels, and the thin edge, is prone to induce too low intensity in the speckle images at the moving gel edge, resulting in high d_2 noise artefacts. All calculations and analysis in this

chapter are carried out on speckle images where a small integer value, ΔI =5, is added to all pixels based on d_2 noise check and elaborated in section 5.A.2.

To achieve calculation of $\langle \Delta r^2(\tau) \rangle$, d_2 is first converted into the electric field correlation function, g_1, according to $g_1(\tau) = \sqrt{1 - d_2(\tau)/2\beta}$. This is based on the Siegert relation that, $g_1(\tau) = \sqrt{[g_2(\tau) - 1]/\beta}$ and the fact that $d_2(\tau) \approx 2[g_2(\tau = 0) - g_2(\tau)]$.[30] β is the spatial coherence factor, accounting for the number of speckles detected. In the ideal case, when fluctuations of only a single speckle are detected in each pixel, β equals 1.[31] Due to the limitations in camera-based detection, $\beta < 1$. Here β is determined such that $g_2(\tau)$ - 1 $\rightarrow \beta$ for $\tau \rightarrow 0$. The mean square displacement, $\langle \Delta r^2(t, \tau) \rangle$, can then be extracted based on:

$$g_1(\tau) = \exp[-\gamma k_0 \sqrt{\langle \Delta r^2(\tau) \rangle}] \tag{5.3}$$

where $k_0 = 2\pi n/\lambda$ is the wave vector, with n, being the refractive index of water, λ, being the wavelength of the impinging coherent light and γ is a numerical prefactor that is obtained from literature to be 1.5.[15,16,35]

5.A Appendix

5.A.1 movies

PS movie: d_2 maps of PS gel during syneresis, τ=0.125 s, colormap inferno. Left end of d_2 maps represents the capillary wall. 2fps

PBA movie: d_2 maps of PBA gel during syneresis, τ=0.125 s, colormap inferno. Left end of d_2 maps represents the capillary wall. 2fps

Both movies can be viewed from this link or the QR-code in figure 5.A.1.

Figure 5.A.1. QR code to the LSI movies of the PS and PBA syneresis.

5.A.2 Noise artefacts check at the gel edge

Fast macroscopic movement of the syneresing colloidal gels is prone to induce too low intensity in the speckle images at the moving gel edge, resulting in high d_2 noise artefacts. To check for this possible effect, a series of images with ΔI = 1, 2, 5 and 8 added to the speckle images for the PBA gel are shown in Fig. 5.A.2. Intensity fluctuations in properly illuminated areas are conserved but the fluctuations in poorly illuminated areas are less overestimated.

With increasing ΔI, the high d_2 stripe, indicating high mobility, at the sample moving edge vanishes and a stripe with low mobility, low d_2 developed indicating that the high d_2 is indeed related to noise artifacts. This may be related to incomplete randomization of photons in this area due to the fast macroscopic movement and the resulting thin edge. Therefore, all calculations and analysis in this chapter are carried out on speckle images with ΔI =5.

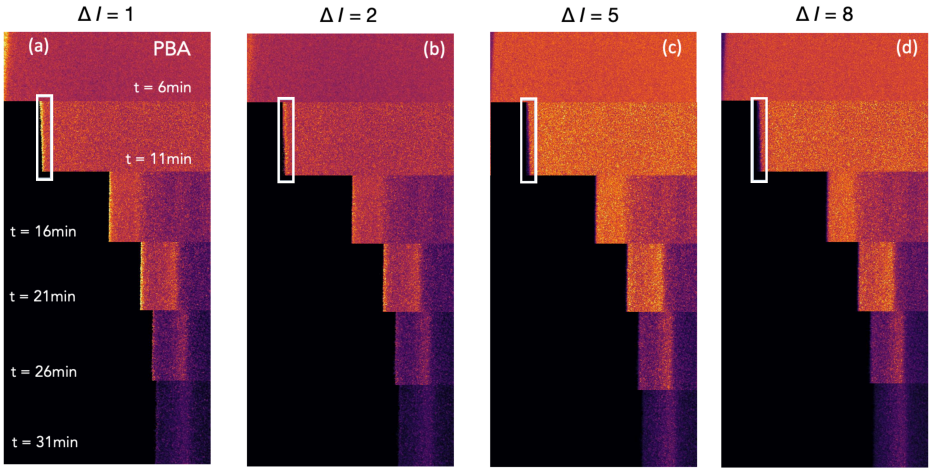

Figure 5.A.2. Time-lapse d_2 maps of PBA gel, τ=0.125 s, calculated from ΔI = 1, 2, 5 and 8 to the speckle images, colormap inferno. Left end of d_2 maps represents the capillary wall. Region of interest with low intensity at the moving edge of the gels is marked with white rectangles for t = 11 min.

References

[1] H. Verduin, J. K. Dhont. *Journal of colloid and interface science* **172**, 425–437 (1995).

[2] M. Grant, W. Russel. *Physical Review E* **47**, 2606 (1993).

[3] E. Dickinson, *Food polymers, gels and colloids*, no. 82 (Elsevier, 1991).

[4] J. Kreuter, *Colloidal drug delivery systems*, vol. 66 (CRC Press, 2014).

[5] L. Cipelletti, S. Manley, R. Ball, D. Weitz. *Physical review letters* **84**, 2275 (2000).

[6] H. Tsurusawa, M. Leocmach, J. Russo, H. Tanaka. *Science advances* **5**, eaav6090 (2019).

[7] H. van Dijk, P. Walstra. *Netherlands Milk and Dairy Journal* **40** (1986).

[8] G. W. Scherer. *Journal of Non-Crystalline Solids* **108**, 18–27 (1989).

[9] R. R. Panthi, A. L. Kelly, D. J. O'Callaghan, J. J. Sheehan. *Trends in Food Science & Technology* (2019).

[10] P. Walstra, H. Van Dijk, T. Geurts. *Netherlands Milk and Dairy Journal* **39**, 209–246 (1985).

[11] S. Roefs, T. v. Vliet, H. Van den Bijgaart, A. de Groot-Mostert, P. Walstra, *et al.*. *Netherlands Milk and Dairy Journal* **44**, 159–188 (1990).

[12] H. van den Bijgaart, P. Walstra, *MILK the vital force* (Springer, 1986), pp. 89–89.

[13] T. Van Vliet, P. Walstra, *Water in Foods* (Elsevier, 1994), pp. 75–88.

[14] T. van Vliet, H. J. M. van Dijk, P. Zoon, P. Walstra. *Colloid & Polymer Science* **269**, 620–627 (1991).

[15] D. Pine, D. Weitz, J. Zhu, E. Herbolzheimer. *Journal de Physique* **51**, 2101–2127 (1990).

[16] H. M. Van Der Kooij, R. Fokkink, J. Van Der Gucht, J. Sprakel. *Scientific reports* **6**, 34383 (2016).

[17] C. Zhou, G. Yu, D. Furuya, J. H. Greenberg, A. G. Yodh, T. Durduran. *Optics express* **14**, 1125–1144 (2006).

[18] M. Draijer, E. Hondebrink, T. van Leeuwen, W. Steenbergen. *Lasers in medical science* **24**, 639 (2009).

[19] D. Briers, D. D. Duncan, E. R. Hirst, S. J. Kirkpat-rick, M. Larsson, W. Steenbergen, T. Stromberg, O. B. Thompson. *Journal of biomedical optics* **18**, 066018 (2013).

[20] A. Nadort, K. Kalkman, T. G. Van Leeuwen, D. J. Faber. *Scientific reports* **6**, 25258 (2016).

[21] H. M. van der Kooij, A. Susa, S. J. García, S. van der Zwaag, J. Sprakel. *Advanced materials* **29**, 1701017 (2017).

[22] H. M. van der Kooij, S. Dussi, G. T. van de Kerkhof, R. A. Frijns, J. van der Gucht, J. Sprakel. *Science advances* **4**, eaar1926 (2018).

[23] R. Paschotta, *et al.*, *Encyclopedia of laser physics and technology*, vol. 1 (Wiley Online Library, 2008).

[24] P. Faccia, O. Pardini, J. Amalvy, N. Cap, E. Grumel, R. Arizaga, M. Trivi. *Progress in Organic Coatings* **64**, 350–355 (2009).

[25] Q. Wu, J. van der Gucht, T. Kodger. *Physical Review Letters* **125**, 208004 (2020).

[26] A. R. Thiam, N. Bremond, J. Bibette. *Langmuir* **28**, 6291–6298 (2012).

[27] T. E. Kodger, J. Sprakel. *Advanced Functional Materials* **23**, 475–482 (2013).

[28] P. Zakharov, F. Scheffold, *Light Scattering Reviews 4* (Springer, 2009), pp. 433–467.

[29] P. Zakharov, F. Scheffold. *Soft Materials* **8**, 102–113 (2010).

[30] K. Schätzel. *Applied Physics B* **42**, 193–213 (1987).

[31] P. Zakharov, F. Scheffold. *Advances in dynamic light scattering, Springer-Praxis Publishing Ltd., Chichester, UK* (2009).

[32] V. Prasad, V. Trappe, A. D. Dinsmore, P. N. Segre, L. Cipelletti, D. A. Weitz. *Faraday Discussions* **123**, 1–12 (2003).

[33] F. Zhang, L. Cao, W. Yang. *Macromolecular Chemistry and Physics* **211**, 744–751 (2010).

[34] T. W. Graul, J. B. Schlenoff. *Analytical Chemistry* **71**, 4007–4013 (1999).

[35] D. Bicout, G. Maret. *Physica A: Statistical Mechanics and its Applications* **210**, 87–112 (1994).

Chapter 6

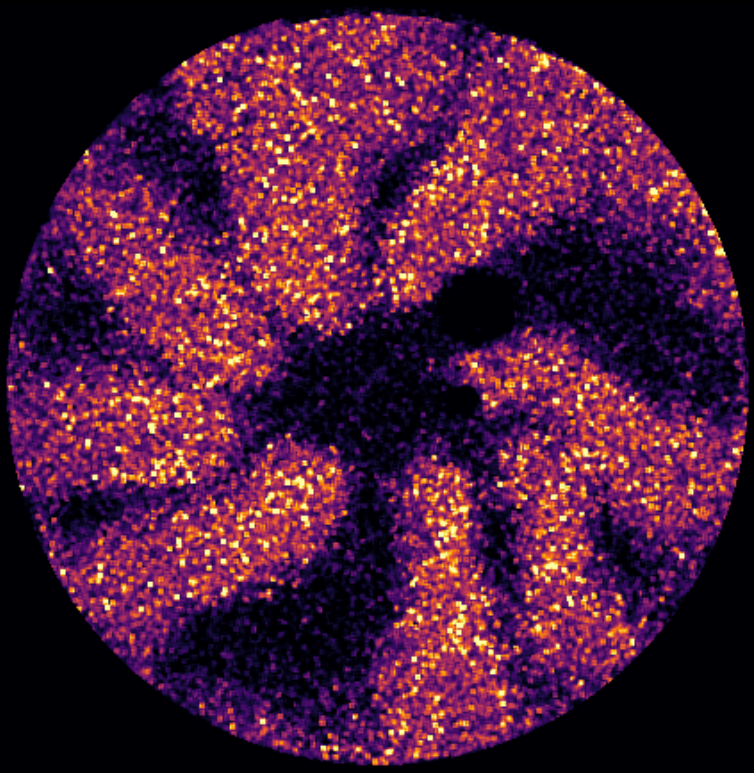

Laser speckle imaging for sensitive and full-frame wall-stress imaging in rheology

Rheological properties of complex fluids are often governed by localized events such as cooperative motions, shear banding or wall slip. Current methods to perform rheological imaging either lack the resolution to resolve individual events or rely on optical imaging which requires transparent samples thereby precluding the study of many industrially-relevant materials. We show how laser speckle imaging can be used to measure the local flow behavior with a high sensitivity over the full field of view. We quantitatively visualize localized areas with jamming in a concentrated corn starch suspension under oscillatory deformation in a double plate geometry. The approach is not limited to the rheological constraints of this test type and geometry. With a constant shear stress tests we capture intermittent jamming and un-jamming events in the same concentrated corn starch suspension.

This chapter is in preparation as manuscript as: Buijs, J., Majhi, A., Dijksman, J. & Gucht, J van der, 'Laser speckle imaging for sensitive and full-frame wall-stress imaging in rheology'

6.1 Introduction

Complex fluids, such as concentrated emulsions and suspensions, are characterized by their non-Newtonian rheological behaviour which can be shear thinning or shear thickening.[1,2] The rheometer is an excellent tool to measure these bulk-material properties and characterize the global rheology. As it measures the average strain and stress on the material, it is not suited to characterize the localized events like cooperative motion,[3,4] shear banding[5] or wall slip[6,7] that underlie this non-Newtonian rheology. To fully understand the global rheology of complex fluids, we also need to understand the local rheology and link it to the global properties. Therefore methods are required that measure local strain or stress with high spatial and temporal resolution. In this chapter we will study the discontinuous shear thickening regime of concentrated corn starch emulsions, where it is known that there are huge variations in the local rheology in space and time,[8–11] and we will develop a method that can link those variations to the bulk behaviour.

Current methods to resolve the local rheology have to balance the size of the field of view (fov) with the sensitivity. Nowadays, it is possible to study the whole sample at once with a full fov camera, but not at a high enough resolution to capture variations in local rheology. It is also possible to very precisely study the local phenomena at a high resolution, for example with traction force microscopy,[12] ultrasonic imaging[11] or particle image velocimetry (piv) analysis,[13,14] but so far it is not possible to do this for the whole sample at once. Upcoming methods such as rheo-MRI can capture subtle differences over the full sample, but here the time resolution is insufficient to capture short events and the data is averaged over several seconds or minutes.[15,16] The rheo-mri instrument is also quite expensive and complex, which decreases the accessibility of the technique. Another approach employed a normal force sensor array with a high temporal resolution, but only a $4.5x4.5mm^2$ spatial resolution. Even with this low spatial resolution it was shown that there are spatial variations in normal force that can not be measured with just a rheometer, as they get averaged out by the rheometer plate.[17] If it becomes possible to measure local flow behaviour with a large fov and high spatial- and time-resolution, it will allow us to link localized events to the global properties of a material.

To solve this conflict between resolution and fov, we propose to use a light scattering technique called Laser Speckle Imaging (LSI). LSI was developed as a medical imaging technique that obtains contrast from the motion inside opaque materials and is essentially the imaging variant of Diffusing Wave Spectroscopy (DWS).[18,19] LSI and DWS make use of the interference pattern that emerges when a coherent laser illuminates an opaque material, and by quantifying the changes

in the interference it can detect displacements as small as a few nanometers. This extremely high sensitivity comes at the cost of not being able to detect the motion of separate particles, but only collective dynamical processes. But LSI can do so, spatially resolved at resolutions of $10 - 100\mu m$ and with a large fov at frame-rates of up to kHz.[20,21] With its high displacement resolution and large fov we think LSI can become an excellent tool to resolve local rheology.

To make LSI ready to be used for local rheology imaging, we use an approach and geometry that is similar to the one used by Rathee et al.[22] They replaced the fixed rheometer bottom plate by a glass slide coated with an elastomer with sparse fluorescent microspheres. By tracking the position of those microspheres with a miscroscope the deformation of the elastic layer can be tracked, which is a measure for the local wall stress. In the case of a concentrated corn starch dispersion, above a certain applied shear rate jamming occurs.[9,10] The jamming will increase the wall stress which is measured with the microscope. This is a sensitive wall stress measurement, but the fov of the microscope is so small that only a fraction of the whole sample is measured. By replacing the microscope with a large fov camera and switching the elastomer deformation detection to LSI, we are able to asses the whole sample without compromising sensitivity.

In this chapter we will show the approach how to combine rheology and LSI to image wall stress with high sensitivity and a large field of view. First we will calibrate our signal with a known deformation by shearing the elastic slab directly with the rheometer probe and we will compare this signal to a theoretical model that we developed. With this calibrated elastic slab, we will compare the deformation as a result of rheological experiments with a high viscosity silicon oil, water and a concentrated corn starch dispersion between the elastomer and rheometer probe. After we have characterized the quantitative response of our setup, we will image wall stress heterogeneities in a corn starch suspension around the discontinuous shear thickening regime. We will explore two imaging configurations, one uses an oscillating rheology probe and the other applies a constant shear stress. The oscillatory approach is quantitative while the constant shear stress approach is qualitative, but seems to be more sensitive for changes in wall stress.

6.2 Methods & calibration

We will image the wall stresses in the rheometer by measuring the deformation of a soft elastic slab (modulus 16 kPa) of which the preparation is described in section 6.A.1. The elastomer slab contains enough Titania particles to make it opaque, so that the laser light undergoes multiple-scattering, which is a requirement for LSI to detect deformation. We will start by calibrating the LSI signal by measuring

the elastomer with a known deformation. To ensure good adhesion, the elastomer is cured directly between the rheometer's bottom glass plate and top plate probe (fig. 6.1a). The elastomer is measured with LSI through the glass bottom plate (fig. 6.1c). The top plate applies an F =5 Hz oscillatory deformation with a mean amplitude γ_0 as a fraction of the gap size. γ_0 is increased logarithmically every 60 seconds, and speckle images are collected at 100 frames per second. From these speckle images, correlation maps are calculated according to the workflow described in section 6.A.2.

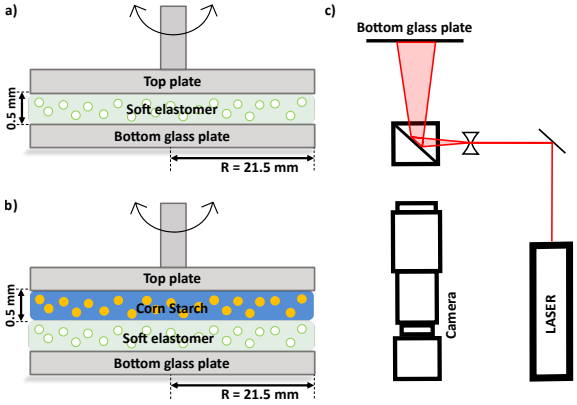

Figure 6.1. a) Rheology geometry for the calibration measurement. The elastomer is cured between the top and bottom plate to ensure good adhesion. The bottom glass plate is fixed. The top plate is controlled by the rheometer to apply an oscillation. **b)** Rheology geometry for the sample measurements. The elastomer is cured with a mold on the bottom glass plate and the bottom glass plate is fixed into the rheometer after curing. Then the sample is applied, the gap size set and the top plate is controlled by the rheometer to apply an oscillation. For the silicon oil and water measurements the gap size is set to 0.10mm, for corn starch 0.50mm. **c)** LSI setup which is fixed below the rheometer and images the elastomer through the glass bottom plate. The laser light is expanded and projected through a polarizing beamsplitter onto the bottom glass plate. Light scatters through the elastic slab and a part of it is scattered back to the polarizing beamsplitter which also acts as a cross-polarizer to filter out reflections and light that has scattered only a few times. The camera collects the resulting speckle patterns which then are analyzed to obtain the deformation map of the elastomer slab.

For the plate-plate geometry, the deformation is not constant along the radius: the material at the edge of the probe is deformed more than the material closer to the center. Therefore the LSI data is collected for a rectangular area that that covers both the center R_0 and the edge R_{max}. The data from this area is split up into radial bins with increasing radius R/R_{max}. For each bin the correlation function is calculated which exhibits the periodic behaviour that was imposed by the rheometer (symbols in fig 6.2a). $g_2 - 1 = 1$ at $\tau = 0, 1/F, 2/F, ...$ which shows

that the slab relaxes back to its original position after a full oscillation. g_2 has a minimum at $\tau = 0.5/F, 1.5/F, 2.5/F, ...$ This minimum decreases with increasing R/R_{max} showing that the decorrelation increases with the local deformation. This is further confirmed with an amplitude sweep where we plot the minimum g_2 value against the (radial corrected) strain amplitude $\gamma_R = \gamma_0 * R/R_{max}$ (symbols in fig. 6.2b). For all bins the g_2 decreases for increasing γ_R and the amplitude corrected curves overlap to form a master curve.

The shape of the correlation function of a material under oscillatory deformation has previously been described for DWS experiments[23,24] as:

$$g_1(t, t_0) = \int_0^\infty P(s) e^{-x(t,t_0) s l^*} ds \tag{6.1}$$

with $P(s)$ the optical path length distribution, l^* the transport mean free path of the photons and $x(t, t_0)$ a function that depends on the motion of the light-scattering particles:

$$x(t, t_0) = \frac{1}{15}[k_0 l^* |\gamma(t + t_0) - \gamma(t_0)|]^2 \tag{6.2}$$

with $k_0 = 2\pi n/\lambda$ the wavevector, n the refractive index of the elastomer, λ the laser wavelength, the oscillatory deformation $\gamma(t) = \gamma_0 sin(\omega_0 t)$, γ_0 the strain amplitude and ω_0 the frequency in $rads^{-1}$. To find the measured intensity correlation function, we use the Siegert relation and average over all initial values t_0 during one oscillation period:

$$g_2 - 1 = \frac{\omega_0}{2\pi} \beta \int_0^{2\pi/\omega_0} |g_1[x(t, t_0)]|^2 dt_0 \tag{6.3}$$

where β is an experimental stretching parameter that can be determined by measuring $g_2(\tau = 0) - 1$. We solved this integral analytically which gives:

$$g_2 - 1 = \beta[I_0(y) - L_0(y)] \tag{6.4}$$

with I_0 and L_0 modified Bessel and Struve functions. y is given by

$$y = k|sin(\omega_0 * \tau/2)| \tag{6.5}$$

with the prefactor k described by

$$k = 4 k_0 l^* \gamma_R / \sqrt{5} \tag{6.6}$$

We fit the experimental data in figure 6.2 with equation 6.4 and use k as a fitting parameter as it is difficult to determine l^* experimentally. The model describes

the experimental data very well and therefore the measured g_2 is a quantitative measure for the elastomer slab deformation, which is linearly related to the wall stress. This allows us to take the next step and measure the wall stress as a result of the oscillation of a sample of interest between the elastic slab and the top probe (fig. 6.1b). Depending on the visco-elastic properties of the sample of interest, part of the oscillation will be transferred to the slab. We can now quantify this wall stress by measuring the deformation of the elastic slab. We can even quantify this locally by measuring the elastomer deformation for every pixel in the LSI image.

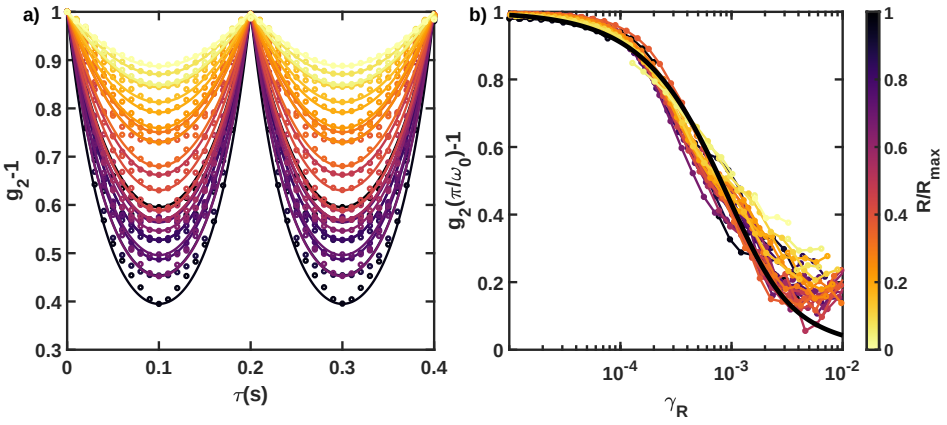

Figure 6.2. a) The symbols show the experimental g_2 for different radial positions in the gap R/R_{max}, which are fitted with the theoretical model (eq. 6.4). Each correlation function shows a minimum after half a 5Hz oscillation and returns back to 1 for a full oscillation. With increasing R/R_{max} the minimum lowers. **b)** The g_2 value of the minimum decreases when the amplitude of the oscillation is increased. If we plot this for each R/R_{max} and correct for the difference in effective amplitude, they form a master curve which corresponds to the analytical expression: the black solid line is the fit of eq. 6.4, evaluated at the minimum and averaged over all radial positions. This master curve can be used as a calibration curve to relate the measured g_2 to an effective deformation, which is directly related to the wall stress.

6.3 Results & discussion

Before we start imaging wall stresses, we first quantitatively compare the averaged measured wall stress of several samples. We compare high viscosity silicon oil (Gelest DMS- T51, 97.7 Pa s), water and a 41 wt% density-matched corn starch suspension (fig. 6.1b) with the elastomer calibration (fig. 6.1a) and use the elastomer calibration shown in Fig. 6.2b to obtain the elastomer deformation

at different radial positions in the gap. For silicon oil and water we use a thin 0.10mm sample thickness between the elastic slab and the rheometer probe to maximize the wall stress. For cornstarch we increase the thickness to 0.50mm to reduce wall effects since the particle diameter is roughly $20\mu m$ which would be significant for a $100\mu m$ gap size. The resulting LSI data is plotted in figure 6.3a, as a function of the local strain amplitude γ_R. Notice that the amplitude is based on the combined thickness of the elastic slab and sample since they will both deform, but not equally. This means that if we would not measure any wall stress the deformation of the slab is negligible and the actual deformation of the sample would be 2x (for cornstarch) or 6x (for silicon oil and water) the specified value.

To relate the measured correlation values to the deformation of the elastomer slab we calculate γ_{eff}, the true deformation of the elastic slab using the calibration measurement as a trend-line. By dividing the measured γ_{eff} by the imposed γ_R, we calculate which fraction of the applied wall stress is transferred from the rheometer to the elastomer slab. For a Newtonian fluid this fraction should be independent of γ_R as the viscosity does not change under changing shear rate. But for a non-Newtonian fluid this fraction should increase with shear-thickening and decrease with shear-thinning. The results of this comparison are shown in figure 6.3b. The rheology result for each amplitude sweep is shown in figure 6.3c, which we can only quantitatively compare to the LSI images in figure 6.3d as they both use γ_0 in stead of γ_R.

With a liquid on top the elastic slab will deform in the same manner as when in direct contact with the rheometer probe, but with reduced amplitude and with a different phase. This reduced amplitude γ_{eff} can be predicted from a simple model based on a force balance between the elastomer slab and the fluid layer which are modeled as an elastic spring and a viscous dashpot in series:

$$|\gamma_{eff}| = \frac{\gamma_R \eta \omega_0 (1-x)}{\sqrt{(Gx)^2 + ((1-x)\eta\omega_0)^2}} \tag{6.7}$$

with η the viscosity of the liquid, G the shear modulus of the elastomer slab and x the fraction of the gap filled with fluid (where the rest of the gap is filled with the elastomer). From this model we learn that for the elastomer, the amplitude of the oscillation should increase with increasing γ_R, η and ω_0, and decrease with increasing G. For a Newtonian fluid, η is constant with increasing γ_R and thus γ_{eff} is directly proportional to γ_R. The concentrated cornstarch emulsion is shear-thickening which should give rise to a sharp increase of γ_{eff} around the jamming point.

The silicon oil g_2 curve has the same shape as the calibration curve, and the deformation ratio γ_{eff}/γ_R in figure 6.3b is roughly 0.2. Thus, roughly 20% of

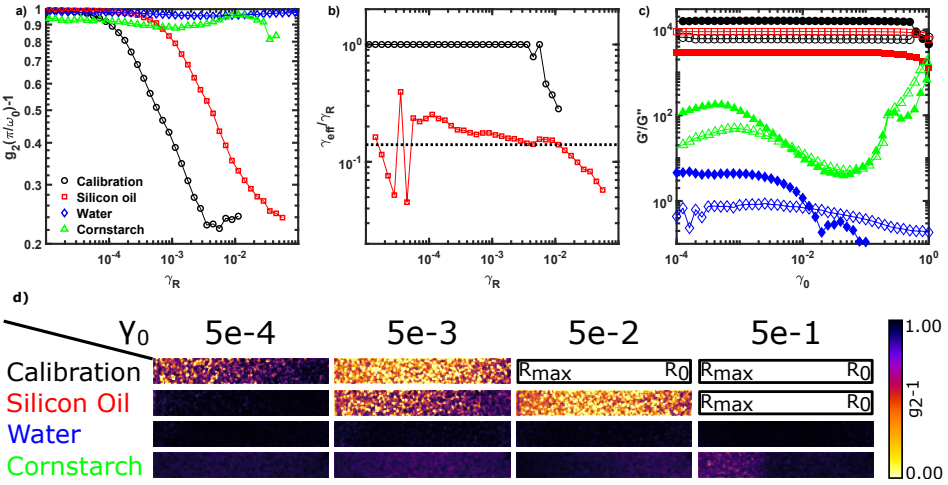

Figure 6.3. a) LSI results of the amplitude sweeps. The silicon oil measurement follows the same trend as the calibration curve, but a higher amplitude is needed for the same slab deformation. Water shows no significant deformation of the elastomer, while the corn starch suspension starts to show slab deformation at high amplitudes. **b)** Relative deformation of the slab as a fraction of the imposed deformation by the rheometer. For the calibration this is 1.0 for most of the probed amplitudes. Deviations are the result of the calibration curve having sections with a positive slope. For the silicon oil measurement the deformation ratio is between 0.1 and 0.2 for most of the sweep range. The black dotted line is the model prediction of 0.14 for this silicon oil. The water and cornstarch measurements are not shown as γ_{eff} cannot be accurately calculated since $g_2 - 1$ is almost 1.0 for the whole amplitude sweep. **c)** Rheology results of the amplitude sweeps, with filled symbols for the storage modulus G' and empty symbols for the loss modulus G". These results are not directly relatable to a and b since γ_0 is an amplitude averaged over the whole sample, while γ_R is localized per spatial bin, and thus contains data from multiple γ_0 values. The elastomer slab and silicon oil both show Newtonian rheology with a constant G'/G" where for the slab the G' is higher than the G" and for silicon the G" is higher than the G'. The water measurement does not show a clear trend which can be attributed to the difficulty of measuring such a low viscosity. The corn starch suspension shows shear-thinning at intermediate amplitudes and shear-thickening at larger amplitudes. **d)** LSI images which can be directly related to the rheology experiment in c since each image is a snapshot at a constant γ_0. However, the effective amplitude is different over the field of view as R_{max} is on the left edge of each image and R_0 is at the right edge. For the calibration and silicon oil measurements we observe a gradual decrease in elastomer slab deformation from R_{max} to R_0 and an overall increase in elastomer slab deformation for increased γ_0. For the highest amplitudes it was not possible to obtain reliable LSI data as the β would increase due to speckle blurring. For water we see no elastomer slab deformation at all amplitudes. For the corn starch suspension the most notable observation is at $\gamma_0 = 5e^{-1}$: There is a sharp decrease in elastomer slab deformation from R_{max} to R_0.

the movement of the rheometer probe is transferred to the elastic slab through the layer of silicon oil. This corresponds very well with the deformation ratio of 0.14 that is predicted by equation 6.7 by filling in the experimental parameters. We use water as a control experiment as it is also a Newtonian fluid, but with a much lower viscosity. This results in no significant wall stress and indeed we measure a g_2 curve which stays around 1.0. The slight dip is most probably a vibration in the setup that is measured as a collective motion over the whole fov. For the corn starch suspension we would expect a g_2 curve with a shape that diverges from the calibration curve. Around the jamming point, the measured deformation should suddenly increase with increasing amplitude. Although we see a decrease in g_2 at amplitudes from $0.01 - 0.1$, we can not conclude that the shape is significantly different from the calibration data. However, if we look at the images we see a sharp transition between a high wall stress region close to R_{max} and a low wall stress region for the rest of the sample. This transition is much sharper than for the calibration and silicon oil measurements, so it most probably is the jamming front as it is also visible at a γ_0 where we observe shear-thickening in the rheology results. Most probably the shear thickening is not visible in the LSI sweep data because the β suddenly decreases in the jamming region as a result of speckle blurring, and therefore this data is discarded according to the data analysis workflow described in section 6.A.2.

To visualise the heterogeneities in the wall stress as a result of the corn-starch jamming, we continue with full-field wall stress imaging. The experimental workflow and sample preparation is the same as for the amplitude sweep, but instead of increasing the amplitude step-wise, only one amplitude is imposed for 60 seconds. This experiment is repeated for a range of amplitudes and the movies can be found in appendix 6.A.3. By averaging the frames of each movie we obtain the images in figure 6.4.

The spatial variation in wall stress around the jamming point is immediately visible from the images. We observe a high wall stress edge and a low wall stress center with a very sharp transition in between. At the edge the effective amplitude is higher which results in jamming at lower γ_0 than in the center. With increasing γ_0 the jammed region moves inward and the non-jammed center shrinks. In the time-averaged images both regions look homogeneous, but from the movies it becomes clear that this is not true. Especially on the boundary between the two regions, which has an effective amplitude that equals the strain at the jamming point, we observe intermittent areas with increased wall stress that move along the boundary circle. For the 80 and 90% amplitudes a periodic pattern perpendicular to the shearing direction is visible. Before we can determine the nature of this pattern, a deeper investigation is required into what is the origin of the shape and

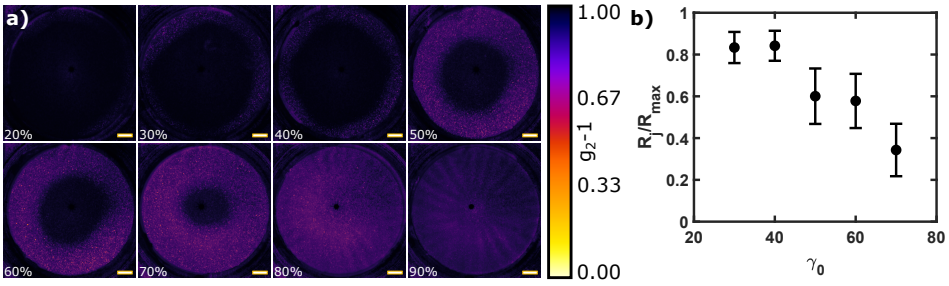

Figure 6.4. a) Time-averaged LSI images showing the wall stress as a result of oscillating a corn starch suspension for 60 seconds at 5Hz with the amplitude specified in the top-left corner. With increasing amplitude, the purple high wall stress area starts appearing at the edge and expands inward. The scale bar is 5.0mm wide and 1.0mm high. Movies of the 60 second measurements, where much more small-scale heterogeneities and changes in time are visible, are available from appendix 6.A.3. **b)** The radial location of the jamming front moves inward with increasing amplitude. R_j was obtained by fitting a sigmoidal function to the radial intensity profile of the images from panel a and extracting the characteristic decay location. The slope of the decay is used as error bar. For 20, 80 and 90% a positive slope was found, instead of the expected negative decay from R_{max} to R_0, so these results were discarded. However, from the images in a it is clear that they qualitatively fall in the decreasing trend where the R_j/R_{max} for the 20% amplitude is close to 1.0 and for 80 and 90% close to 0.0. The fits are shown in section 6.A.4.

locations of the structure. If the pattern is hugely influenced by the frequency of the oscillation, we hypothesize that it originates from a standing wave of particle densities.[25] If it is more influenced by the sample thickness, it might be more closely related to shear banding.[26,27]

To more closely study the inhomogeneous jamming phenomenon, we adjust the approach slightly by using a constant shear stress profile in stead of an oscillation. This will result in a constant wall stress if the sample also has constant visco-elastic properties. The elastomer slab will deform when we start applying the stress, but will soon reach a constantly stretched state. Even in the case of a jammed outer ring and a liquid center region, the slab will reach a constant deformation where the outer ring is stretched more than the center. Only when a change from jammed to liquid or vice versa occurs, the wall stress will change and the elastic slab will deform. Since LSI is sensitive for changes in deformation and not for wall stress directly, we will only observe the changes in wall stress. However, it is not possible to distinguish an increase from a decrease in wall stress. A few stills from a movie captured for a constant shear stress experiment of $80Pa$ are shown in figure 6.5. The full movies of a few experiments at shear stress values of $5, 20, 80$ and $160Pa$ are available from appendix 6.A.3.

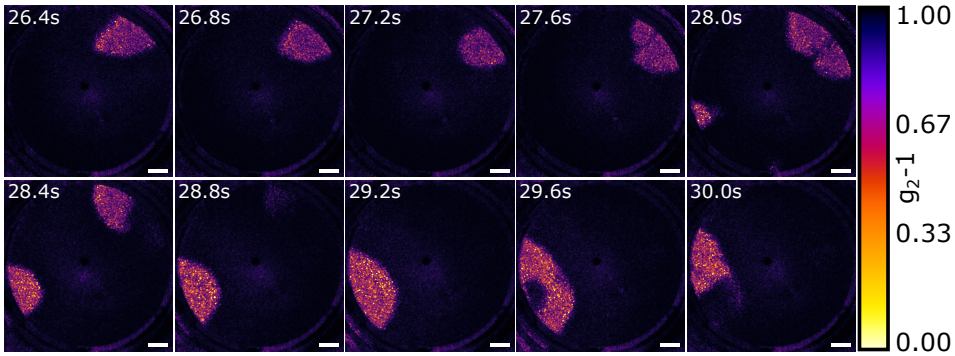

Figure 6.5. LSI images from a 60s movie of wall stress changes as a result of a constant shear stress (80Pa) on a corn starch suspension. The timestamp is shown in the top-left corner of each image and the scale bar is 5.0mm wide and 1.0mm high. The images show areas with a changing wall stress that are very dynamic: they emerge, fluctuate in size and position, move around, split up and disappear. The full movie as well as movies for a 5,20 and 160 Pa constant shear stress are available from appendix 6.A.3.

In the stills we clearly see areas with a changing wall stress and we can observe them emerging, moving around and disappearing. Interestingly, the area size can be larger than a centimeter, which is at least an order of magnitude larger than for example the gap sample thickness, the displacement of the probe during the integration time or the particle size. Also the areas move and expand clockwise and counter-clockwise while the probe only moves in one direction. Even under constant shear stress, the material properties are dynamical in space and time as the jammed regions constantly change in size, shape and location and often appear and disappear. Further work is required to fully determine the origin of these dynamic events and to understand their effect on the global properties of the material.

6.4 Conclusion and outlook

In this chapter we have shown how LSI can be applied to obtain high resolution information on the flow properties of heterogeneous materials with high sensitivity to local fluctuations and a large fov. First we have calibrated the LSI signal of a known deformation of the elastomer sensor slab which agrees very well with theory for a range of amplitudes. With LSI we measure the deformation of this elastomer slab as a sensor for the wall stress during oscillatory rheology measurements of high viscosity silicon oil, water and a high concentration corn starch suspension. We also perform wall stress imaging in the plate-plate geometry and are able to

visualize the jamming front of the concentrated corn starch suspension, which moves to a smaller radius of the rheometer probe as the amplitude of the oscillation increases. Finally we also visualize jamming and un-jamming events in the concentrated corn starch suspension during constant shear stress tests. With those experiments we have shown that LSI is a very promising technique to visualize local flow properties and that it solves the current trade-off between sensitivity and fov size.

We performed our experiments in the plate-plate rheology geometry and chose oscillatory tests, which both might not be the first choice for many rheology experiments. Luckily, the application of LSI to rheology is not limited by the geometry or the type of test. The double plate geometry is often not chosen because the shear rate is not equal over the radius of the plate. Instead the cone-plate is preferred because there the shear rate is equal over the radial direction and thus there is a homogeneous deformation. With full fov imaging the plate-plate shear rate gradient actually is an advantage as we can measure and visualize a range of shear rates at once. Also the plate is easier to align after addition of the elastomer slab, but it is still technically possible to align a conical probe correctly if desired, so this is not a limitation. Using a Couette geometry should even be possible by coating the Couette cup with a homogeneous layer of elastomer, although imaging the curved glass surface is a bit more challenging. With the constant shear stress imaging experiments on the concentrated corn starch suspension we have already shown that performing oscillatory experiments is not a requirement for using LSI to measure local rheology. However, it is a requirement for doing so quantitatively, so when performing a non-oscillatory test one has to be careful when interpreting the data.

The biggest limitation we experienced during these experiments is the range of strains we could measure. The lowest amplitude that we could measure during the calibrations was 10^{-5} times the gap size and the highest amplitude was almost 10^{-2} times the gap size as the speckles would blur too much for higher amplitudes. Although three orders of magnitude is quite good, not all materials will automatically fall in this range. To prevent the need of endless fine-tuning of experimental parameters like gap size and oscillation frequency we propose a few adjustments. Smaller wall stresses can be measured easier with a softer elastomer slab,[28,29] as this will result in larger deformations which are easier to measure. The sensitivity range can also be increased with a more powerful laser which results in shorter required camera exposure times to capture sufficient light. This will in turn result in less speckle blurring and thus usable beta values for a larger wall stress range. Finally changing experimental parameters such as the freqency and

the elastomer/fluid sample thickness can also be used to fine-tune the wall stress without significant changes in the experimental protocol.

In our view the combination of rheology with LSI is a very promising method to obtain information on the local rheology of heterogeneous materials. The method is very versatile and there are not many limitations on which samples can be measured or which rheological experiments can be performed. Therefore we hope this work is just the start of a new avenue of research.

6.A Appendix

6.A.1 Elastomer slab preparation

The elastomer was prepared by mixing Sylgard 184 base in a 30:1 weight ratio with cross-linker. Before mixing, $1.0wt\%$ Titania nano powder with a silica coating was added to the cross-linker and dispersed in a sonication bath for 20 minutes. The Sylgard base was added and mixed with a spatula until a homogeneous white liquid was obtained. The mixture was degassed under multiple vacuum cycles since degassing by centrifuging would cause the Titania to sink. The mixture was cast in a circular mold with a depth of 500μm and a radius of 43mm and covered with the rheometer glass bottom plate. The mold was designed with guides to ensure that the glass plate was centered on the center of the elastomer. Finally the glass plate was clamped tightly against the mold and the whole contraption was placed in a 70°C oven for 48 hours. For the calibration measurement the mixture was not cast in a mold, but directly in the rheometer. The liquid was poured on the rheometer glass bottom plate and the top plate was lowered to a 500μm gap size and the stage temperature was kept at 70°C for 48 hours. Excess elastomer was cut away with a scalpel along the edges of the 43mm diameter top plate. From the rheology measurement shown in figure 6.3c we determine that the modulus of the elastomer slab is 16kPa.

6.A.2 LSI data analysis

First the experimental stretching factor β was determined by collecting 10.000 speckle images of the elastomer slab at rest without a fluid sample loaded on top and no rheometer testing. β can be determined by measuring $g_2(\tau = 0) - 1$ which is equal to $< I^2 > / < I >^2$, where I is the pixel intensity matrix. For our experiments this resulted in a β of 0.50 which means that the maximum correlation we can measure is 1.5 out of the theoretical maximum of 2. To be able to better compare the theory and experiments we scale our further experimental results by $1/\beta$. For the quantitative sweeps we use the same approach to calculate β during our experiments to check if the data is still reliable. If the speckles change faster than the camera exposure time, blurring will occur, we will lose accuracy and the data is not quantitative anymore. If $\beta < 0.45$, which is 90% of the initial value, we do not use the data.

The g_2 was not calculated directly, but was calculated from the d_2. Both correlation functions are interchangeable and are related by $g_2 = g_2(\tau = 0) - \frac{1}{2}d_2$, but the d_2 is less sensitive to noise and intensity drifts.[21] The d_2 is given by

$$d_2(t,x,y,\tau) = \frac{< [I(t,x,y) - I(t+\tau,x,y)]^2 >}{< I(t,x,y) >< I(t+\tau,x,y) >} \tag{6.8}$$

where t is the time the image was recorded, x and y the spatial coordinates of each pixel and τ the correlation time between two images. For the comparison with theory in figure 6.2 this was repeated for a range of τ and temporal averaging occurred over the full range of 3000 images that were collected in 30 seconds for each γ_0. Spatial averaging was done for every radial bin, which contained 10x32 pixels each. Almost the same protocol was used for the amplitude sweep data in figure 6.3a and b with the exception that now only the τ of 0.1 second was used, half the time of one oscillation. For the images in figures 6.3d and 6.4 no spatial averaging was performed but temporal averaging was still done over the whole measuring period of 30 and 60 seconds respectively. For the movies that correspond to the images in figure 6.4a temporal averaging is reduced to 0.2 seconds, one oscillation period. This 0.2 seconds averaging and a 0.1 second τ was also used for the constant shear stress test images in figure 6.5 and the corresponding movies. For the oscillatory tests this full-period averaging and half-period τ should be used. For the constant shear stress tests it is not as critical but we keep the analysis parameters the same for consistency.

6.A.3 Movies

Oscillation tests

The LSI movies of the oscillation tests with 20−90% amplitude show the deformation of the elastomer slab during the full 60 seconds of each measurement. The movies are displayed at a 5x real-time speed and can be viewed from this link or the QR-code in figure 6.A.1.

Figure 6.A.1. QR code to the LSI movies of the oscillatory tests.

Constant shear stress tests

The LSI movies of the constant shear stress tests for $5, 20, 80, 160 Pa$ show the deformation of the elastomer slab during the full 60 seconds of each measurement. The movies are displayed at a 5x real-time speed and can be viewed from this link or the QR-code in figure 6.A.2.

Figure 6.A.2. QR code to the LSI movies of the constant shear stress tests.

6.A.4 Jamming location fit

The radial intensity profiles of the images in figure 6.4a and the sigmoidal fits to obtain the radial location of the jamming front R_j are shown in figure 6.A.3

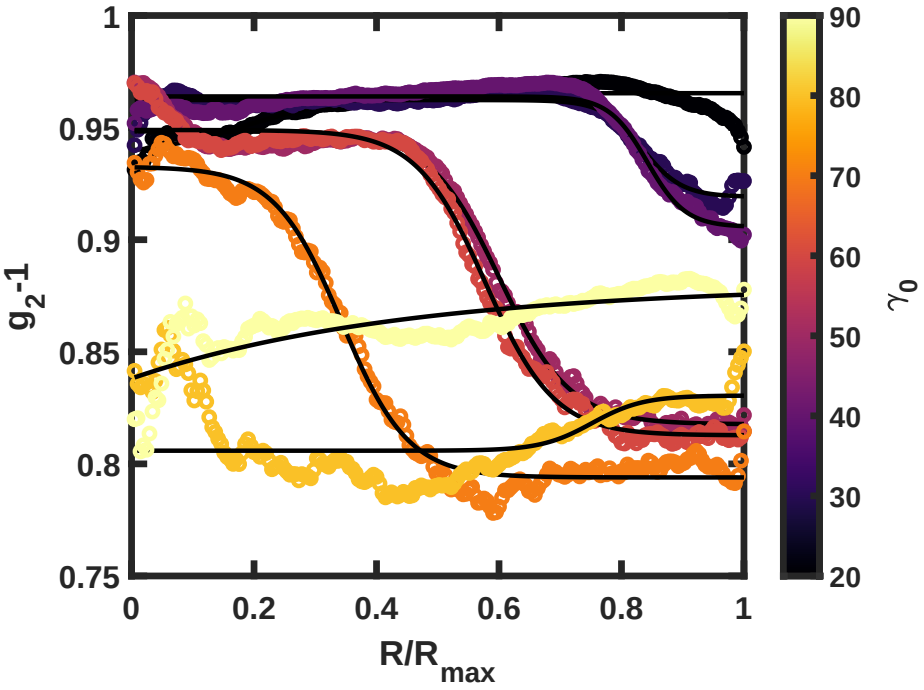

Figure 6.A.3. Sigmoidal fits of the radial intensity profiles of the images in figure 6.4a to obtain the radial jamming front locations R_j/R_{max} for figure 6.4b.

References

[1] T. A. Waigh. *Reports on progress in physics* **68**, 685 (2005).

[2] W. M. Gelbart, A. Ben-Shaul. *The Journal of Physical Chemistry* **100**, 13169–13189 (1996).

[3] R. Kotsilkova, D. Fragiadakis, P. Pissis. *Journal of Polymer Science Part B: Polymer Physics* **43**, 522–533 (2005).

[4] H. H. Winter. *Macromolecules* **46**, 2425–2432 (2013).

[5] P. D. Olmsted. *Rheologica Acta* **47**, 283–300 (2008).

[6] S.-Q. Wang, S. Ravindranath, P. Boukany. *Macromolecules* **44**, 183–190 (2011).

[7] R. Buscall, J. I. McGowan, A. J. Morton-Jones. *Journal of Rheology* **37**, 621–641 (1993).

[8] J. F. Morris. *Annual Review of Fluid Mechanics* **52**, 121–144 (2020).

[9] R. Seto, R. Mari, J. F. Morris, M. M. Denn. *Physical review letters* **111**, 218301 (2013).

[10] A. Fall, F. Bertrand, D. Hautemayou, C. Méziere, P. Moucheront, A. Lemaitre, G. Ovarlez. *Physical review letters* **114**, 098301 (2015).

[11] B. Saint-Michel, T. Gibaud, S. Manneville. *Physical Review X* **8**, 031006 (2018).

[12] R. W. Style, R. Boltyanskiy, G. K. German, C. Hyland, C. W. MacMinn, A. F. Mertz, L. A. Wilen, Y. Xu, E. R. Dufresne. *Soft matter* **10**, 4047–4055 (2014).

[13] C. J. Dimitriou, G. H. McKinley, R. Venkatesan. *Energy & Fuels* **25**, 3040–3052 (2011).

[14] E. Boek, J. Padding, V. Anderson, W. J. Briels, J. Crawshaw. *Journal of non-newtonian fluid mechanics* **146**, 11–21 (2007).

[15] P. T. Callaghan. *Rheologica Acta* **47**, 243–255 (2008).

[16] M. R. Serial, T. Nikolaeva, F. J. Vergeldt, J. van Duynhoven, H. van As. *Magnetic Resonance in Chemistry* **57**, 766–770 (2019).

[17] A. Gauthier, M. Pruvost, O. Gamache, A. Colin. *Journal of Rheology* **65**, 583–594 (2021).

[18] M. Erpelding, A. Amon, J. Crassous. *Phys. Rev. E* **78**, 046104 (2008).

[19] M.-Y. Nagazi, G. Brambilla, G. Meunier, P. Marguerès, J.-N. Périé, L. Cipelletti. *Optics and Lasers in Engineering* **88**, 5–12 (2017).

[20] L. Brunel, A. Brun, P. Snabre, L. Cipelletti. *Optics express* **15**, 15250–15259 (2007).

[21] H. M. Van Der Kooij, R. Fokkink, J. Van Der Gucht, J. Sprakel. *Scientific reports* **6**, 1–10 (2016).

[22] V. Rathee, D. L. Blair, J. S. Urbach. *Proceedings of the National Academy of Sciences* **114**, 8740–8745 (2017).

[23] P. Hébraud, F. Lequeux, J. Munch, D. Pine. *Physical Review Letters* **78**, 4657 (1997).

[24] R. Höhler, S. Cohen-Addad, H. Hoballah. *Physical review letters* **79**, 1154 (1997).

[25] G. Ovarlez, A. V. N. Le, W. J. Smit, A. Fall, R. Mari, G. Chatté, A. Colin. *Science advances* **6**, eaay5589 (2020).

[26] S. Caserta, M. Simeone, S. Guido. *Physical review letters* **100**, 137801 (2008).

[27] H. Mohammadigoushki, S. J. Muller. *Soft Matter* **12**, 1051–1061 (2016).

[28] K. E. Jensen, R. Sarfati, R. W. Style, R. Boltyanskiy, A. Chakrabarti, M. K. Chaudhury, E. R. Dufresne. *Proceedings of the National Academy of Sciences* **112**, 14490–14494 (2015).

[29] L.-H. Cai, T. E. Kodger, R. E. Guerra, A. F. Pegoraro, M. Rubinstein, D. A. Weitz. *Advanced Materials* **27**, 5132–5140 (2015).

Chapter 7

General Discussion

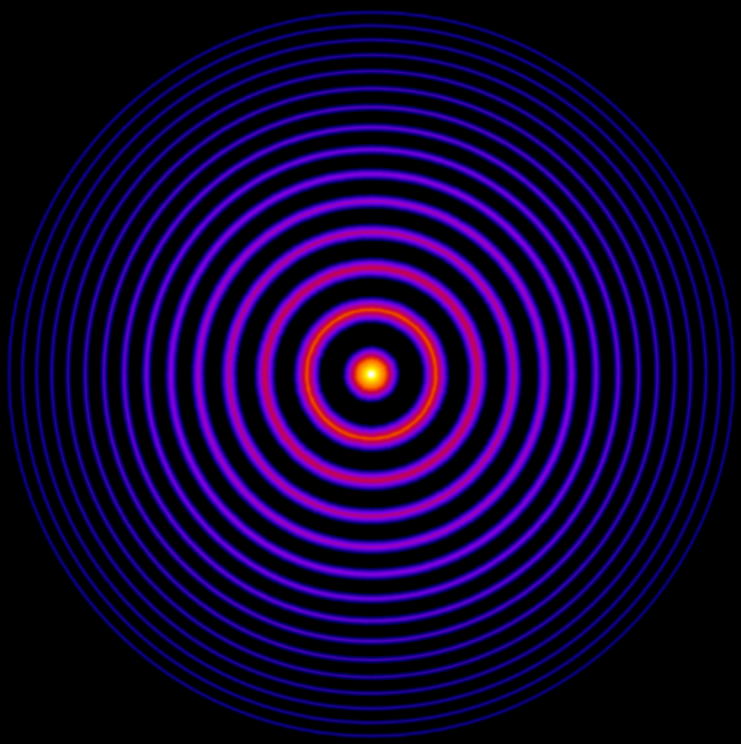

In this thesis, the aim was to make LSI broadly applicable with specific attention for art conservation and soft matter. To make LSI more accessible for these fields, our main focus was on making the technique real-time, portable, simpler and cheaper to use. In this final chapter I will reflect on the developments accomplished and the applications we explored. I will share my view on how LSI can be applied to the art conservation and soft matter topics that were described in the previous chapters. Furthermore, I will show examples and preliminary results of several potential applications which we couldn't fully explore in the time that was available. Finally, I will show the results of a first try at expanding LSI to become a fully three-dimensional imaging technique. The goal of showing those examples is not to fence off possibilities, but to merely show the potential of the technique and inspire even broader application.

7.1 Accessible Laser Speckle Imaging

Before we started applying LSI on a range of materials, we focused on two technological developments: fast data analysis and a simplified set-up. The data analysis was sped up considerably by using the fast Fourier transform (fft) algorithm which is computationally very efficient. Although using the algorithm is as simple as a single line of code, much effort was put in proving that the data contains the same quantitative information as the slower correlation approach. The results obtained from the fft are in a scientific sense the same as the results obtained from the correlation function. However I believe the information from the fft can be accessed a bit more intuitively: when visualizing dynamics with a low frequency, it is clear that the dynamics are slow, and for a high frequency they are fast because frequency and speed both have the s^{-1} unit. When visualizing dynamics with a low correlation time, it is counter-intuitive that the dynamics are fast, and they are slow for a high correlation time because the correlation time's unit is in seconds which is the inverse of the movement speed unit. This is just a small difference, but simpler interpretation will make LSI more accessible.

The fft algorithm realizes a reduction in computation time, and it is extra fast because overhead operations can be skipped in real-time. It removes the need to first save the speckle images, read them from disk afterwards, do the analysis and finally save the result. Because the analyzed data is less than the full set of speckle images, this saves a lot of disk space and removes the need for a high speed hard disk drive. Further simplification of the set-up falls in the trend of increasing availability of smaller, better and faster digital cameras and computers.[1,2] This trend will continue making future LSI machines even smaller, faster and cheaper. Even nowadays, it should already be possible to perform LSI with a high-end

smartphone camera, and the analysis can be done directly on the phone's processor. Only laser illumination should be added since that's typically not included in a phone, but it could be a small clip-on laser. It should be noted that mounting the phone will make the results much better since with handheld smartphone-LSI it will be difficult to keep the phone steady enough. A sturdy tripod should be stable enough as active vibration reduction is expensive for the small effect it will have. It is more efficient to invest in a laser that is more stable, since this will also increase the sensitivity for motion detection.

For LSI to become broadly applied, it has to be accessible. With the mentioned developments the technique has become more accessible by becoming cheaper and less time-consuming. However, to determine a flow speed or diffusion coefficient, one has to do in depth analysis which is not easy to learn. Although this analysis is not very accessible, the data obtained directly from the easily programmable fft algorithm already has a lot of easy to understand quantities available. This result is already enough to directly determine time- and length-scales of dynamical processes. These are quantitative results as well and sufficient for many applications.

7.2 Laser Speckle Imaging for art conservation

The portable set-up makes it possible to apply LSI to art conservation since it is often not desired to move artifacts, so the set-up should move to the artifact.[3,4] The real-time analysis opens up application during cleaning or restoration treatments, or continuous monitoring of objects on display. But before this is put to practice we had to explore which information can be gained from applying LSI to art conservation.

7.2.1 Oil paintings

Our main effort was put into exploring several aspects of oil painting conservation, which is described in *Chapter 3*. We used model paint systems so that we could experiment at will without damaging artworks. First we checked that we could indeed measure the motion of the pigment particles as a result of solvent presence. After soaking the paint in ethanol for 2 hours, we were able to measure pigment motion for over 20 hours, which was much longer than expected. With this experiment we established that LSI is a sensitive technique to measure pigment motion as a result of solvent presence. We did not compare the sensitivity with other techniques, as it is technically challenging to do simultaneous analytical measurements on one paint model. However, a parallel gravimetric analysis with

an electronic balance is easy and should give at least an indication of the LSI sensitivity. It was not possible to exactly determine the nature of the motion, which could be (capillary) flow, diffusion, or swelling of the paint film. With this knowledge, we performed experiments to explore how to employ LSI in a way that can give conservators valuable information that can help them make decisions.

We measured pigment motion as a result of changing air humidity. Monitoring like this can help decide on the optimal storage conditions. Before making decisions more research along this line should be performed. Most importantly for a longer duration and for a range of paint compositions, but perhaps also under different temperature and lighting conditions.

Our initial findings on varnish removal with solvents promised potential for application in the conservation studio. We used LSI to extract two types of information about solvents in oil paint: the retention time, how long the solvent stays in the paint, and spatial variation in solvent application. Those results showed the suitability of LSI to observe changes in the retention time as a result of subtle differences in the painting, such as the aging state, and the cleaning procedure, solvent type and solvent application method. Also spatial variation was only observed for some solvent application methods and for the oldest, cracked paint. This information is useful for a conservator to fine-tune the varnish removal process and minimize solvent exposure, especially since LSI is non-invasive and gives the results in real-time. But the LSI results on its own are not useful since they need to be compared to the actual cleaning result. The goal is to maximize the cleaning result while minimizing the solvent retention time. [5–8]

Working towards a usable protocol for LSI in the conservation studio we performed an in-depth study of the Evolon application method. In *Chapter 3* we learned that Evolon has a homogeneous and reproducible solvent application which can be controlled by varying the solvent loading and application time. Besides determination of the solvent retention time after varnish removal with LSI, the cleaning result was assessed with UV-fluorescence imaging in *Chapter 4*. By adding LSI to the already existing methods that are used during initial cleaning tests, conservators can now finally base their decision on how to clean the rest of the painting on which approach is least invasive.

We have proven that LSI can give important insights in how to minimize varnish removal and the approach is viable. The final hurdles to move from model paint systems to actual oil paintings are purely of practical nature but were not overcome by us since it requires a full redesign of the set-up. First, the working distance needs to increase to give the conservator space to easily perform the cleaning tests in between the set-up and the painting. This lens should also accommodate a bigger field of view so that aiming the LSI becomes less critical. The set-up should

be mounted on a sturdy frame so that it can be aimed at a vertical painting easily in stead of horizontal tabletop measurements on small paint models. The biggest paintings will have a bit of sway since the canvas is not rigid. Since this motion is on a much lower timescale than the pigment motion this noise will not suppress the actual signal. By using a faster camera this effect can be reduced even more. Finally I recommend to add a second camera which collects brightfield light in stead of the speckle light. This will make it easier for the conservator to pick the right spot on the painting and follow the varnish removal process. The two channels should be spectrally split with a bandpass or notch filter under a small angle. Alignment of the two cameras on the same area should be done only once during the construction of the machine and will increase the user-friendliness greatly.

7.2.2 Crack imaging

One application of LSI in art conservation that we explored, but has not yet been discussed in this thesis, is the imaging of crack formation and propagation. In our lab it was shown that LSI can show crack formation and propagation in drying paint[9] and visualize the stresses that build up around a weak part of an elastomer just before it breaks.[10] We apply this knowledge to study cracking in metal and glass as a result of internal stresses.

Cracking is always the result of stress, which leads to local failure of the material.[11,12] External stress, for example bending or stretching of the material, will lead to failure on a weak spot.[13,14] Internal stress buildup, for example as a result of corrosion, can be much more local.[15,16] In both cases the result is eventually the same: in one or a few places the stress buildup will be higher than the strength of the material and a crack will emerge. First a few atoms will split apart and since this makes the material locally even weaker, the crack will start to grow from there to release the stress until a macroscopic crack can be observed. LSI is sensitive to motion, and can thus detect those rearrangements. To observe crack formation with traditional optical methods, the crack has to be at least a few hundred nanometers wide to overcome the diffraction limit. Since LSI can observe nanometric rearrangements, it can detect crack growth much earlier. It is even possible to observe rearrangements as a result of the localized stress and predict where the material will break if the stress continues.

Metal cracking

In metal art objects it is often not the question if an object is cracked, but if the cracks are active. Some cracks are actively cracking as a result of corrosion or

internal stresses. Especially thin metal parts that were hammered into shape at low temperatures contain residual stresses from the crafting process.[17,18] If these internal stresses are slightly increased by minimal corrosion, cracks can appear such as in the plaquette in figure 7.1a. However, if an object is cracked, it does not mean that it is the result of internal stresses. It could also be that in the long history of the object it has not been treated carefully, tipped over and fell, or experienced some other form of external stress. The short extreme stress caused a crack, which now is stable and does not propagate. A stable crack does not need to be treated to conserve the object, while an active crack asks for treatment as soon as possible to prevent structural failure. To release the internal stresses, the object is heated to such a temperature that the metal becomes soft and the atoms can rearrange without crack formation. This treatment is invasive and non-reversible, and is therefore only used as a last resort.[17] It is difficult to determine if a crack is active and to be sure that a crack is the result of internal stress conservators often wait till it grows considerably. LSI is well suited to detect crack activity at an earlier stage and prevent further cracking.

To prove that LSI can detect crack activity we observed metal cracking on a metal dummy object. This dummy piece of brass was bent to induce internal stress and placed in a corrosive ammonia vapor environment. This resulted in enough internal stress to induce cracking, which we were able to image clearly with LSI (example in figure 7.1b). The main challenges were similar to those discussed in section 7.2.1: due to the limited field of view size, it was hard to capture a crack in the field of view and with an added brightfield channel it would be much easier to link observed crack activity to locations in the object. When using LSI on metal objects it is important to keep in mind that the light is scattered extremely strongly, which results in a low penetration depth of a few tens of microns at best.[19] So LSI can only be used to characterize cracks that extend to the surface. Most active cracks are the result of the combination of stress and corrosion cracking (scc). Since corrosion happens at the object surface we expect that LSI is able to capture the vast majority of active cracks.[20]

Glass crizzling

Ancient glass objects can also start cracking apparently spontaneously, but in this case the origin is often chemical. To decrease the melting point of the glass and make it easier to manipulate during production, sodium- or potassium- oxide was added. The cations get embedded in the silica matrix, but they are not fixed. When stored at high humidity, the ions migrate out of the matrix and are replaced by hydrogen ions. Since the hydrogen ions are much smaller, the matrix conformation

changes which results in stress and eventually cracking of the surface layer.[21,22] This surface cracking is called crizzling, which gives the glass a matte appearance (figure 7.1c). No glass is perfectly stable, and even modern glass will crizzle eventually after repeated exposure to aggressive cleaning agents, for example in dishwashers.[23]

Since glass is transparent, there will not be multiple-scattering of light which makes it inherently unsuitable to measure with LSI. Crizzled glass is slightly opaque, which allows some light to be scattered and thus it should be able to monitor some glass crizzling processes with LSI. Specifically the formation of cracks and the cleaning or filling up of the cracks with a restoration glue. It should be noted that the interpretation of the signal is different than normally with LSI. The light scattering entities change during the experiment, thus the resulting dynamics measured are not motion of the light scattering parts, but changes in the presence of light scattering parts. In the case of crack formation, new glass-air interfaces appear which scatter light due to difference in refractive index. When adding cleaning solvent or glue, the interfaces change to glass-liquid which have a lower difference in refractive index and thus scatter less light. To use LSI's unparalleled sensitivity, one has to be sure that the measured intensity changes are a result of the interference pattern changing, and not the absence and presence of single scattering. This can be done by adding a white and non-dynamic background behind the glass that gives a full speckle pattern.

We used LSI to successfully monitor artificially accelerated crizzling in a glass dummy object (figure 7.1d). We were able to accurately visualize the crack formation and also delamination events, where chips of glass will detach from the surface. This result shows that LSI is a promising tool for research in glass conservation as it can reliably visualize the cracking under different circumstances. However, if it is possible to study crizzling opaque glass with light-scattering particles,[24,25] it would be possible to visualize the stress field during and even before the cracking starts.

7.3 LSI for soft matter

In *Chapter 5* we applied LSI to study syneresis, and developed a standardized workflow to systematically study syneresis model systems. We studied the difference between two colloidal gels with a different particle hardness and observed differences in the speed, magnitude and spatial heterogeneity in which they undergo syneresis. This study can be expanded to better understand the phenomenon of syneresis in an effort to ultimately prevent it in food products.[28] First the model systems should be understood better by confirming that the

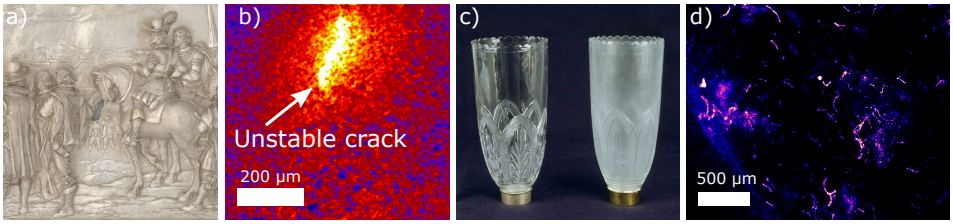

Figure 7.1. a) The hole in the middle of this silver plaquette is the result of untreated cracks.[26] **b)** LSI image of an unstable crack tip in a metal dummy object. **c)** The matte appearance of the right glass is the result of glass disease.[27] **d)** LSI image of accelerated glass disease crizzling in a glass dummy.

differences in behavior between the two are purely because of the particle hardness or softness, and do not depend on other experimental factors such as particle size, concentration, sample chamber dimensions or the heating speed. With those model systems many factors can be easily tuned systematically to understand the mechanisms underlying syneresis.[29] The next step is to investigate food products that commonly exhibit syneresis, and measure those with LSI. The first question to answer is how those products relate to the model systems in terms of spatial dynamics. This will give the first clues on how to prevent syneresis, if the underlying mechanisms of each model system are understood.

Syneresis is a problem that is very specific to a few food products, but LSI can give insight in many more industrial product development processes. LSI has two main types of application that are useful for product development: timescale standardization and imaging of heterogeneities. Timescale standardization is tracking the amount of motion over time so that the magnitude of the syneresis or any other dynamic process can be quantified and compared. LSI can thus objectively show if a different formulation indeed gives an improved result. In our group it was also shown that LSI can accurately determine the open time of paint films, which is an important property that determines how long after application the paint stays liquid enough to merge with paint that is applied later next to it.[9] In the development of more sustainable water-borne coatings it is important to keep properties, such as the open time, similar to solvent based paints. LSI can easily and accurately compare many different formulations to work towards a desired property reliably. Imaging heterogeneities, such as visualization of the spatial heterogeneity during syneresis, can give an insight in the mechanisms underlying certain product properties. Additionally, the imaging part of LSI can also be employed to visualize how a formulation behaves. For example, a homogeneous

application and drying is important for the structural integrity of a coating later on. LSI can help decide early on which formulations are most promising.

Next to the food and coatings industry, LSI is well suited to be applied to products in the cosmetics industry. Products like shampoo, shaving foam and skin cream all are soft materials and scatter light without the addition of tracer particles.[30–32] For example, LSI can reliably compare foam stability if that's a desired property for product performance. Food, coatings and cosmetics are three of the biggest industries worldwide so any improvement that LSI can help achieve will have a huge impact in making products better, cheaper or more sustainable.

Outside of R&D, LSI could be applied to monitoring industrial processes, to maintain production quality or to fine-tune input of ingredients of fluctuating quality. One possibility is to take small samples during production and check the desired properties, much like how different formulations can be compared during the R&D process. The other possibility is to quantitatively check the flow properties directly during production. Regular and light-mayonnaise for example, have very different flow profiles as a result of their composition. Regular mayonnaise is an emulsion at such a high oil droplet concentration that the droplets cannot easily move past each other, the emulsion is jammed. This results in a plug flow, where all droplets move at the same velocity. In light-mayonnaise, the oil fraction is reduced and the product is stabilized by structuring the continuous phase with a biopolymer network. The polymer chains can slide past each other and will do so under flow to minimize friction at the wall. Therefore the flow pattern of light mayonnaise will follow Poiseuille flow, slow at the wall and fast in the middle.[33] Those two patterns can be easily distinguished from each other using LSI (figure 7.2). This approach can be extended to live production monitoring, for example to check if the emulsification of mayonnaise is completed.

When LSI is applied in a lab based setting, such as R&D in industry, ideally samples are chosen so that they only scatter light and not absorb it. The result is that in general only white samples are measured, such as white paint, mayonnaise, yogurt, foam or suspensions with titania, polystyrene or silica particles. Light absorption is avoided because longer photon paths have a bigger chance to be absorbed and thus the assumptions do not hold so expansion of the theorethical framework is required to calculate the flow speed or diffusion coefficient.[34] Light absorption will also heat the sample if the laser power is high, and a higher laser power will be needed since a part of the light is absorbed. But, light absorption can very often be avoided by choosing the wavelength of the laser in a non-absorptive range. Lasers with different wavelengths are often fabricated in the same form-factor, which allows switching the laser with minimal alignment adjustments. Black materials will remain challenging to study with LSI, but it might not be

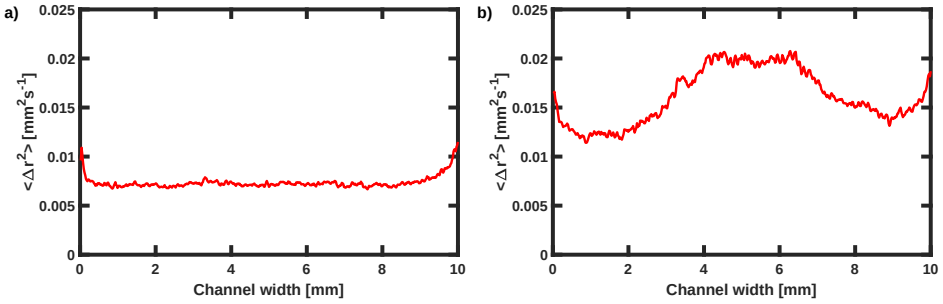

Figure 7.2. a) Flow profile of regular full-fat mayonnaise through a channel with a 10x1.0mm cross-section measured with the portable LSI setup. The high oil droplet content results in jamming of the emulsion, leading to plug flow, where the flow speed is constant over the whole channel width. **b)** Flow profile of light low-fat mayonnaise through a channel with a 10x1.0mm cross-section measured with the portable LSI setup. The polymer network, that gives structure to the mayonnaise at rest, yields under flow. This results in a non-uniform flow, where the flow speed is higher in the middle compared to the edges. The flattened flow speed in the middle of the channel could be a constant flow speed or it could be saturation of the LSI signal.

completely impossible. If the absorption is homogeneously distributed over the material and does not change over time, a speckle pattern can be obtained without heating by decreasing the laser power and increasing the camera shutter time. This limits the measurement to slow dynamics and it is not quantitative, but time-scales and heterogeneities of changes in dynamics can still be measured.

7.4 Rheo-LSI

We briefly explored the combination of LSI with rheology and the first results presented in *Chapter 6* are promising. The information about the local rheology that can now be obtained complementary to the bulk rheological data can be used to link local phenomena such as cooperative motion, shear banding or wall slip to the bulk properties of a material. Our results show that there is a big group of existing rheological experiments that LSI can be applied to, be it quantitative for oscillatory tests, or qualitative for any other test.

In *Chapter 6* the power of LSI becomes most clear: LSI measures dynamics on the nanoscale, which can explain how materials behave on a global scale. This linking of length-scales is a central theme in many scientific disciplines such as chemistry, where the molecular structure explains the bulk material properties, biology, where the nature of cells explains how a multi-cellular organism behaves, or soft matter, where the microscale structure explains the bulk material properties.

The more we know what happens at the different length-scales involved, the better we can explain and predict how materials will behave at the global scale. In this light it is huge advantage if a diagnostic technique can be easily combined with other measurements. Since LSI is a non-invasive and non-contact measurement method, it can complement virtually any other existing analytical technique.

7.5 3D-LSI

A major drawback of LSI is that it is purely a 2D technique, while often 3D information would be valuable. For example in medical imaging, it can be important to know how deep under the skin an observed blood vessel lies.[35,36] Or in the case of solvent penetration into oil paintings, it would be even better if we would be able to measure how deep the solvent penetrates. To date, it is not possible to know if the observed dynamics are close to the surface that is being imaged or that the motion is deeper inside the material.

Each photon, on its random walk through the material, walks an unknown path through the sample. During the collection of many photons, which feature a path length and penetration depth distribution, this results in the mixing of signal from different positions in the sample both in the lateral and depth directions.[37–39] This is much more complicated when compared to existing medical 3D-imaging such as computed tomography (CT). During a CT-scan it is known at all moments where the x-ray originates and where it is detected. Since x-rays travel in a straight line between the source and detector, each location where the photons have been is exactly known. The only variable is whether the photon is absorbed, for example by a bone, which then can be measured. By varying the x-ray source and detector locations a full 3D reconstruction of the bone can be computed from the absorption coefficients of each straight trajectory.[40,41] To reconstruct LSI information in 3D we need to selectively detect photons with a well-defined trajectory and use the correlation information from these trajectories to reconstruct the dynamics in 3D.

7.5.1 Path length selection by time gating

To allow selective detection of photons with a well-defined path, a setup is needed where the source (x_0, y_0, z_0) and detector locations (x_d, y_d, z_d), with separation (ζ) are exactly known, and ideally the path length (s) of the detected photons can be selected (fig. 7.3a). Based on those parameters it is not possible to reconstruct the random walk of a single photon, but many photons will probe roughly the same region if ζ and s are the same. To reconstruct the 3D volume of dynamics, we will need a precise description of the spatial photon distribution for each measurement.

This distribution can be obtained from either random-walk simulations or an analytical solution for the diffusion approximation.[39,42]

Gaining control over the entry and exit-positions can be achieved with relative ease. In regular 2D-LSI with camera detection we already know the exit positions, where each camera pixel corresponds to a different exit-position. To control the entry position we need to change the illumination from plane-illumination with an expanded laser beam, to point-illumination with a focused laser so that all the photons will enter the material from this focus point. The further away the entry and exit point lie, the deeper the photon will have traveled on average (fig. 7.3b).[43–45] However, photon trajectories show a large distribution in path length around their average which results in a large probing region. For a more precise detection, we need to select for photons with a specific path length. The longer the photon path-length, the deeper it has explored into the material (fig. 7.3c). This is again on average, but the deviation is smaller, especially for the shorter path-lengths.

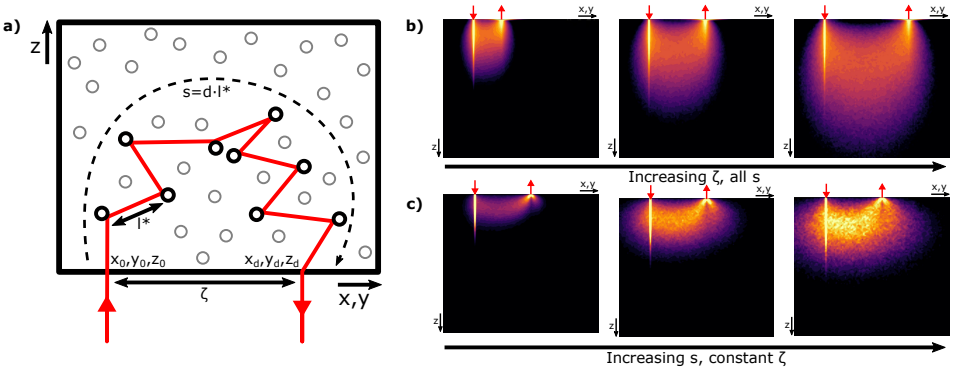

Figure 7.3. **a)** Example of a multiple-scattering trajectory of a photon in an opaque material. The photon enters the material at position x_0, y_0, z_0 and is on average scattered to a random direction after each distance l* that it travels. After travelling a total distance s the photon will exit the material at position x_d, y_d, z_d. ζ is the distance between the entry and exit points on the detection plane xy. This is a 2D representation, but in reality the photons will scatter in three dimensions. **b)** 2D average of many simulated photon-paths with a fixed ζ that increases from left to right. The averages contain a statistical average of the variation in s. With increasing ζ, the photons probe a deeper volume in the sample on average. **c)** 2D average of many simulated photon-paths with a fixed s that increases from left to right. In all three panels ζ is fixed and constant. With increasing s, the photons probe a deeper volume in the sample on average.

7.5.2 Experimental setup

We have designed and built a machine that can measure photon correlation functions with point illumination, point detection and path-length selection. The optical design of this machine is shown in figure 7.4. Point illumination is performed by focussing the laser beam on the sample and scanning the illumination location with galvo mirrors. The detection is now done with an avalanche photon detector (APD) connected to an autocorrelator for maximum sensitivity, but this can later be replaced by a camera. We will measure in the back-scatter geometry as it will give us more specific information on how deep the photons have penetrated before they back-scatter. This is because in the transmission geometry photons will necessarily have traveled through the complete sample thickness to be detected.

For path-length selection we use time-gating, which was proven to work for DWS in the transmission geometry.[46] For the time-gating we illuminate the sample with 200 femtosecond laser pulses from a mode-locked Ti:Sapphire laser source (Mira Optima 900-F), which was pumped by a coherent 5W laser (λ = 532nm, Verdi V5) and tuned to λ = 808nm. The photons from each pulse will scatter randomly in the sample which will result in path-length differences and thus the photons with a longer path will arrive at the detector with a delay. We focus the stretched pulse in a non-linear BBO crystal together with a reference pulse that is still only 200 femtoseconds long. If two photons arrive at the same moment in the crystal, they will form a single photon with double the frequency and energy, and thus half the wavelength.[47] Thus the reference beam will combine with a part of the sample beam that arrives at the same moment and we will be able to measure the correlation of photons with a very narrow range of path-lengths. By changing the exact arrival time of the reference beam with an optical delay stage, we can choose exactly which path-lengths we will detect. A non-colinear frequency doubling geometry is used to spatially separate the time-gated signal from the original two beams. By having both beams hit the crystal under a different angle, the resulting frequency doubled light will have an exit angle in between the exit angle of the sample and reference beams. To also spectrally minimize stray light we use a 420nm short-pass filter in front of the detector so that only the desired 404nm light is left over.

Alignment of the whole setup can be quite tricky as the margins for error are very small, so we developed the following workflow: First align the optical delay stage correctly so that the reference beam remains on target for all possible delays. Replace the sample by a mirror to have maximum light power in the crystal. By using a mirror the amount of light is so high that the whole alignment can be done by eye if the detector is replaced by a fluorescent laser alignment card or a

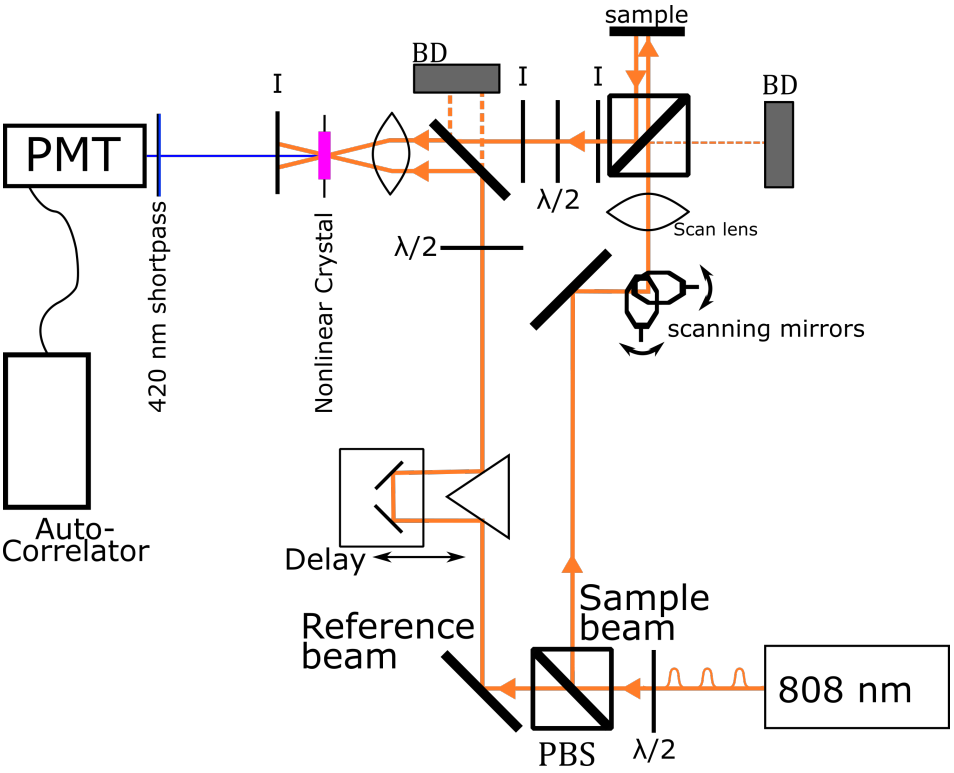

Figure 7.4. Experimental setup to record photon correlation functions with point-illumination, point-detection and time-gating for path-lenth selection. PBS are polarizing beam splitters BD are beam dumps, I are irisses and $\lambda/2$ are half-wave plates. After the PBS below the sample, two irisses are drawn to ensure light from only a small sample area falls on the nonlinear crystal. The half-mirror to recombine the reference and sample beams is a 50/50 non-polarizing beam splitter plate. Another iris is used after the nonlinear crystal to block the frequency-doubled light of each individual beam and to isolate the desired frequency-doubled light that comes from the combination of both beams.

white viewing screen (eg. teflon). Replace the nonlinear crystal by a 100μm or smaller pinhole and focus the sample and reference beams through the pinhole under opposite angles. Put the nonlinear crystal in place of the pinhole again and put a white viewing screen behind the crystal. Rotate the nonlinear crystal and the polarization of the sample and reference beams and try to observe blue light in extension of the two separate beams. Each of the beams will also have frequency-doubling with itself, which contains no usable information for 3D-LSI, but helps in the alignment. Find the rotation angles of the crystal for maximum blue light in each of the two beams and leave the polarization of the beams as

they are. Rotate the crystal to the angle in-between the two optima, move the delay stage quickly back and forth and try to observe blue flashes in the location in between the previous two blue dots. Now you can find the exact location for the delay stage, but this is very delicate as it needs to be within 60μm of the optimal position for 200 femtosecond pulses.

To show that with this 3D-LSI setup we indeed can measure correlation functions for photons with a well-defined path, we show some preliminary results in figure 7.5. In panels a and b we compare the amount of light that we collect of photons with selected path-lengths for two latex nanoparticle dispersions with different concentrations. With increased concentration we detect more photons with shorter paths, but fewer photons with longer paths as l* decreases and thus the photons scatter more often per traveled distance. If we look at the measured correlation functions for increasing path-lengths we see that they decorrelate at shorter τ values. Although the same homogeneous sample is probed and thus each path-length probes exactly the same dynamics, the increasing amount of scattering events increase how much the photons decorrelate as a result of the probed dynamics.

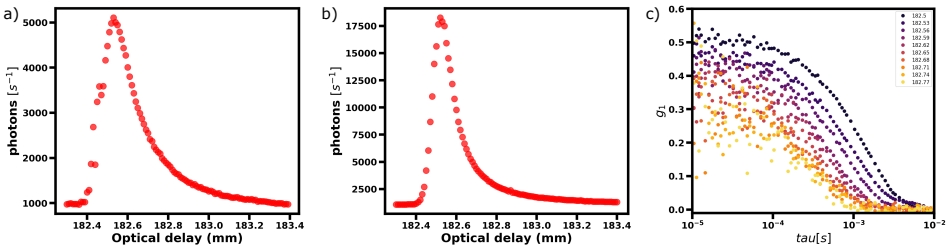

Figure 7.5. a) Photon counts for a range of path-lengths, measured with the 3D-LSI machine for a $3.76wt\%$ dispersion of 240nm diameter latex particles in water. This was measured at an entry-exit distance of 0. **b)** Photon counts for a range of path-lengths, measured with the 3D-LSI machine for a $15.04wt\%$ dispersion of 240nm diameter latex particles in water. For this concentration the measured peak is higher and narrower compared to the lower concentration in panel a, as the photons scatter more often and take a shorter path. This was measured at an entry-exit distance of 0. **c)** Measured correlation functions for the high concentration dispersion from b. For longer path-lengths the correlation functions decay faster as each scattering event results in more dynamics being probed.

7.5.3 Data analysis

Now that we can measure correlation functions with a well-defined path-length, entry- and exit-location, we need a method to convert this to a 3D volume of dynamical information. This 3D volume will be the output of the 3D-LSI machine

and will visualize for example, flow in a blood vessel or a solvent gradient in an oil painting. However, to go from measured correlation functions to a 3D-volume of diffusion coefficients or flow speeds is a difficult task. The other way around is an easier task. If we have a certain 3D volume of dynamical properties, we can accurately predict what we would measure with analytical methods or numerical simulations. However, the inverse problem cannot be solved exactly. Based on this premise we explored two approaches to ultimately perform the operation from measured data to result. First, a numerical deconvolution which used the analytical description of the photon density distribution to iteratively solve the 3D-volume that best fits the measured correlation functions.[48] Secondly, we trained a convolutional neural network (CNN) with simulated data to make a prediction of the 3D-volume based on the measured correlation functions.[49] In this section we will shortly summarize the basics and prime results of each approach. In both cases we assumed that only diffusive motion was present in the measured volume for simplicity, but the approach can be expanded to also determine the nature of the motion or the flow speed.

Deconvolution

The measured correlation functions can be predicted by performing a convolution of the diffusion coefficient matrix with the spatial density distributions of photons through the sample (ρ) for each measurement parameter. In matrix notation:

$$\begin{pmatrix} \Gamma(\boldsymbol{v})_1 \\ \Gamma(\boldsymbol{v})_2 \\ \vdots \\ \Gamma(\boldsymbol{v})_m \end{pmatrix} = \begin{pmatrix} \rho(\boldsymbol{r};\boldsymbol{v})_{1,1} & \rho(\boldsymbol{r};\boldsymbol{v})_{1,2} & \cdots & \rho(\boldsymbol{r};\boldsymbol{v})_{1,n} \\ \rho(\boldsymbol{r};\boldsymbol{v})_{2,1} & \rho(\boldsymbol{r};\boldsymbol{v})_{2,2} & \cdots & \rho(\boldsymbol{r};\boldsymbol{v})_{2,n} \\ \vdots & \vdots & \ddots & \vdots \\ \rho(\boldsymbol{r};\boldsymbol{v})_{m,1} & \rho(\boldsymbol{r};\boldsymbol{v})_{m,2} & \cdots & \rho(\boldsymbol{r};\boldsymbol{v})_{m,n} \end{pmatrix} \begin{pmatrix} D(\boldsymbol{r})_1 \\ D(\boldsymbol{r})_2 \\ \vdots \\ D(\boldsymbol{r})_n \end{pmatrix}$$

Where Γ is the slope of the logarithm of the correlation function versus τ, v contains the measurement parameters ($x_0, y_0, x_d, y_d, s, \zeta$) and D are the diffusion coefficients at locations r(x,y,z). There are m unique sets of measurement parameters and n discretized locations in the sample with a diffusion coefficient. Γ and D are connected through ρ, which is $m \times n$, and gives the chance that each D has been probed during measurement Γ. ρ can either be obtained from an analytical description, or from photon random walk simulations such as in figure 7.3. For the deconvolution we use the analytical description. Matrix multiplication of $\rho * D = \Gamma$ is straightforward, but matrix division to obtain D is not.[50] Therefore we use an iterative approach where we adjust D until the resulting Γ matches the measured

Γ best. The D at which they match is then the solution for the sample that we measured.

To test if it indeed is possible to reconstruct the 3D motion volume for LSI, we performed deconvolutions of computer generated data so that we know what the expected outcome is. We generate a 3D object with a heterogeneous diffusion mapping, multiply it with ρ and add noise that is comparable to the expected experimental noise. Then we use the simultaneous iterative reconstruction technique (SIRT) to perform the deconvolution and obtain the 3D diffusion volume.[51,52] With this approach we could successfully reconstruct the spatial distribution of diffusion coefficients. The results for two geometries are shown in figure 7.6.

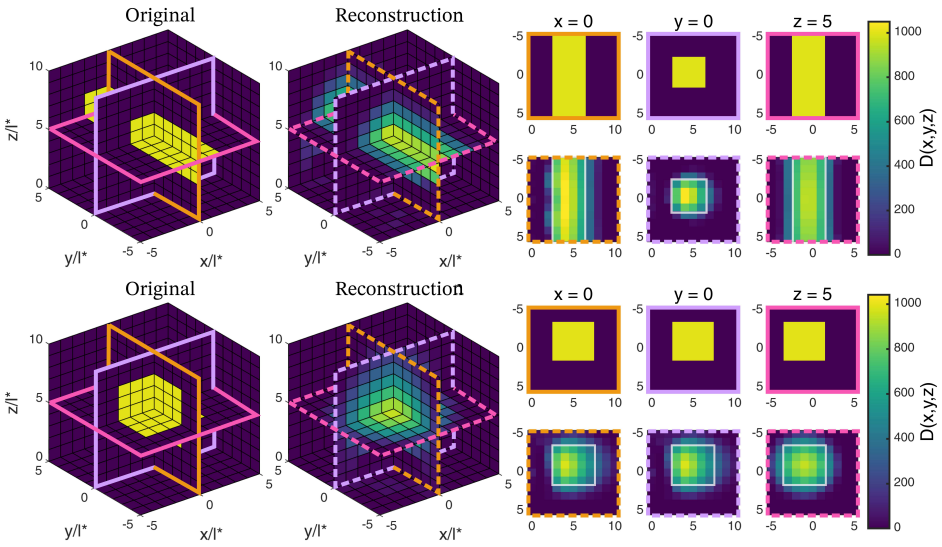

Figure 7.6. On the left are 3D volumes of the objects that were generated (Original), and the results after adding noise and performing the SIRT reconstruction. On the right we show some 2D slices of the original and results to confirm that the algorithm could successfully determine the location and absolute diffusion coefficients of the generated heterogeneity.

Machine learning

We also explore machine learning as a tool to calculate a 3D volume of dynamics from a set of correlation functions. A well-trained neural network is very efficient in recognizing patterns and does predictions in a fraction of the time of an iterative approach as it will complete its work in one set of mathematical operations. We use a CNN as it normally uses filtering to extract features from images.[53,54] The

convolutional layers will extract patterns from the distribution of correlation functions at varying ζ, s and xy_0, and output a map of depth-resolved dynamics. Before the CNN can be used to solve this problem, it needs to be trained on a large set of data where the outcome is known. At first the CNN will do random predictions of 3D-dynamics based on a set of measured correlation functions. We will compare this outcome with the known result to asses how good the prediction was. Then we will adjust the weights of the internal decision network to alter the next outcome. If the new outcome is better, we will keep the changed network, if not we will discard the change and try again. By iterating through a large set of measurements and corresponding outcomes the CNN will learn to recognize patterns and it will become a generalized method to analyze our data.

To generate the training data set we again exploit the fact that it easier to go from a 3D-structure to correlation functions than the other way around. We generate a set of almost 5000 dynamically heterogeneous objects, but this time in 2D to save time and be able to experiment more easily. However, there are no technical or conceptual barriers to go from a 2D to a 3D-reconstruction. The correlation functions are again calculated using a ρ matrix that is $m \times n$, but now we obtain ρ from photon random walk simulations as these results might give a better fit for short path-lengths. Experimental noise is added to the obtained correlation functions and the data is randomly split into a training and a testing set. The CNN is trained on the training set and the testing set is used at regular intervals, without altering the weights, to check for overfitting. A few example objects from the testing set and their predictions are shown in figure 7.7. The CNN was never trained on those objects, so we can treat those predictions as the first time it has seen this data. The predictions correspond very well with the original objects, and thus the CNN has a good predictive power.

7.5.4 Discussion and outlook

We have shown that it is experimentally viable to collect photon correlation functions for light with a well-defined entry-location, exit-location and path-length. We also have shown that with this data it is possible to reconstruct a 3D volume of diffusion coefficients and thus visualize heterogeneous dynamics in 3D. The reconstruction can be successfully performed by either using a deconvolution algorithm with the numerical solution of the photon density distribution ρ as input, or using a CNN which is trained on data that is simulated with photon random walks. However, we could not yet perform this reconstruction on experimental data as the measurement parameters do not match the reconstruction parameters yet. The biggest issue at this moment is that experimentally we can only measure

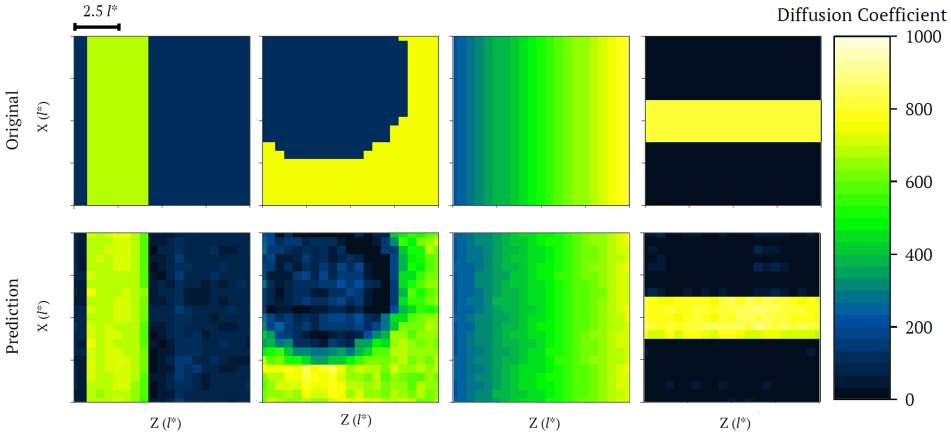

Figure 7.7. A few examples of 2D objects that were generated for the machine learning dataset with a heterogeneous diffusion profile are shown in the top row. Noise was added to the calculated correlation functions and the resulting prediction from the trained CNN is shown in the bottom row. The CNN is capable of predicting both the location of the heterogeneities and the magnitude of the diffusion coefficient accurately.

relatively short path-lengths (few l*) as the photon counts drop off sharply with increasing s and ζ because the majority of photons scatter only a few times. Especially the deconvolution algorithm relies heavily on the data collected with large s and ζ (10-100l*) as for those values the theoretical ρ best matches reality. For the machine learning approach this could be less of a problem as the data can be simulated using only shorter s and ζ. To further advance this project, it is most important to optimize the experimental setup to collect the light more efficiently and allow accurate collection of correlation functions at higher s and ζ. As the amount of light for the longer path-lengths is so limited, I don't think it is viable to combine time-gating with camera detection. To do so would require a broad-field projection of the speckles and reference beam on the nonlinear crystal, which would heavily decrease frequency-doubling as the efficiency of this process increases with the light intensity.[55] Therefore time-gating will always require scanning of both the illumination location with galvo mirrors, as well as scanning the detection location or the sample for full 3D imaging. However it should be possible to collect a profile of the dynamics in z for a material that is homogeneous in x and y without scanning of the detection position or scanning the sample. This would still yield information that was not available before and will be a valuable addition to classical 2D-LSI.

We explored two different methods to perform the data analysis, each with their respective advantages and disadvantages. The deconvolution algorithm is robust

for the measurement parameters such as which s and ζ values are exactly chosen, as ρ can be easily re-calculated to fit the experiment. The algorithm is quantitative as it will predict the correct value and location for D, but loses accuracy with sharp transitions and when getting closer to the edges. A major drawback of the SIRT algorithm is that it is not designed for LSI data, and it takes 10^4 iterations to converge to a solution as the LSI matrices are dense. Compared to 10-100 iterations at maximum for CT data this takes hours extra to calculate a small volume.[51] The machine learning approach also takes a few hours to train the CNN, but when the network is trained it can do reconstructions within seconds. The main drawback is that if you change the measurement parameters, you also have to re-train the network. Generating a data set to train on has to be done carefully because if you train the CNN only on reconstructing sharp transitions in D, it will not learn to reconstruct subtle gradients and vice versa. Although both methods proved to be reliable stand-alone solutions, they can benefit from being combined. If the result that is predicted by the CNN is used as the starting guess for the deconvolution, we can use the advantages of both methods. We will have the speed of the machine learning, and the SIRT algorithm will converge much quicker if the initial guess is good. Furthermore, potential bias from an unbalanced training set will be filtered out by the deconvolution.

Before continuing the project in the described direction I'd like to propose to explore another approach that is experimentally much simpler and can potentially also result in a 3D volume of dynamics. By omitting the time-gating, but keeping the scanning point-illumination the amount of light collected can be greatly increased. I think there should still be enough depth-information left in the point illumination light, as is already shown in figure 7.3b. By increasing ζ, we select photons that have travelled deeper into the sample on average. This will allow us to use a camera for detection, which will save a lot of time because the sample does not need to be scanned. Before building this setup it can be checked if the data will indeed contain enough information to reconstruct a 3D diffusion volume with one or both of the previously described approaches. The only difference is that the signal should be integrated over s. To compensate for the loss of this parameter, Γ can be replaced by the g_1 correlation function for a range of τ values as the correlation cannot be linearized anymore as a result of mixing multiple pathlengths. If this approach indeed results in accurate 3D-reconstructions of the diffusion volumes, the simplicity of the experimental approach will make 3D-LSI much easier to use and will prepare it for broader application.

7.6 Conclusion

In this thesis we have explored ways in which we can improve LSI to make it more accessible and easier to use. We have also explored applications where LSI can be applied to provide insight into existing knowledge gaps. We have looked specifically into art conservation and soft matter, hoping that the developed methods can also be used for application in other fields. It is certain that there are many more insights that LSI can give as there are only few materials where it cannot be applied to. Combining this versatility with the unparalleled sensitivity and the large range of length- and time-scales it can study, LSI really is a unique technique. Although the technology is ready to be used as a mainstream analytical technique, it is still worth it to further study possible avenues to improve on such as expanding the imaging capabilities to 3D.

There will never be an ultimate LSI design as different applications require changes. This can be compared to the differences in technological complexity between the Michelson-Morley experiment and LIGO's gravitational wave measurements. In essence both experiments are identical, but due to the sensitivity requirements the complexity of both measurement devices is vastly different. Similarly, I envision LSI machines which are much simpler than the portable setup from *Chapter 2*, coexist with machines that are much more complex than the time-gating 3D-LSI from this chapter. Hopefully technological development will continue and allow us to study what we now can't even imagine. At the start of this thesis we saw how technological advancement inspired artists. In this thesis we have shown that art can in turn inspire technological advancement to help us explore the unknown.

References

[1] S. Thompson. *Economic of Innovation and New Technology* **18**, 93–106 (2009).

[2] F. H. Khan, M. A. Pasha, S. Masud. *Micromachines* **12**, 665 (2021).

[3] C. L. Sitwell. *The conservator* **7**, 29–33 (1983).

[4] T. Doherty, B. Metro, R. Gomez. *Studies in Conservation* **53**, 50–55 (2008).

[5] A. Phenix, K. Sutherland. *Studies in Conservation* **46**, 47–60 (2001).

[6] S. Prati, G. Sciutto, F. Volpi, C. Rehorn, R. Vurro, B. Blümich, L. Mazzocchetti, L. Giorgini, C. Samorì, P. Galletti, *et al.*. *New Journal of Chemistry* **43**, 8229–8238 (2019).

[7] A. Phenix, R. C. Wolbers, J. Townsend, S. Zumbühl, A. Bartoletti, J. Lee, B. Ormsby, *Conservation of easel paintings* (Routledge, 2020), pp. 549–573.

[8] L. Baij, J. Hermans, B. Ormsby, P. Noble, P. Iedema, K. Keune. *Heritage Science* **8**, 1–23 (2020).

[9] H. M. Van Der Kooij, R. Fokkink, J. Van Der Gucht, J. Sprakel. *Scientific reports* **6**, 1–10 (2016).

[10] H. M. van der Kooij, S. Dussi, G. T. van de Kerkhof, R. A. Frijns, J. van der Gucht, J. Sprakel. *Science advances* **4**, eaar1926 (2018).

[11] G. Colombier, *Prevention of reflective cracking in pavements* (CRC Press, 2004), pp. 14–29.

[12] G. Ghosh, P. Rostron, R. Garg, A. Panday. *Engineering Fracture Mechanics* **199**, 609–618 (2018).

[13] Y. Deng, T. Hajilou, D. Wan, N. Kheradmand, A. Barnoush. *Scripta Materialia* **127**, 19–23 (2017).

[14] E. Tzimas, G. Papadimitriou. *Surface and Coatings Technology* **145**, 176–185 (2001).

[15] D. Van Rooyen. *Corrosion* **31**, 327–337 (1975).

[16] A. Eslami, B. Fang, R. Kania, B. Worthingham, J. Been, R. Eadie, W. Chen. *Corrosion Science* **52**, 3750–3756 (2010).

[17] V. Costa. *Studies in Conservation* **46**, 18–34 (2001).

[18] R. Wanhill. *Journal of failure analysis and prevention* **11**, 178–185 (2011).

[19] T. Wakamatsu, K. Aizawa. *Japanese journal of applied physics* **44**, 4272 (2005).

[20] J. Galvele. *Corrosion science* **35**, 419–434 (1993).

[21] R. H. Brill. *Bulletin of the American Group-The International Institute for Con-servation of Historic and Artistic Works* **12**, 46–47 (1972).

[22] S. P. Koob. *Glass Technology-European Journal of Glass Science and Technology Part A* **53**, 225–227 (2012).

[23] F. Alloteau, O. Majérus, V. Valbi, I. Biron, P. Lehuédé, D. Caurant, G. Lefèvre, A. Seyeux. *Journal of the American Ceramic Society* **104**, 2039–2051 (2021).

[24] I. C. Freestone. *Early vitreous materials* **56**, 173–91 (1987).

[25] R. Arletti, M. Dalconi, S. Quartieri, M. Triscari, G. Vezzalini. *Applied Physics A* **83**, 239–245 (2006).

[26] M. Melin, *Ambrogio Spinola voor de stad Gulik* (1636).

[27] F. . C. Osler, *The Osler Candelabrum* (1883).

[28] S. Mizrahi, *Chemical deterioration and physical instability of food and beverages* (Elsevier, 2010), pp. 324–348.

[29] T. E. Kodger, *Mechanical failure in colloidal gels* (Harvard University, 2015).

[30] G. Maret. *Current opinion in colloid & interface science* **2**, 251–257 (1997).

[31] M. Reufer, A. H. Machado, A. Niederquell, K. Bohnenblust, B. Müller, A. C. Völker, M. Kuentz. *Journal of pharmaceutical sciences* **103**, 3902–3913 (2014).

[32] S. Amin, F. Scheffold, D. Guadino, M. Reufer (2018).

[33] S. Abdali, E. Mitsoulis, N. Markatos. *Journal of Rheology* **36**, 389–407 (1992).

[34] D. J. Pine, D. A. Weitz, J. Zhu, E. Herbolzheimer. *Journal de Physique* **51**, 2101–2127 (1990).

[35] A. K. Dunn. *Annals of biomedical engineering* **40**, 367–377 (2012).

[36] J. Senarathna, A. Rege, N. Li, N. V. Thakor. *IEEE reviews in biomedical engineering* **6**, 99–110 (2013).

[37] P. Zakharov, A. Völker, A. Buck, B. Weber, F. Scheffold. *Optics letters* **31**, 3465–3467 (2006).

[38] P. Barthelemy, J. Bertolotti, D. S. Wiersma. *Nature* **453**, 495–498 (2008).

[39] L. Vitomir, J. Sprakel, J. Van Der Gucht. *Scientific reports* **7**, 1–10 (2017).

[40] W. A. Kalender. *Physics in Medicine & Biology* **51**, R29 (2006).

[41] G. Wang, H. Yu, B. De Man. *Medical physics* **35**, 1051–1064 (2008).

[42] D. Bicout, R. Maynard. *Physica A: Statistical Mechanics and its Applications* **199**, 387–411 (1993).

[43] D. A. Boas, A. G. Yodh. *JOSA A* **14**, 192–215 (1997).

[44] C. W. Lee, R. J. Cooper, T. Austin. *Pediatric research* **82**, 376–386 (2017).

[45] K. Lee. *World journal of clinical oncology* **2**, 64 (2011).

[46] A. Yodh, P. Kaplan, D. Pine. *Physical review B* **42**, 4744 (1990).

[47] e. P. Franken, A. E. Hill, C. Peters, G. Weinreich. *Physical Review Letters* **7**, 118 (1961).

[48] A. Kok, laser speckle imaging for resolving heterogeneous dynamics in three spatial dimensions, Master's thesis, Wageningen University (2021).

[49] B. Visser, Machine learning for 3d-laser speckle imaging, Master's thesis, Radboud University (2021).

[50] S. M. Riad. *Proceedings of the IEEE* **74**, 82–85 (1986).

[51] R. A. Brooks, G. Di Chiro. *Physics in Medicine & Biology* **21**, 689 (1976).

[52] M. Beister, D. Kolditz, W. A. Kalender. *Physica medica* **28**, 94–108 (2012).

[53] R. Yamashita, M. Nishio, R. K. G. Do, K. Togashi. *Insights into imaging* **9**, 611–629 (2018).

[54] S. M. Anwar, M. Majid, A. Qayyum, M. Awais, M. Alnowami, M. K. Khan. *Journal of medical systems* **42**, 1–13 (2018).

[55] S. Suresh, A. Ramanand, D. Jayaraman, P. Mani. *Rev. Adv. Mater. Sci* **30**, 175–183 (2012).

Summary

Laser Speckle Imaging (LSI) is a technique that employs interference of laser light to visualize motion inside materials. Based on the interference of visible light, it can detect motion as small as a few to hundreds of nanometers. LSI is also unique because it is an optical technique that requires an opaque material. Most light-based methods require a transparent material to be able to visualize the inside structure. However, most daily-life materials are not transparent, so their inner structure is not easily studied with optical methods. LSI was originally developed as a medical imaging tool to visualize the motion of red blood cells in veins. It has also been applied in materials science, but only in a few research groups over the world.

While most optical methods visualize structure in semi-transparent materials, LSI visualizes dynamics in opaque materials, and does so with unparalleled sensitivity. Also, the hardware required to perform LSI is relatively simple, just a laser and camera pointed at the same location on the sample surface. With this combination of yielding unique information, while being an experimentally accessible technique, it is surprising that LSI is not more widely applied.

In this thesis we explore a few adaptations to LSI that will help to make it more accessible. We also explore new applications in the fields of art conservation and soft matter science to show the techniques potential and inspire an even broader application.

The interference pattern captured by the camera has to be processed to obtain the spatially resolved dynamics. In **Chapter 2** we develop a new processing algorithm based on the fast Fourier transform, which is both fast and quantitative, providing a dynamic spectrum of the material over a frequency range spanning several decades. In this chapter we show how to apply this algorithm and how to measure a diffusion coefficient with it. We show that this method is quantitative and several orders of magnitude faster than the existing quantitative method. We harness the potential of this new approach by constructing a portable laser speckle imaging setup that performs quantitative data processing in real-time on a tablet.

In **Chapter 3** we put this portable and real-time LSI setup to work, and we explore potential applications in the conservation of oil paintings. We use LSI to measure pigment motion as a proxy for solvent presence in the paint layer. The exposure of oil paintings to organic solvents for varnish removal or to water for the removal of surface dirt can affect the chemical and physical properties of oil paint in an undesired way. Solvents can temporarily plasticise and swell the

polymerised oil paint binding medium, enhancing both the thermal mobility and mechanical displacement of pigments embedded in this film. The enhancement of these microscopic motions can affect both the chemical and physical stability of the object as a whole. By quantifying the amount of solvent in the paint layer, LSI can help gaining insight in the solvent uptake in order to ultimately minimize it during cleaning treatments.

We study mobility in paint films caused by air humidity, spreading of solvents as a result of several cleaning methods, the protective capabilities of varnish and the influence of paint age on the solvent penetration and retention. Our results show that LSI is a powerful technique to study solvent penetration during oil paint cleaning and can visualize both the solvent retention time in the paint and how homogeneous several popular solvent application methods are.

We more closely study one of those solvent application methods in **Chapter 4**. Evolon® CR is increasingly used in paintings conservation for varnish removal from oil paintings. Its key benefits over traditional cotton swabs are limiting solvent exposure and reducing mechanical action on the paint surface. However, this non-woven microfilament textile was not originally engineered for conservation use and little is known about its chemical stability towards organic solvents. Moreover, the physical processes of solvent loading and release by Evolon® CR, as well as solvent retention inside paint after cleaning, have not been studied. We investigate these three topics using a multi-analytical approach, aiming for an improved understanding and optimized use of Evolon® CR for varnish removal. Our results show that the tissue is generally chemically and physically stable to organic solvents when exposed on timescales that are typical in conservation practice. However, a pre-treatment step of Evolon® CR is necessary to avoid the release of unwanted saturated fatty acids into the paint during varnish removal. We show that the primary mechanism of solvent uptake by the fibers is *ad*sorption rather than *ab*sorption and that the dominant factor dictating the maximum solvent load is the volume of the voids between the fibers. Finally, solvent induced dynamics after application of solvent-loaded Evolon® CR within the paint film was monitored using LSI on model paints. We developed a method to quantify solvent-retention in real-time and revealed that the presence of varnish on paintings results in lower dynamics of solvents within the paint in comparison to unvarnished paint. Comparing various solvents, it was found that cleaning with acetone resulted in a roughly six-fold increase in dynamics compared to ethanol and isopropanol. We also combine LSI with UV-imaging to compare the degree of varnish removal with the amount of solvent in the paint. By combining those two measures, a conservator could find the optimal treatment by maximizing the cleaning result with minimal solvent penetration.

In **Chapter 5** we move our attention from art conservation to soft matter. Syneresis, the compaction of a material accompanied by fluid expulsion, is a typical mechanical instability which exists among colloidal gel based materials and that negatively affects the quality of relevant applications such as yoghurt and mayonnaise. We shed light onto the internal dynamics of model colloidal gels undergoing syneresis with LSI. The resulting dynamical maps capture the distinct differences in spatial and temporal relaxation patterns between colloidal gels comprising solid and liquid particles. This indicates different mechanisms of syneresis between the two systems and highlights the importance of the constituent particles and their mobile or restrictive interfaces in the mechanical relaxation of the colloidal gels during syneresis.

In **Chapter 6** we combine LSI with rheology to simultaneously measure the global and local flow properties during one measurement. Rheological properties of complex fluids are often governed by localized events such as cooperative motions, shear banding or wall slip. Current methods to perform rheological imaging either lack the resolution to resolve individual events or rely on optical imaging which requires transparent samples thereby precluding the study of many industrially-relevant materials. We show how LSI can be used to measure the local flow behavior with a high sensitivity over the full field of view. We quantitatively visualize localized areas with jamming in a concentrated corn starch suspension under oscillatory deformation in a double plate geometry. The approach is not limited to the rheological constraints of this test type and geometry. With a constant shear stress tests we capture intermittent jamming and un-jamming events in the same concentrated corn starch suspension.

In the **General Discussion** we reflect on the progress we made to making LSI more accessible, and discuss potential applications, limitations and how to proceed. A major part of this chapter is an approach to extend LSI to 3D-imaging. We discuss how performing LSI with point-illumination and time-gated detection can provide enough information to reconstruct the full 3D-volume of dynamics in a material. We build the machine that can do this measurement and show the proof of concept. We also develop two separate methods, using a decorrelation algorithm or machine learning, to reconstruct the 3D-volume of dynamics from a set of correlation functions. We have made technical progress and we have shown a few examples of potential applications for LSI in this thesis. Although our work may help in making LSI more accessible, we mainly hope to inspire application in other fields by showing what is possible.

List of publications

This thesis

- Jesse Buijs, Jasper van der Gucht and Joris Sprakel, 'Fourier transforms for fast and quantitative Laser Speckle Imaging', *Scientific reports* **9.1**, 1–9 (2019). **(Chapter 2)**
- Lambert Baij, Jesse Buijs, Joen J. Hermans, Laura Raven Piet D. Iedema, Katrien Keune and Joris Sprakel, 'Quantifying solvent action in oil paint using portable laser speckle imaging', *Scientific reports* **10.1**, 1–12 (2020). **(Chapter 3)**
- Lambert Baij, Chun Liu, Jesse Buijs, Alba Alvarez Martin, Dorien Westert, Laura Raven, Norbert Geels, Petria Noble, Joris Sprakel and Katrien Keune, 'Understanding and optimizing Evolon® CR for varnish removal from oil paintings', *Heritage Science* **9.1**, 1–17 (2021). **(Chapter 4)**
- Qimeng Wu, Jesse Buijs, Sanne de Groot, Hanne M. van der Kooij, Jasper van der Gucht and Thomas E. Kodger, 'Spatially heterogenous dynamics in colloidal gels during syneresis', *submitted* **(Chapter 5)**
- Jesse Buijs, Akankshya Majhi, Joshua Dijksman and Jasper van der Gucht, 'Laser Speckle Imaging for sensitive and full-frame wall-stress imaging in rheology', *in preparation*. **(Chapter 6)**

Other work

- Hanne M. van der Kooij, Slav A. Semerdzhiev, Jesse Buijs, Dirk J. Broer, Danqing Liu and Joris Sprakel, 'Morphing of liquid crystal surfaces by emergent collectivity', *Nature communications* **10.1**, 1–9 (2019).
- Jochem Bronkhorst, Michiel Kasteel, Stijn van Veen, Jessica M. Clough, Kiki Kots, Jesse Buijs, Jasper van der Gucht, Tijs Ketelaar, Francine Govers and Joris Sprakel, 'A slicing mechanism facilitates host entry by plant-pathogenic Phytophthora', *Nature Microbiology* **6.8**, 1000–1006 (2021).

Acknowledgements

Ik heb de afgelopen vier jaar met veel passie gewerkt aan dit boekwerk. Het was echter niet tot stand gekomen zonder mijn medewetenschappers met wie ik heb samengewerkt en die mij hebben geinspireerd. Ik ben er van overtuigd dat wetenschap een teamsport is. Alle inhoudelijke hoofdstukken in deze thesis zijn immers het gevolg van een samenwerking. Zelfs hoofdstuk 2, waar alleen de namen van mij en mijn begeleiders boven staan, is deels geinspireerd op mijn leerzame afstudeerstage. Ik wil in dit stuk de tijd nemen om iedereen te bedanken die op welke manier dan ook heeft bijgedragen aan dit project.

Jasper en Joris, enorm bedankt dat jullie mij de kans hebben gegeven om aan dit onderwerp te werken. Voordat ik begon, wist ik zeker dat dit een buitenkans was. Dat het onderwerp LSI en jullie manier van begeleiden goed bij mij pasten heb al tijdens mijn BSc en MSc theses ondervonden. Daardoor wist ik dat ik van een uitermate fijne sfeer en werkomgeving verzekerd zou zijn. Jullie zijn erg betrokken en hebben mij tegelijkertijd de ruimte gegeven om zelfstandig dingen te onderzoeken. Dankzij jullie flexibele opstelling kreeg ik altijd hulp en input als ik ergens tegenaan liep. Dankzij jullie geweldige begeleiding heb ik ruim vier jaar met veel plezier onderzoek gedaan en is deze thesis geworden zoals hij nu is.

I want to thank everyone from PCC. You are wonderful colleagues and the atmosphere in the lab convinced me to start this job in the first place. Thank you for all the useful meetings and discussions, the coffee, cake and lunch breaks, labtrips, borrels and bbq's. I hope the frequency of social events will go back to pre-corona levels this coming year. PCC has a very large and diverse shared knowledge base and I have definitely learned something from all of you. There are two people I want to mention separately as they have learned me how to use LSI. Hanne: you're the true LSI queen, and Remco: thanks for your help with solving all the ad-hoc technical details. A special thanks to my wonderful colleagues from the quarantine-zone. I'm happy that I can share the office with you for a bit longer. Jochem, carpooling in the final two years has resulted in a nice start and end to our working days. I'm going to miss this!

Our collaboration with the Rijksmuseum was the surprise of my PhD: four years ago, we all had no idea that combining our fields would be possible. And now we have two published collaborative papers and we will continue with a follow-up project. Thanks to everyone involved in this collaboration, especially Katrien, Lambert, Joen and Tracy, for your enthusiasm and dedication. It was only possible to make our research successful because you want to fully understand LSI. I think you are all role-models for multi-disciplinary scientists. I enjoyed working with

you and am very happy that I can continue working with you in the coming months!
Ik wil graag de studenten bedanken die ik met erg veel plezier heb mogen begeleiden: Thijmen, Sanne, Dorien, Bas, Brent, Aimee en Sven. Ik ben bevoorrecht door jullie enorme enthousiasme, positieve energie en tomeloze inzet. Dit heeft geleid tot mooie resultaten, waarvan ik er veel in deze thesis heb laten zien.
Ondanks dat ik van mijn hobby mijn werk heb gemaakt, had ik buiten mijn werk ook genoeg om naar uit te kijken zoals lekker eten, spelletjes doen, gamen of muziek maken. Hiervoor wil ik mijn familie en vrienden bedanken. Jullie toonden altijd oprechte interesse in mijn werk, wat het extra leuk maakte. Marlon, heel fijn dat je met zoveel enthousiasme de thesis-draft hebt doorgelezen en dat je er nog schoonheidsfoutjes uit hebt gevist.
Dankzij de opvoeding en steun van mijn ouders ben ik gekomen waar ik nu sta. bedankt voor deze goede basis, papa en mama. Dankzij jullie goede voorbeeld heb ik geleerd om zelf keuzes te maken. Dat hebben jullie ook altijd gesteund, zelfs toen ik wat sneller het huis uit ging dan jullie hadden verwacht.
Als laatste, maar ook als belangrijkste: Annelie, ik vond het heel fijn dat ik er bij was toen jij dokter werd, en ik ben ook heel blij dat jij er bij bent als ik afstudeer. Met jou gaan samenwonen was de beste beslissing uit mijn leven, ook al hebben we nu een uit de hand gelopen hoeveelheid cavia's.

About the Author

Jacob Jesse Buijs was born on 23 August 1993 in Schiedam, The Netherlands. He obtained his VWO diploma from the Christelijk College Nassau-Veluwe in Harderwijk in 2011 with a major in Nature & Technology.

Jesse went on to study Molecular Life Sciences at Wageningen university. During the bachelor thesis, his interest in optical methods started to grow when he researched the melting of colloidal crystals induced by optical tweezers. In this period he also completed an educational minor, for which he taught chemistry at his former high school under the supervision of his previous chemistry teachers Henk van Nijhuis and Peter Breure. During his masters Jesse specialized in physical chemistry. He learned about Laser Speckle Imaging during his masters thesis for which he built a low-cost LSI setup from a Raspberry Pi, a smartphone-grade camera and a six-dollar laser. He got more training in optics during a research project at the Colorado State University, USA, where he used 2D-infrared spectroscopy to study aggregation of conjugated polymers under the supervision of Prof. Amber Krummel.

After finishing his masters in 2017, Jesse joined the Laboratory of Physical Chemistry and Soft Matter as a PhD candidate. During the following four years he worked on the development and application of Laser Speckle Imaging under the supervision of Prof. Joris Sprakel and Prof. Jasper van der Gucht. The research performed during that project has resulted in this thesis. In 2022 Jesse will continue this work in a project that aims to design a LSI setup and software that art conservators can use in their daily work.

Overview of completed training activities

Discipline-specific activities

- Course 'Big Data', VLAG/SSB, Wageningen, 2019.
- SoftComp Annual Meeting, SoftComp, Primosten (HR), 2018.†
- NanoRestart Workshop, Uva/Rijksmuseum, Amsterdam, 2018.†
- Interpore Conference, Interpore, Valencia (ES), 2019.‡
- JMBC Meeting, JM Burgers Centrum, Lunteren, 2019.†
- CHAINS, NWO, Veldhoven, 2019.
- CHAINS, NWO, Online, 2020.
- Physics at Veldhoven, NWO, Online, 2021.
- SoftComp Annual Meeting, SoftComp, Online, 2021.
- Mini Symposium Rheology, VLAG/PCC, Wageningen, 2021.†

General courses

- VLAG PhD week, VLAG, Baarlo, 2018.
- Journal Club, PCC, Wageningen, 2018–2019.
- Competence Assessment, WGS, Wageningen, 2020.
- Critical Thinking and Argumentation, WGS, Wageningen, 2020.
- Research Data Management, WGS, Wageningen, 2020.
- Scientific Integrity Session, AFSG-PCC, Wageningen, 2021.
- Scientific Integrity, WGS, Wageningen, 2021.
- Career Assessement, WGS, Wageningen, 2021.
- Proposal Writing, VLAG, Wageningen, 2021.

Other activities

- Preparation of research proposal, PCC, 2018.
- Controlling Multiphase Flow consortium meetings, ISPT, Wageningen & Amsterdam, 2018–2021.†
- Group Meetings and Colloquia, PCC, 2018–2021.†
- Lab Journal Discussions, PCC, 2018–2021.
- Course 'Deep Learning in Data Science', GRS, 2020.
- Sprakel group meetings, PCC, 2018–2021.†

---

† oral presentation

‡ poster presentation

The work in this thesis is part of the research programme Controlling Multiphase Flow with project number 680-91-012, which is (partly) financed by the Dutch Research Council (NWO) and cofunded by TKI-E&I with the supplementary grant *TKIToeslag* for Topconsortia for Knowledge and Innovation (TKI's) of the Ministry of Economic Affairs and Climate Policy.

LaTeX template by Hanne van der Kooij

Printed by ProefschriftMaken || www.proefschriftmaken.nl